

**ENSURING FATIGUE PERFORMANCE VIA LOCATION-SPECIFIC  
LIFING IN AEROSPACE COMPONENTS MADE OF TITANIUM  
ALLOYS AND NICKEL-BASE SUPERALLOYS**

by

**Ritwik Bandyopadhyay**

**A Dissertation**

*Submitted to the Faculty of Purdue University*

*In Partial Fulfillment of the Requirements for the degree of*

**Doctor of Philosophy**



School of Aeronautics and Astronautics

West Lafayette, Indiana

May 2020

**THE PURDUE UNIVERSITY GRADUATE SCHOOL  
STATEMENT OF COMMITTEE APPROVAL**

**Dr. Michael D. Sangid, Chair**

School of Aeronautics and Astronautics

**Dr. Weinong Chen**

School of Aeronautics and Astronautics

**Dr. Fionn P. E. Dunne**

Department of Materials, Imperial College, London

**Dr. Ganesh Subbarayan**

School of Mechanical Engineering

**Dr. Tyler N. Tallman**

School of Aeronautics and Astronautics

**Approved by:**

Dr. Gregory A. Blaisdell

*Dedicated to the Women in my life – my mother, wife, mother-in-law, and grandmothers. It is their unconditional love, sacrifice, and blessings, which have made this thesis possible.*

## ACKNOWLEDGMENTS

Words are not enough to express my gratitude towards Prof. Michael D. Sangid, my thesis supervisor. His meticulous advice mingled with care and compassion has shaped the present thesis from conception to completion. The research problems presented here have been engaging, exciting, and challenging. Again, thanks to Prof. Sangid for allowing me to work on topics that are scientifically important and industrially relevant. My journey during the work of this thesis has not always been smooth and pleasant. However, irrespective of the situation, Prof. Sangid still stood by my side and did what the situation demanded. Going beyond a mere thesis supervisor, Prof. Sangid took a keen interest in my career aspirations. He ensured I publish research articles in the top-tier international journals, present my work in well-renowned conferences, interact with some of the leading international experts in my area of research, get teaching experience at Purdue University, and become committee members of professional bodies. Being an extraordinary advisor, Prof. Sangid made sure I flourish as a professional. At the same time, he set the highest standards in the advisor-advisee relationship, which is quite a challenge for me to uphold in future career endeavors.

I have been fortunate enough to work and collaborate with the bright minds in our ACME<sup>2</sup> lab. My sincere thanks are due to Mr. Prithivirajan Veerappan, Mr. John Rotella, Mr. Ajey Venkataraman, Dr. Alberto Mello, Dr. Kartik Kapoor, and Dr. Diwakar Naragani. Prithivi taught me how to create statistically equivalent microstructures and wrote Section 3.1.1 of this thesis. John carried out all backscatter electron imaging in Section 5.1.4. Alberto, along with one of our past summer interns, Mr. Michael Reinhold, performed all experiments in Section 5.2. Prithivi, Ajey, and Kartik provided me with the ABAQUS UMATs that I used while solving problems in Chapters 3, 4, and 5, respectively. Diwakar characterized all the inclusions using micro-computed tomography for the work presented in Chapter 4 and offered discussion during the reconstruction of energy dispersive X-ray diffraction experiments data in Section 5.1. Additionally, I am grateful to Ms. Priya Ravi, Mr. Saikiran Gopalakrishnan, Mr. Gregory Scofield, Mr. Sven Gustafson, Mr. Brandon Mackey, Mr. John Ferguson, Ms. Alejandra Ortiz, Mr. Ronald Agyei, Mr. Imad Hanan, Mr. Stephen Carter, Mr. Michael Waddell, Mr. Samuel Noone, Mr. Paul Gardener, Mr. Alexander Finch, Ms. Alexandra Mallory, Dr. Andrea Rovinelli, and last but not the least Dr. Andrea Nicolas for making the lab a vibrant place to work.

It would have been impossible to carry out the present research without the generous financial support from Rolls-Royce Corporation, DARPA (Grant/contract numbers N66001-14-1-4041 and HR0011-12-C-0037), LIFT (Grant Number LIFT TMP-3a), Purdue University (Lynn Fellowship from OIGP and Teaching Scholarship from the School of Aeronautics and Astronautics), and NSF (Grant Number CMMI 16-51956). Thanks are due to Mr. Jonathan P. Dubke, Mr. David E. Mills and Dr. Michael G. Glavicic from Rolls-Royce Corporation, and Dr. Mark Hardy, Dr. Christos Argyrakis, Dr. Duncan Maclachlan and Dr. Han Tai from Rolls-Royce Plc for providing with the materials/experimental data and offering critical discussions; Dr. Alonso D. Peralta from Honeywell Aerospace for input on the DARPA Open Manufacturing Program; Dr. Tom Broderick from AFRL, Dr. Austin Mann from Boeing, and Dr. Michael Eff from EWI for assistance on the LIFT Linear Friction Welding project. Additionally, I acknowledge the help from beamline scientists Dr. Jun-Sang Park and Dr. Andrew Chuang from Advanced Photon Source at Argonne National Laboratory during the energy dispersive X-ray diffraction experiments and subsequent data reconstruction. Use of the Advanced Photon Source was supported by the US Department of Energy, Office of Science, Office of Basic Energy Sciences, under contract number DE-AC02-06CH11357.

My family has been a lifeline during the entire course of the work of this thesis. It would have been impossible to survive as a graduate student at Purdue in the absence of unconditional love and support from my parents, mainly from my mother. Although they were more than 8000 miles away from me, I have always felt their presence in spirit. Almost six months after I joined Purdue, I met Sneha, whom I married very recently (in Jan 2020). Almost throughout my entire thesis work, she has extended her support beyond my imagination and expectation. Moreover, the kind of support, love, and encouragement I received from my in-laws have been exemplary. I have been lucky to be surrounded by some of the strongest women I have ever seen – my mother, wife, mother-in-law, and my grandmothers. It is their unconditional love, support, sacrifice, and blessings, which have made this thesis possible. I dedicate this thesis to them.

# TABLE OF CONTENTS

LIST OF TABLES .....	10
LIST OF FIGURES .....	11
ABSTRACT .....	18
1. INTRODUCTION .....	22
1.1 Background .....	22
1.2 Pertinent research questions .....	23
1.3 Research Contributions .....	25
1.4 The layout of the thesis .....	26
2. LITERATURE REVIEW .....	28
2.1 A brief review on fatigue life prediction approaches .....	28
2.2 Challenges in the fatigue life prediction in Ni-base superalloys .....	30
2.3 Linear friction welding in Ti alloys: residual stress and fatigue performance .....	33
2.4 Anomalous mean stress sensitivity in Ti-6Al-4V .....	35
2.5 Uncertainties from crystal plasticity finite element simulations .....	38
3. BUILDING CONFIDENCE IN THE CRYSTAL PLASTICITY FINITE ELEMENT SIMULATIONS .....	40
3.1 Uncertainty quantification in the mechanical response of crystal plasticity simulation... 40	
3.1.1 Genetic algorithm-based crystal plasticity parameter estimation framework .....	40
Creation of 3D finite element model of the polycrystalline material .....	41
Crystal plasticity model .....	44
Parameter estimation using genetic algorithm .....	45
3.1.2 First-order second-moment method .....	48
3.1.3 Results and discussion .....	49
3.1.4 Summary .....	56
3.2 Microstructure-sensitive critical plastic strain energy density criterion for fatigue life prediction across various loading regimes .....	58
3.2.1 Crystal plasticity finite element simulation framework .....	58
Materials processing .....	58
Discretized 3D polycrystalline microstructures .....	59

Crystal plasticity model and parameter estimation .....	61
Slip system averaging scheme.....	63
3.2.2 Critical plastic strain energy density criterion for fatigue life estimation .....	64
3.2.3 Bayesian calibration of the critical plastic strain energy density .....	65
Bayesian inference method .....	68
Markov Chain Monte Carlo sampling and Metropolis-Hastings algorithm .....	69
3.2.4 Results.....	70
Critical stored plastic strain energy density .....	70
Fatigue life prediction .....	72
3.2.5 Discussion.....	74
3.2.6 Summary.....	79
<b>4. ANALYSIS AND PREDICTION OF COMPETING FAILURE MODES IN A NICKEL- BASE SUPERALLOY .....</b>	<b>80</b>
4.1 Analysis of competing failure modes .....	80
4.1.1 Crystal plasticity finite element simulation framework.....	81
Material characterization.....	81
Polycrystalline microstructure with inclusion and debonded region .....	82
Crystal plasticity model and parameter estimation .....	84
4.1.2 Damage indicative parameter .....	87
4.1.3 Results.....	89
Effect of loading direction.....	89
Effect of inclusion stiffness.....	90
Effect of the debonded region and its location.....	91
Effect of the microstructural variabilities around the inclusion .....	92
Effect of the inclusion size .....	94
Effect of the dissimilar coefficient of thermal expansion .....	95
Effect of the residual stress .....	97
Effect of the distance of the inclusion from the free surface .....	98
4.1.4 Discussion.....	99
4.1.5 Summary.....	102
4.2 Prediction of competing failure modes .....	103

4.2.1	Statistically equivalent microstructures with and without inclusions.....	103
	Thermo-mechanical properties of the inclusions .....	104
	Inclusion size and morphology .....	105
	Inclusion position within the polycrystalline aggregate.....	106
4.2.2	Results.....	107
	Critical stored plastic strain energy density as a function of temperature.....	107
	Fatigue life prediction with associated failure modes .....	110
4.2.3	Summary.....	113
5.	ASSURANCE OF PERFORMANCE IN THE LINEAR FRICTION WELDED TITANIUM ALLOYS.....	115
5.1	Residual strain analysis in linear friction welds of similar and dissimilar Ti alloys using energy dispersive X-ray diffraction .....	115
5.1.1	Materials and methodology .....	115
	Materials.....	115
	Weld parameters and heat treatment .....	118
	Electron microscopy characterization .....	118
5.1.2	Residual strain measurement .....	119
	Energy dispersive X-ray diffraction experiment.....	119
	Data post-processing .....	123
5.1.3	Residual strain results .....	126
5.1.4	Discussion.....	130
	Ti64-Ti64 LFW in the as-welded condition.....	131
	Ti64-Ti64 LFW in the heat-treated condition .....	134
	Ti64-Ti5553 LFW in the as-welded condition.....	137
	Ti64-Ti5553 LFW in the heat-treated condition .....	140
5.1.5	Summary.....	142
5.2	Crack initiation and heterogeneous deformation of Ti-6Al-4V during high cycle fatigue at high R ratios.....	143
5.2.1	Material and experimental methods.....	143
5.2.2	Crystal plasticity finite element simulation framework.....	146
	Kinematics and kinetics .....	146

Discretized polycrystalline microstructures and crystal plasticity model parameters .....	148
5.2.3 DIC results .....	151
Crack initiation .....	151
Strain accumulation in macrozones .....	154
5.2.4 Crystal plasticity results and discussion .....	158
Crack initiation .....	158
Heterogeneous deformation as a function of stress ratio .....	163
Heterogeneity in microstructure having random texture .....	164
Heterogeneity in the micro-textured regions .....	170
5.2.5 Summary .....	175
6. CONCLUDING REMARKS AND FUTURE WORK .....	178
6.1 Concluding remarks .....	178
6.2 Future work .....	179
REFERENCES .....	180

## LIST OF TABLES

Table 3.1. The statistics of the crystal plasticity parameters. ....	49
Table 3.2. Microstructural statistics of the statistically equivalent microstructures. ....	59
Table 3.3. Anisotropic elastic constants and calibrated crystal plasticity parameters. ....	62
Table 3.4. Prior and posterior distributions for the critical stored plastic strain energy density and hyper-parameter. ....	71
Table 5.1. Material for welded components. All heat treatments are followed by air cooling... 117	
Table 5.2. Linear friction weld parameters used to fabricate the weld samples. The programmed burn-off is defined as the displacement of the weld platen. The upset is the total loss in length of the joined component after welding.....	117
Table 5.3. Description of first six alpha and first three beta peaks.....	123
Table 5.4. Grain size measurements of different alpha grain structures in the Ti64-Ti64 AW sample. The thickness or width of the basket-weave and lamellar structures are reported and the average grain size of the globular alpha are reported using the line intercept method to measure grain size. ....	135
Table 5.5. Grain size measurements of different alpha grain structures in the Ti64-Ti64 HT sample. The thickness or width of the basket-weave and lamellar structures are reported and the average grain size of the globular alpha are reported using the line intercept method to measure grain size. ....	135
Table 5.6. Grain size measurements of different alpha grain structures from the Ti64 side of the LFW Ti64-Ti5553 AW sample. The thickness or width of the basket-weave and lamellar structures are reported and the average grain size of the globular alpha are reported using the line intercept method to measure grain size.....	138
Table 5.7. Grain size measurements of different alpha grain structures from the Ti64 in the LFW Ti64-Ti5553 HT sample. The thickness or width of the basket-weave and lamellar structures are reported and the average grain size of the globular alpha are reported using the line intercept method to measure grain size.....	138
Table 5.8. Elastic constants and crystal plasticity model parameter details. ....	151

## LIST OF FIGURES

Figure 2.1. Constant life Haigh diagram for Ti-6Al-4V (reproduced from [14]).	36
Figure 3.1. Automated creation of a 3D finite element model for a polycrystalline aggregate, which is statistically equivalent to the microstructural attributes from the EBSD characterization.	42
Figure 3.2. The schematic of an automated framework for the estimation of crystal plasticity parameters using a genetic algorithm.	47
Figure 3.3. (a) The points of interest on a cyclic stress-strain curve. (b) Standard deviation of stress along loading direction due to the variability associated with the crystal plasticity parameters.	51
Figure 3.4. Percentage contribution of the crystal plasticity parameters to the total uncertainty in the stress along loading direction.	52
Figure 3.5. The coefficient of variation of the plastic strain accumulation (PSA) at the (a) maximum and (b) median locations, and accumulated plastic strain energy density ( $W_p$ ) at the (c) maximum and (d) median locations due to the variability associated with the crystal plasticity parameters.	53
Figure 3.6. Percentage contribution of the crystal plasticity parameters to the total uncertainty in the plastic strain accumulation at the maximum ((a)-(i)) and median ((j)-(r)) locations within the microstructure during cyclic loading with the load step displayed in the inset.	54
Figure 3.7. Percentage contribution of the crystal plasticity parameters to the total uncertainty in the accumulated plastic strain energy density at the maximum ((a)-(i)) and median ((j)-(r)) locations within the microstructure during cyclic loading with the load step displayed in the inset.	55
Figure 3.8. (a) EBSD characterization of the Ni-base superalloy 718Plus. (b) Statistically equivalent microstructures are corresponding to the EBSD map.	61
Figure 3.9. (a) Discretized statistically equivalent microstructure. (b) Applied boundary conditions on the discretized polycrystalline microstructure model.	62
Figure 3.10. (a) Macroscopic stress-strain response of all SEMs using the CP parameters reported in Ref. [161]. (b) Experimental and simulated macroscopic stress-strain response from SEM 1 using calibrated CP parameters for 718Plus in this study.	63
Figure 3.11. (a) Slip system based averaging scheme at an arbitrary integration point. (b) The averaging volume for an integration point near the grain boundary is not allowed to cross the grain boundary.	64
Figure 3.12. A schematic of the Bayesian inference framework to calibrate the critical stored plastic strain energy density.	68
Figure 3.13. Evolution of plastic strain energy density per cycle with the number of cycles at the critical location within SEM 1 under macroscopically applied strain, $\Delta\varepsilon = 0.5\%$ at (a) $R\varepsilon = -1$ and (b) $R\varepsilon = 0.05$ .	71

Figure 3.14. Posterior distributions for (a) the critical stored plastic strain energy density, $W_{criticalp}$ , and (b) the hyper-parameter, $s$ . .....	72
Figure 3.15. The probability of failure plots considering log-normal distribution as reference... 73	73
Figure 3.16. Experimental and predicted fatigue life data at (a) $R\epsilon = -1$ and (b) $R\epsilon = 0.05$ . ... 74	74
Figure 3.17. The location of maximum $\Delta w_{10p}$ within SEM 1 at (a) $\Delta\epsilon = 1.2\%$ , $R\epsilon = -1$ , (b) $\Delta\epsilon = 0.95\%$ , $R\epsilon = -1$ , (c) $\Delta\epsilon = 0.75\%$ , $R\epsilon = -1$ , (d) $\Delta\epsilon = 0.675\%$ , $R\epsilon = -1$ , (e) $\Delta\epsilon = 0.625\%$ , $R\epsilon = -1$ , (f) $\Delta\epsilon = 0.5\%$ , $R\epsilon = -1$ , (g) $\Delta\epsilon = 0.5\%$ , $R\epsilon = 0.05$ , (h) $\Delta\epsilon = 0.43\%$ , $R\epsilon = 0.05$ , and (i) $\Delta\epsilon = 0.36\%$ , $R\epsilon = 0.05$ . The yellow arrows indicate the critical location near or at the free surface and the white arrows indicate hot spots at the twin boundaries. Each color map is a cross-sectional view of the SEM 1 on the $x$ - $z$ plane, normal to the loading direction $y$ . .....	78
Figure 4.1. (a) Inverse pole figure of RR1000 microstructure from EBSD characterization. Cumulative probability distribution plot of (b) equivalent diameter and (c) sphericity of inclusions in five RR1000 specimens. ....	81
Figure 4.2. Cross-section view of (a) a polycrystalline microstructure with an inclusion, (b) a discretized polycrystalline microstructure with local mesh refinement, and (c) a discretized polycrystalline microstructure with an inclusion and a debonded region.....	83
Figure 4.3. Boundary conditions on a given SEM (a) without an inclusion during CP parameter fitting with loading applied along the $y$ -direction, (b) with an inclusion during fatigue simulation with loading applied along the $y$ -direction, and (c) with an inclusion during the fatigue simulation with loading applied along the $z$ -direction; $u_0$ is the specified displacement based on desired applied strain and SEM dimension along the loading direction. ....	86
Figure 4.4. Experimental and simulated stress-strain response of RR1000 at (a) 20°C, (b) 300°C, (c) 600°C, and (d) 750°C. ....	87
Figure 4.5. A schematic of the radial distribution plot for plastic strain accumulation demonstrating inclusion-driven (curve A) and matrix-driven (curve B) failure modes. ....	88
Figure 4.6. Effect of the loading direction on the plastic strain accumulation around the inclusion. In the figure, 2D sectional view of the microstructure is presented, where the cross-sectioned plane passes through the centroid of the inclusion. ....	90
Figure 4.7. The radial distribution plots of the plastic strain accumulation, showing the effect of the inclusion stiffness at (a) 0.3%, (b) 1.0% and (c) 3.0% applied strain ranges. ....	91
Figure 4.8. The radial distribution plots for the plastic strain accumulation showing the effect of the debonded region in the inclusion-matrix interface. ....	92
Figure 4.9. The radial distribution plots for the plastic strain accumulation showing the effect of microstructural variability around the inclusion. Each of the subplots corresponds to a different grain environment around the inclusion. ....	93
Figure 4.10. Inverse pole density figures, with the applied loading direction as a reference, representing the orientations of the grains around the inclusion in each microstructure corresponding to Figure 4.9. Please note, the color scale in each subplot is normalized with respect to its own set of data. ....	93

Figure 4.11. Plastic strain accumulation at the inclusion as a function of the inclusion volume and Gaussian curvature ( $\kappa$ ) at the tip of the major axis as a parameter in three different statistically equivalent microstructures. ....	95
Figure 4.12. The effect of the dissimilar CTE values of the inclusion and matrix on the radial distribution plots for plastic strain accumulation at 600°C and for (a) 0.3% and (b) 1.0% applied strain ranges. ....	96
Figure 4.13. The radial distribution plots for plastic strain accumulation for (a) inclusion CTE greater than matrix CTE and (b) inclusion CTE smaller than matrix CTE with temperature as a parameter. The relative difference between the plastic strain accumulation near (location A) and far (location B) from the inclusion as a function of temperature for (c) the inclusion CTE greater than the matrix CTE and (d) the inclusion CTE smaller than the matrix CTE.....	97
Figure 4.14. The effect of residual stress on the radial distribution of plastic strain accumulation around the inclusion. The residual stress is initialized by simulating cooling during the manufacturing process with $\Delta T < 0$ and fatigue simulations are performed with 0.3% applied strain.....	98
Figure 4.15. The effect of decreasing the distance of the inclusion from the free surface on the localization of plastic strain accumulation around the inclusion. ....	99
Figure 4.16. Distributions of inclusion attributes for microstructure modeling. Inclusion stiffness, CTE, equivalent diameter, and sphericity values are sampled from the shaded regions of their respective distributions. The Young's modulus and CTE values of RR1000 are indicated for reference and obtained from Refs. [203] and [204], respectively.....	105
Figure 4.17. Evolution of plastic strain energy density per cycle with the number of cycles at the critical location within one of the SEMs under macroscopically applied strain, $\Delta\varepsilon = 0.4\%$ (left column), $0.6\%$ (middle column), $0.75\%$ (right column), and temperature, $T = 20^\circ\text{C}$ (top row), $750^\circ\text{C}$ (bottom row). ....	109
Figure 4.18. Variation of $W_{\text{criticalp}}$ as a function of temperature. ....	109
Figure 4.19. The probability of failure plots considering log-normal distribution as reference. Each row corresponds to a constant temperature with $T = 20^\circ\text{C}$ for the first row (from top), $T = 300^\circ\text{C}$ for the second row, $T = 600^\circ\text{C}$ for the third row, and $T = 750^\circ\text{C}$ for the fourth row. Each column corresponds to a constant applied strain with $\Delta\varepsilon = 0.4\%$ for the first column (from left), $\Delta\varepsilon = 0.6\%$ for the second column, and $\Delta\varepsilon = 0.75\%$ for the third column. MDF stands for matrix-driven failure and IDF stands for inclusion-driven failure. 'free surface' represents failure originating from the free surface of the microstructure and 'interior' represents cases where failure originates within the bulk of the microstructure.....	111
Figure 4.20. Comparison of percentage of free surface failure from simulation and experiments. ....	113
Figure 5.1. Schematic of the weld region showing fiducial marks for BSE imaging. Images are taken along the fiducially marked path, continuously 2 mm from the weld in both directions and every 500 $\mu\text{m}$ after that. ....	119
Figure 5.2. The overall experimental setup for the EDD measurement. ....	120

Figure 5.3. A schematic of the experimental setup, in which the X-Y-Z coordinate system is fixed in the lab..... 121

Figure 5.4. (a) 2D schematic of the gauge volume interrogated by a detector in the experimental setup. (b) The projection of the gauge volume on the X-Y plane. For the residual strain characterization of each specimen, multiple line scans 300  $\mu\text{m}$  apart are taken. Experimentally obtained lattice strain at a ‘point’ is defined by the average value of the same over the illuminated gauge volume, the centroid of which coincides with the ‘point’. In the figure  $i, j, k$  represent three such consecutive ‘points’ and the overlap of the illuminated gauge volume is shown. .... 121

Figure 5.5. A schematic of the linear friction weld part is shown. The 1-2-3 coordinate system is fixed to the sample and rotates with the sample. .... 122

Figure 5.6. The diffraction pattern from Ti64-Ti5553 HT sample near the weld interface obtained at  $\Omega = 0^\circ, \Phi = 0^\circ$  configuration. In the plot  $\alpha_i$  represents  $i$ th peak corresponding to the alpha phase and  $\beta_i$  represents  $i$ th peak corresponding to the beta phase. The first six alpha peaks correspond to the  $\{100\}$ ,  $\{002\}$ ,  $\{101\}$ ,  $\{102\}$ ,  $\{110\}$  and  $\{103\}$  planes, respectively. The first three beta peaks correspond to the  $\{110\}$ ,  $\{200\}$  and  $\{211\}$  planes, respectively. .... 124

Figure 5.7. Residual strain components in the as-welded and heat-treated joints of Ti64-Ti64 LFW sample are shown. These are obtained from fitting the 4<sup>th</sup> peak of the alpha phase. Different markers in the plots correspond to different lines of scans..... 127

Figure 5.8. Residual strain components in the as-welded and heat-treated joints of Ti64-Ti64 LFW sample are shown. These are obtained from fitting the 2<sup>nd</sup> peak of the beta phase. Different markers in the plots correspond to different lines of scans..... 128

Figure 5.9. Residual strain components in the as-welded and heat-treated joints of Ti64-Ti5553 LFW sample are shown. These are obtained from fitting the 4<sup>th</sup> peak of the alpha phase. In the figure, Ti64 is to the left and Ti5553 is to the right. Different markers in the plots correspond to different lines of scans. .... 129

Figure 5.10. Residual strain components in the as-welded and heat-treated joints of Ti64-Ti5553 LFW sample are shown. These are obtained from fitting the 2<sup>nd</sup> peak of the beta phase. In the figure, Ti64 is to the left and Ti5553 is to the right. Different markers in the plots correspond to different lines of scans. .... 130

Figure 5.11. The Ti64-Ti64 sample in the as-welded condition, (a) a schematic representing the location of the following images, in relation to the weld area, (b) an overview of the weld area, (c) an enlarged region, 1.23 mm in height taken across the weld region, approximately 0.6 mm in each direction, (d) a field of view (FOV) 1.0 mm above the weld region, (e) a FOV 4.5 mm above the weld region, (f) a FOV 1 mm below the weld region, and (g) a FOV 4.5 mm below the weld region. .... 133

Figure 5.12. The Ti64-Ti64 sample in the heat-treated condition, (a) a schematic representing the location of the following images, in relation to the weld area, (b) an overview of the weld area, (c) an enlarged region, 1.23 mm in height taken across the weld region approximately 0.6 mm in each direction, (d) a FOV 1.0 mm above the weld region, (e) a FOV 4.5 mm above the weld region, (f) a FOV 1 mm below the weld region, (g) a FOV 4.5 mm below the weld region, and (h) the weld interface created at the joining point of the two materials..... 136

Figure 5.13. The Ti64-Ti5553 sample in the as-welded condition, (a) a schematic representing the location of the following images, in relation to the weld area, (b) an overview of the weld area, (c) an enlarged region, 1.23 mm in height taken across the weld region, approximately 0.6 mm in each direction, (d) a FOV 1.0 mm above the weld region, (e) a FOV 4.5 mm above the weld region, (f) a FOV 1 mm below the weld region, (g) A FOV 4.5 mm below the weld region, and (h) the weld interface created at the joining point of the two materials..... 139

Figure 5.14. The Ti64-Ti5553 sample in the heat-treated condition, (a) a schematic representing the location of the following images, in relation to the weld area, (b) an overview of the weld area, (c) an enlarged region, 1.23 mm in height taken across the weld region, approximately 0.6 mm in each direction, (d) a FOV 1.0 mm above the weld region, (e) a FOV 4.5 mm above the weld region, (f) a FOV 1 mm below the weld region, (g) a FOV 4.5 mm below the weld region, and (h) the weld interface created at the joining point of the two materials. .... 141

Figure 5.15. Schematic of the dog-bone specimen with two areas of interest (AOI). Both AOIs are characterized using electron backscattered diffraction before HCF loading and displayed different micro-textured regions (MTRs). In the perpendicular MTR, the basal planes of most of the grains are almost perpendicular to the loading direction ( $x$ -axis), whereas in the parallel MTR, the basal planes are nearly parallel to the loading direction. The inverse pole figures of the MTRs are obtained considering  $z$ -axis as reference..... 144

Figure 5.16. (a) Slightly modified dog-bone specimen and the area of interest for the optical microscopy digital image correlation. (b) The fiducial markings divide the entire AOI into thirds. (c) The inverse pole figure of the AOI..... 145

Figure 5.17. (a) Discretized microstructure corresponding to a portion of the middle third microstructure, shown in Figure 5.16(c). (b) The orientation of the grains within the microstructure with respect to the loading direction  $x$ . .... 148

Figure 5.18. Discretized microstructures corresponding to the (a) perpendicular and (b) parallel MTRs as shown in Figure 5.15. .... 149

Figure 5.19. (a) Macroscopic stress-strain response during a uniaxial tension test, (b) cyclic and monotonic response of the calibrated model. The cyclic loading is performed at the same level as that of the experiment. .... 150

Figure 5.20. Strain along loading direction after 10000 cycles from optical microscopy DIC.. 152

Figure 5.21. (a) Scanning electron microscope image around the crack after 45000 cycles. Several slip bands are observed around the crack. Slip bands are indicated by yellow arrows. (b) Maximum in-plane shear strain after 10000 cycles. The strain map is obtained from optical microscopy DIC. .... 153

Figure 5.22. In-plane shear strain evolution around the crack initiation site during high R ratio HCF loading. The location of crack initiation is within the white circle. DIC strain maps are obtained via optical microscopy and overlaid on top of the scanning electron microscope image at 45000 cycles..... 154

Figure 5.23. Grain level strain localization after the first loading cycle in both the micro-textured areas of interest that are shown in Figure 5.15. The strain maps are obtained via HR-DIC. .... 156

Figure 5.24. Evolution of strain localization along the loading direction at two micro-textured areas of interest during HCF loading using HR-DIC.....	157
Figure 5.25. (a) Fracture of the specimen near the perpendicular MTR at 2921 cycles. (b) DIC strain map after 1000 cycles for the perpendicular MTR. (c) Multiple slip bands within a grain and accentuated out of plane slip are observed in the scanning electron microscope image. ....	158
Figure 5.26. Identification of <i>soft-hard-soft</i> grain combinations based on the orientation of individual grains with respect to the loading direction before the application of fatigue loading. ....	160
Figure 5.27. Normal stress on the basal plane from CPFÉ simulation. ....	161
Figure 5.28. Strain accumulation on the prismatic slip systems. At each material point, the maximum value from the three prismatic slip systems is plotted. ....	162
Figure 5.29. Strain accumulation on the basal slip systems. At each material point, the maximum value from the three basal slip systems is plotted. ....	163
Figure 5.30. Strain heterogeneity and degree of plastic deformation as a function of stress ratio, while keeping the stress amplitude fixed: top row, $\sigma_a = 40$ MPa, and bottom row, $\sigma_a = 540$ MPa. ....	165
Figure 5.31. Strain heterogeneity and degree of plastic deformation as a function of stress ratio, while keeping the mean stress fixed: top row, $\sigma_m = 675$ MPa, and bottom row, $\sigma_m = 75$ MPa. ....	166
Figure 5.32. Strain heterogeneity, degree of plastic deformation and percentage of grains plasticized as a function of the stress ratio, while keeping the maximum stress fixed at $\sigma_{max} = 900$ MPa. ....	167
Figure 5.33. Degree of incremental slip on each slip system as a function of the R ratio for the random-textured region. Each subplot represents a family of slip systems ((a) basal, (b) prismatic, (c) first order pyramidal with a type slip direction, and (d) first order pyramidal with c + a type slip direction) and each curve within one subplot represents the behavior of each slip systems in that family. ....	168
Figure 5.34. Heterogeneity associated with incremental slip on each slip system as a function of the R ratio for the random-textured region. Each subplot represents a family of slip systems ((a) basal, (b) prismatic, (c) first order pyramidal with a type slip direction, and (d) first order pyramidal with c + a type slip direction) and each curve within one subplot represents the behavior of each slip systems in that family. ....	169
Figure 5.35. Effect of texture on the heterogeneous deformation as a function of R ratio, while keeping the maximum stress fixed at $\sigma_{max} = 900$ MPa. ....	170
Figure 5.36. Degree of incremental slip on each slip system as a function of R ratio for the perpendicular MTR. Each subplot represents a family of slip systems ((a) basal, (b) prismatic, (c) first order pyramidal with a type slip direction, and (d) first order pyramidal with c + a type slip direction) and each curve within one subplot represents the behavior of each slip systems in that family. ....	172

Figure 5.37. Heterogeneity associated with incremental slip on each slip system as a function of R ratio for perpendicular MTR. Each subplot represents a family of slip systems ((a) basal, (b) prismatic, (c) first order pyramidal with a type slip direction, and (d) first order pyramidal with c + a type slip direction) and each curve within one subplot represents the behavior of each slip systems in that family. .... 173

Figure 5.38. Degree of incremental slip on each slip system as a function of R ratio for the parallel MTR. Each subplot represents a family of slip systems ((a) basal, (b) prismatic, (c) first order pyramidal with a type slip direction, and (d) first order pyramidal with c + a type slip direction) and each curve within one subplot represents the behavior of each slip systems in that family. 174

Figure 5.39. Heterogeneity associated with incremental slip on each slip system as a function of R ratio for parallel MTR. Each subplot represents a family of slip systems ((a) basal, (b) prismatic, (c) first order pyramidal with a type slip direction, and (d) first order pyramidal with c + a type slip direction) and each curve within one subplot represents the behavior of each slip systems in that family. .... 175

## ABSTRACT

In this thesis, the role of location-specific microstructural features in the fatigue performance of the safety-critical aerospace components made of Nickel (Ni)-base superalloys and linear friction welded (LFW) Titanium (Ti) alloys has been studied using crystal plasticity finite element (CPFE) simulations, energy dispersive X-ray diffraction (EDD), backscatter electron (BSE) images and digital image correlation (DIC).

In order to develop a microstructure-sensitive fatigue life prediction framework, first, it is essential to build trust in the quantitative prediction from CPFE analysis by quantifying uncertainties in the mechanical response from CPFE simulations. Second, it is necessary to construct a unified fatigue life prediction metric, applicable to multiple material systems; and a calibration strategy of the unified fatigue life model parameter accounting for uncertainties originating from CPFE simulations and inherent in the experimental calibration dataset. To achieve the first task, a genetic algorithm framework is used to obtain the statistical distributions of the crystal plasticity (CP) parameters. Subsequently, these distributions are used in a first-order, second-moment method to compute the mean and the standard deviation for the stress along the loading direction ( $\sigma_{\text{load}}$ ), plastic strain accumulation (PSA), and stored plastic strain energy density (SPSED). The results suggest that an ~10% variability in  $\sigma_{\text{load}}$  and 20%-25% variability in the PSA and SPSED values may exist due to the uncertainty in the CP parameter estimation. Further, the contribution of a specific CP parameter to the overall uncertainty is path-dependent and varies based on the load step under consideration. To accomplish the second goal, in this thesis, it is postulated that a critical value of the SPSED is associated with fatigue failure in metals and independent of the applied load. Unlike the classical approach of estimating the (homogenized) SPSED as the cumulative area enclosed within the macroscopic stress-strain hysteresis loops, CPFE simulations are used to compute the (local) SPSED at each material point within polycrystalline aggregates of 718Plus, an additively manufactured Ni-base superalloy. A Bayesian inference method is utilized to calibrate the critical SPSED, which is subsequently used to predict fatigue lives at nine different strain ranges, including strain ratios of 0.05 and -1, using nine statistically equivalent microstructures. For each strain range, the predicted lives from all simulated microstructures follow a log-normal distribution; for a given strain ratio, the predicted scatter is seen to be increasing with decreasing strain amplitude and are indicative of the scatter

observed in the fatigue experiments. Further, the log-normal mean lives at each strain range are in good agreement with the experimental evidence. Since the critical SPSED captures the experimental data with reasonable accuracy across various loading regimes, it is hypothesized to be a material property and sufficient to predict the fatigue life.

Inclusions are unavoidable in Ni-base superalloys, which lead to two competing failure modes, namely inclusion- and matrix-driven failures. Each factor related to the inclusion, which may contribute to crack initiation, is isolated and systematically investigated within RR1000, a powder metallurgy produced Ni-base superalloy, using CPFEM simulations. Specifically, the role of the inclusion stiffness, loading regime, loading direction, a debonded region in the inclusion-matrix interface, microstructural variability around the inclusion, inclusion size, dissimilar coefficient of thermal expansion (CTE), temperature, residual stress, and distance of the inclusion from the free surface are studied in the emergence of two failure modes. The CPFEM analysis indicates that the emergence of a failure mode is an outcome of the complex interaction between the aforementioned factors. However, the possibility of a higher probability of failure due to inclusions is observed with increasing temperature, if the CTE of the inclusion is higher than the matrix, and vice versa. Any overall correlation between the inclusion size and its propensity for damage is not found, based on inclusion that is of the order of the mean grain size. Further, the CPFEM simulations indicate that the surface inclusions are more damaging than the interior inclusions for similar surrounding microstructures. These observations are utilized to instantiate twenty realistic statistically equivalent microstructures of RR1000 – ten containing inclusions and remaining ten without inclusions. Using CPFEM simulations with these microstructures at four different temperatures and three strain ranges for each temperature, the critical SPSED is calibrated as a function of temperature for RR1000. The results suggest that critical SPSED decreases almost linearly with increasing temperature and is appropriate to predict the realistic emergence of the competing failure modes as a function of applied strain range and temperature.

LFW process leads to the development of significant residual stress in the components, and the role of residual stress in the fatigue performance of materials cannot be overstated. Hence, to ensure fatigue performance of the LFW Ti alloys, residual strains in LFW of similar (Ti-6Al-4V welded to Ti-6Al-4V or Ti64-Ti64) and dissimilar (Ti-6Al-4V welded to Ti-5Al-5V-5Mo-3Cr or Ti64-Ti5553) Ti alloys have been characterized using EDD. For each type of LFW, one sample is chosen in the as-welded (AW) condition and another sample is selected after a post-weld heat

treatment (HT). Residual strains have been separately studied in the alpha and beta phases of the material, and five components (three axial and two shear) have been reported in each case. In-plane axial components of the residual strains show a smooth and symmetric behavior about the weld center for the Ti64-Ti64 LFW samples in the AW condition, whereas these components in the Ti64-Ti5553 LFW sample show a symmetric trend with jump discontinuities. Such jump discontinuities, observed in both the AW and HT conditions of the Ti64-Ti5553 samples, suggest different strain-free lattice parameters in the weld region and the parent material. In contrast, the results from the Ti64-Ti64 LFW samples in both AW and HT conditions suggest nearly uniform strain-free lattice parameters throughout the weld region. The observed trends in the in-plane axial residual strain components have been rationalized by the corresponding microstructural changes and variations across the weld region via BSE images.

In the literature, fatigue crack initiation in the LFW Ti-6Al-4V specimens does not usually take place in the seemingly weakest location, i.e., the weld region. From the BSE images, Ti-6Al-4V microstructure, at a distance from the weld-center, which is typically associated with crack initiation in the literature, are identified in both AW and HT samples and found to be identical, specifically, equiaxed alpha grains with beta phases present at the alpha grain boundaries and triple points. Hence, subsequent fatigue performance in LFW Ti-6Al-4V is analyzed considering the equiaxed alpha microstructure.

The LFW components made of Ti-6Al-4V are often designed for high cycle fatigue performance under high mean stress or high R ratios. In engineering practice, mean stress corrections are employed to assess the fatigue performance of a material or structure; albeit this is problematic for Ti-6Al-4V, which experiences anomalous behavior at high R ratios. To address this problem, high cycle fatigue analyses are performed on two Ti-6Al-4V specimens with equiaxed alpha microstructures at a high R ratio. In one specimen, two micro-textured regions (MTRs) having their c-axes near-parallel and perpendicular to the loading direction are identified. High-resolution DIC is performed in the MTRs to study grain-level strain localization. In the other specimen, DIC is performed on a larger area, and crack initiation is observed in a random-textured region. To accompany the experiments, CPFEE simulations are performed to investigate the mechanistic aspects of crack initiation, and the relative activity of different families of slip systems as a function of R ratio. A critical *soft-hard-soft* grain combination is associated with crack initiation indicating possible dwell effect at high R ratios, which could be attributed to the high-

applied mean stress and high creep sensitivity of Ti-6Al-4V at room temperature. Further, simulations indicated more heterogeneous deformation, specifically the activation of multiple families of slip systems with fewer grains being plasticized, at higher R ratios. Such behavior is exacerbated within MTRs, especially the MTR composed of grains with their c-axes near parallel to the loading direction. These features of micro-plasticity make the high R ratio regime more vulnerable to fatigue damage accumulation and justify the anomalous mean stress behavior experienced by Ti-6Al-4V at high R ratios.

# 1. INTRODUCTION

## 1.1 Background

High specific strength and high-temperature resistance are two major requirements in aerospace materials. A single material does not meet both requirements simultaneously. For example, Titanium (Ti) alloys offer higher specific strength, but they are not well-suited for high-temperature applications because of their chemical affinity towards oxygen, whereas Nickel (Ni)-base superalloys have relatively lower specific strength but exhibit superior high-temperature strength, high resistance to creep, corrosion and oxidation, making them well-suited for the high-temperature applications [1], [2]. Fatigue is the primary mode of failure in aerospace components and there exists multiple protocols, such as fail-safe approach, safe-life approach, and damage tolerance approach, to ensure safe operation [3], [4]. Therefore, safe performance of the components made of Ti alloys and Ni-base superalloys can be ensured via an in-depth understanding of the fatigue failure mechanisms in these materials and predicting fatigue life with an appropriate confidence interval.

Aerospace components made of Ti alloys and Ni-base superalloys are often tailored to produce location-specific properties to achieve optimized performance. The location-specific properties are realized by generating spatially varying microstructure in terms of grain size, morphology and orientation distribution, phase distribution via manufacturing the components through advanced techniques. For example, dual microstructure heat treatment (DMHT) is one of the material processing strategies, which leads to location-specific microstructural attributes and thereby location-specific material properties in turbine disks made of Ni-base superalloys [5], [6]. Specifically, DMHT leads to a fine grain microstructure near the bore region of the disk, whereas a coarse grain microstructure is formed near the rim region. Typically, a fine grain microstructure leads to higher strength and superior fatigue performance, whereas a coarse grain microstructure offers better creep resistance. On the other hand, linear friction welding (LFW), a solid-state joining process, is an attractive technique to produce compressor blisks (bladed disks) often made of Ti alloys. LFW can join two similar as well as dissimilar Ti alloys together and hence, offers a path to exploit the best of thermo-mechanical properties of different Ti alloys to achieve an optimized performance of the component. However, LFW leads to high localized residual stresses

in the weld region [7]–[9], and the role of residual stress in the fatigue failure of engineering components cannot be overstated [10]. Therefore, using a combination of (a) experimental characterization of parameters influencing fatigue failure, such as grain size, morphology, and orientation distribution, phase distribution, residual stress distribution, distribution of defects (e.g., inclusions, pores), and (b) computational materials tools to analyze spatially varying micromechanical response, arising due to the complex interaction between microstructural heterogeneities, the location-specific fatigue performance can be ensured in the aerospace components made of Ti alloys and Ni-base superalloys.

Irreversibility, associated with microscopic cyclic plasticity, is the origin of fatigue damage in metals [3], [4]. Hence, microstructural features or characteristics should undoubtedly play a vital role in fatigue life prediction. However, microstructure-sensitive approaches are not used in practice. Instead, empirical equations, such as Basquin’s [11] relation and Coffin-Manson’s [12], [13] equation, are fitted to the experimental fatigue life data, and a factor of safety is used for design purpose. Such an approach has two significant drawbacks. First, it requires extensive experimental data, and a large amount of resources goes behind generating such data. Second, depending on the material system, traditional approaches using large-scale testing, may be inadequate to capture some of the life-limiting failure mechanisms. For example, in Ti-6Al-4V, macrozones or micro-textured regions (MTRs) are usually associated with a significantly lower fatigue life [14]–[18]. Basquin’s empirical equation cannot capture such occasional, abnormally low fatigue life. Due to such limitations, the empirical lifing approaches are not trustworthy for the qualification of the aerospace components. Consequently, many experiments, including coupon testing, are prerequisites for qualification, which takes around 15 years to conduct and costs more than \$130 M [19]. Hence, location-specific fatigue lifing is not only necessary to predict microstructure-sensitive fatigue life but also crucial to reduce the number of testing necessary to qualify a component and thereby reducing both costs as well as time to develop, qualify and introduce new materials in the aero-industry.

## **1.2 Pertinent research questions**

Ti alloys and Ni-base superalloys show several unique characteristics regarding fatigue performance, some of which are not yet well understood in the research community. For example, fatigue crack initiation in the LFW of Ti-6Al-4V alloy does not usually take place in the seemingly

weakest location, i.e., the weld region [20], [21]. Further, these components are typically subjected to a high (positive) mean stress and designed for high cycle fatigue (HCF) life. Traditional mean stress correction criteria, such as Goodman relation, can satisfactorily capture the mean stress sensitivity of most of the metallic materials [22]. However, Ti-6Al-4V is known for showing large scatter in HCF life at higher mean stress leading to anomalous behavior [14]. On the other hand, due to the chemical composition, inclusions are unavoidable in Ni-base superalloys. Consequently, there exists a competition between the inclusion- and matrix-driven failure modes, which is influenced by a multitude of parameters. The emergence of either of the failure modes is stochastic (see Section 2.2). A comprehensive understanding of such stochastic emergence and a framework to predict the failure modes with associated fatigue life is still outstanding. To address these gaps, the following research questions are posed in this thesis:

- How do the microstructure and residual stress vary across the LFW joints of similar and dissimilar Ti alloys?
- What is the mechanism of crack initiation in Ti-6Al-4V at high mean stress?
- How does the heterogeneous deformation in Ti-6Al-4V change with mean stress within a random-textured region as well as MTRs? Does the trend explain anomalous mean stress sensitivity in Ti-6Al-4V?
- How do different microstructural parameters influence the emergence of inclusion- and matrix-driven competing failure modes in Ni-base superalloys?
- Is it possible to construct a unified microstructure-sensitive scalar metric to predict fatigue life and associated failure modes, namely inclusion- and matrix-driven failures in Ni-base superalloys, as a function of applied strain, strain ratio, and temperature?

Although differences are evident in the macroscopic fatigue behavior of these two materials, there exists an underlying unity in terms of the origin of fatigue damage, namely irreversible motion of dislocations on well-defined slip systems. Crystal plasticity finite element (CPFE) method is well-suited to simulate the mechanical response of metals accounting for elastic and plastic anisotropies that originate from specific orientations of the individual grains and plastic deformation via slip on well-defined slip systems, respectively. In the past three decades, CPFE simulations have been used to offer mechanistic insights into fatigue failure mechanisms [23]. In this thesis, such simulations are utilized along with accompanying experiments to answer the above questions. CPFE simulations have immense potential to ensure the safe performance of

aerospace components and expedite the material development/improvement and qualification processes via location-specific lifing. However, a lack of thorough uncertainty quantification (UQ), validation, and verification of the crystal plasticity (CP) constitutive relations at the microstructural length-scale have impeded their implementation in the modern engineering workflows [24]. In order to partially bridge the gap, the following research questions are also posed in this thesis:

- How much variability one might expect in each of the CP parameters, due to the poor calibration of these parameters?
- How does the variability in the CP parameters lead to the uncertainty in the mechanical response from CPFEM simulations?

### **1.3 Research Contributions**

The specific research contributions of the present thesis are summarized below.

- Using a genetic algorithm (GA)-based framework, the variability in the CP parameters that might originate due to the poor calibration of these parameters is quantified for additively manufactured (AM) Inconel 718 (IN718), a Ni-base superalloy.
- The uncertainties in the mechanical response of AM IN718 from the CPFEM simulations, originating due to the variability in the CP parameters, are quantified. Further, the contribution of each CP parameter towards the overall uncertainty is quantified at different instances on a cyclic load-path.
- In AM 718Plus, a Ni-base superalloy, a critical value of the microstructure-sensitive stored plastic strain energy density (SPSED) is shown to be sufficient to predict the mean and the scatter trends in fatigue life at multiple applied strain ranges including strain ratios of 0.05 and -1.
- The role of a multitude of parameters that influence the emergence of inclusion- and matrix-driven competing failure modes in Ni-base superalloys are studied. Further, the parameters are ranked based on their importance to result in one of the failure modes preferentially.
- The critical value of the microstructure-sensitive SPSED is calibrated as a function of temperature for the coarse grain variant of RR1000, a powder metallurgy (PM) produced

Ni-base superalloy. Subsequently, inclusion- and matrix-driven failure modes are predicted as a function of applied strain range and temperature.

- The residual strain in the LFWs of similar as well as dissimilar Ti alloys is characterized using energy dispersive X-ray diffraction (EDD) experiments. Subsequently, spatial distributions of residual strains are rationalized by characterizing spatially varying microstructure in the same LFW joints via backscatter electron (BSE) images.
- A critical *soft-hard-soft* grain combination is shown to be associated with the crack initiation in Ti-6Al-4V at high stress ratio (R), which could be attributed to the high applied mean stress and high creep sensitivity of Ti-6Al-4V at room temperature.
- CPFЕ simulations indicate more heterogeneous deformation in Ti-6Al-4V, specifically the activation of multiple families of slip systems with fewer grains being plasticized, at higher R ratios. Such behavior is exacerbated within MTRs, especially the MTR composed of grains with their c-axes near parallel to the loading direction.

#### 1.4 The layout of the thesis

The organization of this thesis is described below.

In Chapter 2, the literature pertinent to the research questions posed in Section 1.2 is reviewed, and the specific gaps are identified.

The focus of Chapter 3 is to build confidence in the CPFЕ simulation framework. To this end, (a) uncertainty in the mechanical responses from the CPFЕ simulations, arising due to the uncertainty of the CP parameters is quantified in Section 3.1 and (b) using the well-calibrated CPFЕ framework from Section 3.1, a microstructure-sensitive energy-based framework is offered to predict fatigue life at multiple applied strain ranges and strain ratios using a single scalar metric, namely critical SPSED, in Section 3.2. The work presented in Section 3.1.1 has been carried out in collaboration with Mr. Prithvirajan Veerappan. Sections 3.1 and 3.2 have been published in Refs. [25] and [26], respectively.

Chapter 4 (a) examines the role of a multitude of parameters that influence two competing failure modes, namely inclusion- and matrix-driven failures, in Ni-base superalloys in Section 4.1 and (b) extends the proposed microstructure-sensitive energy-based approach from Section 3.1.4 to predict competing modes of failures and associated fatigue life as a function of applied strain

and temperature in a Ni-base superalloy in Section 4.2. The work presented in Section 4.1 has been published in Ref. [27].

Attention is shifted towards Ti alloys in Chapter 5. Specifically, in Chapter 5, (a) spatial variation of residual strain in the LFWs of similar and dissimilar Ti alloys are characterized, and the spatial trends in the residual strain are rationalized via microstructural characterization in Section 5.1, (b) mechanism of crack initiation in Ti-6Al-4V is investigated at high R ratio, and heterogeneous deformation is studied in the same material as a function of R ratio in Section 5.2. The work presented in Sections 5.1.4 has been conducted in collaboration with Mr. John Rotella. Dr. Alberto Mello performed all experiments in Section 5.2. Sections 5.1 and 5.2 have been published in Refs. [28] and [29], respectively.

Finally, concluding remarks are presented, and possible future works are discussed in Chapter 6.

## 2. LITERATURE REVIEW

### 2.1 A brief review on fatigue life prediction approaches

Engineering components, subjected to cyclic loading, accumulate damage over the period of their operation due to the irreversibilities associated with microscopic cyclic plasticity. Such degradation is usually referred to as fatigue and associated with a finite safe life operation of the component [3], [4]. The estimation of the safe life, referred to as fatigue life throughout this thesis, is one of the critical tasks in the successful design of components. Especially for aircraft structures, where the factor of safety is almost equal to one, accurate prediction of fatigue life is crucial.

In the past hundred years, scores of researchers offered numerous criteria including simple phenomenological relationships and elegant physics-based models to predict fatigue life at a specified loading condition. Basquin proposed a phenomenological model relating applied stress amplitude to the fatigue life via a power law relationship [11]. Later, Coffin [12] and Manson [13] emphasized the importance of plastic strain, as opposed to stress, to predict life in the low cycle fatigue (LCF) regime. They related plastic strain amplitude to fatigue life via a similar power law relationship which is widely used in the industry to date. In his classic paper on cyclic plasticity, Morrow commented that at the microscopic level neither plastic strain (arising due to the to and fro motion of the dislocations) nor the shear stress (resistance to the motion of the dislocations) was individually responsible for fatigue damage accumulation [30]. He postulated that the plastic work was a composite measure of fatigue damage and thus a unified metric for life prediction. Based on the data from a series of fatigue experiments, Morrow proposed another power law relationship relating plastic work or energy to fatigue life. Following the footsteps of Morrow, a series of researchers employed a similar energy-based approach to predict fatigue life [31]–[55]. In each of these works, plastic work or energy was computed from the area enclosed within macroscopic stress-strain hysteresis loops.

Fatigue failure can be physically considered as a sequence of three successive events, namely crack initiation, crack growth/propagation, and the final fracture. In the second half of the last century, many research efforts were centered on understanding the physics of crack initiation. Based on extensive research of face centered cubic (FCC) materials, it was discovered that persistent slip bands (PSBs) were primarily responsible for fatigue crack initiation [23]. In 1956,

Thompson et al. first described PSBs as specific slip characteristics that would reappear on the surface during cyclic loading even after removing these features by electropolishing [56]. They observed that cracks originated mostly in the interface between the PSB and the matrix. It was also found that the early stage of crack growth was strongly influenced by microstructural attributes (e.g., grain size distribution, texture, etc.) ahead of the crack tip [3], [4]. Therefore, microstructural features or characteristics should undoubtedly play a key role in the fatigue life prediction. However, in all of the energy-based approaches, as mentioned before, heterogeneities arising in the plastic strain energy at the microstructural length-scale were not considered. Instead, a homogenized plastic strain energy density, obtained from the macroscopic stress-strain response, was regarded as a metric for life estimation.

With the advent of high-performance computing, researchers have used CPFЕ and molecular dynamics (MD) simulations to offer microstructure-sensitive fatigue life prediction frameworks. For example, inspired by the critical plane approach proposed by Fatemi and Socie [57], McDowell and his colleagues suggested a fatigue indicative parameter accounting for microstructural heterogeneities in CPFЕ simulations [58]–[65]. Sinha and Ghosh proposed a cyclic ratcheting-based model using CPFЕ simulation results [66]. Further, Ghosh and his colleagues used effective traction-based approaches to predict crack initiation during dwell fatigue in Ti alloys [67], [68]. On the other hand, using MD simulations, Sangid et al. introduced a PSB-driven failure metric for crack initiation [69] and fatigue life prediction [70]. Building on this approach, Yeratapally et al. used both MD and CPFЕ simulations to propose another framework combining two different length-scales simultaneously (atomic and mesoscopic) and paying particular attention to the role played by twin boundaries in Ni-base superalloys [71]. All of these models capture the physics of crack initiation and satisfactorily predict life. However, these models either involve physical parameters which are very difficult to measure from currently available experiments or include non-physical parameters which are impossible to calibrate using experiments. Thus, calibration of these models poses an unavoidable hindrance towards their applicability in industry.

Almost four decades after Morrow’s classic paper on cyclic plasticity [30], researchers have returned to energy-based approaches to address microstructure-sensitive fatigue life performance. For example, building on the work by Korsunsky et al. in 2007 [72], Wan et al. proposed a Griffith or Stroh type critical stored energy density (energy per unit area) as a mesoscale

driving force for crack initiation and fatigue life prediction in 2014 [73]. Using the same model, Jiang et al. [74] and Chen et al. [75] predicted multiple crack initiations around non-metallic inclusions within Ni-base superalloys, and Wilson et al. [76]–[78] predicted crack growth within polycrystalline microstructures. In a separate work, Cruzado et al. proposed a similar model involving two material parameters [79]. The microstructure-sensitive energy-based approach, introduced by Dunne and co-workers [72]–[78], is undoubtedly promising because it (a) is inherently physics-based, (b) involves only one parameter, namely, critical stored energy density, (c) takes care of microstructural heterogeneities, and (d) offers a path forward for calibration via advanced experimental techniques. However, several aspects, associated with such an approach, have not been addressed so far in the literature. First, it has not been investigated whether a single critical stored energy density value can reasonably predict fatigue lives at multiple loading regimes, including low and high cycle fatigue and different stress/strain ratios. Second, experimental fatigue life data at a given stress/strain amplitude shows a scatter which is typically observed to be (a) log-normally distributed [80] and (b) increasing with decreasing applied stress/strain amplitude. A microstructure-sensitive framework should be able to capture both trends in the scatter; however, this has not been verified systematically. In this thesis these two unexplored aspects are addressed in Section 3.2.

## **2.2 Challenges in the fatigue life prediction in Ni-base superalloys**

Ni-base superalloys offer a unique set of characteristics, such as high-temperature strength, high resistance to creep, corrosion and oxidation, making them well-suited for gas turbine engine applications, especially in the high-temperature regime [1]. Since their inception in the 1940s, these materials went through substantial development regarding composition specification, material processing, and microstructural engineering [1], [81]. Many contemporary Ni-base superalloys are produced via PM, which leads to homogeneous and well-controlled microstructure resulting in improved mechanical performance. However, non-metallic inclusions, having a wide range of chemical and mechanical properties, are unavoidable in these materials. Since the components, made of Ni-base superalloys, are subjected to cyclic loading, fatigue is an inevitable issue in these materials. Consequently, mechanistic understanding of the failures, originating from the inclusions as well as the matrix material, has been a focus of substantial research in the past several decades.

Inclusions obstruct the motion of dislocations [82]. Thus, damage accumulates near inclusions throughout cyclic loading resulting in the initiation of cracks, which eventually grow leading to failure of the material. Much work has been carried out in the past to characterize fatigue failure in these materials experimentally. For example, Caton et al. experimentally studied fatigue failure in René 88 DT at different applied stresses [83]. They identified two failure modes, namely inclusion-driven failure and failure originating at crystallographic facets. The second category of failure may be referred to as a matrix-driven failure. In their work, a clear bifurcation in the stress-life curve from high to low applied stress is observed. In their LCF experiments with IN718DA, Texier et al. observed fatigue cracks initiating primarily from the surface and sub-surface non-metallic inclusions [84], [85]. However, they also observed that all surface and sub-surface inclusions did not systematically result in crack initiation. Qiu and Wu also made similar observations in terms of failure due to surface and sub-surface inclusions in their four point bending and tensile-tensile fatigue experiments with RR1000 [86]. Alexandre et al. showed a critical grain size below which particle-induced failures are more prominent [87]. Further, Hyzak and Bernstein reported higher evidence of inclusion- and pore-driven failures at a higher temperature, while matrix-driven failures were more prevalent at room temperature in AF-115 and AF2-1DA [88]. In a similar work, Huron and Roth also reported almost 98.7% failures due to inclusions at 649°C compared to over 80% failures due to grain facets at 204°C in René 88 DT [89]. However, Bhowal and Wusatowska-Sarnek reported counter evidence regarding the percentage of inclusion- versus matrix-driven failures at lower and higher temperatures in Refs. [88], [89] in notched LCF experiments with IN718 [90]. In their work, all failures at 17°C were associated with carbide inclusions, whereas a mixture of inclusion- and matrix-driven failures was observed at 607°C. Further, at 17°C, the debit in fatigue life due to inclusion-driven failure was significant, whereas, at 607°C, both matrix- and inclusion-driven failures resulted in similar fatigue life. From the works in Refs. [83]–[90], the following general comments can be made: (a) the existence of matrix-driven failures, for materials containing inclusions, suggests that the inclusions do not always contribute to the failure mechanism and (b) two competing failure mechanisms depend on the operating temperature but no direct correlation exists in terms of preferential emergence of inclusion-driven failures with increasing temperature.

Modeling of deformation heterogeneity within a solid body in the presence of inclusions dates back to the classic works by Eshelby [91], [92]. Ashby and Brown complemented Eshelby's

contributions by experimentally characterizing the state of strain around the inclusions using diffraction contrast within a transmission electron microscope [93]. In relation to the damage caused by the inclusions, Tanaka and Mura proposed a model for fatigue crack initiation based on dislocation dipole accumulation at inclusions [82]. Later, Shenoy et al. explicitly modeled an inclusion embedded within a single crystal of a directionally solidified Ni-base superalloy. They investigated the role of loading parameters, such as strain range and strain ratio, and microstructural parameters, such as inclusion shape, debonded interface between inclusion and matrix, in the resulting damage due to the inclusions using finite element analysis [94]. However, their analysis was restricted in 2D and did not explicitly take into account the polycrystalline grain environment around the inclusion. With the advent of high-performance computing and advanced experimental techniques, researchers have explicitly considered the polycrystalline neighborhood as well as the 3D aspects of deformation around the inclusions in these materials. For example, Dunne, Britton and their colleagues performed a series of coupled experimental and numerical modeling works to investigate the mechanistic aspects of crack initiation events near inclusions embedded within Ni-base superalloys – RR1000 and FGH96 [74], [75], [95]–[98]. They used high-resolution digital image correlation (HR-DIC) and high-resolution electron backscatter diffraction (HR-EBSD) to obtain plastic deformation and elastic distortion of the matrix surrounding the inclusion, respectively. Subsequently, they used CPFEM simulations to investigate the role of several micromechanical field variables in the crack initiations from the inclusions. On the other hand, Naragani and Sangid et al. studied crack initiation near a non-metallic inclusion, embedded within the RR1000 matrix, using high energy diffraction microscopy (HEDM) and micro-computed tomography ( $\mu$ -CT) techniques [99]. Recently, Stinville et al. also investigated competing mechanisms of crack initiation from non-metallic inclusions and crystallographic facets in René 88 DT using a combination of HR-DIC and transmission scanning electron microscopy [100]. From these works, significant gradient in the strain, higher stored energy density, decohesion between the inclusion and the matrix, and residual stress around the inclusion are found to be some of the critical factors which are associated with fatigue crack initiation at the inclusion. The works in Refs. [74], [75], [94]–[99] are concerned with investigating inclusion-driven failure mechanisms in Ni-base superalloys. However, inclusions are also observed in other structural engineering alloys, such as steels and aluminum alloys (see Refs. [101]–[104] for similar works in these materials).

From the literature review, as presented above, it is evident that there is an inherent stochastic aspect associated with the inclusion- and matrix-driven failure modes in Ni-base superalloys. To address this stochastic nature, Pineau and Antolovich offered a probabilistic model based on a damage tolerance approach to predict fatigue life in these materials [105]. From a physical standpoint, the stochastic aspect is caused and influenced by several parameters including the microstructural features, loading regime, and temperature. Previous advanced experimental and computational studies focused on investigating the mechanistic aspects of inclusion-driven failures. However, a systematic study of the influence of several parameters to offer a holistic view on the two competing failure modes has not been carried out in the literature. Hence, there exists a critical challenge to develop a framework which is capable of predicting fatigue life and associated failure modes, i.e., inclusion- and matrix-driven failures, as a function of applied load and temperature. To address such a gap in the literature, in Section 4.1, the role of a multitude of parameters that influence the emergence of two competing failure modes is studied in-depth. Subsequently, based on the outcome of the parametric study in Section 4.1, realistic 3D microstructures with and without inclusions are created in Section 4.2 and the microstructure-sensitive energy-based fatigue life prediction framework, proposed in Section 3.2, is extended to predict the competing failure modes as a function of applied strain range and temperature.

### **2.3 Linear friction welding in Ti alloys: residual stress and fatigue performance**

LFW is commonly used in the aerospace industry to produce cost effective and high-quality welds in components made from Ti alloys, such as bladed disks or blisks. One of the benefits of the LFW process is joining dissimilar materials, thereby allowing components to possess location-specific properties. During the welding process, one reciprocating surface is brought into contact with a stationary surface at high frequency under applied load. This results in a steep temperature gradient across the weld interface. Such localized heating along with microstructural variations and poor thermal conductivity of Ti alloys result in high localized residual stresses in the weld region [7]–[9]. The role of residual stress in the failure of engineering component is well recognized [10]. Therefore, it is necessary to provide a detailed characterization of the residual stress present in LFW joints of similar and dissimilar Ti alloys to ensure fatigue performance of the corresponding components.

Residual stress distributions can be characterized using a wide range of techniques [106]. In particular, diffraction-based techniques using X-rays or neutron beam measure the lattice strains at the crystal length-scale. These lattice strain measurements coupled with appropriate constitutive relationships provide information regarding the residual stress in the material [107]. The EDD method has been used to quantify the residual stresses in engineering components [108]–[112]. This method is particularly attractive because (i) high energy X-rays can penetrate tens of millimeters of typical engineering alloys, (ii) the incident X-ray beam can be reduced to offer sub-millimeter spatial resolution in the directions perpendicular to the beam in a typical setup, and (iii) acquisition time is short. These characteristics enable spatial mapping of residual strain in an engineering component. Additionally, the sample can be manipulated to measure the strains along multiple directions to determine the strain tensor (and thereby stress tensor).

There are a few studies available in literature characterizing the residual stress distributions in the LFW joints of Ti alloys [113]–[117]. Most of the works involve welds of similar Ti alloys [113]–[116] and only one work considers dissimilar Ti alloys [117]. Daymond and Bonner measured the residual strains in the LFW joint of Ti-6Al-4V of different grades using pulsed neutron diffraction method [113]. Preuss et al. did a similar study on as-welded and heat-treated samples of IMI550 (Ti-4Al-2Sn-4Mo-0.5Si) [114]. Romero et al. studied the effect of forging pressure on the microstructural features and residual stresses in the LFW joint of Ti-6Al-4V [115]. Frankel et al. did a comparative study on the residual stress distribution in two similar LFW joints made of Ti-6Al-4V and Ti-6Al-2Sn-4Zr-2Mo [116]. Unlike the aforementioned works, Xie et al. studied residual stresses in welds composed of two dissimilar Ti-5Al-2Sn-2Zr-4Mo-4Cr (Ti17) alloys, namely beta Ti17 and alpha + beta Ti17 [117].

The previously mentioned works, related to LFW of Ti alloys, [113]–[117], considered either in-plane components or three axial components of stress/strain for only the alpha phase in the Ti alloy. These studies emphasized that corrections should be made to the strain free lattice parameter as a function of the distance from the weld center for an accurate description of the residual stress/strain and concluded that tensile stresses predominantly exist in the weld region [113]–[117]. Although residual stress/strain distributions are found to be symmetric about the center of the weld for similar Ti alloys [113], [115], [116], the reported distributions of residual stress/strain in the welds of dissimilar alloys are not, strictly speaking, symmetric [117].

In Section 5.1, residual strains in the LFW joints of similar (Ti-6Al-4V welded to Ti-6Al-4V) and dissimilar (Ti-6Al-4V welded to Ti-5Al-5V-5Mo-3Cr) Ti alloys are studied using the EDD method considering both alpha and beta phases. As opposed to the existing literature, five components of the residual strain tensor are reported (three axial and two shear). Comparative studies for similar and dissimilar welds are presented. Further, observed trends in the in-plane axial components of the residual strains are explained and supported by microstructural changes and variations across the weld interface via BSE images. In Section 5.1, the residual strain data are presented, as opposed to residual stresses, based on uncertainty in the elastic modulus, especially for the dissimilar LFWs. Additionally, the strain free lattice parameter is taken as constant over the weld region, which is a simplification. Here, the intention is to focus on a tensorial description of the residual strain and the corresponding micrographs. The data are presented with minimal modifications to allow other researchers to apply gradients in the elastic modulus or strain free lattice parameter, as necessary.

As discussed above, significantly high residual stress is developed in the weld region of LFWs of similar as well as dissimilar Ti alloys. However, in the fatigue experiments with Ti-6Al-4V welded to Ti-6Al-4V, cracks do not usually initiate in the seemingly weakest location, i.e., the weld region [20], [21]. Hence, it is necessary to look into the failure mechanisms in the base material to ensure fatigue performance of the LFW Ti components.

#### **2.4 Anomalous mean stress sensitivity in Ti-6Al-4V**

Analysis of the heterogeneities arising in the cyclic plastic deformation at the microstructural length-scale is crucial towards the understanding of the fatigue failure mechanisms and thus the reliable design of the engineering components subjected to dynamic loading. Such understanding is non-intuitive for material like alpha Ti-6Al-4V, which involves multiple families of slip systems having different critical resolved shear stresses and can exhibit different grain morphologies (equiaxed, lamellar, bimodal) with multiple textures (including macrozones) leading to a wide range of macroscopic mechanical properties and response. Some of the critical gas turbine engine components, such as compressor blades and disks, are made of Ti-6Al-4V because of its higher specific strength with resistance to elevated temperature and corrosive environments [2]. Often, these rotating components are subjected to HCF with a low applied stress amplitude and high mean stress (i.e., at high R ratio). Therefore, fatigue research in Ti-6Al-4V, especially at

high R ratio, is of paramount importance, in order to explore mechanisms associated with heterogeneous microplasticity to avoid catastrophic failure of these materials.

Mean stress sensitivity during HCF is traditionally represented in the form of a constant life Haigh diagram, also known as Goodman diagram. An example Haigh diagram for Ti-6Al-4V is shown in Figure 2.1 (reproduced from [14]).

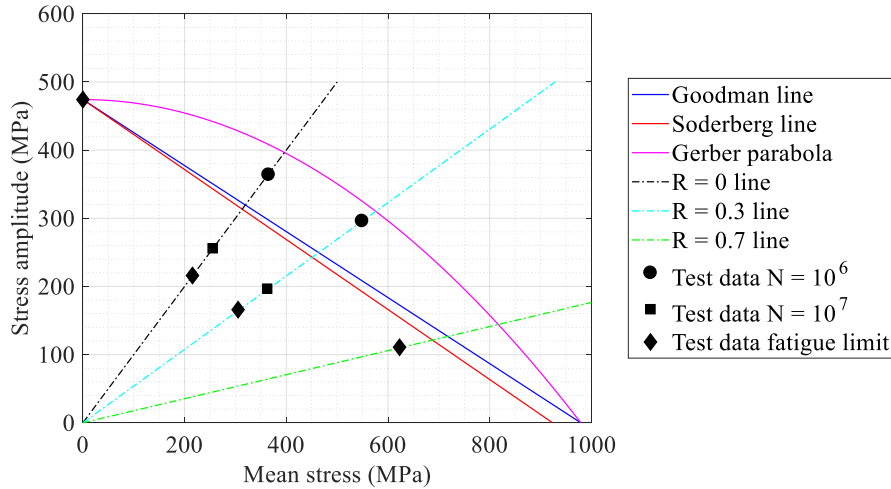


Figure 2.1. Constant life Haigh diagram for Ti-6Al-4V (reproduced from [14]).

From the Haigh diagram, one can assess the allowable stress amplitude for a known mean stress and a desired life. Multiple criteria exist to relate the allowable stress amplitude and operating mean stress, such as the Goodman relation, Soderberg relation, Gerber parabola, etc. Most of the metallic materials follow these relationships [22]. However, Ti-6Al-4V is known for large scatter in HCF life at higher mean stress leading to an anomalous behavior. Depending on the desired life, each of these criteria either leads to a conservative estimation of life or an underestimate of the life (see Figure 2.1). The anomalous HCF behavior can be attributed to the cleavage fracture in  $\alpha$  Ti-6Al-4V [14], which is often observed in the presence of MTRs, where the  $c$ -axes of the cluster of grains are near parallel to the loading direction [15]–[18]. For a detailed review of the anomalous mean stress sensitivity of Ti-6Al-4V, the reader is referred to Ref. [14].

In addition to the presence of MTRs, it has been shown in the literature that the HCF life of Ti-6Al-4V is sensitive to grain morphology (equiaxed, lamellar, bimodal, etc.) [118], stress ratio (R), and loading frequency [119]–[121]. Wu et al. have shown that the HCF strength of Ti-6Al-4V decreases in the order of bimodal, lamellar, and equiaxed microstructure [118]. Morrissey et

al. observed microscale plasticity dominated by cyclic ratcheting and transition from surface cracking to ductile failure mode at  $R > 0.7$  [119], [120]. They also showed HCF testing at higher frequencies resulted in higher fatigue strength. In a similar work, Liu et al. performed HCF experiments at  $R = -1, -0.5, -0.1, 0.5$  and observed three failure modes, namely (i) surface without facets, (ii) surface with facets, and (iii) interior with facets [121]. The occurrence of the surface without facets mode decreased and the surface with facets mode increased with increasing R ratio. However, the interior with facets mode showed an increasing, followed by a decreasing, trend at higher R ratios. On the other hand, with the advent of high-performance computing facilities, microstructure-sensitive CPFGE modeling of fatigue in Ti alloys (mostly Ti-6Al-4V, Ti-6Al-2Sn-4Zr-2Mo and Ti-6Al-2Sn-4Zr-6Mo) was employed by several researchers in the last fifteen years [64], [67], [68], [122]–[129]. The early works were primarily focused on proposing suitable CP models for fatigue simulations. Later, fatigue problems of practical interest (e.g., dwell sensitivity in Ti-6Al-2Sn-4Zr-2Mo alloy, extreme value probabilities in Ti-6Al-4V, etc.) were analyzed using these models. In particular, works related to HCF modeling in Ti-6Al-4V can be found in [64], [123]–[125].

In a typical HCF loading situation, components are subjected to stresses which are well below the macroscopic yield point. However, the onset of microscopic yield and plastic strain localization at the microstructural length-scale result in progressive damage within the material leading to finite HCF life. In the recent past, researchers have experimentally studied the effect of MTRs and bimodal microstructure on heterogeneous deformation of Ti-6Al-4V [130]–[133]. Book and Sangid studied strain localization within AM Ti-6Al-4V under monotonic and cyclic loading using HR-DIC techniques [130]. They found that the prior beta phase boundaries and alpha lath's major axis orientation influence heterogeneous deformation. Echlin et al. used similar HR-DIC techniques and observed long-range strain localization within MTRs under uniaxial monotonic loading far below the macroscopic yield point [131]. Lunt et al. studied heterogeneous deformation in three different microstructures of Ti-6Al-4V having strong-, intermediate-, and no-macrozone under uniaxial tensile loading condition using DIC with optical microscopy [132]. The microstructure having no-macrozones showed relatively homogeneous deformation, whereas deformation was highly heterogeneous within macrozones, which were favorably oriented for the basal or prismatic slip. In a separate work, Lunt et al. also studied the effect of different aging treatments in the strain localization of a bimodal two-phase Ti-6Al-4V alloy using HR-DIC [133].

On the other hand, Kasemer et al. performed a systematic computational study on the effect of relative initial slip system strengths on long-range strain localization within MTRs in equiaxed alpha/beta Ti-6Al-4V using the CPFE method [126]. The majority of the HR-DIC or optical microscopy DIC characterization works of microscopic heterogeneous deformation in Ti-6Al-4V, as described before, were performed under uniaxial, monotonic and tensile loading conditions except for the cyclic loading in Ref. [130].

From this review, as presented above, it is evident that the design against HCF of Ti-6Al-4V demands special attention, especially at higher stress ratios, unlike other metallic materials. Although a lot of work has been done to experimentally characterize the performance and failure modes, still there are several outstanding questions to be investigated, including identifying the micromechanical basis of crack initiation at higher R ratios and determining how heterogeneous deformation during HCF depends on micro-texture and the stress ratio, and evolves with fatigue loading at the continuum scale as well as the slip system level. The first question is especially important because crack initiation accounts for a significant amount of the fatigue life experienced by the material during HCF. The second question is important in relation to locally engineered microstructures of future materials for highly reliable performance. These two questions are answered in Section 5.2.

## **2.5 Uncertainties from crystal plasticity finite element simulations**

It is evident from the literatures reviewed above that the CPFE analysis has been widely used in the past three decades to offer mechanistic insights into plasticity-driven damage phenomena, such as fatigue, in engineering alloys. In the literature pertaining to CPFE analysis, the kinematic description of elasto-plastic deformation is well-posed [134]. However, the kinetic description of plasticity, such as the flow-rule and hardening behavior, can have multiple physics-based or phenomenological representations. For example, the flow-rule can be expressed as either a power law or hyperbolic sine type expression. These kinetic descriptions involve material parameters, a few or all of which cannot be obtained directly from existing experimental techniques. Therefore, one needs to fit a few or all of the material parameters using suitable methods. The experimental data to assist in parameter estimation can come from various sources, including single crystal experiments [135], rate-dependent uniaxial tension coupon tests [136], hysteresis loops from cyclic loading [59], strain-maps produced from DIC [137], and lattice strains

via high-energy X-ray diffraction [138]. Recently, Pagan et al. used the distribution of slip system strengths from the grain-averaged stress tensor obtained from HEDM to calibrate a CP model of their material [139]. DIC and HEDM datasets offer information regarding both macroscopic and microscopic states of the deformation and thereby providing additional constraints during the fitting process. Such a practice is often difficult due to the limited computational resources and accessibility issues associated with the advanced experimental techniques, such as HEDM. Hence, the data from the monotonic or cyclic stress-strain curves are more widely used.

When the CP parameters, defined for a single crystal, are calibrated based on the macroscopic experimental response of a polycrystalline material, there exists a uniqueness issue because different mesoscopic deformation states along with spatial composition variations in the material can result in the same macroscopic homogenized values. Consequently, the quantitative predictions, such as fatigue life, using the results from CPFEM simulations involve uncertainty. Strictly speaking, the uncertainty in the quantitative predictions primarily originates from two sources: (a) the uncertainty due to the CP parameters and (b) the variability associated with the model parameters used in quantitative predictions. In the past, researchers have addressed the latter by quantifying the uncertainty in the fatigue life prediction due to the variability associated with life prediction model parameters [71], [140]. However, the quantification of the uncertainty in the mechanical responses from the CPFEM simulations, arising due to the uncertainty of the CP parameters, is less frequently covered in literature, and is addressed in Section 3.1.

### **3. BUILDING CONFIDENCE IN THE CRYSTAL PLASTICITY FINITE ELEMENT SIMULATIONS**

The focus of the present chapter is to build confidence in the CPFE simulation framework. To this end, uncertainties in the mechanical response of CPFE simulations, originating due to the variabilities associated with the CP parameters, are quantified in Section 3.1. Subsequently, using the well-calibrated CPFE simulation framework, a microstructure-sensitive energy-based approach is used to predict fatigue life at multiple applied strains and strain ratios in Section 3.2.

#### **3.1 Uncertainty quantification in the mechanical response of crystal plasticity simulation**

The Bayesian inference method is a powerful but computationally expensive tool for UQ in the output of a mathematical model [141]. Therefore, it is not well-suited for UQ of the results of CPFE simulations which are themselves time-consuming. The first-order, second-moment (FOSM) method is a computationally efficient tool to estimate the variability, accurate up to the first-order, in the output of a mathematical model and hence chosen for the present study [142]. However, the FOSM method requires prior knowledge of the variability (mean, variance and covariance) of the model parameters. In the present context, it implies that the statistical distribution of the CP parameters is a prerequisite for UQ in the mechanical response from CPFE simulations. To this end, UQ is carried out in two steps. First, a GA-based framework is used to obtain the statistical distributions of the CP parameters. Second, the FOSM method is used to quantify uncertainties in the CPFE simulations and contributions of the CP parameters towards the total uncertainty. With this, the GA framework is described in Section 3.1.1 and the FOSM method is outlined in Section 3.1.2. Subsequently, results are presented and discussed in Section 3.1.3.

##### **3.1.1 Genetic algorithm-based crystal plasticity parameter estimation framework**

Here, the task is to obtain the statistical distributions of the CP parameters, which is accomplished by calibrating the CP parameters using multiple microstructural instantiations. The usage of multiple instantiations captures the possible variability in the CP parameters arising from the stochastic nature of a polycrystalline aggregate. To this end, the creation of the microstructural instantiations is described in “Creation of 3D finite element model of the polycrystalline material”

section. After that, the description of CP material model is outlined in “Crystal plasticity model” section. Subsequently, the GA-based CP parameter fitting framework is discussed in “Parameter estimation using genetic algorithm” section.

### ***Creation of 3D finite element model of the polycrystalline material***

AM IN718, a Ni-base superalloy, is chosen for this work. The details of the material and its microstructural characterization can be found in Ref. [143]. The steps involved in the creation of the discretized polycrystalline microstructural instantiations starting from the EBSD characterization of the material is shown in Figure 3.1 and is discussed below.

In the first step, the microstructural statistical information, namely, the grain sizes and orientations, and twin length fraction are obtained from the EBSD data. The grain sizes and orientations are extracted using the reconstruction filters in DREAM.3D [144]. The reconstruction procedure involves: (a) cleaning the experimental noise in the EBSD data, (b) segmentation of grains using a misorientation threshold value\*, and (c) measuring grain sizes and orientations. The reader may refer to the DREAM.3D reconstruction tutorial and associated algorithms for additional details of these procedures [145], [146]. The grain size corresponds to the diameter of an equivalent circle, as is appropriate for equiaxed microstructures, and the orientations are obtained in the form of Bunge Euler angles. From a single EBSD scan, only the 2D grain sizes are available, hence stereological methods are necessary to obtain the 3D grain sizes (diameter of the equivalent sphere) for accurate microstructure representation. The 2D grain sizes are converted to 3D data by multiplying a stereological factor of  $\frac{4}{\pi}$  [146]. Annealing twins are generally prevalent in Ni-base superalloys, including IN718, owing to the material’s relatively low stacking fault energy, and these features need to be included in subsequent modeling activities due to their significant effect on the corresponding mechanical behavior. The twin boundaries are identified from the EBSD data using the procedure detailed in Ref. [147]. Later, the twin length fraction, defined as the total length of the twin boundaries to that of all the grain boundaries, is obtained using DREAM.3D.

---

\* For a material with a random texture, as is the case for the present material, a misorientation threshold value of 5° is generally used. For highly textured materials, a misorientation threshold value of ~1°-2° would be more appropriate.

The second step involves the creation of 3D synthetic microstructures, including twins, using the statistics as obtained in the previous step. The synthetic building filters within DREAM.3D are used to obtain the 3D synthetic microstructure, which is referred to as parent microstructure. The inputs to the parent microstructure creation are the 3D grain sizes and the orientation information (obtained in the previous step), desired volume of the microstructure, and the size of a voxel.

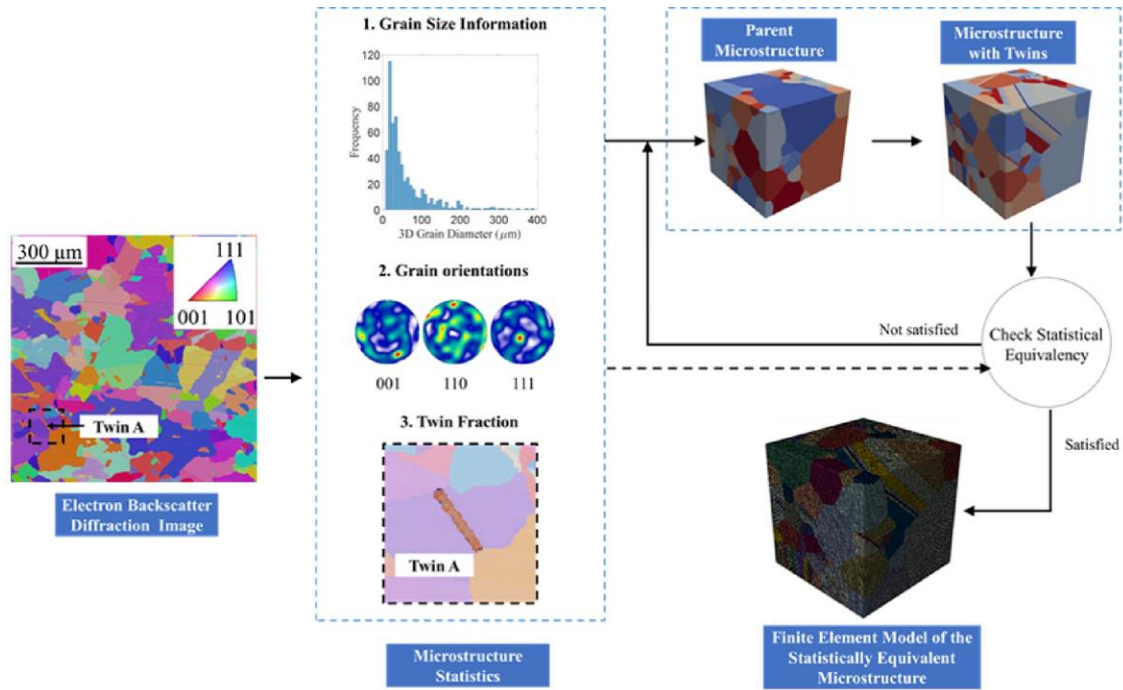


Figure 3.1. Automated creation of a 3D finite element model for a polycrystalline aggregate, which is statistically equivalent to the microstructural attributes from the EBSD characterization.

The primary steps in the parent microstructure creation involve packing the grains inside the specified volume and matching the crystallography to the specified texture; the reader is referred to Refs. [145], [146] for additional details. The parent microstructure generation is random in nature, i.e., different microstructures are obtained when the DREAM.3D pipeline is run multiple times with the same set of inputs. The parent microstructure is deliberately created with a higher mean grain size<sup>†</sup>, as compared to the actual mean obtained from the EBSD, which is necessary to

<sup>†</sup> The increased grain size is dependent on the twin length fraction of the material. For the present material, the twin length fraction is ~0.5 corresponding to an increase of the mean parent grain size of 30%. In the present analysis, the parents and twins are treated independently in determining the grain size.

compensate for the reduction in the mean grain size after insertion of twins. The twins are inserted into the parent microstructure using the methodology described in Ref. [148]. The segmentation of a twin is performed along a randomly chosen  $\{111\}$  plane in a randomly chosen grain. The Euler angles for the twin are assigned such that the misorientation between the parent and twin is a  $60^\circ$  twist with respect to the  $\{111\}$  plane normal. Twins are restricted to be inserted in large grains (greater than 80% of the largest grain) to preserve the average grain size of the microstructure with twins. The maximum number of twins per grain is restricted to three to avoid the creation of very small grains (diameter less than the minimum 3D grain size) after twin insertion. Also, only one twin variant per grain is permitted to avoid the intersection of twins. The creation of the parent microstructure, as well as the twin insertion process, is an iterative process and is continued until statistical equivalency is achieved between the attributes of the synthetic microstructure with twins and the EBSD data. The statistical equivalency criteria are defined using three metrics: (a) within 5% of the average grain size, (b) within 5% of the twin length fraction<sup>‡</sup>, and (c) within 2% of the Taylor factor with respect to the applied loading direction of the simulation. The Taylor factor serves as a scalar measure of the texture [149]–[151]. A tighter bound is enforced on the Taylor factor criterion to preserve the sensitivity of the mechanical response to the texture and a 5% tolerance for the grain size is acceptable as the CP model used in the present study is length-scale independent. The microstructure instantiation containing twins is referred to as the statistical equivalent microstructure (SEM) throughout the remainder of this thesis. Fifteen SEMs are created for this study. Each SEM is a cube of  $300\ \mu\text{m}$  length. The number of grains in the SEMs vary from 190-204, which is sufficient to capture the random texture and the homogenized stress-strain behavior at the macroscale [71].

The final step involves the creation of a volume mesh of the SEMs for subsequent CPFE simulations. First, non-smooth surface meshes of the grain boundaries are obtained using DREAM.3D. Second, non-smooth surface meshes are smoothed using the Laplacian smoothing algorithm available within DREAM.3D. The grain boundary smoothing is an important step to obtain realistic grain morphologies. The reader is referred to Ref. [145] for the usage of relevant DREAM.3D filters<sup>§</sup>. Third, the 3D volume mesh for each grain is obtained from the smooth surface

---

<sup>‡</sup> For the 3D synthetic microstructures, area fraction of the twins is estimated and is used to compare with the length fraction of twins obtained from 2D EBSD.

<sup>§</sup> Laplacian smoothing requires multiple parameters as input. In this work, the default parameters given in DREAM.3D software are used.

mesh using Gmsh [152]. Finally, all grain meshes are combined using Gmsh to obtain the mesh for the entire SEM volume while maintaining the compatibility between nodes at the grain interfaces. Linear tetrahedron elements (C3D4) are used in this study. The details of the mesh size are mentioned in “Parameter estimation using genetic algorithm” section.

The above procedure is automated within an in-house MATLAB program. Thus, the entire workflow, including calling the necessary DREAM.3D pipelines, twin insertion, identifying statistical equivalency, grain boundary smoothing and meshing, and volume meshing in Gmsh, is completed with a single execution of the program, via scripting between the various suite of programs and algorithms. Hence, a set of SEMs can be quickly created, which can be used to study the role of microstructure variability on the associated mechanical response. The automation of this process ensures that the associated features are statistically equivalent and thereby the input microstructure to the CP model is reliable.

### *Crystal plasticity model*

A phenomenological CP model [153]–[155] is used, which considers the twelve FCC slip systems:  $\langle 110 \rangle \{111\}$ . The model is incorporated in ABAQUS within a user-defined material subroutine (UMAT). The kinematics of slip is captured using the multiplicative decomposition [134] of the total deformation gradient,  $\mathbf{F}$ , as

$$\mathbf{F} = \mathbf{F}^e \cdot \mathbf{F}^p \quad (3.1)$$

Here,  $\mathbf{F}^e$  and  $\mathbf{F}^p$  are the elastic and plastic portions of the total deformation gradient, respectively. The plastic velocity gradient,  $\mathbf{L}^p$ , is related to the shearing rates,  $\dot{\gamma}^j$ , on the  $j^{\text{th}}$  slip system as [156]

$$\mathbf{L}^p = \sum_{j=1}^{12} \dot{\gamma}^j \mathbf{s}^j \otimes \mathbf{n}^j \quad (3.2)$$

Here,  $\mathbf{s}^j$  is the slip direction and  $\mathbf{n}^j$  is the slip plane normal. A Hutchinson type flow-rule [157] is used to relate the shear strain rates to the resolved shear stress,  $\tau^j$ , as

$$\dot{\gamma}^j = \dot{\gamma}_0 \left| \frac{\tau^j - \chi^j}{g^j} \right|^n \text{sgn}(\tau^j - \chi^j) \quad (3.3)$$

where  $\dot{\gamma}_0$  is the reference shear strain rate;  $g$  and  $\chi$  are the reference stress and backstress, respectively;  $n$  is the inverse strain-rate sensitivity exponent. The evolution laws for the reference

stress and the backstress are based on the Armstrong-Frederick type equations [158], [159] and are given by

$$\dot{g}^j = H \sum_{k=1}^{12} q^{jk} |\dot{\gamma}^k| - H_d g^j \sum_{k=1}^{12} |\dot{\gamma}^k| \quad (3.4)$$

and

$$\dot{\chi}^j = A \dot{\gamma}^j - A_d \chi^j |\dot{\gamma}^j| \quad (3.5)$$

where  $H$  and  $H_d$  are the direct hardening and dynamic recovery coefficients, respectively, for the reference stress;  $A$  and  $A_d$  are the direct hardening and dynamic recovery coefficients, respectively, for the backstress;  $q^{jk}$  is the hardening matrix which has values of 1 for self-hardening (diagonal terms) and 1.2 for latent hardening (off-diagonal terms) [160]. The single crystal elastic constants for the chosen material are  $C_{11} = 225.7$  MPa,  $C_{12} = 151.2$  MPa, and  $C_{44} = 112.3$  MPa [161]. The displacement boundary conditions for CPFEM simulations are specified in Ref. [161]. There are eight CP parameters:  $\dot{\gamma}_0$ ,  $n$ ,  $g_0$  (initial value of  $g$ ),  $H$ ,  $H_d$ ,  $\chi_0$  (initial value of  $\chi$ ),  $A$ , and  $A_d$ . These parameters are obtained using GA as described below.

### ***Parameter estimation using genetic algorithm***

In this study, the objective is to obtain a combination of the eight CP parameters that would accurately capture the macroscopic response of the material (both forward and reverse behavior) under uniaxial loading. The simplest approach is to manually adjust the CP parameters and carry out a series of simulations until the desired homogenized output is achieved. However, such an approach is time consuming and not suitable to accurately capture the reverse loading behavior (Bauschinger's effect) because the parameters are highly coupled and cannot be sequentially changed with a high degree of precision. Hence, the CP parameter estimation is posed as an unconstrained optimization problem given by:

$$\min_{\xi} f(\xi) = \sqrt{\frac{1}{N_{\text{tot}}} \sum_{i=1}^{N_{\text{tot}}} \left(1 - \frac{S_{\text{sim}}^i(\xi)}{S_{\text{expt}}^i}\right)^2} \quad (3.6)$$

where  $\xi$  is the set of CP parameters;  $S_{\text{expt}}^i$  is the stress value from the experiment and  $S_{\text{sim}}^i(\theta)$  is the volume averaged stress value along loading direction from the CPFEM simulation corresponding

to the  $i^{\text{th}}$  point on the macroscopic stress-strain curve;  $N_{\text{tot}}$  is the total number of equidistant points chosen on the stress-strain curve.

The optimization problem can be solved using many different approaches, including: (a) machine learning techniques, (b) gradient-based optimization methods, and (c) non-gradient based optimization methods. The application of machine learning techniques requires a significant quantity of training data and, hence, are not chosen in this work. To make use of the gradient based approaches, one needs to numerically evaluate the gradients at  $\xi$ , because  $f(\xi)$  does not have a closed-form expression in terms of  $\xi$ . Each function evaluation at  $\xi$  involves a CPFE simulation to obtain  $S_{\text{sim}}^i(\xi)$ . The numerical evaluation of gradients requires at least 9 CPFE simulations (using either forward or backward difference schemes) for each iteration and hence, is too computationally expensive. Moreover, the continuity and differentiability of  $f(\xi)$  is not guaranteed for all  $\xi \in \mathbb{R}^8$ , where  $\mathbb{R}^8$  is the eight-dimensional space of real numbers corresponding to the number of CP parameters and hence, a convergence using any gradient-based method is not guaranteed. So, a non-gradient based method is well-suited to solve the problem given by Eq. (3.6), and due to its simplicity, a GA is chosen for this work. The automated framework for the GA implementation in a high-performance computing domain involving multiple software platforms is shown in Figure 3.2. The ABAQUS input file, containing mesh geometry, CP parameters ( $\xi$ ), and boundary conditions, is created using MATLAB. Subsequently, CPFE simulations are performed in ABAQUS. Next,  $S_{\text{sim}}^i(\xi)$  is extracted from ABAQUS using a Python script. Afterwards,  $f(\xi)$  is evaluated in MATLAB. The stopping criterion is set as  $f(\xi) \leq 0.03$ , which corresponds to the percentage error determined to be acceptable in calibrating the model to the macroscopic experimental stress data ( $S_{\text{expt}}^i$ ). The built-in MATLAB function `ga` is used for updating the parameters if the stopping criterion is not met.

Based on a sensitivity study with different mesh sizes, a coarse mesh of size  $7.5 \mu\text{m}$  is found to yield a similar macroscopic stress response as compared to fine meshes and hence, is chosen for the present work. The model reduction resulted in a computational cost saving of  $\sim 100\text{x}$  (compared to a mesh size of  $3 \mu\text{m}$ )\*\*, which is necessary to make this a tractable means for parameter estimation in an engineering workflow. The maximum number of generations (corresponds to global iteration number) is taken as 10 and the population size (corresponds to

---

\*\* One CPFE simulation, comprised of two loading cycles, in the present study with a mesh size of  $7.5 \mu\text{m}$  takes about 12-18 minutes using 160 processors.

sub-iterations within each generation) is given as 100. For most cases, the convergence is achieved within a generation or two. The number of model evaluations can be estimated as the population size  $\times$  (number of generations + 1). The lower and upper bounds for the CP parameters are decided based on previously available data from Ref. [161] and are given in Table 3.1. For each SEM, the GA framework is run fifteen times and fifteen different solutions of  $\xi$  are obtained. The initial guess is randomly generated (within the designated bounds) every time the GA program is executed; and hence, different solutions are obtained for every GA run. In total, 225 different solutions of  $\xi$  are obtained from all the fifteen SEMs. The estimated values of each CP parameter over the set of SEMs form a statistical distribution, which is used as an input to the FOSM method as described in the next section to quantify the variability in the mechanical response from the CPFE simulations.

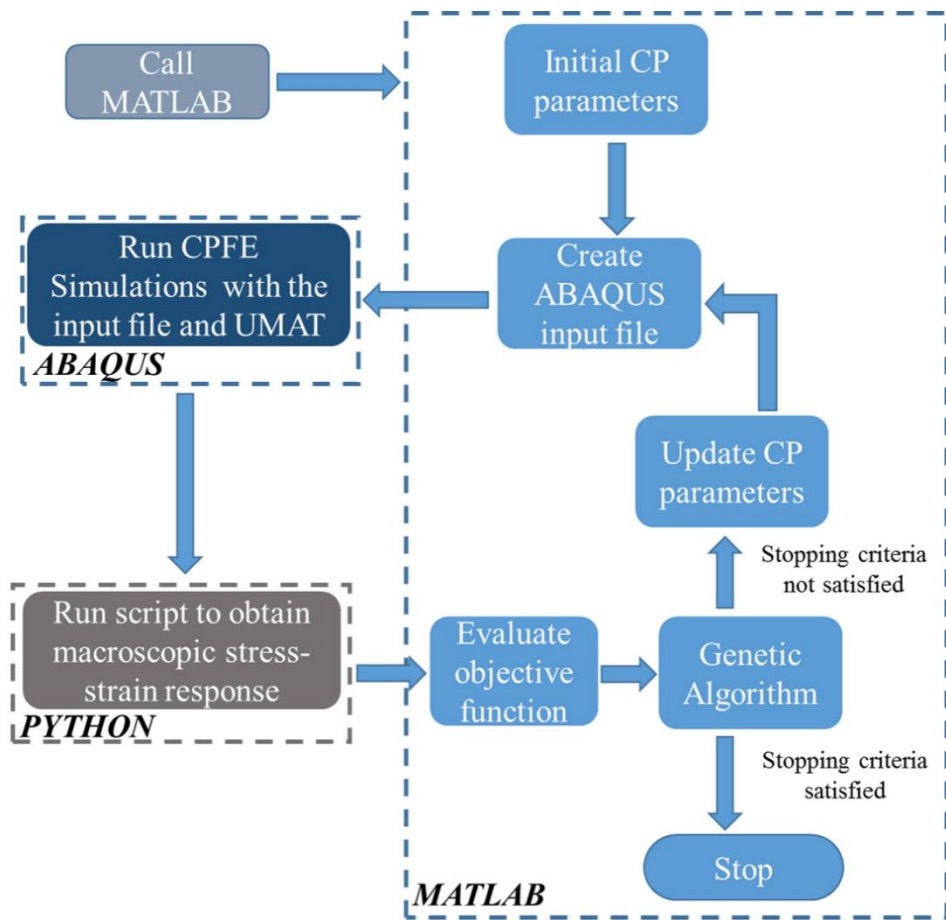


Figure 3.2. The schematic of an automated framework for the estimation of crystal plasticity parameters using a genetic algorithm.

### 3.1.2 First-order second-moment method

Let  $\phi(\boldsymbol{\xi})$  be any scalar-valued output from the CPFPE simulations, such as the average stress along the loading direction ( $\sigma_{\text{load}}$ ), plastic strain accumulation (PSA), and accumulated plastic strain energy density ( $W^P$ ). Here,  $\boldsymbol{\xi}$  represents a vector containing the CP parameters;  $\sigma_{\text{load}}$  represents a scalar which is homogenized over the entire microstructure; PSA and  $W^P$  represent values of the respective quantities at a material point, which can be chosen as hot spots within the microstructure. Given the statistics of  $\boldsymbol{\xi}$ , the problem of interest is to quantify the uncertainty in  $\phi(\boldsymbol{\xi})$ . In other words, the mean and the standard deviation of  $\phi(\boldsymbol{\xi})$  are sought for the known mean, variance and covariance values of  $\boldsymbol{\xi}$ . As per the FOSM method, the mean of  $\phi(\boldsymbol{\xi})$ ,  $\bar{\phi}$ , is given by [142]

$$\bar{\phi} = \phi(\bar{\boldsymbol{\xi}}) \quad (3.7)$$

where  $\bar{\boldsymbol{\xi}}$  is the mean value of  $\boldsymbol{\xi}$ , and the variance of  $\phi(\boldsymbol{\xi})$ ,  $V_\phi$ , is given by [142]

$$V_\phi = \nabla\phi^T(\bar{\boldsymbol{\xi}}) \mathbf{S} \nabla\phi(\bar{\boldsymbol{\xi}}) \quad (3.8)$$

where  $\mathbf{S}$  represents the covariance matrix of  $\boldsymbol{\xi}$  and  $\nabla(\cdot)$  operator represents the gradient of a scalar with respect to  $\boldsymbol{\xi}$ . If all CP parameters, represented by  $\boldsymbol{\xi}$ , are uncorrelated,  $\mathbf{S}$  becomes a diagonal matrix, where the diagonal elements represent the variance of each CP parameter. Under such a situation, the percentage contribution of each CP parameter to the total uncertainty of  $\phi(\boldsymbol{\xi})$ , i.e.,  $V_\phi$ , can be computed as

$$c_i^\phi = \frac{\left[ \left. \frac{\partial\phi(\boldsymbol{\xi})}{\partial\xi_i} \right|_{\boldsymbol{\xi}=\bar{\boldsymbol{\xi}}} \right]^2 V_{\xi_i}}{V_\phi} \times 100\% \quad (3.9)$$

where  $c_i^\phi$  is the contribution of the  $i^{\text{th}}$  CP parameter to the variance of  $\phi(\boldsymbol{\xi})$ , and  $V_{\xi_i}$  is the variance of the  $i^{\text{th}}$  CP parameter.

Using the GA-based framework, as described in Section 3.1.1, the distribution of the CP parameters, i.e.,  $\bar{\boldsymbol{\xi}}$  vector and  $\mathbf{S}$  matrix, is obtained. Subsequently, a central difference scheme is used to obtain the gradient terms numerically using the CPFPE simulation results as

$$\left. \frac{\partial\phi(\boldsymbol{\xi})}{\partial\xi_i} \right|_{\boldsymbol{\xi}=\bar{\boldsymbol{\xi}}} \approx \frac{\phi(\bar{\boldsymbol{\xi}} + \varepsilon\bar{\xi}_i\mathbf{e}_i) - \phi(\bar{\boldsymbol{\xi}} - \varepsilon\bar{\xi}_i\mathbf{e}_i)}{2\varepsilon\bar{\xi}_i} \quad (3.10)$$

where  $\mathbf{e}_i$  is the  $i^{\text{th}}$  column of an identity matrix having a number of rows/columns which are the same as the dimension of  $\boldsymbol{\xi}$  and  $0 < \varepsilon \ll 1$ . In the present work,  $\varepsilon$  is taken as 0.1. Thus, using the

$\bar{\xi}$  vector, the  $\mathbf{S}$  matrix and the  $\nabla\phi(\bar{\xi})$  vector from the GA-based CPFE simulation framework,  $V_\phi$  and  $c_i^\phi$  are computed as per Eqs. (3.8) and (3.9), respectively.

### 3.1.3 Results and discussion

Using the GA-based fitting framework and the experimental cyclic stress-strain response of IN718 at 1% applied strain range and zero strain ratio, i.e.,  $R_\epsilon = 0$ , multiple sets of CP parameters are obtained from each SEM. The results from all SEMs give rise to the statistical distribution of the CP parameters. The mean and the coefficient of variation of all CP parameters as well as the imposed bounds during fitting are reported in Table 3.1.

Table 3.1. The statistics of the crystal plasticity parameters.

Parameter ( $\xi_i$ )	Imposed lower bound during fitting	Imposed upper bound during fitting	Fitted mean value ( $\bar{\xi}_i$ )	Coefficient of variation of the fitted value $\left(\frac{\sqrt{V_{\xi_i}}}{\bar{\xi}_i}\right)$
$\dot{\gamma}_0$	$0.00004 \text{ s}^{-1}$	$0.01 \text{ s}^{-1}$	$0.004 \text{ s}^{-1}$	0.6641
n	20	50	35	0.2405
$g_0$	350 MPa	425 MPa	386.2 MPa	0.0564
H	3000 MPa	10000 MPa	7124.0 MPa	0.2668
$H_d$	0	40	19.5	0.4339
$\chi_0$	0	50 MPa	20.5 MPa	0.6518
A	5000 MPa	50000 MPa	32702.8 MPa	0.3266
$A_d$	0	1000	397.8	0.6470

The correlation coefficient matrix  $\mathbf{R}_{\text{CP}}$  of the set of the CP parameters is obtained using the `corrcoef` function in MATLAB as

$$\mathbf{R}_{\text{CP}} = \begin{pmatrix} 1 & 0.1219 & 0.2294 & 0.1771 & -0.0279 & 0.0288 & 0.1728 & -0.2422 \\ & 1 & 0.3010 & 0.1693 & 0.0655 & -0.1179 & -0.1286 & 0.0062 \\ & & 1 & -0.1081 & 0.3038 & -0.0805 & 0.0525 & 0.1732 \\ & & & 1 & 0.4718 & -0.1738 & 0.0973 & -0.0073 \\ & & & & 1 & -0.1991 & 0.2756 & -0.3016 \\ & & \text{sym.} & & & 1 & -0.1928 & 0.0170 \\ & & & & & & 1 & 0.3515 \\ & & & & & & & 1 \end{pmatrix} \quad (3.11)$$

where the rows and columns of the  $\mathbf{R}_{\text{CP}}$  matrix follow the same order of the CP parameters as in Table 3.1. It is evident from Eq. (3.11) that no strong correlation exists between the statistical variabilities of the CP parameters. Therefore, as discussed in Section 3.1.2,  $\mathbf{S}$  is a diagonal matrix with the variance of each of the CP parameters as diagonal elements. Further, based on Eq. (3.10), the gradient vector,  $\nabla\phi(\bar{\boldsymbol{\xi}})$ , is computed numerically via a central difference scheme using the CPFGE simulations, also performed at 1% applied strain range and  $R_\varepsilon = 0$ , in a randomly chosen SEM out of fifteen SEMs used for the GA-based fitting. The simulations are carried out for two cycles to investigate the role of the variability in the CP parameters in the uncertainty of the macroscopic as well as microscopic state of the deformation.

In this study, three quantities, namely  $\sigma_{\text{load}}$ ,  $\text{PSA}(\mathbf{x})$ , and  $W^{\text{P}}(\mathbf{x})$ , from the CPFGE simulation are chosen as  $\phi(\boldsymbol{\xi})$ . Here,  $\sigma_{\text{load}}$  is representative of the macroscopic state of the deformation, whereas  $\text{PSA}(\mathbf{x})$  and  $W^{\text{P}}(\mathbf{x})$  are representative of the microscopic state of the deformation.  $\sigma_{\text{load}}$  is computed as

$$\sigma_{\text{load}} = \int_V \boldsymbol{\sigma}(\mathbf{x}) : (\mathbf{n}_{\text{load}} \otimes \mathbf{n}_{\text{load}}) dV \quad (3.12)$$

where  $\boldsymbol{\sigma}(\mathbf{x})$  is the Cauchy stress at the material point  $\mathbf{x}$ ,  $\mathbf{n}_{\text{load}}$  is the unit vector along the loading direction, and  $V$  is the volume of the simulation domain. The plastic strain accumulation,  $\text{PSA}(\mathbf{x})$ , at a material point  $\mathbf{x}$  is defined as [162]

$$\text{PSA}(\mathbf{x}) = \int_t \sqrt{\frac{2}{3} \mathbf{L}^{\text{P}}(\mathbf{x}, t) : \mathbf{L}^{\text{P}}(\mathbf{x}, t)} dt \quad (3.13)$$

The accumulated plastic strain energy density,  $W^{\text{P}}(\mathbf{x})$ , at the same point is computed as

$$W^{\text{P}}(\mathbf{x}) = \int_t \left( \sum_{j=1}^{12} |\tau^j(\mathbf{x}, t) \dot{\gamma}^j(\mathbf{x}, t)| \right) dt \quad (3.14)$$

In Eq. (3.14), the summation is performed over all twelve FCC slip systems.

The mean response of  $\sigma_{\text{load}}$  is shown in Figure 3.3(a) and the standard deviation of the same is shown in Figure 3.3(b) at different points on the cyclic stress-strain curve as indicated in Figure 3.3(a). Overall, the standard deviation of  $\sigma_{\text{load}}$  is observed to be approximately within 10% of the maximum stress value (by magnitude).

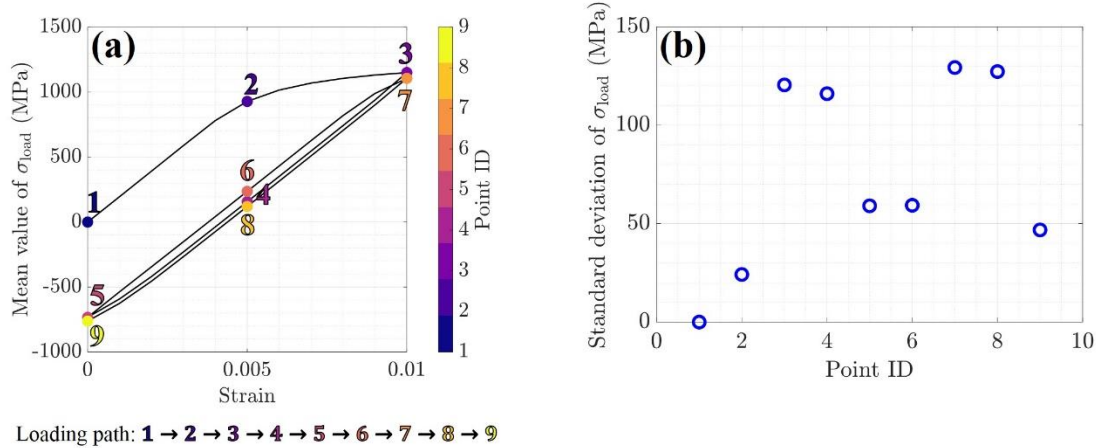


Figure 3.3. (a) The points of interest on a cyclic stress-strain curve. (b) Standard deviation of stress along loading direction due to the variability associated with the crystal plasticity parameters.

The contribution of each CP parameter on the variance, i.e., total uncertainty, of  $\sigma_{load}$  at different points on the cyclic stress-strain curve is shown in Figure 3.4. All CP parameters do not contribute equally to the total uncertainty of  $\sigma_{load}$  at each point along the cyclic stress-strain curve. Overall, the contributions from  $\chi_0$ ,  $\dot{\gamma}_0$  and  $n$  are not appreciable. Further, the dominance of a parameter or a set of parameters is consistent with its or their relevance to the physics of deformation. For example, in Figure 3.4(b), the contribution of  $g_0$ , which is related to the initial critical resolved shear stress of the material, is significantly higher at the point on the stress-strain curve, which is associated with initial yielding. Further, in Figure 3.4(e), (f) and (i) one can observe that the parameters  $A$  and  $A_d$ , associated with the backstress evolution equation, dominate. We recall that the corresponding points on the stress-strain curve are associated with the Bauschinger effect which is a consequence of kinematic hardening of the material. Hence, the higher contribution of  $A$  and  $A_d$  is consistent with the dominance of the backstress term at those locations of the cyclic stress-strain curve.

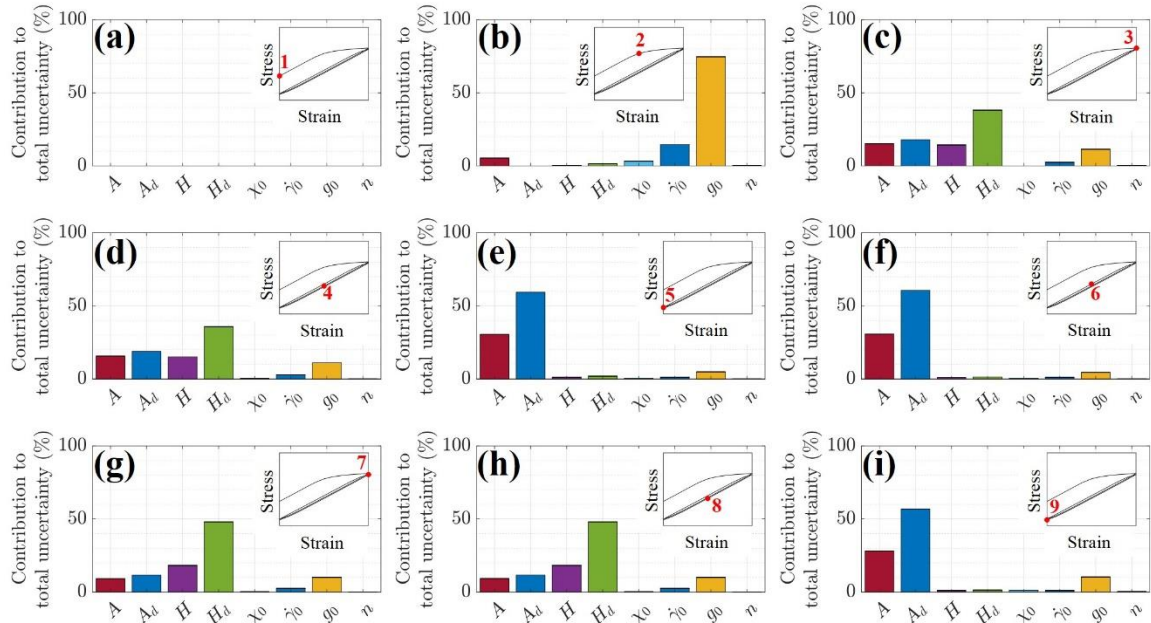


Figure 3.4. Percentage contribution of the crystal plasticity parameters to the total uncertainty in the stress along loading direction.

To study the uncertainty in  $PSA(\mathbf{x})$  and  $W^P(\mathbf{x})$ , two locations, namely  $\mathbf{x}_{\max}$  and  $\mathbf{x}_{\text{median}}$  are chosen within the same microstructure based on the values of the respective quantities identified at state 9 (Figure 3.3(a)). The  $\mathbf{x}_{\max}$  represents the location corresponding to the maximum value, such as a hot spot, and the  $\mathbf{x}_{\text{median}}$  represents a location associated with the cumulative probability value of 0.5 of the quantity. Such a choice allows investigation into the role of the CP parameters in the uncertainty of the micromechanical responses at the locations where plasticity is significantly high or indicative of the average response of the polycrystalline aggregate. In the subsequent discussion,  $\mathbf{x}$  is dropped from  $PSA(\mathbf{x})$  and  $W^P(\mathbf{x})$  for simplicity;  $\mathbf{x}_{\max}$  and  $\mathbf{x}_{\text{median}}$  are referred to as the ‘max location’ and ‘median location’, respectively.

As per Eqs. (3.13) and (3.14), both  $PSA$  and  $W^P$  are path-dependent, positive, and monotonically increasing quantities. Therefore, in order to represent the evolution of the true uncertainties in these quantities with cyclic loading, the coefficient of variation, i.e., the ratio of the standard deviation and the mean, is plotted for both the max and median locations in Figure 3.5(a) and (b) for  $PSA$ , and in Figure 3.5(c) and (d) for  $W^P$ . From Figure 3.5, it can be observed that the uncertainty in both quantities saturates at approximately 20%-25% of the mean values.

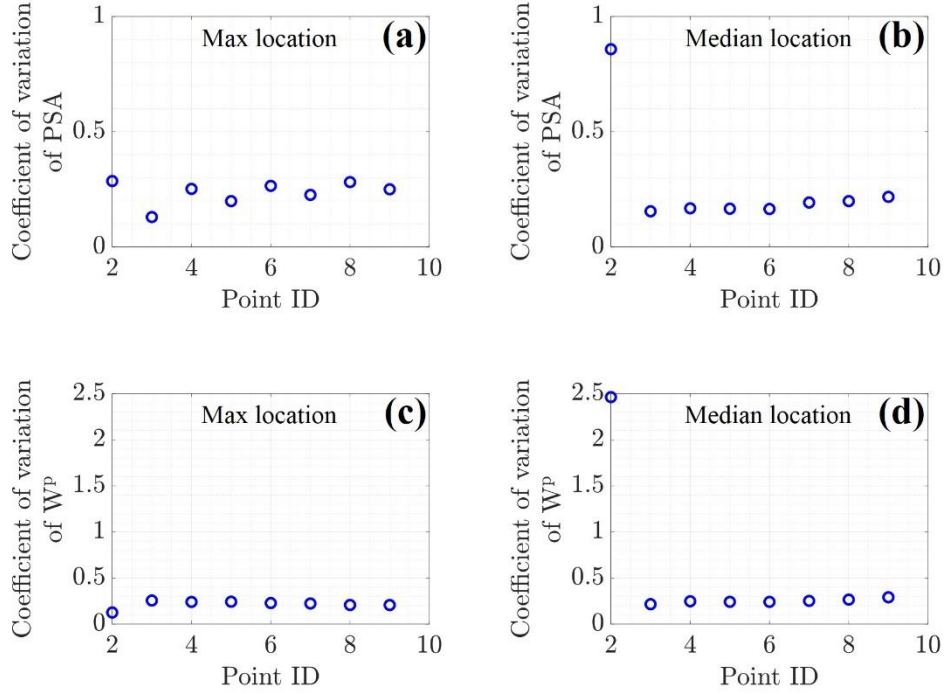


Figure 3.5. The coefficient of variation of the plastic strain accumulation (PSA) at the (a) maximum and (b) median locations, and accumulated plastic strain energy density ( $W^P$ ) at the (c) maximum and (d) median locations due to the variability associated with the crystal plasticity parameters.

The percentage contribution of the CP parameters to the total uncertainty in the PSA and  $W^P$  is plotted in Figure 3.6 and Figure 3.7, respectively. From Figure 3.6(a)-(i) and Figure 3.7(a)-(i), it is evident that at the location of maximum PSA and  $W^P$ , isotropic hardening parameters ( $H$  and  $H_d$ ) primarily contribute to the total uncertainty. However, from Figure 3.6(j)-(r) and Figure 3.7(j)-(r) one can observe that significant contributions at the median location are made by  $\chi_0$ ,  $g_0$ ,  $A$  and  $A_d$ . Since all material points within the microstructure do not experience similar stress levels, the plastic deformation at the microstructural length-scale is heterogeneous. Consequently, at the material points where plastic deformation is relatively lower than other locations within the same microstructure, a significant evolution of the state dependent quantities is not expected. Therefore, plastic slip at the median location is expected to be significantly influenced by the initial critical resolved shear stress ( $g_0$ ), initial value of the backstress ( $\chi_0$ ) and the parameters ( $A$  and  $A_d$ ) associated with its evolution. Thus, the observed trends in the uncertainties of the micromechanical field variables, associated with plastic deformation, are consistent with the physics of the deformation.

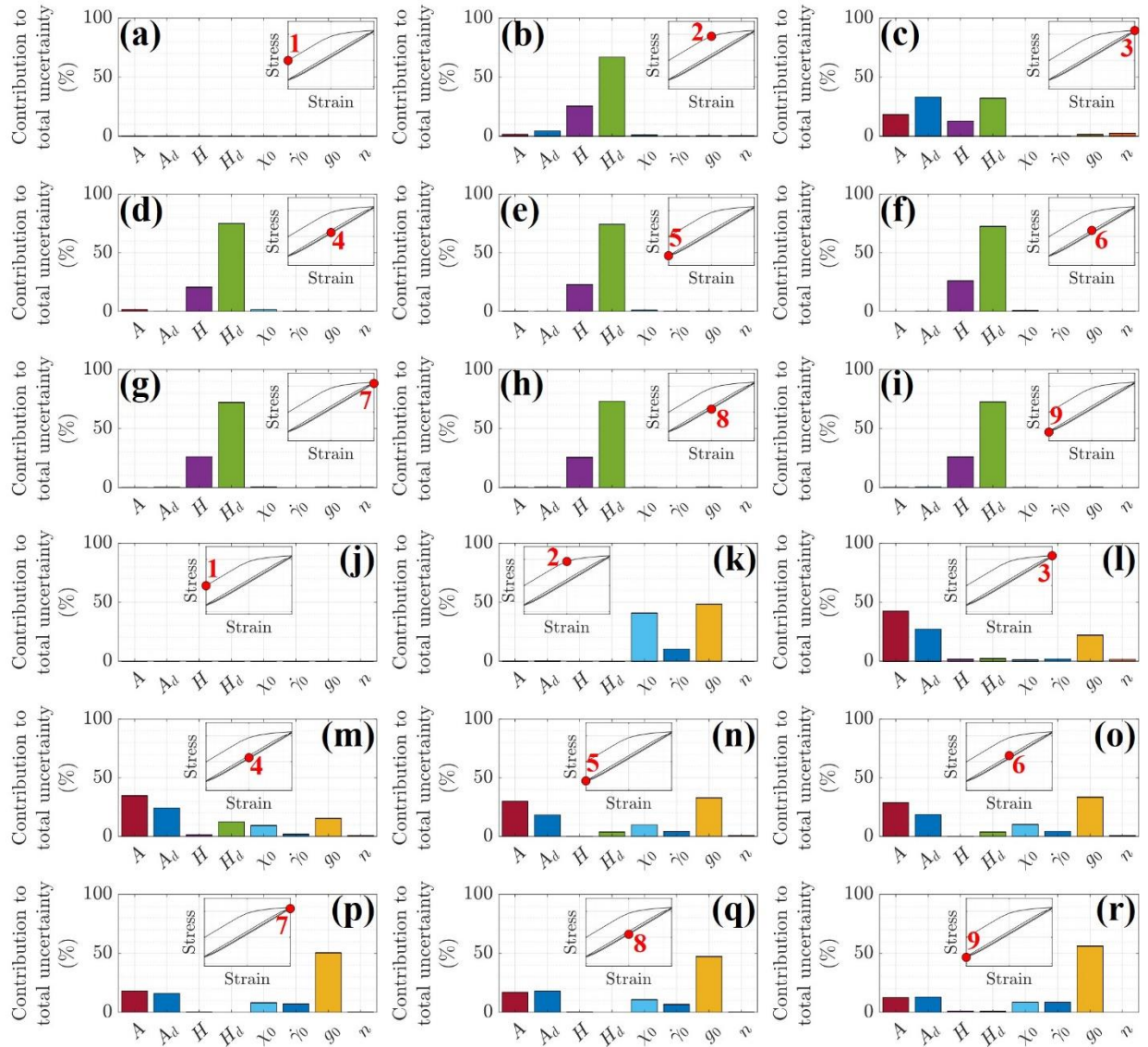


Figure 3.6. Percentage contribution of the crystal plasticity parameters to the total uncertainty in the plastic strain accumulation at the maximum ((a)-(i)) and median ((j)-(r)) locations within the microstructure during cyclic loading with the load step displayed in the inset.

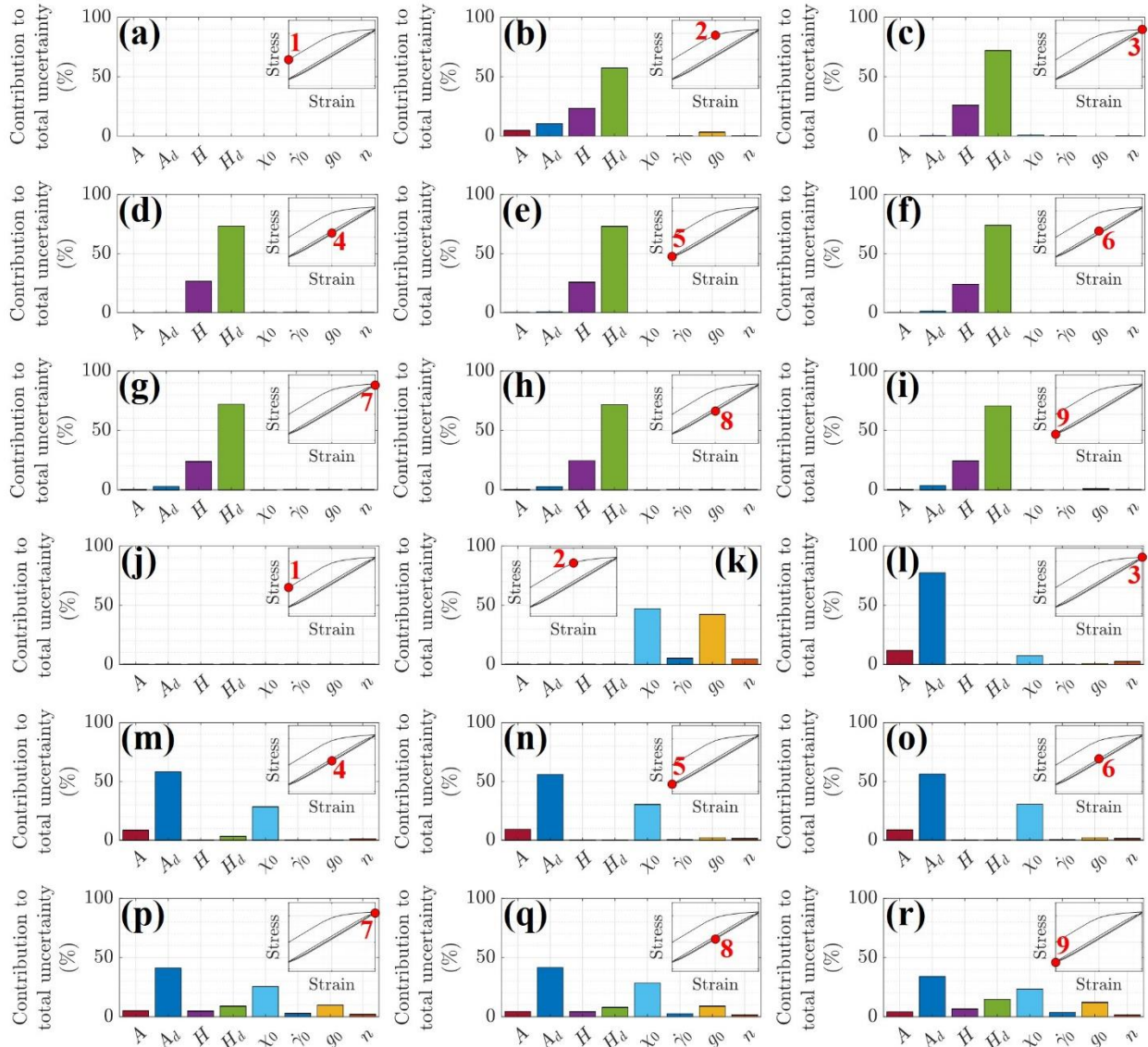


Figure 3.7. Percentage contribution of the crystal plasticity parameters to the total uncertainty in the accumulated plastic strain energy density at the maximum ((a)-(i)) and median ((j)-(r)) locations within the microstructure during cyclic loading with the load step displayed in the inset.

From the results, as presented above, it is evident that the role of a CP parameter towards the total uncertainty in a quantity, associated with the mechanical response, is inherently dependent on the quantity and the point on the macroscopic loading path. For example, the percentage contributions of the CP parameters to the uncertainty of  $\sigma_{load}$  and PSA are different. However,

their contribution is consistent with their relevance to the physics of the deformation, as discussed above. Such observation has significant implications for predictive modeling practices. In predictive modeling practices, one needs to first identify the set of the CP parameters which contributes most to the uncertainty in the prediction. Subsequently, corresponding set of the CP parameters should be calibrated using suitable experimental dataset to result in the least uncertainty, due to the CP parameters, in the prediction. For illustration, consider the example of fatigue life predictions using  $W^P$ . It has been observed that the uncertainty in the  $W^P$  value at the max, i.e., critical, location is mostly contributed by  $H$  and  $H_d$  (see Figure 3.7(a)-(i)). Further, the uncertainties in the cyclic evolution of  $\sigma_{load}$  is seen to be most sensitive to  $g_0$  (see Figure 3.4(b)),  $A$  and  $A_d$  (see Figure 3.4(e), (f) and (i)), and  $H$  and  $H_d$  (see Figure 3.4(c), (d), (g) and (h)) at various points on the cyclic stress-strain curve. Hence, macroscopic stress-strain hysteresis loop can provide reasonable information to calibrate these parameters. Consequently, uncertainty in fatigue life of polycrystalline materials, predicted using  $W^P$  at the critical location from CPFEE simulations, would not significantly suffer due to the choice of the experimental dataset at the macroscopic length-scale to fit the CP parameters (formulation defined for a single crystal). However, such a dataset, i.e., macroscopic stress-strain at a single applied strain-rate, is not useful for the calibration of  $\dot{\gamma}_0$ ,  $\chi_0$ , and  $n$ , because the uncertainty in  $\sigma_{load}$  is not sensitive to the variabilities of these parameters. As evident in the present analysis, depending on the goal of the CPFEE analysis, multiple experimental datasets capturing the state of the deformation at multiple length-scales may be necessary to accurately calibrate pertinent or all CP parameters, which is elucidated in the present analysis.

### 3.1.4 Summary

In the present study, the uncertainty in the mechanical response from CPFEE simulations, arising due to the uncertainty in the CP parameters of the constitutive model, is quantified in two steps. First, multiple statistically equivalent microstructures are used to determine the statistical distributions of the CP parameters using a GA-based framework. Subsequently, the distributions are used to quantify the mean and the standard deviation in the average stress along the loading direction, plastic strain accumulation and accumulated plastic strain energy density using the first-order, second-moment method at different loading points along a cyclic stress-strain curve. The key findings of the present study are summarized below.

- Due to the uncertainty of the CP parameters, the standard deviation in the average stress along the loading direction is found to be bounded by 10% of the maximum stress value (by magnitude); the standard deviation of plastic strain accumulation and accumulated plastic strain energy density is observed to saturate within 20%-25% of the mean value of the respective quantities.
- The relative contribution of each CP parameter to the overall uncertainty is found to be path-dependent, i.e., dependent on the loading point under consideration on the cyclic stress-strain curve, and consistent with their relevance to the physics of the deformation.
  - At the onset of the macroscopic yield, the initial critical resolved shear stress is found to be dominant, whereas, during reverse yielding, the parameters associated with the backstress evolution are found to contribute significantly to the uncertainty in the average stress along the loading direction.
  - At the microscopic level, the isotropic hardening parameters are seen to dominate the uncertainty in the plastic strain accumulation and accumulated plastic strain energy density at the location of their maximum value, whereas the initial value of the backstress and critical resolved shear stress along with the parameters associated with their evolution are seen to be more dominant at a location where plastic deformation is significantly lower.
- In the predictive modeling practices using CPFEM simulations, it is extremely important to identify the set of the CP parameters that contribute significantly to the total uncertainty in the prediction. Once the pertinent CP parameters are identified, suitable experiments can be conducted to calibrate these parameters.

The framework of the analysis and the results of the present research will help a practitioner to – (a) select a suitable experimental dataset to calibrate the CP parameters, (b) identify the set of the CP parameters which will be most critical for a particular quantitative prediction, (c) impose reasonable bounds while fitting the CP parameters, and (d) quantify the approximate variability in the CP results to inform subsequent uncertainty propagation within an integrated computational materials engineering (ICME) modeling framework that utilizes the results of CP simulations.

### **3.2 Microstructure-sensitive critical plastic strain energy density criterion for fatigue life prediction across various loading regimes**

The amount of work done by the externally applied forces during cyclic loading can be equated to the summation of the elastically stored energy, which is recoverable upon unloading, and the internal plastic work, which is nonrecoverable upon unloading. The material stores a portion of the internal plastic work by forming dislocation structures and sub-structures, such as PSBs, and the rest is primarily dissipated as heat energy. In the context of fatigue failure, it is the stored portion of the internal plastic work, which is of interest. Here, it is postulated that there exists a critical value of the stored plastic strain energy density (SPSED) for a material, which is associated with fatigue failure and independent of applied loading. In the present study, based on CPFE simulations, the critical plastic strain energy density is calibrated using experimentally available fatigue life data for 718Plus, a Ni-base superalloy. Subsequently, the calibrated energy is used to predict fatigue lives at several loading regimes including multiple applied strain amplitudes and strain ratios. Moreover, SEMs are used to generate a scatter in the prediction to test for (a) log-normal distribution at a given applied strain and (b) increasing spread in the prediction with decreasing applied strain. With this, the CPFE simulation framework is outlined in Section 3.2.1. In Section 3.2.2, the calculation of the plastic strain energy density and the identification of the critical location for failure are discussed. A Bayesian calibration framework is outlined in Section 3.2.3 to estimate the critical SPSED and quantify the associated uncertainties. In Section 3.2.4, the results for the critical SPSED and predicted fatigue lives are reported. In Section 3.2.5, the results are discussed.

#### **3.2.1 Crystal plasticity finite element simulation framework**

##### ***Materials processing***

In this study, the material under consideration is 718Plus, a Ni-base superalloy. In particular, this material is processed via AM, specifically selective laser melting, using an EOS M280 laser powder bed machine at Honeywell Aerospace. The build parameters are optimized based on process modeling, discussed in Ref. [163], to result in minimal porosity [164]. The optimized parameter values are: 300 W laser power, 0.09 mm hatch spacing, 1.65 m/s laser speed, and stripe width of 5 mm. The powder used is ATI 718Plus® [165] which is referred to as 718Plus throughout this thesis. Following build, the material is subjected to a stress relief heat treatment at

1010°C for 1.5 h with a flue gas quench followed by a hot isostatic pressure cycle at 1163°C and 103 MPa for 4 h. Subsequently, the material is solution heat treated at 1010°C for 2 h with a flue gas quench and aged at 788°C for 8 h followed by a ramp down at 39°C/h to achieve a temperature of 704°C. At 704°C, the material is held for 8 h then cooled in a furnace. This heat treatment procedure has been shown to provide optimal microstructures and preferred strength characteristics [164]. The resulting microstructure, obtained via EBSD, is shown in Figure 3.8(a).

The bulk material is machined into specimens with a gauge length and diameter of 12.7 mm and 5 mm, respectively. Each specimen is polished to mitigate surface defects due to roughness. A total of 76 samples are tested according to ASTM E606 standards [166]. The fatigue testing is performed on smooth bars at room temperature with a constant amplitude loading frequency of 0.33 Hz. The load values are recorded and from this information, crack initiation and failure are defined at 10% and 50% load drops, respectively, in the stabilized maximum stress values. Experiments are performed at applied strain ratios of 0.05 and -1 across a range of applied strain amplitudes necessary to achieve a complete strain-life curve, as shown in Section 3.2.4. From the fractography analyses, the failure locations are typically associated with grain facets, hence crack initiation are not observed at features such as pores or inclusions. Therefore, microstructural defects, such as pores and inclusions, are not modelled in the CPFE analysis.

### ***Discretized 3D polycrystalline microstructures***

Using the methodology as described in Section 3.1.1, nine 3D SEMs are synthesized for the present work (see Figure 3.8(b)). The SEMs are cubes of dimension 180  $\mu\text{m}$ . Microstructural statistics of the SEMs are summarized in Table 3.2.

Table 3.2. Microstructural statistics of the statistically equivalent microstructures.

SEM	Number of grains	Grain size ( $\mu\text{m}$ )			Twin area fraction
		Minimum	Mean	Maximum	
1	135	15.67	35.13	134.19	0.50
2	139	17.68	34.59	159.08	0.51
3	139	14.24	35.76	132.30	0.51
4	140	16.76	34.65	138.22	0.49
5	140	19.92	36.14	141.83	0.53
6	141	16.48	35.58	137.86	0.54
7	137	16.37	35.40	140.29	0.54
8	146	16.18	35.43	136.82	0.51
9	133	16.67	35.30	136.56	0.55

For the present study, computationally efficient C3D4 elements, having the mean element size  $\sim 3.75 \mu\text{m}$ , are chosen to discretize the SEMs. The choice of the C3D4 elements often leads to numerical artifacts in the results from an elasto-plastic analysis. A possible mitigation strategy, adopted in the present study, is discussed in the “Slip system averaging scheme” section below. A discretized version of the SEM 1 is shown in Figure 3.9(a).

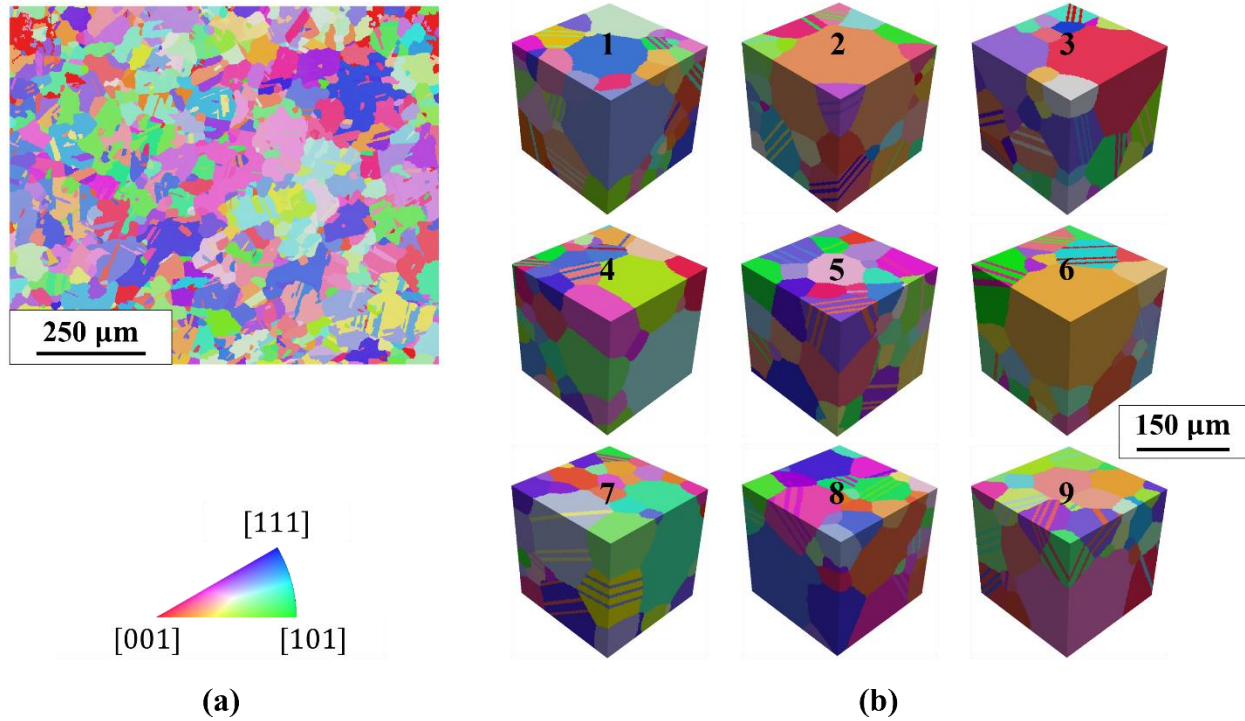


Figure 3.8. (a) EBSD characterization of the Ni-base superalloy 718Plus. (b) Statistically equivalent microstructures are corresponding to the EBSD map.

### *Crystal plasticity model and parameter estimation*

The CP constitutive equations, described in Section 3.1.1, are used for the present study. Starting with the CP parameters reported for AM IN718 in Ref. [161], the GA-based framework, as described in Section 3.1.1, is used to identify an optimal set of the CP parameters such that the homogenized macroscopic response of the model matches the experimentally obtained macroscopic stress-strain response of 718Plus. During simulations, normal displacements on three mutually orthogonal adjacent surfaces of the SEMs are restricted, and normal displacement is specified on another face as shown in Figure 3.9(b) to mimic uniaxial applied loading condition. The anisotropic elastic constants are adopted from Ref. [167]. For the CP parameters reported in Ref. [161], the macroscopic responses of all SEMs are similar (see Figure 3.10(a)). Therefore, only SEM 1 is used to calibrate the CP parameters. The anisotropic elastic constants along with the calibrated CP parameters are reported in Table 3.3. The simulated macroscopic stress-strain response with the calibrated CP parameters is compared to the experimental stress-strain data for

718Plus in Figure 3.10(b). A good agreement between simulated and experimental stress-strain response is observed in Figure 3.10(b).

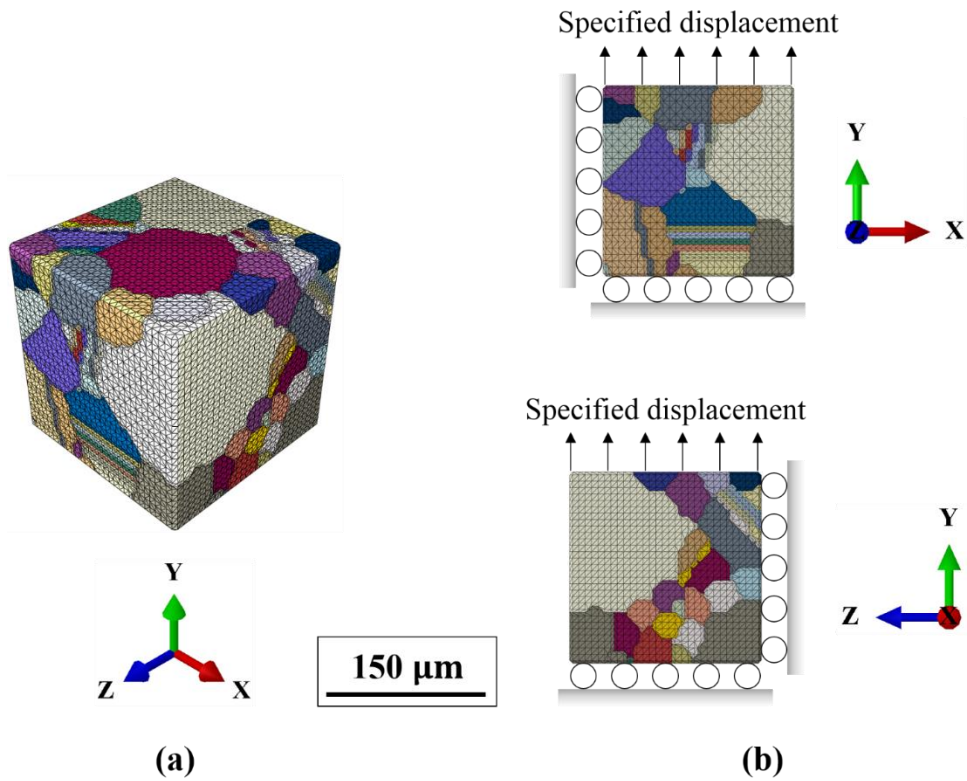


Figure 3.9. (a) Discretized statistically equivalent microstructure. (b) Applied boundary conditions on the discretized polycrystalline microstructure model.

Table 3.3. Anisotropic elastic constants and calibrated crystal plasticity parameters.

Parameter	Value	Parameter	Value
$C_{11}$	239.57 GPa	H	1885 MPa
$C_{12}$	141.18 GPa	$H_d$	8
$C_{44}$	107.04 GPa	A	5997 MPa
$\dot{\gamma}_0$	$4.25 \times 10^{-4} s^{-1}$	$A_d$	31
n	12	$\chi(0)$	10.2 MPa
$g(0)$	290.3 MPa	—	—

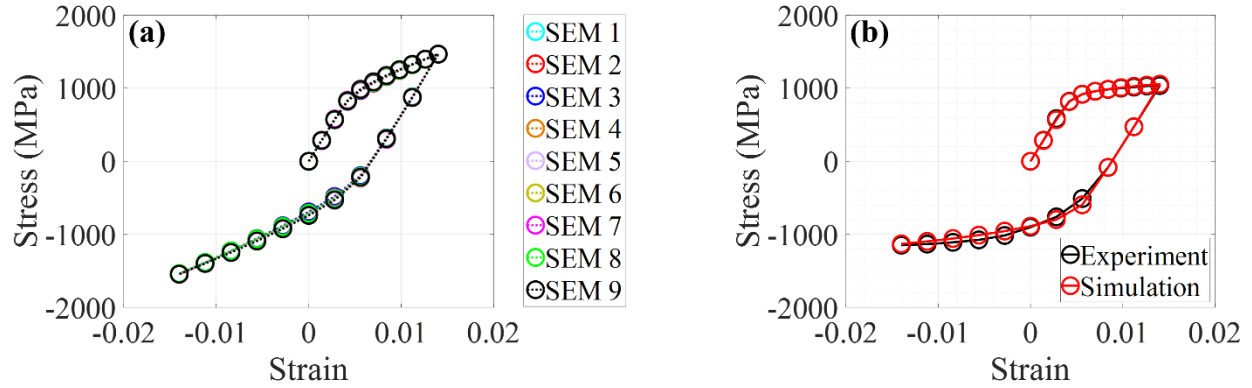


Figure 3.10. (a) Macroscopic stress-strain response of all SEMs using the CP parameters reported in Ref. [161]. (b) Experimental and simulated macroscopic stress-strain response from SEM 1 using calibrated CP parameters for 718Plus in this study.

### *Slip system averaging scheme*

The mechanical field variables (e.g., stress, plastic strain accumulation, etc.) from CPFE simulations often show spurious numerical oscillations within the simulation domain [161], [168]. Such behavior can be related to one or a combination of the following: (a) volumetric locking or shear locking due to the choice of the C3D4 elements [168], (b) lack of mesh refinement near the grain boundaries across which high gradients in field variables are expected, and (c) the effect of the boundary conditions on the elements near the corresponding surfaces. Under such a situation, one needs to adopt a homogenization scheme which can regularize numerical oscillations preserving the inherent spatial gradient associated with the field variable. One possibility is a slip system based averaging [27], [161], [169]–[172]. To illustrate the averaging scheme, let's consider an integration point as shown in Figure 3.11(a). Three directions are identified passing through the integration point, namely, slip direction ( $\mathbf{s}$ ), slip plane normal ( $\mathbf{n}$ ) and a transverse vector ( $\mathbf{t}$ ) on the slip plane such that these directions form a right-hand coordinate system at the integration point. Now, a small rectangular cuboid is considered having the centroid coinciding with the integration point and the faces parallel to the three directions defined before. The region enclosed by the rectangular cuboid is called the averaging volume. The field variable is averaged over all the elements whose centroids lie within the averaging volume. One can construct twelve such volumes, one for each slip system, around the same integration point. After performing averaging for all twelve volumes, the maximum (by magnitude) of the averaged values is assigned as the slip system averaged number to that integration point. If an integration point is near the grain boundary,

the averaging volume is not allowed to cross the grain boundary (see Figure 3.11(b)) to preserve the gradient, which is often expected across the grain boundary. The size of the averaging volume is dependent on the size of the finite elements. Presently, the lengths of the averaging volume are defined by 4, 3, 3 elements along the slip direction ( $\mathbf{s}$ ), slip plane normal ( $\mathbf{n}$ ) and transverse direction ( $\mathbf{t}$ ), respectively. Such an averaging scheme is implemented for all relevant field variables under present consideration during the post-processing phase of the CPFE fatigue simulations.

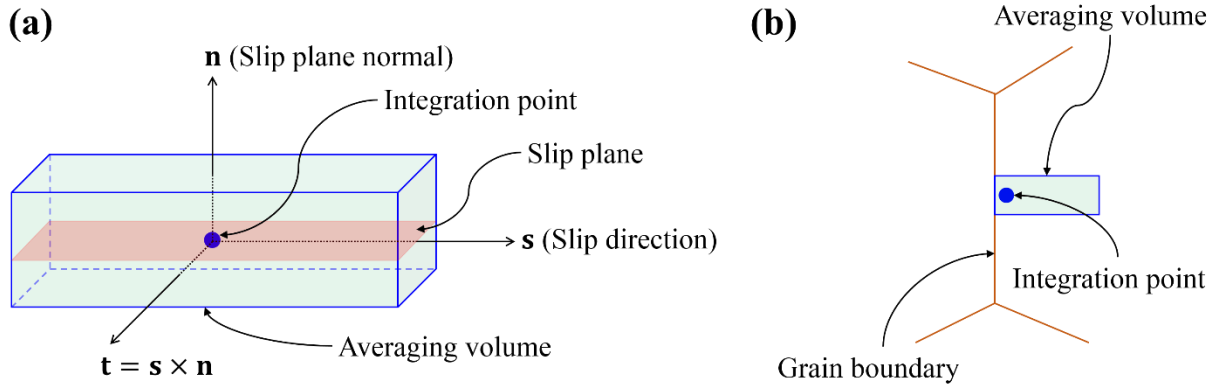


Figure 3.11. (a) Slip system based averaging scheme at an arbitrary integration point. (b) The averaging volume for an integration point near the grain boundary is not allowed to cross the grain boundary.

### 3.2.2 Critical plastic strain energy density criterion for fatigue life estimation

In CP analysis, plastic strain energy density at a material point  $\mathbf{x}$  is defined as a sum of contributions from all slip systems and its increment over the  $y^{\text{th}}$  cycle is written as

$$\Delta w_y^p(\mathbf{x}) = \oint_{y^{\text{th}} \text{ cycle}} \left( \sum_{k=1}^{12} |\tau^k(\mathbf{x}, t) \dot{\gamma}^k(\mathbf{x}, t)| \right) dt \quad (3.15)$$

Here,  $\Delta w_y^p(\mathbf{x})$  is the increment of the plastic strain energy density at the point  $\mathbf{x}$  over the  $y^{\text{th}}$  loading cycle. Now, the total accumulated plastic strain energy density after the  $y^{\text{th}}$  cycle at the same point,  $w_y^p(\mathbf{x})$ , is expressed as

$$w_y^p(\mathbf{x}) = \sum_{i=1}^y \Delta w_i^p(\mathbf{x}) \quad (3.16)$$

In the present study, it is postulated that if the material fails due to fatigue at  $\mathbf{x} = \mathbf{x}^*$  after  $N_f$  cycles,  $w_{N_f}^p(\mathbf{x}^*)$  is a material property and independent of the applied loading conditions. Further,  $w_{N_f}^p(\mathbf{x}^*)$  is referred to as the critical SPSED and denoted as  $W_{\text{critical}}^p$ . With experimentally known fatigue life, one needs to first calibrate  $W_{\text{critical}}^p$ . Thereafter, the calibrated critical SPSED can be used to predict the fatigue life at several loading conditions.

It is practically impossible to run CPFE simulations for thousands of cycles to track the evolutions of  $w_i^p(\mathbf{x})$  and  $\Delta w_i^p(\mathbf{x})$  with the number of cycles. However, it is well-known from experiments that the hysteresis behavior saturate upon cyclic loading, when stable dislocation structures and sub-structures are formed within the material [4]. Here,  $N_s$  is defined as the number of cycles required for saturation of the hysteresis loops. From CPFE simulations,  $N_s$  is identified based on saturation of  $\Delta w_i^p(\mathbf{x})$ . Subsequently, all simulations are continued until  $N_s$  cycles to obtain  $w_{N_s}^p(\mathbf{x})$  and  $\Delta w_{N_s}^p(\mathbf{x})$ . Since hysteresis loops saturate relatively quickly, material points experience an almost steady increment of plastic strain energy density for each loading cycle over a significantly large portion of the material's life. Therefore, from CPFE simulations, failure location,  $\mathbf{x}^*$ , is identified by the location of the maximum value<sup>††</sup> of  $\Delta w_{N_s}^p(\mathbf{x})$ . Finally,  $w_{N_s}^p(\mathbf{x}^*)$  is extrapolated to the experimentally known fatigue life,  $N_f^{\text{expt}}$ , using the following linear relationship to obtain  $w_{N_f}^p(\mathbf{x}^*)$  from CPFE simulations as

$$w_{N_f}^p(\mathbf{x}^*) = w_{N_s}^p(\mathbf{x}^*) + (N_f^{\text{expt}} - N_s) \Delta w_{N_s}^p(\mathbf{x}^*) \quad (3.17)$$

Subsequently,  $w_{N_f}^p(\mathbf{x}^*)$ , as obtained from Eq. (3.17), is used to calibrate  $W_{\text{critical}}^p$  for 718Plus using a Bayesian inference method as described in the next section.

### 3.2.3 Bayesian calibration of the critical plastic strain energy density

Variability is inherent in the experimental fatigue life data of a metallic material for a given loading condition. Such scatter in fatigue life data primarily comes from the variability in the statistical strength within the material associated with the local microstructure (e.g., grain size distributions, texture, pores, inclusions, precipitates, etc.) paired with fatigue crack initiation being

---

<sup>††</sup> While identifying  $\mathbf{x}^*$ , an element is ignored if its centroid lies within 20  $\mu\text{m}$  from the surfaces where boundary conditions are specified.

a locally driven phenomenon. Therefore, one will end up with multiple  $W_{\text{critical}}^{\text{P}}$  values for the same material if calibration is performed taking each experimental fatigue life data and simulated  $w_{N_s}^{\text{P}}(\mathbf{x}^*)$ ,  $\Delta w_{N_s}^{\text{P}}(\mathbf{x}^*)$  information from all SEMs. Since  $W_{\text{critical}}^{\text{P}}$  is hypothesized to be a material property, just like any other material property, one may expect a distribution of the same as opposed to a constant value. Hence, one of the objectives of the present study is to determine a distribution of the  $W_{\text{critical}}^{\text{P}}$  using a suitable method. Subsequently, the statistically expected value of  $W_{\text{critical}}^{\text{P}}$  can be used as a representative number for the material property.

Bayesian inference method is a powerful tool to calibrate model parameters when variability exists in the input and scatter is inevitable in the prior experimental knowledge of the output [173]. In the present work, the fatigue life prediction model is given by

$$N_f^{\text{predict}}(\boldsymbol{\beta}, W_{\text{critical}}^{\text{P}}) = \frac{W_{\text{critical}}^{\text{P}} - w_{N_s}^{\text{P}}(\boldsymbol{\beta}, \mathbf{x}^*)}{\Delta w_{N_s}^{\text{P}}(\boldsymbol{\beta}, \mathbf{x}^*)} + N_s(\boldsymbol{\beta}) \quad (3.18)$$

Here,  $\boldsymbol{\beta}$  is a set of parameters which define the loading conditions, such as the applied strain range, strain ratio, temperature;  $w_{N_s}^{\text{P}}(\boldsymbol{\beta}, \mathbf{x}^*)$ ,  $\Delta w_{N_s}^{\text{P}}(\boldsymbol{\beta}, \mathbf{x}^*)$  and  $N_s(\boldsymbol{\beta})$  come from the CPFÉ simulations, and  $W_{\text{critical}}^{\text{P}}$  is the *only* model parameter which is to be calibrated. For a given loading situation, i.e.,  $\boldsymbol{\beta}$ , variability is expected in  $w_{N_s}^{\text{P}}(\boldsymbol{\beta}, \mathbf{x}^*)$  and  $\Delta w_{N_s}^{\text{P}}(\boldsymbol{\beta}, \mathbf{x}^*)$  from different SEMs and scatter is experimentally observed in  $N_f^{\text{expt}}(\boldsymbol{\beta})$ . Therefore, the Bayesian inference method is an appropriate tool to calibrate  $W_{\text{critical}}^{\text{P}}$ .

From traditional fatigue experiments, it is well-known that scatter in fatigue life is dependent on the applied strain range showing an increasing trend with decreasing applied strain range [80]. Therefore, it is more appropriate to use a subset of the experimental fatigue life dataset at a higher applied strain range to calibrate  $W_{\text{critical}}^{\text{P}}$  to result in less uncertainty. For the present work, the fatigue experiments are carried out from 0.3% to 1.2% applied strain range. Therefore, only 1.2% applied strain range dataset is used for calibration, and the rest of the data are kept *untouched* for subsequent verification.

A broad overview of the Bayesian calibration method is shown in Figure 3.12. Key inputs to the calibration framework are experimental knowledge (i.e., fatigue life data) and prior distribution of the model parameter ( $W_{\text{critical}}^{\text{P}}$ ) based on experience or prior belief. The output from the calibration framework is the posterior distribution which is the calibrated distribution of the

model parameter. Finally, the expected value of the model parameter ( $W_{\text{critical}}^p$ ) is obtained based on its posterior distribution.

The experimentally observed fatigue life ( $N_f^{\text{expt}}$ ) and prediction from the model ( $N_f^{\text{predict}}$ ) can be related using the following equation

$$N_f^{\text{expt}}(\boldsymbol{\beta}) = N_f^{\text{predict}}(\boldsymbol{\beta}, W_{\text{critical}}^p) + \delta(\boldsymbol{\beta}) + e(\boldsymbol{\beta}) \quad (3.19)$$

Here,  $\delta(\boldsymbol{\beta})$  accounts for model's inability to capture the correct physics including limitations associated with the phenomenological evolution equations of the CP model;  $e(\boldsymbol{\beta})$  is the error associated with the experimental measurements and uncertainty. The model discrepancy,  $\delta(\boldsymbol{\beta})$ , can be assumed to be independently and identically distributed, and hence is considered as normally distributed with zero mean and standard deviation,  $s_1$  (unknown). Similarly, without loss of generality,  $e(\boldsymbol{\beta})$  can be assumed to be independently and identically distributed, and hence is considered as normally distributed with zero mean and standard deviation,  $s_2$  (unknown). Since the summation of two normal distributions with identical mean is also a normal distribution, the model discrepancy and experimental error terms are combined to form another normal distribution with zero mean and standard deviation,  $s$  (unknown). Consequently, in addition to  $W_{\text{critical}}^p$ , the parameter  $s$  is also required to be calibrated. Therefore, the new augmented parameter set is given by  $\boldsymbol{\alpha} = \{W_{\text{critical}}^p, s\}$ . The additional parameter,  $s$ , is also known as a hyper-parameter. It is clarified that the fatigue life prediction model, given by Eq. (3.18), still involves only *one* parameter. However, because of the choice of the current calibration framework, the model is required to be calibrated considering Eq. (3.19) which relates stochastic aspects of the model predictions and experimental observations. Consequently, an additional unknown standard deviation parameter,  $s$ , is required to be calibrated. After calibration,  $s$  has no role to play in the subsequent fatigue life prediction.

In the present work, the Bayesian calibration framework is composed of three ingredients, namely the Bayesian inference method, Markov Chain Monte Carlo sampling, and the Metropolis-Hastings algorithm. A brief description of each of these ingredients and their role in the Bayesian calibration framework are provided below.

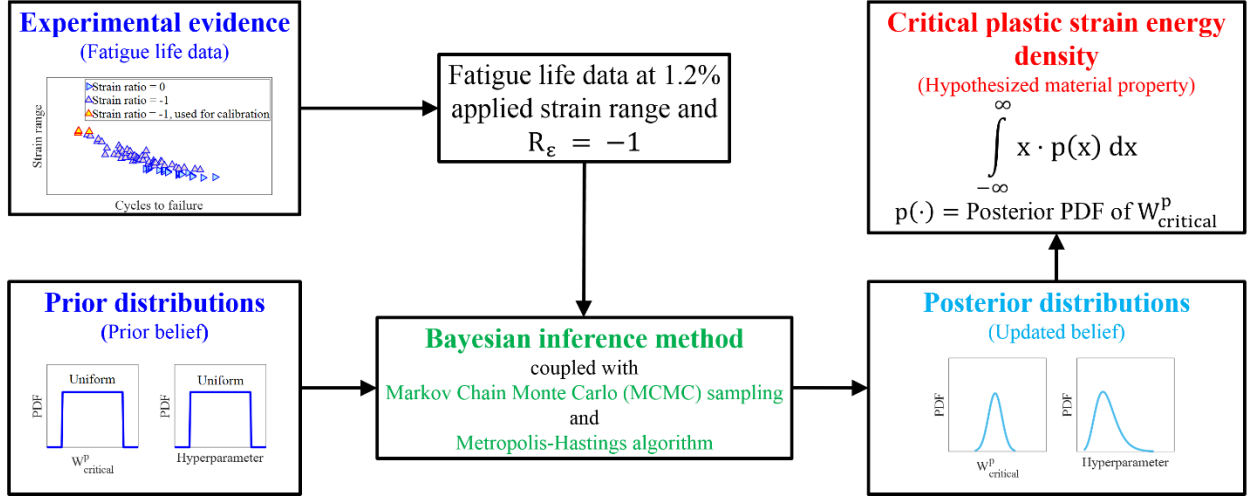


Figure 3.12. A schematic of the Bayesian inference framework to calibrate the critical stored plastic strain energy density.

### ***Bayesian inference method***

The Bayesian inference technique updates the prior distribution of the parameter set  $\alpha$  based on the experimental evidence and likelihood function. The posterior distribution is obtained as output using

$$\pi(\alpha|\mathcal{D}) = \frac{\pi(\mathcal{D}|\alpha)\pi_0(\alpha)}{\pi(\mathcal{D})} = \frac{\pi(\mathcal{D}|\alpha)\pi_0(\alpha)}{\int \pi(\mathcal{D}|\alpha)\pi_0(\alpha) d\alpha} \quad (3.20)$$

Here,  $\pi_0(\alpha)$  represents the prior distribution of the parameter set  $\alpha$ ;  $\pi(\mathcal{D}|\alpha)$  represents the likelihood of observing experimental data,  $\mathcal{D}$ , for the given parameter set  $\alpha$ ;  $\pi(\alpha|\mathcal{D})$  is the posterior distribution of the parameter set  $\alpha$  based on experimental evidence  $\mathcal{D}$  and likelihood term  $\pi(\mathcal{D}|\alpha)$ . Since the error terms, as defined in the Eq. (3.19), are assumed to be independently and identically distributed, the likelihood term is expressed as [173]

$$\pi(\mathcal{D}|\alpha) = \frac{1}{(2\pi s^2)^{\frac{q}{2}}} \exp\left(-\frac{\text{SSE}(\alpha)}{2s^2}\right) \quad (3.21)$$

Here,  $s$  is the hyper-parameter as defined before;  $\text{SSE}(\alpha)$  is the sum of squares of errors for the parameter set  $\alpha$  and expressed as

$$\text{SSE}(\alpha) = \sum_{i=1}^m \sum_{j=1}^k \left(N_i^{\text{expt}} - N_j^{\text{predict}}(\alpha)\right)^2 \quad (3.22)$$

In Eq. (3.22),  $N_i^{\text{expt}}$  is the  $i^{\text{th}}$  experimental fatigue life in a set of  $m$  data and  $N_j^{\text{predict}}$  is the predicted life corresponding to the  $j^{\text{th}}$  SEM in a set of  $k(= 9)$  SEMs at a given loading situation. The parameter  $q$  in Eq. (3.21) is related to  $m$  and  $k$  as

$$q = m \cdot k \quad (3.23)$$

### ***Markov Chain Monte Carlo sampling and Metropolis-Hastings algorithm***

For many practical cases, it is challenging to evaluate the integral in the denominator of Eq. (3.20) analytically or using numerical quadrature. In such situations, the Markov Chain Monte Carlo (MCMC) sampling method is preferred to obtain posterior distributions for the parameter set  $\alpha$ . A Markov Chain is a sequence of random variables that satisfies the Markov property that the  $k^{\text{th}}$  term in the sequence depends only on the  $(k - 1)^{\text{th}}$  term. The  $k^{\text{th}}$  term is proposed via Monte Carlo sampling method based on a proposal distribution. The decision whether the new proposed candidate point will be accepted as the  $k^{\text{th}}$  term in the sequence is taken based on the Metropolis-Hastings algorithm [174], [175]. Stepwise computer implementation of the algorithm has been discussed by Yeratapally et al. [140] in relation to the UQ of a microstructure-sensitive fatigue life prediction model. However, for the sake of completeness and continuity, important aspects and equations of the Metropolis-Hastings algorithm are outlined below.

Let,  $\alpha_j^{k-1}$  be the  $j^{\text{th}}$  parameter ( $j = 1, 2$ ) in the  $(k - 1)^{\text{th}}$  term of the Markov Chain and  $\alpha_j^*$  be the proposed  $j^{\text{th}}$  parameter for the  $k^{\text{th}}$  term in the sequence. Now, the following number is computed

$$p = \min \left( 1, \frac{\pi(\mathcal{D}|\alpha_j^*)\pi_0(\alpha_j^*)\pi(\alpha_j^*|\alpha_j^{k-1})}{\pi(\mathcal{D}|\alpha_j^{k-1})\pi_0(\alpha_j^{k-1})\pi(\alpha_j^{k-1}|\alpha_j^*)} \right) \quad (3.24)$$

Here,  $\pi(\alpha_j^*|\alpha_j^{k-1})$  represents the proposal distribution, used to generate the proposed candidate point  $\alpha_j^*$  based on the current candidate point  $\alpha_j^{k-1}$ . Here, the proposal distribution is assumed to be symmetric for which

$$\pi(\alpha_j^*|\alpha_j^{k-1}) = \pi(\alpha_j^{k-1}|\alpha_j^*) \quad (3.25)$$

Therefore, Eq. (3.24) can be simplified and rewritten as follows

$$p = \min \left( 1, \frac{\pi(\mathcal{D}|\alpha_j^*)\pi_0(\alpha_j^*)}{\pi(\mathcal{D}|\alpha_j^{k-1})\pi_0(\alpha_j^{k-1})} \right) \quad (3.26)$$

The assumption of symmetric proposal distribution is a matter of convenience and simplicity. If the posterior distribution is expected to be symmetric, such a choice leads to quick convergence (as discussed later). Otherwise, it may take a longer time to obtain a converged posterior distribution. After obtaining  $p$  from Eq. (3.26), a uniformly distributed random number  $u$  is generated within the interval  $0 \leq u \leq 1$ . If  $u \leq p$ , the proposed candidate is selected as the  $k^{\text{th}}$  term in the sequence, i.e.,  $\alpha_j^k = \alpha_j^*$ . Otherwise, the  $(k - 1)^{\text{th}}$  term is assigned as the  $k^{\text{th}}$  term, i.e.,  $\alpha_j^k = \alpha_j^{k-1}$ . This process is continued until convergence is achieved. To check for convergence,  $M$  Markov Chains are run in parallel. If  $B_{\alpha_j}$  and  $W_{\alpha_j}$  are the variance of the parameter  $\alpha_j$  between and within chains, respectively, then an estimate of the variance of the parameter  $\alpha_j$ ,  $V_{\alpha_j}$ , is given by

$$V_{\alpha_j} = \frac{M - 1}{M} W_{\alpha_j} + \frac{1}{M} B_{\alpha_j} \quad (3.27)$$

Using  $V_{\alpha_j}$  and  $W_{\alpha_j}$  a convergence parameter  $R_{\alpha_j}$  is defined as

$$R_{\alpha_j} = \sqrt{\frac{V_{\alpha_j}}{W_{\alpha_j}}} \quad (3.28)$$

With the increase in the number of Monte Carlo sampling,  $k$ , in each Markov Chain, the parameter  $R_{\alpha_j}$  approaches unity resulting in a converged/stationary distribution. Such a converged/stationary distribution is the posterior distribution. The reader is referred to Cross et al. [176] for the expressions of  $W_{\alpha_j}$  and  $B_{\alpha_j}$ .

### 3.2.4 Results

#### *Critical stored plastic strain energy density*

For a representative example, evolutions of  $\Delta w^P$  with the number of cycles at the critical location within SEM 1 under macroscopically applied strain  $\Delta \varepsilon = 0.5\%$  at strain ratios  $R_\varepsilon = -1$  and  $0.05$  are shown in Figure 3.13. It is evident from Figure 3.13 that  $\Delta w^P$  saturates immediately after the first cycle. However, simulations are continued until ten cycles in the present work, resulting in  $N_s = 10$ . For Bayesian calibration, the CPFE simulations are performed on all SEMs at  $\Delta \varepsilon = 1.2\%$  with  $R_\varepsilon = -1$  to obtain  $w_{10}^P(\mathbf{x}^*)$  and  $\Delta w_{10}^P(\mathbf{x}^*)$ . Uniform distributions are assumed as prior distributions for both parameters, and the MCMC simulations are continued until  $10^5$  iterations to ensure convergence. Here, convergence is accepted if  $R_{\alpha_j} < 1.005$ . Converged

posterior distributions are shown in Figure 3.14. From Figure 3.14, it is observed that the posterior data for  $W_{\text{critical}}^p$  closely follows a normal distribution, whereas the posterior distribution for the hyper-parameter is found to follow a log-normal distribution. Characteristics of the posterior distributions are reported in the Table 3.4.

Table 3.4. Prior and posterior distributions for the critical stored plastic strain energy density and hyper-parameter.

Parameter	Prior distribution	Posterior distribution			$R_{\alpha_j}$
		Type	Mean	Standard deviation	
$W_{\text{critical}}^p$	Uniform, $U(0, \infty)$	Normal	39.5 J/mm <sup>3</sup>	1.4 J/mm <sup>3</sup>	1.004
s	Uniform, $U(0, \infty)$	Log-Normal	379.0 cycles	104.0 cycles	1.002

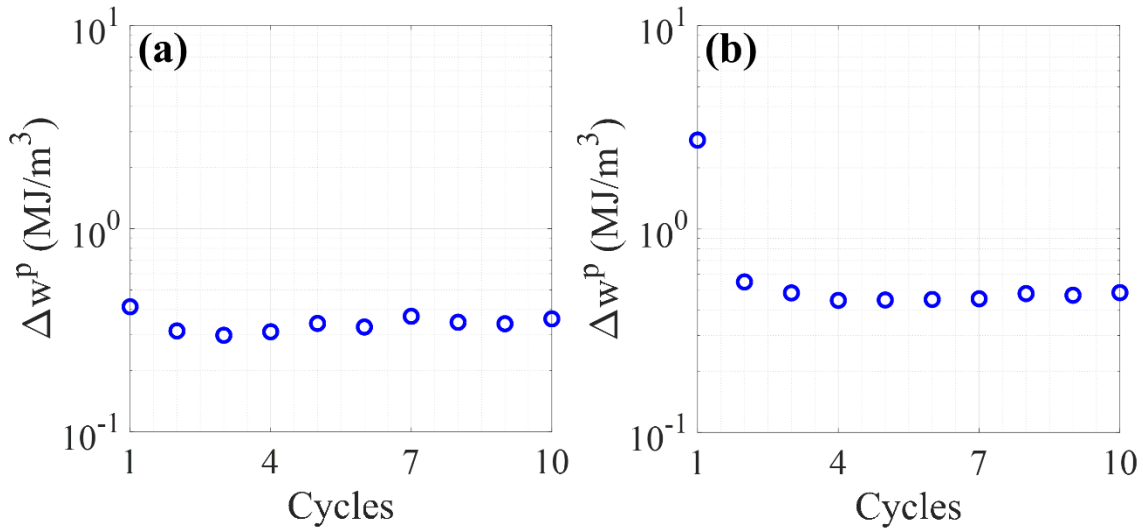


Figure 3.13. Evolution of plastic strain energy density per cycle with the number of cycles at the critical location within SEM 1 under macroscopically applied strain,  $\Delta\varepsilon = 0.5\%$  at (a)  $R_\varepsilon = -1$  and (b)  $R_\varepsilon = 0.05$ .

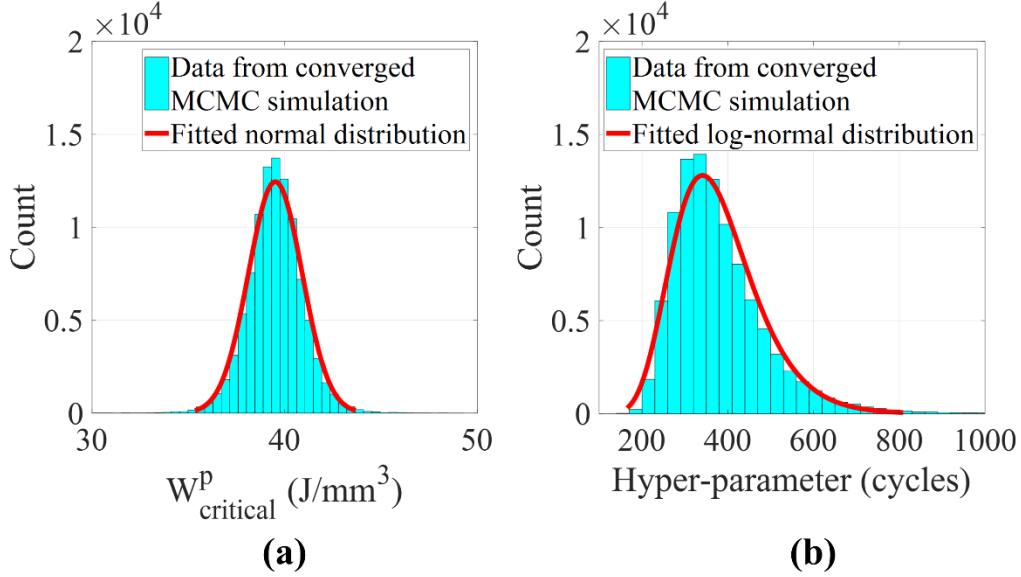


Figure 3.14. Posterior distributions for (a) the critical stored plastic strain energy density,  $W_{\text{critical}}^p$ , and (b) the hyper-parameter,  $s$ .

### *Fatigue life prediction*

The CPFE simulations are performed for  $\Delta\varepsilon = 0.95\%$ ,  $0.75\%$ ,  $0.675\%$ ,  $0.625\%$ ,  $0.5\%$  at  $R_\varepsilon = -1$  and for  $\Delta\varepsilon = 0.5\%$ ,  $0.43\%$ ,  $0.36\%$  at  $R_\varepsilon = 0.05$ . From all simulations and all SEMs,  $w_{10}^p(\mathbf{x}^*)$  and  $\Delta w_{10}^p(\mathbf{x}^*)$  are obtained. Finally, these values are used within Eq. (3.18) along with the  $W_{\text{critical}}^p$  value, as reported in Table 3.4, to predict fatigue lives at each strain ranges from all SEMs. The probability of failure plots are obtained using `probplot` function in MATLAB considering log-normal distribution as a reference and shown in Figure 3.15. In Figure 3.15, the vertical axes are depicted in such a way that if data points are sampled from log-normal distributions, those will be aligned along a straight line. As expected, experimental data points in each plot appear to be aligned along a straight line. Interestingly, all the predicted data points also appear to be aligned along a straight line. Therefore, it can be said that the microstructure-sensitive critical plastic strain energy density criterion consistently predicts log-normally distributed fatigue life across several loading regimes. In each case, predicted lives from all SEMs are fitted to a log-normal distribution. Experimental data, predictions from all SEMs and log-normal mean of predictions are shown in the Figure 3.16. A good agreement between the experimental and predicted lives is seen in Figure 3.15 and Figure 3.16. Further, an increasing spread in the fatigue life predictions, from an identical set of SEMs, is observed with a decreasing applied strain.

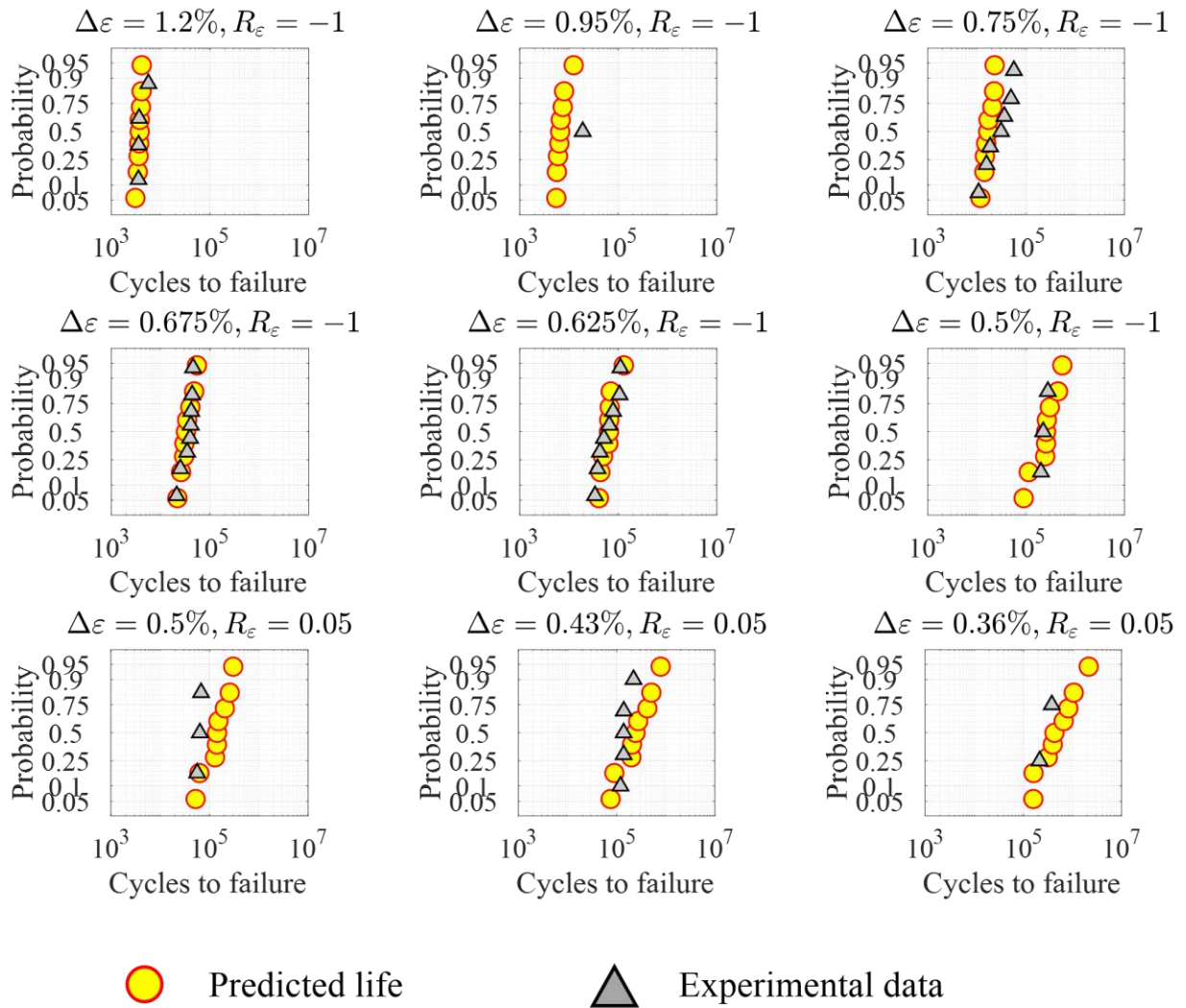


Figure 3.15. The probability of failure plots considering log-normal distribution as reference.

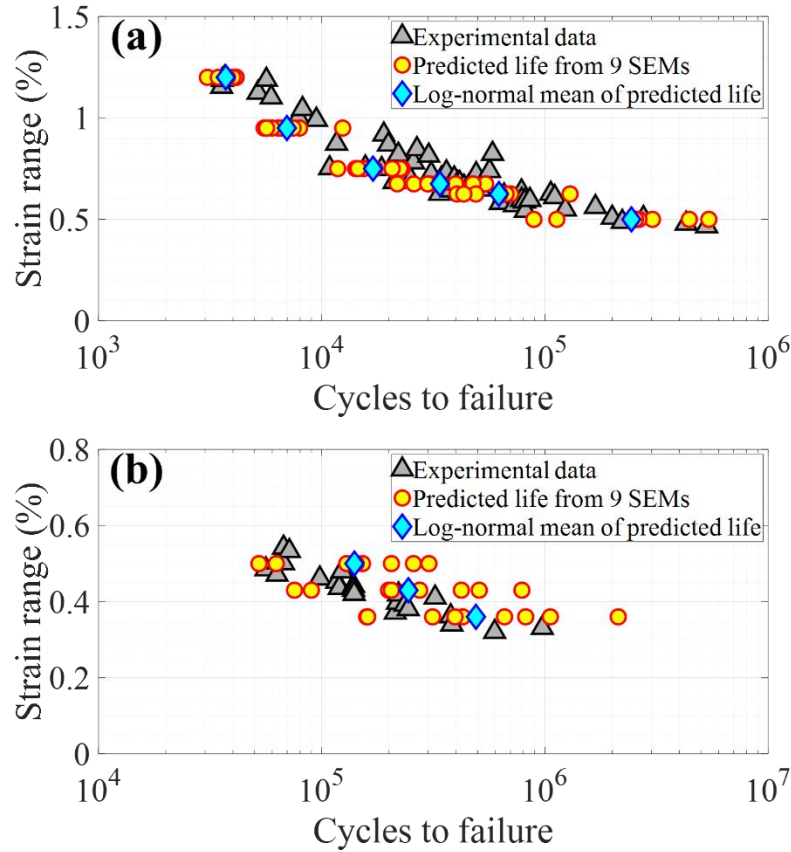


Figure 3.16. Experimental and predicted fatigue life data at (a)  $R_\epsilon = -1$  and (b)  $R_\epsilon = 0.05$ .

### 3.2.5 Discussion

The fatigue life prediction framework, presented in this work, inherently captures the relevant physics or mechanism of the plastic deformation via CP constitutive equations. Hence, it can capture the irreversibilities associated with the deformation even if the material is loaded elastically in a macroscopic sense. In other words, the framework can be used for both HCF, dominated by microplasticity, and LCF, dominated by large amount of plastic deformation, situations. In this study, dislocation glide is the primary deformation mechanism which has been incorporated in the CP framework via Eq. (3.2). In other material systems, additional deformation mechanisms, such as deformation twinning, might be dominant as well. In those situations, kinematic equations (Eqs. (3.1) and (3.2)) for the CP model should be updated appropriately before using Eq. (3.15). Further, the present approach can, in principle, be extended to situations where environment plays an important role (for example, Hydrogen embrittlement, corrosion, etc.) in the

fatigue performance of the material via incorporating suitable constitutive relations in the CP model.

The reader is reminded that the CPFEE simulation results, i.e.,  $w_{10}^p(\mathbf{x}^*)$  and  $\Delta w_{10}^p(\mathbf{x}^*)$ , are key inputs to the fatigue life prediction model given by Eq. (3.18). Therefore, the magnitude of the calibrated  $W_{\text{critical}}^p$  strongly depends on the size of the slip system averaging volume, as discussed in Section 3.2.1. Since the size of the slip system averaging volume has been consistently kept the same throughout the present work, their effect will not be reflected in the fatigue life predictions. However, the reported value for  $W_{\text{critical}}^p$  should not be considered as a benchmarked number for 718Plus. For more rigorous estimation of the  $W_{\text{critical}}^p$ , the following should be considered.

- Non-linear finite elements should be used to avoid volumetric/shear locking and thus eliminating the necessity of the slip system-based averaging.
- The mesh near the grain boundary should be sufficiently refined to accurately capture the gradients associated with the mechanical field variables in that region.

Fatigue life is experimentally obtained using specimens having a gauge length and diameter of 12.7 mm and 5 mm, respectively, whereas the domain size for the CPFEE simulations is restricted to cubes of 180  $\mu\text{m}$  length due to the higher computational cost. Since simulation domain size is kept identical for calibration of  $W_{\text{critical}}^p$  as well as prediction of fatigue life, its effect is not seen in Figure 3.15 and Figure 3.16. In the present study, the uncertainty in  $W_{\text{critical}}^p$  due to the size of the SEM is implicitly taken care of via the hyper-parameter through Eq. (3.19). In Ref. [71], it is shown that if the number of grains within the SEM is around or greater than 150, convergence is achieved in the strength properties of the material (in terms of capturing the macroscopic yield, hardening behavior, Bauschinger effect, etc.). In the present work, the consistent size of the SEMs is necessary to capture the effect of microstructure variability in the fatigue behavior and thereby the fatigue performance, but each SEM is not designed to predict the statistical minimum fatigue life. The appropriate size of the microstructure instantiation, at the mesoscopic length-scale, should be identified more rigorously for fatigue predictions at the length-scale of a component, which is a topic for future work.

When the macroscopic stress-strain data is used to calibrate the CP parameters, as in the present work, the resulting CP parameters may not be unique, which would lead to additional uncertainty in the values of  $w_{10}^p(\mathbf{x}^*)$  and  $\Delta w_{10}^p(\mathbf{x}^*)$ . Detailed UQ of the CP parameters and their

influence on the associated fatigue metrics (e.g. the stored plastic strain energy density) have been performed in Section 3.1. The results indicate that the uncertainty in the CP parameters may propagate to ~25% variability in the values of  $w_{10}^p(\mathbf{x}^*)$  and  $\Delta w_{10}^p(\mathbf{x}^*)$ . In the present context, it would imply that the calibrated distribution of  $W_{\text{critical}}^p$  might result in a slightly higher standard deviation, which would not affect the mean of  $W_{\text{critical}}^p$  and hence the predicted fatigue life.

As discussed before, the material stores a portion of its internal plastic work by forming dislocation structures and sub-structures, and the rest is primarily dissipated as heat energy. The stored portion of the internal plastic work is of interest in the context of fatigue failure. It is often argued that 5% of the total plastic work is stored in the material and the remaining 95% is lost as heat energy [73]. However, the number 95% is not universally accepted (see, for example, Refs. [177], [178]), and in some cases, found to be increasing with increasing plastic strain [177]. Hence, there exists a critical need to carry out rigorous studies to characterize the percentage of plastic work lost as heat energy, and in turn, the percentage of plastic work stored within the material as a function of applied strain and temperature. In the absence of a lack of agreement between the reported values of the partitioning coefficient in the literature, researchers often neglect the partitioning effect in their numerical calculation (see, for example, Refs. [31]–[55]). With this, while computing  $W_{\text{critical}}^p$ , we have not considered the partitioning of the plastic work. The entire plastic work has been assumed to be stored by the material. In the present context, such an assumption only affects the calibrated value of the  $W_{\text{critical}}^p$ , not the predicted fatigue lives. In other words, a more realistic calibration of  $W_{\text{critical}}^p$  would require incorporation of a scalar constant in Eqs. (3.15)-(3.18) to incorporate the partitioning aspect, which would only change the calibrated numerical value of  $W_{\text{critical}}^p$  but not the subsequent fatigue life prediction.

One can observe from Figure 3.16 that the predicted life at lower strain amplitude, especially at  $R_\epsilon = 0.05$ , span from  $\sim 10^5$  cycles to  $\sim 10^6$  cycles. Therefore, if experimental data at these strain amplitudes are used to calibrate  $W_{\text{critical}}^p$ , the resulting posterior distributions will involve a higher level of uncertainty, characterized by a higher standard deviation in  $W_{\text{critical}}^p$  and higher mean and standard deviation for the hyper-parameter  $s$ . In other words, just like model discrepancy  $\delta(\boldsymbol{\beta})$  and experimental uncertainty  $e(\boldsymbol{\beta})$  terms in Eq. (3.19), the hyper-parameter  $s$  is also dependent on the loading conditions defined by  $\boldsymbol{\beta}$ . Since the life predictions from different SEMs involve least scatter at the 1.2% applied strain range, the experimental data corresponding

to the same loading regime is used in the present work to calibrate  $W_{\text{critical}}^{\text{p}}$ . If the entire experimental and simulation datasets for  $R_{\varepsilon} = -1$  are used for the calibration<sup>‡‡</sup>, the resulting mean and standard deviation of  $W_{\text{critical}}^{\text{p}}$  are found to be  $\sim 4\%$  lower and  $\sim 4$  times higher, respectively, whereas the order of magnitude of the hyper-parameter is found to be  $\sim 100$  times higher than the values reported in Table 3.4. These observations further support the forgoing discussion.

It has already been mentioned in Section 3.2.4 that an increasing spread in the fatigue life predictions, from an identical set of SEMs, is observed with a decreasing applied strain. Such progressive uncertainty in predictions, from the same set of SEMs, with decreasing applied strain is certainly a manifestation of the change in  $\mathbf{x}^*$ , i.e., failure location, with applied loading situation. To confirm,  $\mathbf{x}^*$  is tracked within SEM 1 with the change in applied loading. A shift of the failure location from the free surface to an interior twin boundary is observed with the decrease in applied strain (see Figure 3.17). At  $\Delta\varepsilon = 1.2\%$ ,  $0.95\%$ , and  $0.675\%$ , the failure location is observed near or at the free surface (Figure 3.17(a)-(c)). Subsequently, at lower  $\Delta\varepsilon$ , the failure location is identified at interior twin boundaries (Figure 3.17(d)-(i)). The ability of the microstructure-sensitive plastic strain energy density criterion to capture (a) the shift in failure location, often seen in real experiments, and (b) real fatigue life data with reasonable accuracy across various loading regimes certainly demands attention of the industry as well as academia to reduce extensive time and cost associated with experimental fatigue life characterization.

It is well-known that properties associated with the mechanical behavior of materials are inherently microstructure dependent. In the present study, we have hypothesized the critical SPSED as a material property and have characterized its statistical distribution. While predicting fatigue lives, we have used the mean value, which is applicable for the current microstructure. By altering the statistical descriptors of the microstructure, a different mean value of the critical SPSED is expected. However, such dissimilarity has to be verified in future work. Further, for a given statistical description of the microstructure, the applicability of a single critical SPSED is also required to be tested and verified in (a) the presence of defects, such as pores and inclusions

---

‡‡ While using experimental fatigue life data over multiple strain ranges, spanning several orders of magnitudes of life, to calibrate the critical plastic strain energy density, the error in prediction should be scaled while estimating the likelihood function via Eqs. (3.21) and (3.22) to eliminate the effect of varying order of magnitudes in error at different applied strains. Under such a situation, the scaled square of error might be computed as  $\left(\frac{N_{\text{expt}} - N_{\text{predict}}}{10^{\text{order}(N_{\text{expt}})}}\right)^2$ , where the  $\text{order}(x)$  function returns the order of magnitude of the number  $x$ , and used in Eq. (3.23) to calculate the sum of square of errors.

and (b) other loading conditions, including the role of environment, various operating temperatures, and multi-axial applied loading.

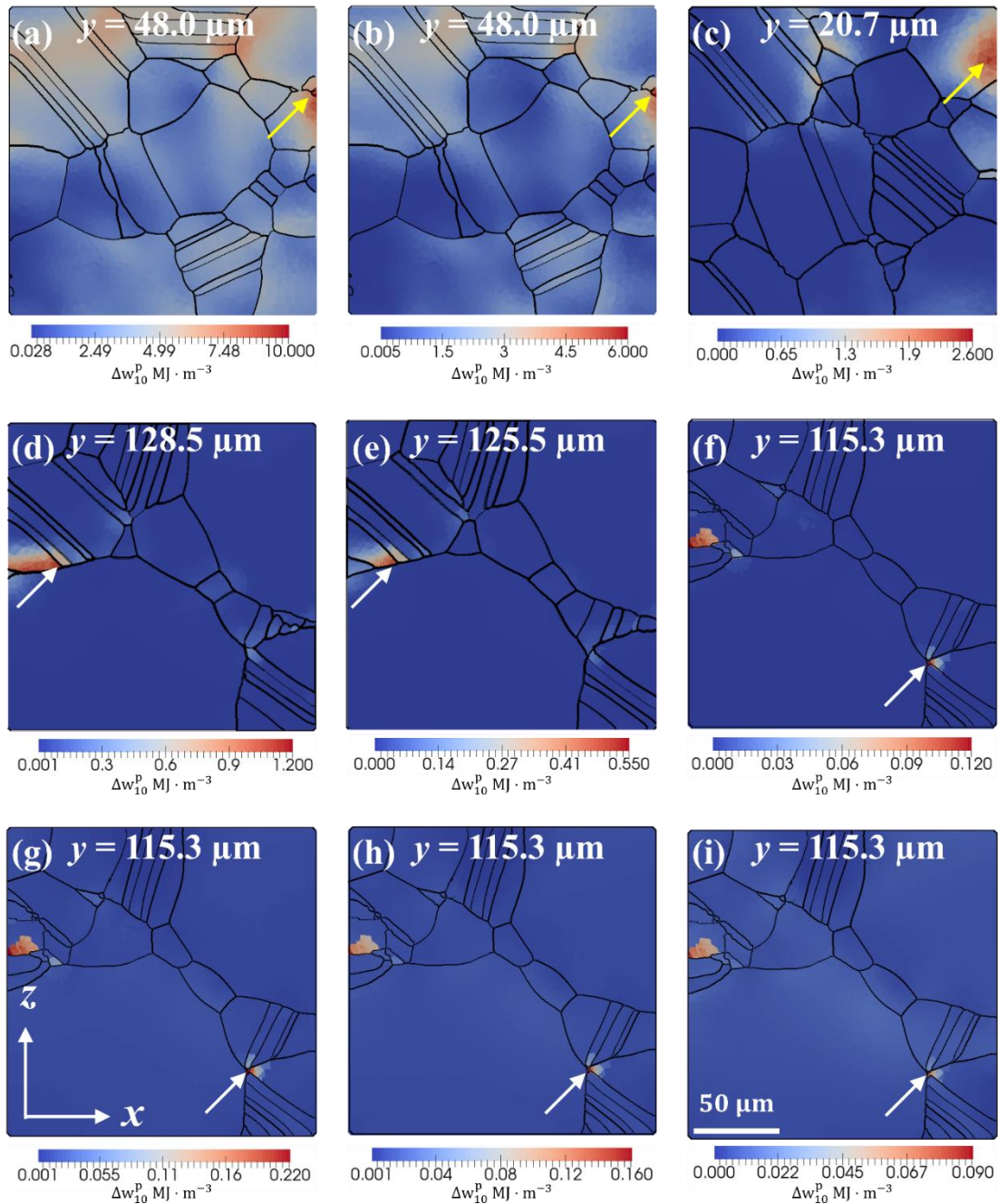


Figure 3.17. The location of maximum  $\Delta w_{10}^p$  within SEM 1 at (a)  $\Delta \varepsilon = 1.2\%$ ,  $R_\varepsilon = -1$ , (b)  $\Delta \varepsilon = 0.95\%$ ,  $R_\varepsilon = -1$ , (c)  $\Delta \varepsilon = 0.75\%$ ,  $R_\varepsilon = -1$ , (d)  $\Delta \varepsilon = 0.675\%$ ,  $R_\varepsilon = -1$ , (e)  $\Delta \varepsilon = 0.625\%$ ,  $R_\varepsilon = -1$ , (f)  $\Delta \varepsilon = 0.5\%$ ,  $R_\varepsilon = -1$ , (g)  $\Delta \varepsilon = 0.5\%$ ,  $R_\varepsilon = 0.05$ , (h)  $\Delta \varepsilon = 0.43\%$ ,  $R_\varepsilon = 0.05$ , and (i)  $\Delta \varepsilon = 0.36\%$ ,  $R_\varepsilon = 0.05$ . The yellow arrows indicate the critical location near or at the free surface and the white arrows indicate hot spots at the twin boundaries. Each color map is a cross-sectional view of the SEM 1 on the  $x$ - $z$  plane, normal to the loading direction  $y$ .

### 3.2.6 Summary

A microstructure-sensitive critical stored plastic strain energy density is postulated to be the driving mechanism of fatigue crack initiation and is applicable to predict failure across several loading regimes. The model is inherently physics-based, and only requires one parameter, namely, the critical stored plastic strain energy density. This critical stored plastic strain energy density is calibrated using experimental fatigue life data under fully reversed type loading at 1.2% applied strain range via Bayesian inference method. Subsequently, the calibrated critical energy value is used to predict fatigue lives at eight strain ranges including strain ratios -1 and 0.05. The key findings are summarized below.

- Predicted lives from nine statistically equivalent microstructures for each applied strain range are found to follow a log-normal distribution which is consistent with observations in traditional fatigue experiments.
- A good agreement is observed between the experimental fatigue life and the log-normal mean of the predictions at eight strain ranges including strain ratios -1 and 0.05.
- For a given strain ratio, increasing spread in the predictions from the identical set of statistically equivalent microstructures is observed with decreasing applied strain amplitude.

## 4. ANALYSIS AND PREDICTION OF COMPETING FAILURE MODES IN A NICKEL-BASE SUPERALLOY

The objective of the present chapter is to extend the microstructure-sensitive fatigue life prediction framework, developed in Section 3.2, to predict two competing failure modes, namely inclusion- and matrix-driven failures, in a Ni-base superalloy. However, as described in Section 2.2, the stochastic nature of the emergence of these two failure modes require an in-depth understanding of a multitude of parameters that influence the emergence of these failure modes. To this end, a parametric study is carried out in Section 4.1 to obtain the insights into the effect of each of these parameters. Subsequently, in Section 4.2, critical stored plastic strain energy density (SPSED), i.e.,  $W_{\text{critical}}^{\text{P}}$ , is calibrated as a function of temperature to predict fatigue life and associated failure modes as a function of applied strain range and temperature.

### 4.1 Analysis of competing failure modes

The inclusions in Ni-base superalloys can be broadly categorized as oxides and carbides. Depending on the chemical composition, one may find an inclusion as a solid hard particle as well as an agglomerate of small particles. In the literature, solid hard particles are known as Type 1 inclusion, whereas agglomerate of small particles are referred to as Type 2 inclusion [179]. Depending on the type, structural stiffness of the inclusions is expected to span a wide range resulting in lower or higher stiffness (Young's modulus) compared to the matrix. Moreover, due to the varying chemical composition and crystallographic structure, one may expect a wide range of coefficient of thermal expansion (CTE) of the inclusions as well, resulting in lower or higher CTE than the matrix material. Some of the inclusions may be perfectly bonded to the matrix, whereas some may have debonded interfaces due to the thermo-mechanical processing conditions. Additionally, one would observe microstructural variability regarding grain morphology, size, and orientation distributions around every inclusion within the material. Here, the influence of each of these parameters are studied, while keeping the others unchanged. In particular, the role of inclusion stiffness, loading regime, loading direction, a debonded region in the inclusion-matrix interface, microstructural variability around the inclusion, inclusion size, dissimilar CTE, temperature, residual stress, and distance of the inclusion from the free surface in the emergence

of competing failure modes are investigated using CPFEE simulations. For simplicity, the inclusion is modeled as a homogeneous, isotropic, linear-elastic material and anisotropic elastic and plastic constitutive relations are incorporated for the matrix material which is PM produced RR1000 in this case. With this, the CPFEE simulation framework is laid out in Section 4.1.1. In Section 4.1.2, the damage indicative parameter, used for the present study to identify failure modes, is discussed. In Section 4.1.3, the results are presented and their significance is discussed in Section 4.1.4.

#### 4.1.1 Crystal plasticity finite element simulation framework

##### *Material characterization*

The Ni-base superalloy, modeled in the present study, is a PM produced coarse grain variant of RR1000. RR1000 is a polycrystalline, FCC material, which is strengthened via secondary and tertiary  $L1_2 \gamma'$  precipitates. For the details of the PM processing for this material the reader may refer to Ref. [180]. An EBSD characterization of this material is shown in Figure 4.1(a).

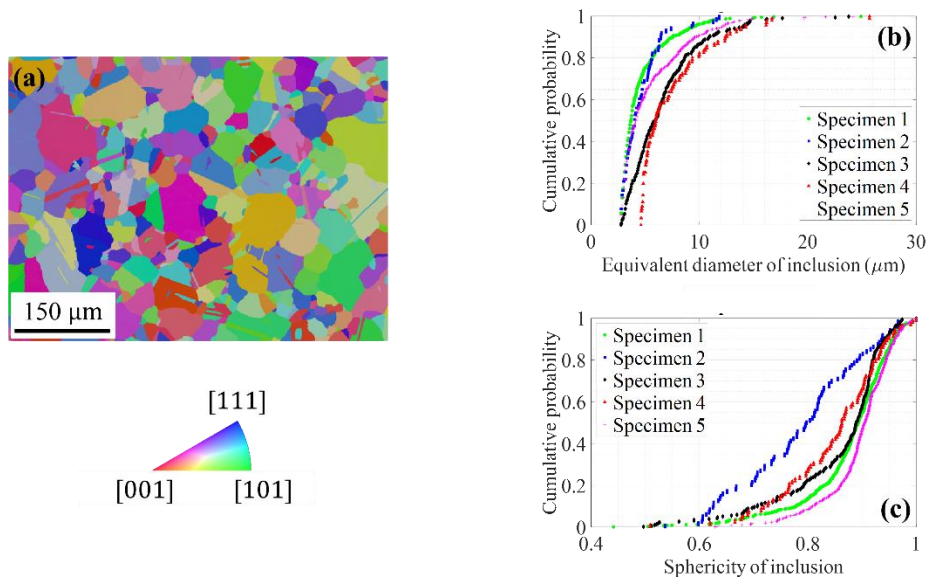


Figure 4.1. (a) Inverse pole figure of RR1000 microstructure from EBSD characterization. Cumulative probability distribution plot of (b) equivalent diameter and (c) sphericity of inclusions in five RR1000 specimens.

The mean grain size (including twins) is found to be 25.24 μm and a random texture is observed. The inclusions within RR1000 are characterized using μ-CT in five different specimens

from earlier work described in Ref. [181]. In the  $\mu$ -CT characterization, effective pixel size is 1.5  $\mu\text{m}$ . Hence, the smallest detectable inclusion volume is 3.3750  $\mu\text{m}^3$ . After processing the scan data in the Avizo software, the maximum and minimum inclusion volumes out of five samples are found to be 11  $\mu\text{m}^3$  and 8875  $\mu\text{m}^3$ , respectively. The cumulative probability distribution plots for the equivalent diameter of the inclusions and their sphericity are shown in Figure 4.1(b) and (c), respectively. The sphericity ( $\Psi$ ) of an object is computed as [182]

$$\Psi = \frac{\frac{1}{\pi^3}(6V_o)^{\frac{2}{3}}}{A_o} \quad (4.1)$$

Here,  $A_o$  and  $V_o$  are the surface area and volume of the object, respectively. The sphericity is a measure of how the shape of the object is close to a sphere (indicated by a value of  $\Psi = 1$ ). One can observe in Figure 4.1(b) that the largest inclusion size is of the order of the mean grain size, and there are several inclusions of this size in the 433  $\mu\text{m} \times 300 \mu\text{m} \times 1250 \mu\text{m}$  rectangular cuboid volume<sup>§§</sup> characterized using  $\mu$ -CT. In Figure 4.1(c), most of the inclusions are observed to be non-spherical. For simplicity, the inclusion is geometrically modelled as an ellipsoid, i.e., a Type 1 inclusion, having a volume corresponding to the largest inclusion observed from the  $\mu$ -CT characterization and sphericity corresponding to the near worst possible scenario. An ellipsoid can be geometrically described by specifying the lengths of three principal axes,  $a$ ,  $b$ , and  $c$ . Here, these parameters are chosen as  $a = 28.34 \mu\text{m}$ ,  $b = 15.18 \mu\text{m}$  and  $c = 4.93 \mu\text{m}$  to result in 8875  $\mu\text{m}^3$  volume or 25.67  $\mu\text{m}$  equivalent diameter with  $\Psi = 0.7$ .

### ***Polycrystalline microstructure with inclusion and debonded region***

Creation of a polycrystalline microstructure with an inclusion and debonded region involves two steps. First, a virtual 3D polycrystalline microstructure or SEM, as previously referred in Chapter 3, without an inclusion is obtained. Subsequently, inclusion is inserted within the SEM as described below. For the present study, five SEMs are created using the methodology described in Section 3.1.1. The SEMs are cubes of dimension 150  $\mu\text{m}$ .

---

<sup>§§</sup> The number of inclusions observed within the rectangular cuboid volume in five specimens are 575, 91, 145, 91, and 434.

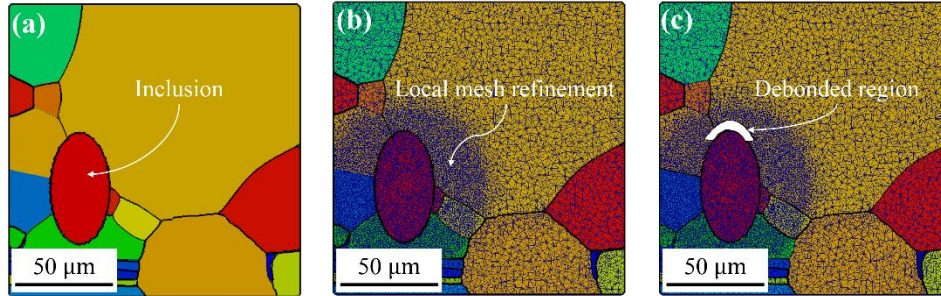


Figure 4.2. Cross-section view of (a) a polycrystalline microstructure with an inclusion, (b) a discretized polycrystalline microstructure with local mesh refinement, and (c) a discretized polycrystalline microstructure with an inclusion and a debonded region.

Before the inclusion is inserted within the SEMs, it is necessary to assign the spatial location of the inclusion relative to the surrounding microstructure. Inclusions are usually seen surrounded by multiple grains. Therefore, in the SEMs, the inclusion is placed at the point which is shared by multiple grains. However, there exists multiple possibilities regarding the choice of such points. Here, the choices are narrowed down by identifying the point which experiences the highest stress and strain values in the absence of the inclusion. Additionally, a case is also simulated, where the inclusion is placed at a point experiencing lowest stress and strain. Once the insertion point is identified, the SEM is discretized using C3D4 elements via the Gmsh software [183] with local mesh refinement around the same point. Based on the mesh sensitivity study in Ref. [161], the mean element size in the refined and coarse regions is set as  $\sim 1.2 \mu\text{m}$  and  $\sim 3.6 \mu\text{m}$ , respectively, resulting in  $\sim 1.9$  million elements within the discretized SEM. Subsequently, a MATLAB code is used to create the inclusion in the desired location. In doing so, it is ensured that the centroid of the inclusion coincides with the selected insertion point. A cross-section view of an SEM with an inclusion is shown in Figure 4.2(a). The local mesh refinement around the inclusion is shown in Figure 4.2(b).

To create the debonded region around the inclusion, the set of elements in the mesh, lying within a selected region, is first identified. Subsequently, a Python script is used to delete this set of elements from the discretized microstructure. The thickness of the debonded region is set to  $\sim 5 \mu\text{m}$  to ensure that the free surface in the debonded region do not self-intersect upon the applied strain during the CPFE simulations. Thus, a polycrystalline microstructure with an inclusion and a debonded region is obtained, as shown in Figure 4.2(c) for a cross-section view.

### *Crystal plasticity model and parameter estimation*

In this study, the total deformation gradient  $\mathbf{F}$  at a material point is attributed to the plastic slip, thermal expansion, and elastic deformation. Therefore,  $\mathbf{F}$  can be decomposed as

$$\mathbf{F} = \mathbf{F}^e \mathbf{F}^\theta \mathbf{F}^p \quad (4.2)$$

Here,  $\mathbf{F}^e$ ,  $\mathbf{F}^\theta$ , and  $\mathbf{F}^p$  are the deformation gradients associated with the elastic deformation, thermal expansion, and plastic deformation, respectively. The deformation gradient associated with thermal expansion is constant at a material point, i.e., does not evolve with deformation, and is written as

$$\mathbf{F}^\theta = (1 + \alpha_{\text{CTE}} \Delta T) \mathbf{I} \quad (4.3)$$

Here,  $\mathbf{I}$  is the identity tensor,  $\alpha_{\text{CTE}}$  is the coefficient of thermal expansion, and  $\Delta T$  is the change in temperature. The velocity gradient associated with the plastic part of the deformation,  $\mathbf{L}^p$ , is written as [156]

$$\mathbf{L}^p = \dot{\mathbf{F}}^p (\mathbf{F}^p)^{-1} = \sum_{j=1}^{N_{ss}} \dot{\gamma}^j (\mathbf{s}^j \otimes \mathbf{n}^j) \quad (4.4)$$

where  $\dot{\gamma}^j$ ,  $\mathbf{s}^j$ , and  $\mathbf{n}^j$  are the shear strain rate, slip direction, and slip plane normal associated with the  $j^{\text{th}}$  slip system, respectively;  $N_{ss}$  is the number of active slip systems. Since RR1000 is an FCC material, the sum is performed over all twelve  $\langle 110 \rangle \{111\}$  slip systems and therefore,  $N_{ss} = 12$ . The shear strain rate ( $\dot{\gamma}^j$ ) on a slip system is related to the resolved shear stress ( $\tau^j$ ) on the same via a flow-rule. Here, a Hutchinson type flow-rule [184] is used, which is given by

$$\dot{\gamma}^j = \dot{\gamma}_0 \left| \frac{\tau^j - \chi^j}{g^j} \right|^n \text{sgn}(\tau^j - \chi^j) \quad (4.5)$$

where  $\dot{\gamma}_0$  is the reference shearing rate,  $g^j$  is the reference shear stress,  $\chi^j$  is the backstress, and  $n$  is the inverse strain-rate sensitivity exponent. In the present work,  $g^j$  is described in terms of a dislocation density-based formulation given by

$$g^j = g_0 + b\mu\sqrt{h_s \rho^j} \quad (4.6)$$

Here,  $g_0$  is the initial slip resistance,  $\rho^j$  is the total dislocation density on the  $j^{\text{th}}$  slip system,  $b$  is the Burger's vector,  $\mu$  is the shear modulus and  $h_s$  is a scaling parameter. The evolution of the dislocation density is defined in terms of a storage term and an annihilation term by means of a Kocks-Mecking type [185]–[187] description given by

$$\dot{\rho}^j = \dot{\gamma}^j \left( k_1 \sqrt{\rho^j} - k_2(\dot{\epsilon}, T) \rho^j \right) \quad (4.7)$$

Here,  $k_1$  and  $k_2(\dot{\epsilon}, T)$  are constants corresponding to the dislocation storage and annihilation rates, respectively;  $T$  is temperature, and  $\dot{\epsilon}$  is the applied strain rate. The constants  $k_1$  and  $k_2(\dot{\epsilon}, T)$  are related as [188], [189]

$$\frac{k_2(\dot{\epsilon}, T)}{k_1} = \frac{h_s b}{\Gamma_{act}} \left[ 1 - \frac{kT}{Db^3} \ln \left( \frac{\dot{\epsilon}}{\dot{\epsilon}_0} \right) \right] \quad (4.8)$$

Here,  $\Gamma_{act}$  is the activation energy,  $D$  is a scaling constant,  $k$  is Boltzmann constant, and  $\dot{\epsilon}_0$  is the reference strain rate. The Eq. (4.8) is applicable for primarily dislocation glide mediated plasticity if  $10^{-5} \text{s}^{-1} \leq \dot{\epsilon} \leq 10^3 \text{s}^{-1}$ . Finally, the backstress evolves according to an Armstrong-Fredrick type [190], [191] description given by

$$\dot{\chi}^j = A \dot{\gamma}^j - A_d \chi^j |\dot{\gamma}^j| \quad (4.9)$$

In a temperature-dependent CP framework, temperature-dependent variations for the elastic constants ( $C_{11}$ ,  $C_{12}$ , and  $C_{44}$ ) is required to compute stress at a material point as a function of temperature. For the current work, the working range of temperature is 20°C to 750°C and the elastic constants can be assumed to be linearly decreasing with temperature [192]. Therefore, the following functional forms are used:

$$\frac{C_{11}(T) - C_{11}(T_0)}{C_{11}(T_0)} = -p_1 \left( \frac{T - T_0}{T_0} \right) \quad (4.10)$$

$$\frac{C_{12}(T) - C_{12}(T_0)}{C_{12}(T_0)} = -p_2 \left( \frac{T - T_0}{T_0} \right) \quad (4.11)$$

$$\frac{C_{44}(T) - C_{44}(T_0)}{C_{44}(T_0)} = -p_3 \left( \frac{T - T_0}{T_0} \right) \quad (4.12)$$

where  $p_1$ ,  $p_2$  and  $p_3$  are positive, temperature-independent, and non-dimensional constants;  $T_0$  is a reference temperature. Here,  $T_0$  is set to 20°C and  $C_{11}(T_0)$ ,  $C_{12}(T_0)$ , and  $C_{44}(T_0)$  values are adopted from Ref. [96]. All equations, as described above, are implemented in ABAQUS UMAT.

In the CP model, as described above, there are fourteen material constants:  $\dot{\gamma}_0$ ,  $n$ ,  $g_0$  (initial value of  $g$ ),  $\chi_0$  (initial value of  $\chi$ ),  $\rho_0$  (initial value of  $\rho$ ),  $k_1$ ,  $\Gamma_{act}$ ,  $D$ ,  $h_s$ ,  $A$ ,  $A_d$ ,  $p_1$ ,  $p_2$  and  $p_3$ ) which are to be fit to the experimental data. These constants are classified as temperature-dependent and independent based on their physical relevance, in addition to observations in the

literature. The constants  $\Gamma_{act}$ ,  $D$ ,  $k_1$ ,  $\dot{\gamma}_0$ ,  $n$ ,  $\rho_0$ ,  $\chi_0$ ,  $p_1$ ,  $p_2$ , and  $p_3$  are temperature-independent and  $g_0$ ,  $h_s$ ,  $A$ , and  $A_d$  are temperature-dependent. Attention is restricted to consider only the temperature variations while maintaining a constant applied strain rate,  $\dot{\epsilon} = 5 \times 10^{-3} \text{ s}^{-1}$ , at which experiments are performed on RR1000. Further, based on the work in Ref. [189],  $\dot{\epsilon}_0$  is set to  $10^7 \text{ s}^{-1}$ . The unknown CP model parameters can be fit using the GA framework, as described in Section 3.1. However, the additional challenge in this study is to fit both the temperature-independent and dependent constants simultaneously. Here, two nested GA loops are used. The outer loop is used to fit the temperature-independent constants, and for a given iteration of the outer loop, a series of inner loops is used to fit the temperature-dependent constants at multiple temperatures. With this, the fitting procedure is executed using experimentally available macroscopic stress-strain hysteresis loop data at  $T = 20^\circ\text{C}$ ,  $300^\circ\text{C}$ ,  $600^\circ\text{C}$ , and  $750^\circ\text{C}$  including strain ratios of 0 and -1. Since the set of fourteen constants only represent properties associated with the elasto-plastic response of the matrix material, only the microstructure without any inclusion and debonded region is considered during the fitting procedure. The boundary conditions applied on the cubic SEM during the fitting procedure is demonstrated in Figure 4.3(a).

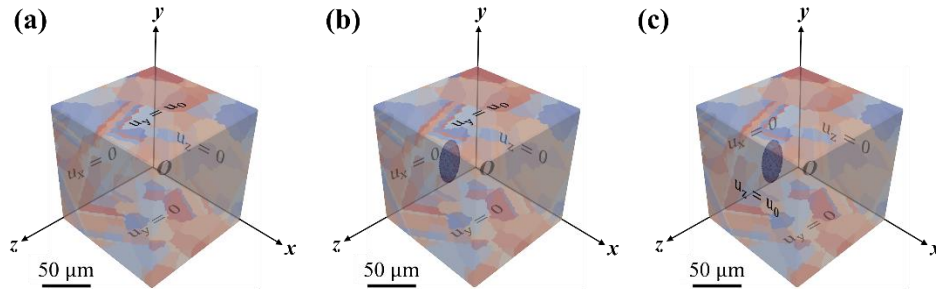


Figure 4.3. Boundary conditions on a given SEM (a) without an inclusion during CP parameter fitting with loading applied along the  $y$ -direction, (b) with an inclusion during fatigue simulation with loading applied along the  $y$ -direction, and (c) with an inclusion during the fatigue simulation with loading applied along the  $z$ -direction;  $u_0$  is the specified displacement based on desired applied strain and SEM dimension along the loading direction.

As indicated in Figure 4.3(a), the normal displacement is restricted on three mutually orthogonal and adjacent surfaces, and non-zero normal displacement is specified on another surface during fitting. In Figure 4.4, one can observe a good agreement between the experimental and simulated macroscopic stress-strain responses using the calibrated elastic and CP parameters across a range of temperatures.

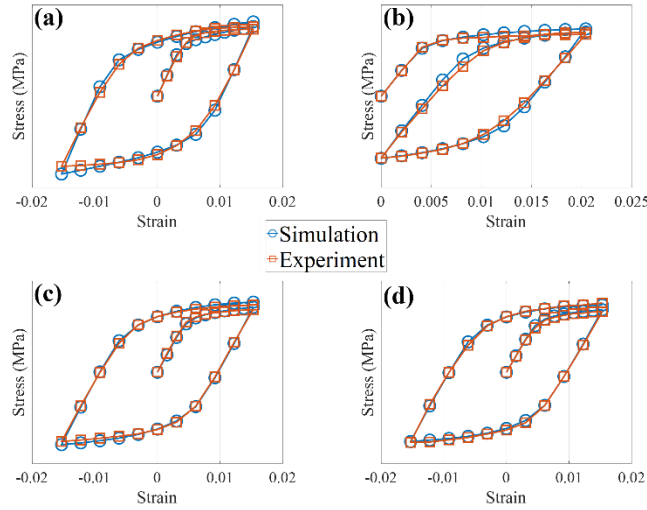


Figure 4.4. Experimental and simulated stress-strain response of RR1000 at (a) 20°C, (b) 300°C, (c) 600°C, and (d) 750°C.

#### 4.1.2 Damage indicative parameter

In a microstructure-sensitive fatigue analysis, the damage indicative parameter helps to identify the location of failure within the microstructure as well as the number of cycles to failure. In this study, primary interest is to identify the location of the failure. If the location is at or adjacent to the inclusion-matrix interface, such a case is referred to as an inclusion-driven failure, or if the location is reasonably far from the inclusion, it is referred to as a matrix-driven failure. Researchers have proposed and used several damage indicative parameters to identify the location, as well as to predict the number of cycles to failure. To name a few, McDowell and his colleagues used a microstructure-sensitive modified Fatemi-Socie criterion [58]–[65]. Ghosh and his colleagues used an effective traction based approach [67], [68]. Dunne and his colleagues investigated the efficacy of PSA [162] and stored energy density [73]–[76] to predict the location as well as number of cycles to failure. In a microstructure-sensitive critical pore size study, Veerappan and Sangid used the PSA, resolved shear stress, elastic stress anisotropy, and tri-axiality as possible damage indicative parameters [161]. Their work showed that the strain-based metric PSA and stress-based metric resolved shear stress performed identically in determining the location of failure and thereby the failure modes, namely pore-driven failure and matrix-driven failure. Since the inclusion is geometrically modeled via a well-defined ellipsoid and there is only one inclusion within an SEM, current simulations are expected to predict the unique failure mode at a distinct

location within the microstructure. Therefore, any one of the metrics, as mentioned before, is expected to serve this purpose. It is well-known that PSA is a precursor to fatigue crack initiation [23], [193]. Hence, in the present work, attention is restricted only to PSA which has been defined in Eq. (3.13).

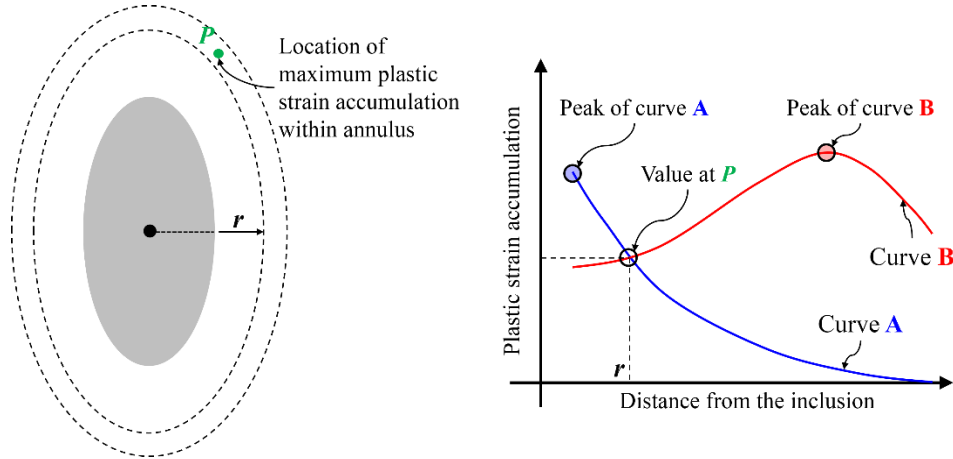


Figure 4.5. A schematic of the radial distribution plot for plastic strain accumulation demonstrating inclusion-driven (curve A) and matrix-driven (curve B) failure modes.

To identify the failure mode, PSA data from a 3D microstructure is represented to a 2D radial distribution plot, as demonstrated in Figure 4.5. First, an ellipsoidal annulus is considered at a distance  $r$  from the inclusion. Second, within the annulus, the integration point  $P$  is identified, where PSA is highest. Finally,  $r$  is plotted on the horizontal axis and PSA at  $P$  on the vertical axis. The process is repeated for several annuli and a curve is traced out as shown in Figure 4.5. As demonstrated in Figure 4.5, one may end up with a curve like A or B. For the curve A, the peak appears near the inclusion. Therefore, it would be indicative of inclusion-driven failure. On the other hand, for curve B, the peak appears far from the inclusion. Therefore, it would indicate a matrix-driven failure. The curves, labeled A or B, are referred to as the radial distribution plots for PSA. While tracing out the radial distribution plot, it is ensured that – (i) none of the successive annuli overlap with each other, (ii) the integration points within 15  $\mu\text{m}$  from the surfaces, where boundary conditions are specified, are not considered, and (iii) each annulus is approximately 6  $\mu\text{m}$  thick.

### 4.1.3 Results

Previously, several factors which influence inclusion- and matrix-driven failure modes were mentioned. Here, the role of each parameter is studied systematically, therefore isolating each parameter while keeping the others fixed. In particular, the critical loading direction is first identified based on the strain localization around the ellipsoidal inclusion. Subsequently, the loading direction is kept unchanged. After identifying the critical loading direction, the effect of the inclusion stiffness and loading regime is studied. Based on these results, an appropriate inclusion stiffness and loading regime are chosen to study the effect of a debonded region at the inclusion-matrix interface, microstructural variability around the inclusion, dissimilar CTE between the inclusion and matrix, residual stress in the surrounding matrix, and the distance of the inclusion from the free surface.

It is observed that the increment in the PSA per cycle saturates after two cycles. Therefore, all simulations are continued until five cycles and PSA at the end of the fifth cycle is reported in the results below. Further, all fatigue simulations are carried out at  $R_\epsilon = 0$  and the simulations which are not indicative of any temperature effect are carried out at 20°C. Finally, all reported PSA values in the following sections are non-locally averaged as per the discussion in Section 3.2.1.

#### *Effect of loading direction*

The effect of the loading direction on the PSA around the inclusion is shown in Figure 4.6. The results in Figure 4.6(a) and (b) corresponds to the boundary conditions demonstrated in Figure 4.3(b) and (c), respectively. In these simulations, the Young's modulus of the inclusion is chosen to be ~50% higher than RR1000. It is evident from Figure 4.6(a) that if the loading direction is aligned with the major axis of the inclusion, such a configuration is undoubtedly more damaging. However, given the anisotropic grain environment surrounding the inclusion, other configurations might also be equally detrimental (see Figure 4.6(b)). In subsequent simulations, the boundary conditions as demonstrated in Figure 4.3(b) are only considered.

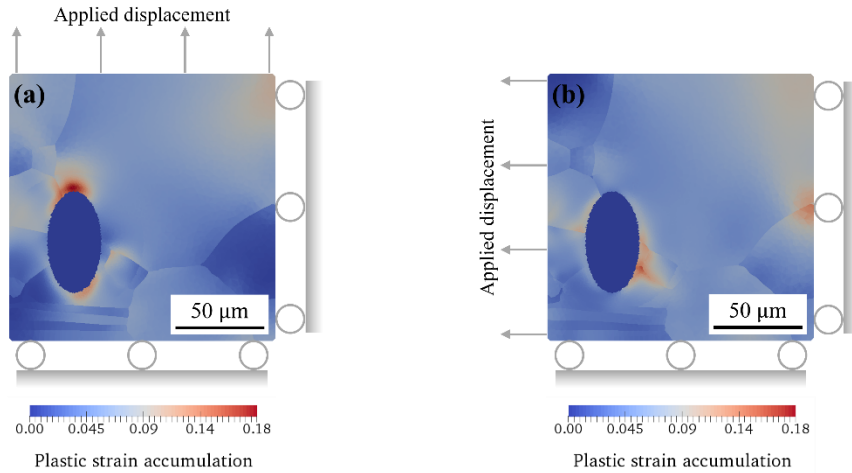


Figure 4.6. Effect of the loading direction on the plastic strain accumulation around the inclusion. In the figure, 2D sectional view of the microstructure is presented, where the cross-sectioned plane passes through the centroid of the inclusion.

### *Effect of inclusion stiffness*

The inclusions in Ni-base superalloys can be found as a solid hard particle (Type 1) or an agglomerate of small particles (Type 2) [179]. Moreover, the inclusions can be highly porous and exhibit a wide range of chemical compositions. In this study, the inclusion is geometrically modeled as a solid ellipsoid and these variabilities are considered by choosing two different structural stiffness values of the inclusion. In the first case, a Young's modulus of the inclusion that is ~50% higher than RR1000 is considered and in the second case, a value ~50% lower than RR1000 is chosen. Also, three loading conditions are simulated – (i) 0.3% applied strain range representing a HCF regime, (ii) 1.0% applied strain range representing an LCF regime, and (iii) 3% applied strain range representing the extreme situation of LCF loading. In Section 4.1.2, it has been demonstrated that, if the peak of the radial distribution plot for PSA appears near (approximately within 30 μm) the inclusion, such a case is referred to as an inclusion-driven failure; otherwise, a fatigue crack would more likely originate from matrix-driven failure. Figure 4.7 suggests that when the inclusion is stiffer than the matrix, one would expect the case of inclusion-driven failure to dominate at any loading situation. However, if the inclusion is softer than the matrix, one may expect to see a shift from inclusion- to matrix-driven failure as a transition is made from high to the low cycle fatigue regime. When the macroscopically applied load is lower than the macroscopic yield stress of the material, the damage is accumulated due to microplasticity.

Defects, such as inclusions, irrespective of its stiffness, obstruct the motion of the dislocation, leading to damage accumulation during such a loading regime, indicating a significant debit in the fatigue life [82]. When the applied load goes beyond the macroscopic yield point, the plastic deformation far from the inclusion also becomes significant, and the winner in the failure mode competition is decided based on the relative stiffness of the inclusion.

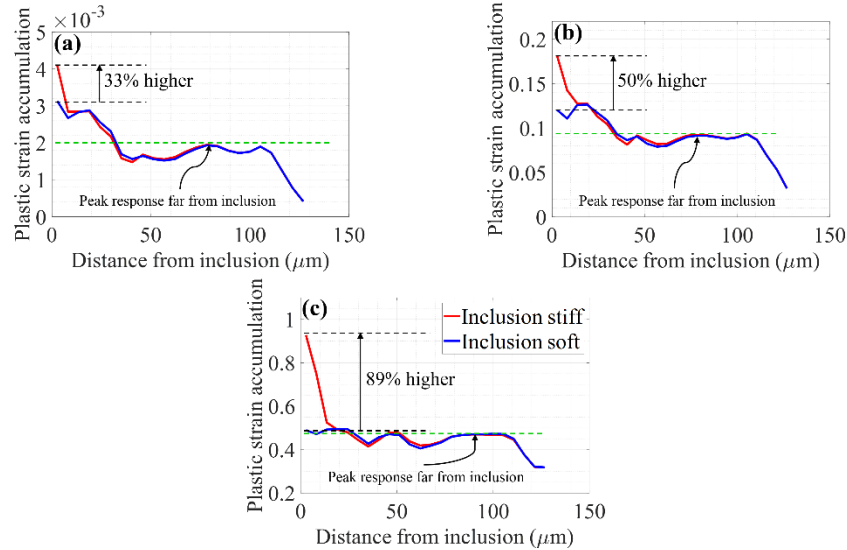


Figure 4.7. The radial distribution plots of the plastic strain accumulation, showing the effect of the inclusion stiffness at (a) 0.3%, (b) 1.0% and (c) 3.0% applied strain ranges.

### ***Effect of the debonded region and its location***

From the thermo-mechanical deformation that occurs during processing of forged Ni-base superalloys, the inclusions are often observed to be partially or even fully debonded from the matrix material. In order to see the effect of the presence of a debonded region in the inclusion-matrix interface, a set of elements of the adjacent matrix in two specific regions is deleted, one at a time, as shown in Figure 4.8. In Figure 4.7, it has been observed that a soft inclusion at a relatively higher applied strain may show a matrix-driven failure. Hence, a case is considered, in which the inclusion has a Young's modulus  $\sim 50\%$  lower than that of RR1000 and the simulation is carried out with a 1% applied strain to investigate the possibility of a transition from matrix- to inclusion-driven failure in the presence of a debonded region. Figure 4.8 suggests that the presence of a debonded region is indeed detrimental regarding fatigue damage accumulation. However, the location of the debonded region is also crucial. From a practical standpoint, this observation

suggests that having a partially bonded inclusion may not necessarily be detrimental depending on the vicinity of the debonded region with respect to the applied loading direction.

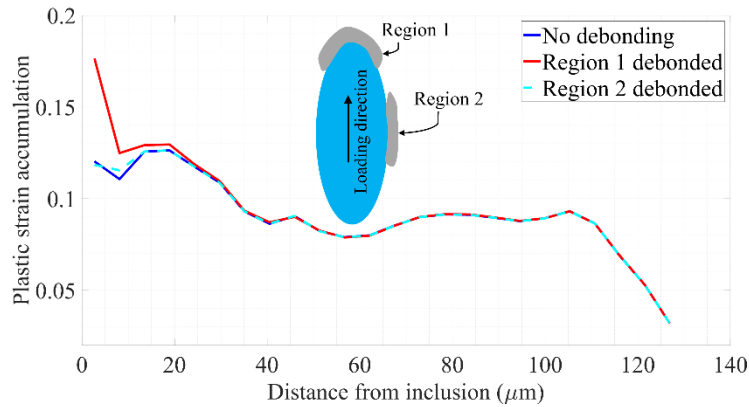


Figure 4.8. The radial distribution plots for the plastic strain accumulation showing the effect of the debonded region in the inclusion-matrix interface.

### ***Effect of the microstructural variabilities around the inclusion***

In the simulations for the present study, the equivalent diameter of the inclusion is of the order of the mean grain size of RR1000. Therefore, the local microstructure around the inclusion is expected to have a significant influence on the emergence of a failure mode. To study the role of microstructural variabilities, the hot spots are identified based on the high stress and strain values within five SEMs and the inclusions are placed at the critical location in each SEMs. In one of the SEMs, a point is also identified on a grain boundary, where the stress and strain values are the lowest and the centroid of the inclusion is placed at this non-critical point. With this, six instantiations of the polycrystalline microstructures are simulated, with each SEM containing a single inclusion.

In Figure 4.7, one can observe that a stiffer inclusion suggests an inclusion-driven failure irrespective of the loading regime. Here, a stiffer inclusion is considered to investigate the possibility of a matrix-driven failure in the six microstructural instantiations. To this end, each inclusion has a Young's modulus value that is ~50% higher than that of RR1000 and 1.0% strain is applied during CPFEE simulations. The radial distribution plots for the PSA in all SEMs are

shown in Figure 4.9<sup>\*\*\*</sup>. Although the inclusion is much stiffer than the matrix, the possibility of a matrix-driven failure is observed in Figure 4.9(b).

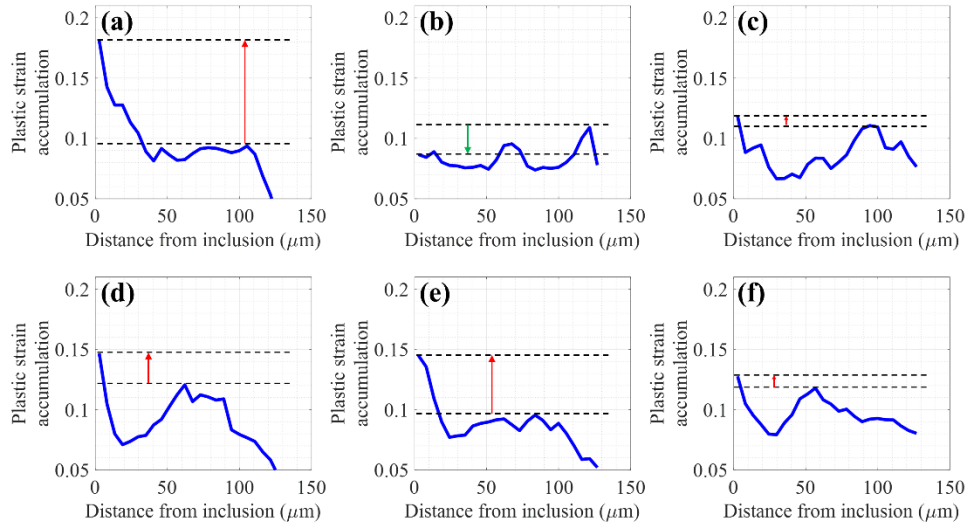


Figure 4.9. The radial distribution plots for the plastic strain accumulation showing the effect of microstructural variability around the inclusion. Each of the subplots corresponds to a different grain environment around the inclusion.

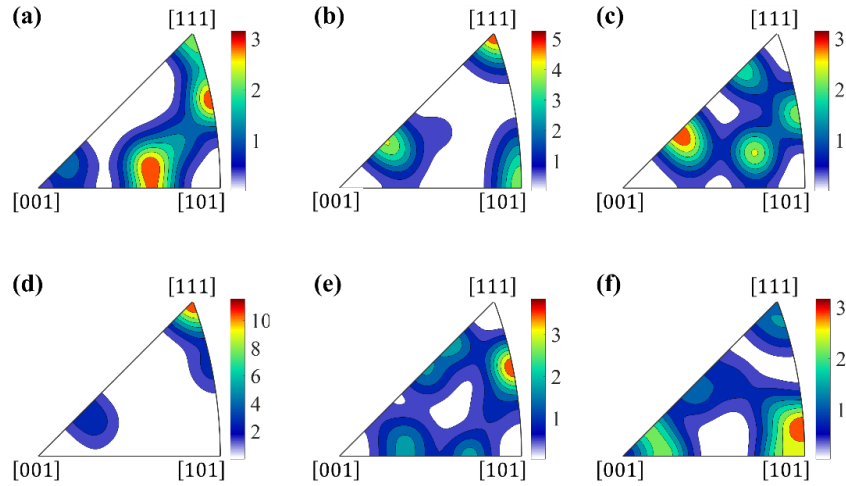


Figure 4.10. Inverse pole density figures, with the applied loading direction as a reference, representing the orientations of the grains around the inclusion in each microstructure corresponding to Figure 4.9. Please note, the color scale in each subplot is normalized with respect to its own set of data.

<sup>\*\*\*</sup> For the results in Figure 4.9(a)-(e), the inclusion is placed at the critical locations in the five different SEMs. The results in Figure 4.9(f) and (a) correspond to the same SEM, but the inclusion position is at a different location within the SEM.

In Figure 4.10, the orientations of the grains, adjacent to the inclusion in each of the microstructural instantiations, are plotted with respect to the loading direction. Figure 4.10(b) and (d) suggest a very similar orientation distribution of the grains surrounding the inclusion with respect to the loading direction, near parallel to the  $\langle 111 \rangle$  direction or near normal to  $\{111\}$  planes, (geometrically) signifying similar and lower slip activity. However, Figure 4.9(b) and (d) show significantly different PSA near the inclusion. Thus, a direct correlation between PSA near the inclusion and the orientation of the surrounding grains is not observed, as is evident in the lack of trends for the orientation of the neighboring grains.

### *Effect of the inclusion size*

For the present study where the inclusion size is of the order of the mean grain size, the effect of the inclusion size on the resulting damage accumulation is evaluated. Here, the effect of inclusion size is investigated in three different SEMs. Within each SEM, the inclusion size is increased keeping the Gaussian curvature<sup>†††</sup> ( $\kappa$ ) at the end of the major axis constant. Subsequently, the procedure is repeated with three different  $\kappa$  values. In Figure 4.7, it has been observed that the damage due to the inclusion is most significant at lower applied strains, irrespective of its stiffness, as the difference in the elastic strains dominate. Therefore, 0.3% strain is applied to study the effect of the inclusion size and inclusions having a Young's modulus  $\sim 50\%$  higher than RR1000 are considered. In Figure 4.11, the PSA at the inclusion is plotted as a function of its volume and considering  $\kappa$  as a parameter. The results indicate the existence of all theoretically possible trends. Figure 4.11(a) suggests smaller inclusions are more detrimental, whereas Figure 4.11(b) shows the exact opposite trend. Figure 4.11(c) shows a combination of both trends as observed in Figure 4.11(a) and (b). These results suggest that the effect of the inclusion size and morphology (partially captured via the Gaussian curvature at the critical location) is coupled with the local microstructure. From a practical standpoint, one may observe failures near small, as well as large, inclusions without any correlation to its size.

---

<sup>†††</sup> The measure of curvature at a point on a surface is not unique. In differential geometry of surfaces, two common measures of curvature of a surface at a point are (a) Gaussian curvature and (b) mean curvature. The Gaussian curvature is the product of two principal curvatures, whereas mean curvature is the mean value of the principal curvatures.

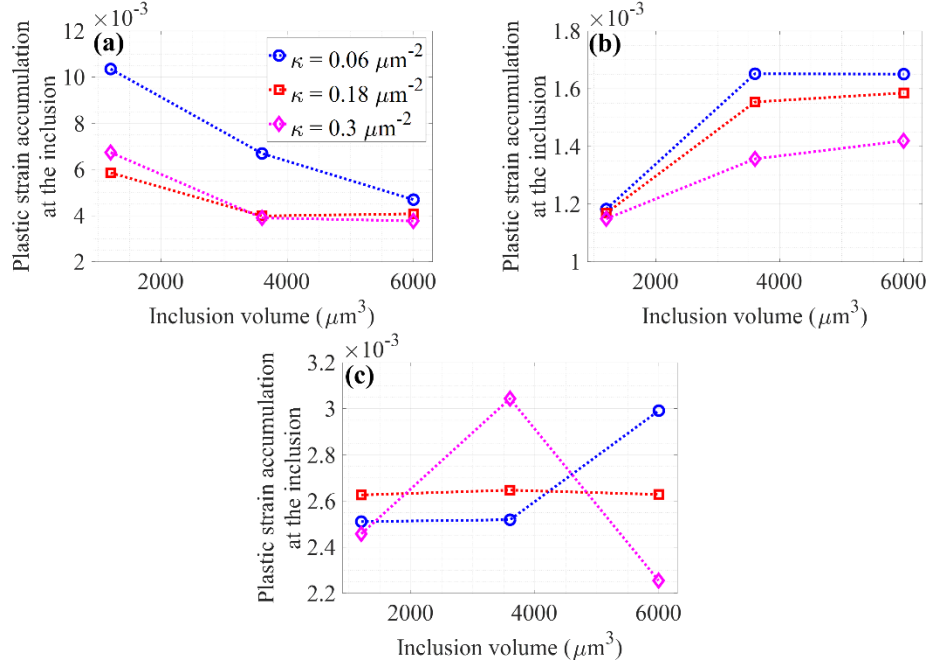


Figure 4.11. Plastic strain accumulation at the inclusion as a function of the inclusion volume and Gaussian curvature ( $\kappa$ ) at the tip of the major axis as a parameter in three different statistically equivalent microstructures.

### *Effect of the dissimilar coefficient of thermal expansion*

Here, the loading regime where the effect of dissimilar CTE would be more pronounced is first identified. After that, the role of dissimilar CTE in the transition of the failure mode from the low to high temperature regime is investigated. To represent the CTE of all possible oxide and carbide inclusions, two different numerical values – one almost 50% lower and the other around 50% higher than the CTE value of RR1000 are chosen. In Figure 4.7, it has been observed that a soft inclusion may show a matrix-driven failure at a relatively higher applied strain. Hence, the inclusion exhibiting a Young's modulus  $\sim 50\%$  lower than RR1000 is considered to investigate the possibility of transitioning from matrix- to inclusion-driven failure with increasing temperature. Figure 4.12 shows radial distribution plots for the PSA at  $600^\circ\text{C}$  under the two different loading conditions. Figure 4.12(a) corresponds to a 0.3% applied strain representing the HCF regime, whereas Figure 4.12(b) corresponds to 1.0% applied strain representing the LCF regime. It is evident from Figure 4.12 that the effect of a dissimilar CTE is most pronounced during HCF where the elastic strains represent a more significant percentage of the total strain. Therefore, attention is restricted to only the HCF regime to investigate the effect of the increasing temperature. In Figure

4.13(a) and (b), the radial distribution plots for the PSA at 20°C, 300°C, 600°C, and 750°C are shown for an inclusion having a CTE value either higher or lower than the matrix, respectively. To better represent the temperature effect, two locations, namely *A* and *B*, are identified. *A* represents a location near the inclusion, whereas *B* represents a location corresponding to a peak response in strain accumulation, far from the inclusion. In Figure 4.13(c) and (d), the relative difference of the PSA between these two locations is plotted as a function of temperature. Both Figure 4.13(c) and (d) suggest an inclusion-driven failure mechanism at all temperatures for the given microstructural instantiation. However, the increasing trend, as observed in Figure 4.13(c), indicates a higher probability of failure near inclusions having a CTE value higher than that of the matrix at a higher temperature. Further, the decreasing trend with temperature, as observed in Figure 4.13(d), indicates a higher probability of matrix-driven failure at higher temperatures, if the inclusion CTE is lower than the matrix.

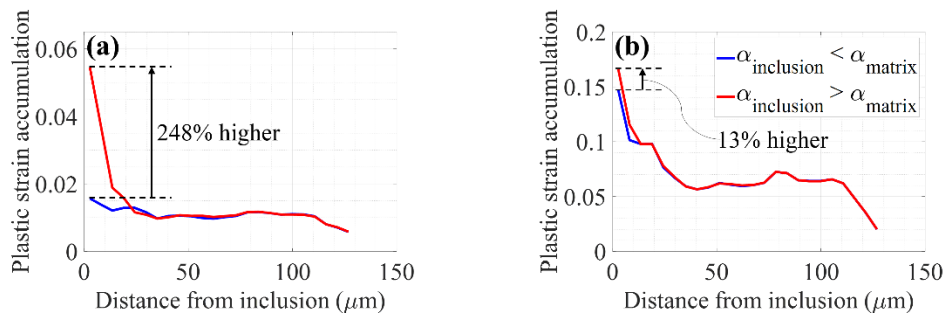


Figure 4.12. The effect of the dissimilar CTE values of the inclusion and matrix on the radial distribution plots for plastic strain accumulation at 600°C and for (a) 0.3% and (b) 1.0% applied strain ranges.

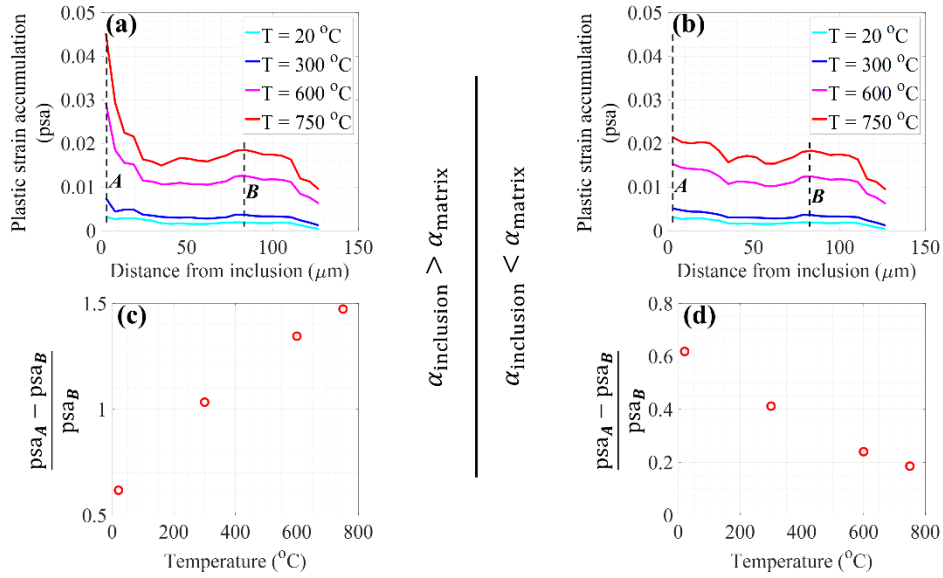


Figure 4.13. The radial distribution plots for plastic strain accumulation for (a) inclusion CTE greater than matrix CTE and (b) inclusion CTE smaller than matrix CTE with temperature as a parameter. The relative difference between the plastic strain accumulation near (location A) and far (location B) from the inclusion as a function of temperature for (c) the inclusion CTE greater than the matrix CTE and (d) the inclusion CTE smaller than the matrix CTE.

### Effect of the residual stress

Due to the dissimilar CTE values between the inclusion and the surrounding matrix, residual stresses are induced in the microstructure during the thermo-mechanical processing of the material, especially upon cooling. Here, the objective is to show the implication of residual stresses in the damage accumulation within the polycrystalline microstructure around the inclusion. To achieve this, the residual stress is initialized within the microstructure before fatigue loading by specifying dissimilar inclusion and matrix CTE values and a static thermal load characterized by  $\Delta T < 0$ . The numerical value of  $\Delta T$  is chosen based on the heat treatment cycle information of RR1000, reported in Refs. [98], [180], [194]. Consequently, the residual stress distribution in the matrix around an alumina inclusion, having a lower CTE than the matrix, is predominantly compressive adjacent to the inclusion and quantitatively, as well as qualitatively, similar to the experimentally characterized values by Naragani and Sangid et al. [99]. It is well-known that residual stresses have a significant influence on the fatigue life in the HCF regime and gets relaxed during LCF or at high temperature [4]. Hence, fatigue simulations are carried out at room temperature with 0.3% applied strain range. From Figure 4.14, it is evident that the residual stress

leads to a higher accumulated damage at room temperature and a strain ratio loading of zero ( $R_\epsilon = 0$ ), irrespective of the lower or higher CTE value of the inclusion with respect to the matrix material. However, as it has been mentioned before, the residual stress would get relaxed at higher applied strains and at higher temperatures.

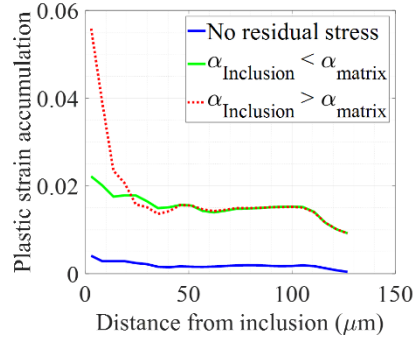


Figure 4.14. The effect of residual stress on the radial distribution of plastic strain accumulation around the inclusion. The residual stress is initialized by simulating cooling during the manufacturing process with  $\Delta T < 0$  and fatigue simulations are performed with 0.3% applied strain.

#### *Effect of the distance of the inclusion from the free surface*

In the present CP framework, it is challenging to isolate the effect of microstructural variability and distance from the free surface. To minimize the influence of microstructural variability, in the next suite of simulations, the location of the inclusion within the SEM is not changed, instead, the SEM is cropped in such a way that the distance of the inclusion decreases from the free surface. In doing so, three microstructural instantiations are generated with the inclusion having a Young's modulus value almost 50% higher than that of RR1000. Subsequently, 1% strain is applied on each instantiation, and the contour plots of PSA are shown in Figure 4.15. It is evident from Figure 4.15 that the magnitude of PSA does not change significantly with the distance of the inclusion from the free surface. However, the nature of the spatial localization around the inclusion changes. With the decrease in the distance from the free surface, the contours of high PSA values bend and extend towards the free surface representing a relative higher damaging situation. Such an observation is also consistent with the fact that the free surface offers a constraint-free site for dislocation activity.

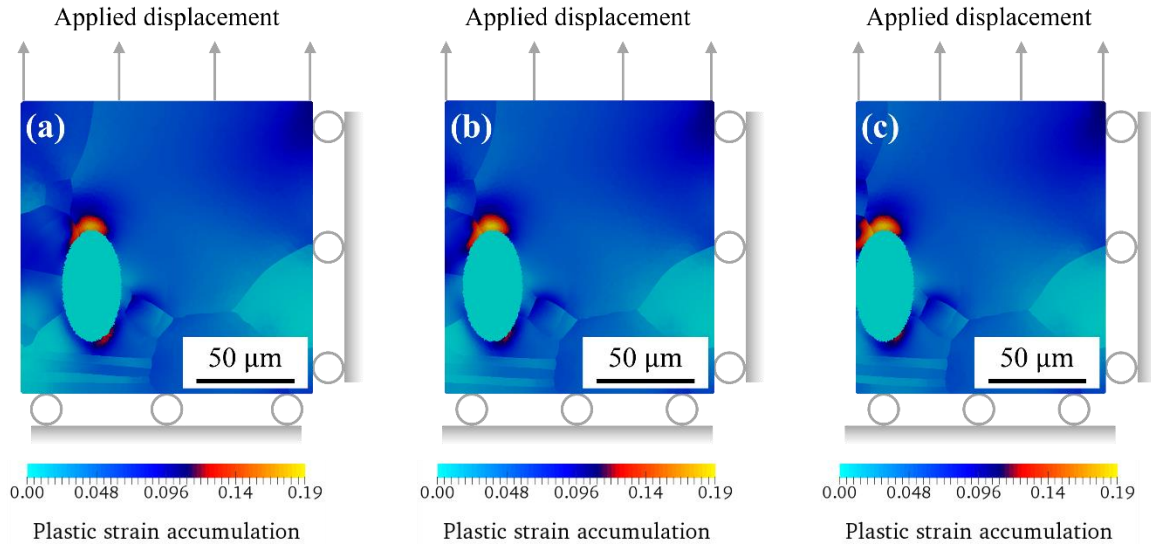


Figure 4.15. The effect of decreasing the distance of the inclusion from the free surface on the localization of plastic strain accumulation around the inclusion.

#### 4.1.4 Discussion

As aforementioned, multiple factors influence the stochastic emergence of the inclusion- and matrix-driven failure modes in Ni-base superalloys. In Section 4.1.3, each of those factors is isolated and their influence is studied on the two competing failure modes systematically. From an analytical perspective, such a study helps to identify the role of each parameter. However, from a practical standpoint, it is the complex interaction between these parameters, which results in the experimentally observed failure mode. Here, the observations from the previous section is synthesized to develop a holistic understanding of the competing failure modes.

In Figure 4.7, it is observed that the difference between the PSA near and far from the inclusion diminishes with increasing applied strain for the soft inclusion. If the PSA is used as a metric for life prediction, such an observation would imply a significant difference between lives due to an inclusion- versus matrix-driven failure mechanism at lower applied loading, and the difference will disappear gradually at higher applied loading conditions. Consequently, one would observe a bifurcation in the stress/strain-life plots, as reported in Ref. [83]. Moreover, in Figure 4.7, it has been observed that the stiffer inclusions are more likely to result in inclusion-driven failures. However, Figure 4.9(b) suggests that depending on the microstructure surrounding the inclusion, one may expect to see matrix-driven failure, even though the Young's modulus for the inclusion is much higher than that of the matrix. Also, comparing Figure 4.9 and Figure 4.10, no

strong correlation between the orientation of the grains surrounding the inclusion and the magnitude of the PSA near the inclusion is observed. Such an observation is attributed to the fact that the local stress state within a microstructure is a result of the complex interaction between different grains having an anisotropic mechanical response and further influenced by the grain morphology, size, and orientation distributions. It is challenging to predict such emerging behavior using an analytical approach. Numerical simulations, such as CPFEM, can help in these situations. The complex interaction between the inclusion and the surrounding matrix is influenced by the structural stiffness of the inclusion but not solely dependent on it.

A strong microstructural influence is also observed in the correlation between the inclusion size and resulting damage around it in Figure 4.11. For relatively larger ( $150\ \mu\text{m} - 300\ \mu\text{m}$ ) inclusions or higher inclusion to mean grain size ratios in these materials, bigger inclusions are reported to result in greater damage [85], [195]. However, as evident in Figure 4.11, no strong correlation is observed between the inclusion size and accumulated damage if the inclusion size is of the order of the mean grain size. Here, it is to be remembered that the inclusion is geometrically modeled as an ellipsoid, i.e., a Type 1 inclusion, and Type 2 and porous inclusions are accounted for via varying the relative stiffness of the inclusion. Hence, the observed lack of correlation between the inclusion size and its propensity for damage is expected to hold for both Type 1 and 2 inclusions as long as the inclusion size is of the order of the mean grain size.

In the present study, the inclusions are modeled as ellipsoids. In reality, the inclusion morphology is often far from a regular geometric body, such as an ellipsoid. Hence, the inclusion morphology is also expected to play a key role in the emergence of a failure mode. In this work, the effect of the morphology has been partially captured by changing the curvature of the ellipsoid at the tip of the major axis keeping the volume constant in Section 4.1.3. In Figure 4.11, no correlation is evident between the curvature and the resulting damage. However, a more rigorous analysis, considering the true inclusion morphology and surrounding grain environment, is necessary to better understand the interaction between inclusion morphology and surrounding microstructure in the emergence of a failure mode.

The results from Figure 4.15 indicate that the localization of PSA for a surface inclusion is more damaging, compared to an inclusion located in the bulk of a material, but does not guarantee an inclusion-driven failure. In the light of the results from Figure 4.9(b), one can argue that due to the local microstructure, a surface connected inclusion could be less damaging than an interior

inclusion. Such an argument is also consistent with the experimental observations in Refs. [84]–[86], because all surface connected inclusions in these works did not systematically result in crack initiation. While assessing the effect of surface inclusions it has been assumed that the surface is smooth and free from any conditionings and treatments, such as scratches, roughness, and residual stresses due to shot peening, brittle oxide layers, etc. However, in practice, such conditionings and defects are unavoidable and would have added implications in the emergence of failure at the free surface.

Under identical loading conditions, higher temperatures are associated with relatively lower fatigue lives in Ni-base superalloys [196]. The results in Figure 4.13(a) and (b) confirm such observation. In Figure 4.13(a) and (b), it is observed that the radial distribution plots shift upwards, implying a larger degree of PSA and associated damage, with increasing temperature, irrespective of the lower or higher CTE of the inclusion compared to that of the matrix material. Further, in Figure 4.13(a) and (c), one can observe the possibility of a higher probability of inclusion-driven failure at a higher temperature, if the CTE of the inclusion is greater than that of the matrix. Such an observation is consistent with the experimental observations in Refs. [88], [89]. Moreover, in Figure 4.13(b) and (d), the possibility of a decreasing probability of inclusion-driven failure with increasing temperature is observed, if the CTE of the inclusion is lower than the matrix. Such an observation is also in agreement with the experimental results in Ref. [90]. In Ni-base superalloys, several oxides, as well as carbide inclusions, are seen. Depending on the chemical composition, the inclusion material may have cubic, as well as non-cubic, crystalline structures. For a non-cubic material, the CTE is a second order anisotropic tensor. Typically, the CTE of most of the inclusion materials are lower than the Ni-matrix. However, there is evidence in the literature that the CTE of some of the inclusion materials along specific crystallographic directions might be well above the values of the Ni-matrix, which has a cubic structure. Examples of such inclusions are, but not limited to, zirconium oxide and hafnium oxide [197]. Here, a possible explanation of the transition in failure mode with increasing temperature is offered using a dissimilar CTE argument. However, there is a need to characterize the inclusion CTE at the location of failures at higher temperatures to further validate this argument.

While investigating the effect of dissimilar CTE at higher temperatures, only octahedral slip systems have been considered in the modeling framework. However, literature suggests activation of cubic slip systems at higher temperatures in the single crystal (see for example [198]–

[202]) as well as polycrystalline (see for example [181]) Ni-base superalloys. Since cubic slip systems have higher critical resolved shear stress than octahedral slip systems, cubic slip systems are expected to be active in the locations within the microstructure, where stresses are very high. Such locations are also likely to show significant octahedral slip system activities. Hence, in the present research, the incorporation of cubic slip systems would only result in a slight upward shift of the PSA peaks at higher temperatures in the radial distribution plots without changing the location of the peaks with respect to the inclusion position and thus the corresponding failure mode.

From the results and discussions, as presented above, one can observe that it is extremely challenging to predict the mode of failure and its location in a deterministic manner by simply looking at the microstructural features and strength properties, such as the inclusion size, presence of a debonded region, Type 1 or Type 2 inclusion, stiffness of the inclusion with respect to the matrix, etc. It is the complex interaction between the inclusion and matrix attributes, which leads to the emergence of a failure mode. Additionally, the present analysis is based on the simulation results for a Ni-base superalloy, but the implications of this study are not limited to a single material. The inclusions are also seen in other materials, such as aluminum alloys and steel. If the sizes of the inclusions are of the order of mean grain size in these materials, the above results and discussion, in principle, will continue to be valid.

#### **4.1.5 Summary**

In this study, the role of the inclusion stiffness, debonded region of the inclusion-matrix interface, microstructural variability around the inclusion, inclusion size, dissimilar coefficient of thermal expansion, residual stress, the distance of the inclusion from free surface, loading regime, and loading direction are systematically investigated to identify the competing failure modes, namely inclusion- and matrix-driven failures, in a Ni-base superalloy RR1000. Based on an experimental characterization, inclusions which are of the order of the mean grain size of the material have only been considered. The key findings are summarized below.

- The emergence of inclusion- or matrix-driven failure is observed to be an outcome of the complex interactions between the inclusion stiffness, microstructure around the inclusion, a debonded region in the inclusion-matrix interface, and loading regime. Simply looking at any one of these parameters in isolation is not sufficient to predict the failure mode.

- No overall correlation between the Type 1 inclusion size and plastic strain accumulation, which is representative of the cumulative damage during fatigue loading, is observed. In other words, smaller Type 1 inclusions are not necessarily exempt from fatigue failure, and larger Type 1 inclusions are not necessarily detrimental in terms of the fatigue failure. Such an observation is crucial in terms of inspection and maintenance practices, if Type 1 inclusion sizes are of the order of the mean grain size.
- If the coefficient of thermal expansion of the inclusion is higher than that of the matrix material, one may expect a higher probability of inclusion-driven failures at higher temperatures. On the other hand, if the coefficient of thermal expansion of the inclusion is lower than the matrix material, a decreasing probability of inclusion-driven failures is more likely to be observed with increasing temperature.
- The contours of higher plastic strain accumulation bend and extend towards the free surface, as the separation between the inclusion and the free surface decreases. Such observation indeed makes the inclusion at the free surface more damaging but does not guarantee an inclusion-driven failure. As per the first summary point, the actual failure mode and the location of the failure is an outcome of the complex interaction between the totality of the inclusion and matrix attributes.

## **4.2 Prediction of competing failure modes**

### **4.2.1 Statistically equivalent microstructures with and without inclusions**

The procedure of creation of SEMs with inclusions has been described in Section 4.1.1. Here, the objective is to create SEMs with inclusion having realistic properties so that these 3D polycrystalline microstructures can be used to predict fatigue life and associated failure modes as a function of applied strain and temperature using the microstructure-sensitive energy-based framework described in Section 3.2. For fatigue life prediction in RR1000, a total of 20 SEMs are created, where each SEM is a cube of 160  $\mu\text{m}$ . In Section 4.1.1, a large number of inclusions were observed from  $\mu\text{-CT}$  characterization of inclusions within 433  $\mu\text{m} \times 300 \mu\text{m} \times 1250 \mu\text{m}$  rectangular cuboid volume of material in five RR1000 samples. However, process parameters in commercial Ni-base superalloys are optimized to produce near pristine materials. Hence, it is fair to expect significantly smaller number of inclusions in commercial Ni-base superalloys within the

same probed volume. Therefore, in this study, all of the 20 SEMs are not created with inclusions. Specifically, 10 SEMs are created with inclusions, with each SEM containing one inclusion. With this, a maximum of 50% inclusion-driven failure can be predicted from this study. In the following paragraphs, inclusion attributes, i.e., thermo-mechanical properties, size and morphology, and position of the inclusions within the SEMs, are described.

### ***Thermo-mechanical properties of the inclusions***

As previously mentioned, depending on the chemistry (oxides, carbides) and type (Type 1 or 2), structural stiffness of the inclusions is expected to span a wide range resulting in lower or higher stiffness compared to the matrix. Here, stiffness of the matrix corresponds to the Young's modulus of RR1000; however, the structural stiffness of the inclusions is different from its Young's modulus which is associated with the chemical composition. For example, by virtue of its chemical composition, alumina would have a well-defined Young's modulus value. However, depending on the type of the alumina inclusion, i.e., Type 1 or Type 2, the structural stiffness, associated with the load carried by the inclusion, would be lower or higher than its Young's modulus. In Section 4.1.3, it has been shown that if the structural stiffness of the inclusion is higher than the Young's modulus of the matrix, one may observe inclusion-driven failures, irrespective of the applied strain magnitude. However, if the structural stiffness of the inclusion is lower than the Young's modulus of the matrix, one would observe higher probability of inclusion-driven failures at lower applied strain compared to higher applied strain. The fatigue life data of RR1000 shows the evidence of inclusion-driven failure for applied strain  $\leq 0.4\%$ . Hence, in this study, inclusions are predominantly modeled as structurally soft material. However, to avoid any bias towards the choice of the stiffness value, the inclusion stiffness values are sampled from a truncated lognormal distribution with 150 GPa as expected value and 99 GPa as standard deviation, as shown in Figure 4.16(a). Here, the distribution is truncated or in other words, the stiffness values are sampled from the shaded region in Figure 4.16(a) to avoid significantly lower (less than 90 GPa) and higher (greater than 320 GPa) stiffness values.

Due to the varying chemical composition and crystallographic structure, one may expect a wide range of CTE of the inclusions as well, resulting in lower or higher CTE than the matrix material. However, in RR1000 as well as in other Ni-base superalloys, inclusion-driven failure is typically observed from alumina and hafnia inclusions. These inclusions have lower CTE than the

RR1000 matrix. Additionally, in the literature, one can observe other possibilities of the inclusion chemistry as well. Hence, the inclusion CTE values for the present study are sampled from a truncated log-normal distribution with  $7.9 \times 10^{-6}$  as expected value and  $4.2 \times 10^{-6}$  as standard deviation, as shown in Figure 4.16(b). The mean value is chosen based on the CTE value of the alumina and hafnia inclusions and the standard deviation is based on the expected variation of the inclusion CTE due to varying chemistry. Like the assumed distribution for inclusion stiffness, the distribution of inclusion CTE is also truncated or in other words, the CTE values are sampled from the shaded region in Figure 4.16(b) to avoid significantly lower (less than  $5 \times 10^{-6}$ ) and higher (greater than  $2 \times 10^{-5}$ ) CTE values.

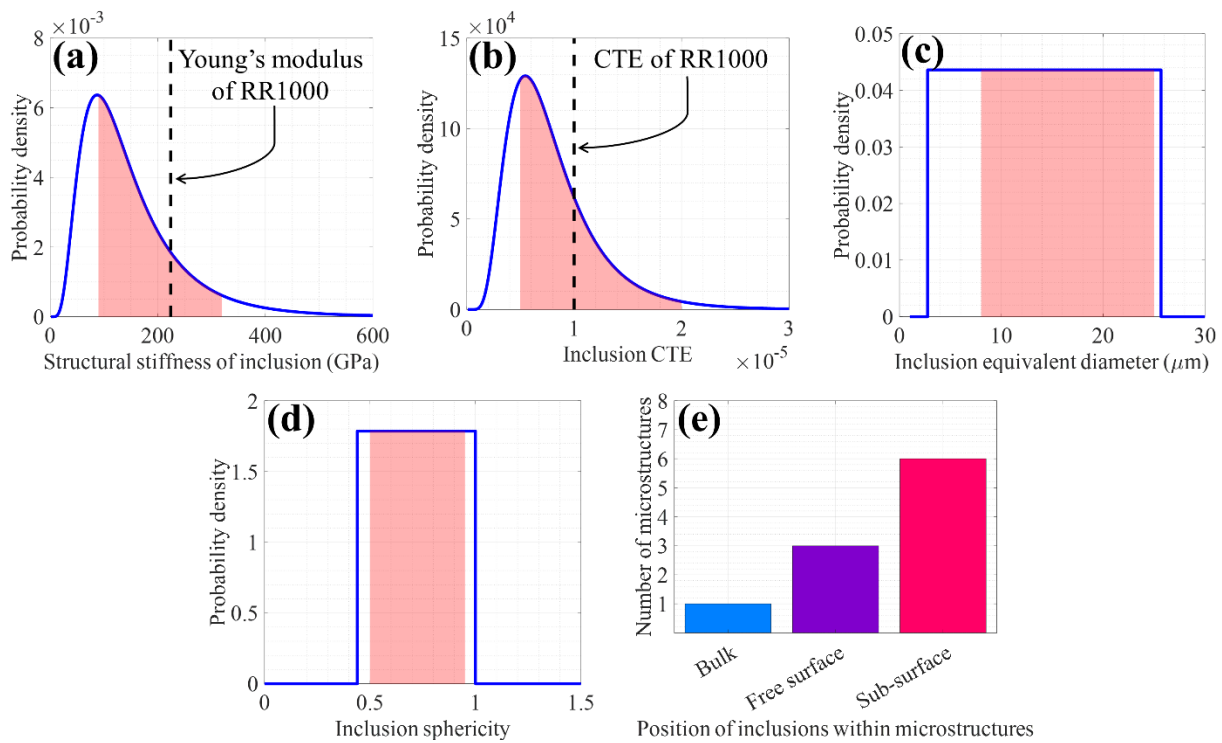


Figure 4.16. Distributions of inclusion attributes for microstructure modeling. Inclusion stiffness, CTE, equivalent diameter, and sphericity values are sampled from the shaded regions of their respective distributions. The Young’s modulus and CTE values of RR1000 are indicated for reference and obtained from Refs. [203] and [204], respectively.

### ***Inclusion size and morphology***

In Section 4.1.4, it has been discussed that the damage due to inclusion is not correlated to its size and curvature if its size is of the order of mean grain size. Hence, equivalent diameter and sphericity of the inclusions are sampled from uniform distributions as shown in Figure 4.16(c) and

(d), respectively. The lower and upper bounds of the uniform distributions in Figure 4.16(c) and (d) are chosen based on the minimum and maximum values of the equivalent diameter and sphericity of the inclusions observed in Figure 4.1(b) and (c). The minimum and maximum equivalent diameter of the inclusions are found to be 2.76  $\mu\text{m}$  and 25.69  $\mu\text{m}$ , respectively. The same for sphericity are 0.44 and 1. From Figure 4.16(c) and (d), it can be observed that the equivalent diameter and sphericity are sampled from the shaded regions or in other words, the uniform distributions are truncated before sampling. In particular, equivalent diameter values are sampled from the interval [8, 25]  $\mu\text{m}$  and sphericity values are sampled from the interval [0.5, 0.95]. Such a choice, especially on the lower bound of the inclusion equivalent diameter, is due to the mesh size which is  $\sim 1.2 \mu\text{m}$  surrounding the inclusion.

In Section 4.1.3, it has been observed that the presence of a debonded region does not necessarily lead to an inclusion-driven failure. Also, experimental fractographies of inclusion-driven failures in RR1000 did not clearly reveal a preferential presence of a debonded region. However, all experimental inclusion-driven failures originated from Type 2 inclusions, i.e., agglomerate of small particles. Therefore, in this study, an integer in between 1 to 10 is randomly sampled so that the number of microstructures with inclusions having a debonded region can be decided without any bias. Following the random sampling process, only one SEM with inclusion is created with a debonded region.

### ***Inclusion position within the polycrystalline aggregate***

It has been shown in Section 4.1.4 that the emergence of inclusion- or matrix-driven failure mode is a consequence of complex interaction between inclusion attributes and microstructure surrounding the inclusion. In other words, a specific location of the inclusion within the microstructure does not preferentially lead to a preferred failure mode. Although all surface-connected or sub-surface inclusions do not lead fatigue failure, experimental evidence shows that most of the inclusion-driven failures originate from surface and sub-surface inclusions. Hence, in this study, the inclusions are placed at randomly chosen points which are shared by multiple grains and it is ensured that inclusions in (a) three SEMs are surface-connected, (b) five SEMs are at the sub-surface, and (c) one SEM is at the interior of the microstructure (see Figure 4.16(e)).

## 4.2.2 Results

To predict fatigue life and failure modes as a function of applied strain and temperature, attention is restricted to zero strain ratio loading regime, i.e.,  $R_\epsilon = 0$ , and four operating temperatures ( $T = 20^\circ\text{C}$ ,  $300^\circ\text{C}$ ,  $600^\circ\text{C}$ , and  $750^\circ\text{C}$ ) are considered. For each temperature, CPFE simulations are carried out at 0.4%, 0.6%, 0.75% applied strain ranges. Subsequently,  $w_{N_s}^p(\mathbf{x}^*)$  and  $\Delta w_{N_s}^p(\mathbf{x}^*)$ , as defined in Section 3.2.2, are non-locally averaged as per discussion in Section 3.2.1. Using non-locally averaged  $w_{N_s}^p(\mathbf{x}^*)$  and  $\Delta w_{N_s}^p(\mathbf{x}^*)$ , and experimental fatigue life data for RR1000 for each simulated loading conditions,  $W_{\text{critical}}^p$  is calibrated for RR1000 as a function of temperature using the Bayesian calibration framework detailed in Section 3.2.3. Finally, using the calibrated  $W_{\text{critical}}^p$ , and  $w_{N_s}^p(\mathbf{x}^*)$  and  $\Delta w_{N_s}^p(\mathbf{x}^*)$  from CPFE simulations, fatigue life and associated failure modes are predicted. With this, the calibrated results for  $W_{\text{critical}}^p$  and comparison of the model prediction with experimental evidence are reported below.

### *Critical stored plastic strain energy density as a function of temperature*

As representative examples, evolutions of  $\Delta w^p$  and  $\frac{d(\Delta w^p)}{dN}$  with the number of cycles ( $N$ ) at the critical location within one of the 20 SEMs are shown in Figure 4.17. It is evident from Figure 4.17 that saturation of  $\Delta w^p$  is inherently dependent on applied strain and temperature. It is practically impossible to carry out CPFE simulations for hundreds of cycles. Therefore, keeping in mind the computation cost, for 0.6% and 0.75% applied strains, simulations are continued for 10 cycles. For 0.4% applied strain, simulations are extended up to 20 cycles. With this,  $N_s$  is set to 10 for  $\Delta\epsilon = 0.6\%$  and  $0.75\%$ , and 20 for  $\Delta\epsilon = 0.4\%$ .

For Bayesian calibration of  $W_{\text{critical}}^p$ , the CPFE simulations are performed on all SEMs, with and without inclusions, at the applied strain and temperature, as prescribed above. Subsequently, non-locally averaged  $w_{N_s}^p(\mathbf{x}^*)$  and  $\Delta w_{N_s}^p(\mathbf{x}^*)$  are obtained. In Section 3.2.4, the posterior distributions of  $W_{\text{critical}}^p$  and the hyper-parameter have been observed to be normal and log-normal, respectively. Hence, for RR1000, normal and log-normal distributions are assumed as prior distributions for  $W_{\text{critical}}^p$  and hyper-parameter, respectively. Subsequently, MCMC simulations are continued until  $10^5$  iterations to ensure convergence. The mean value of  $W_{\text{critical}}^p$ ,

obtained from the posterior distribution, is plotted in Figure 4.18 as a function of temperature. The variability in the calibrated  $W_{\text{critical}}^{\text{p}}$ , shown as error bars in Figure 4.18, is computed as a summation of two numbers. The first number is the standard deviation associated with the posterior distribution of  $W_{\text{critical}}^{\text{p}}$ , which primarily considers the aspect of lack of experimental data in the present context. The second number accounts for the error associated with imprecise calibration of the CP parameters. In Section 3.1.3, it has been shown that one might expect almost 25% variability in the accumulated plastic strain energy density at the critical location within an SEM due to the variability associated with the CP parameters. Although the CP constitutive equations, especially the evolution of the reference stress, i.e.,  $g$ , is not identical in Chapter 3 and 4, the results from Section 3.1.3 at least give a rough estimate of the possible uncertainty in  $w_{\text{N}_s}^{\text{p}}(\mathbf{x}^*)$  and  $\Delta w_{\text{N}_s}^{\text{p}}(\mathbf{x}^*)$  from CPFEM simulations for RR1000. According to Eq. (3.17), the accumulated plastic strain energy density at the location of failure is directly proportional to  $w_{\text{N}_s}^{\text{p}}(\mathbf{x}^*)$  and  $\Delta w_{\text{N}_s}^{\text{p}}(\mathbf{x}^*)$ . Hence, due to the uncertainty in the CP parameter, one would expect approximately 25% variability in the calibrated  $W_{\text{critical}}^{\text{p}}$ . Therefore, the second number in the computation of the total variability in  $W_{\text{critical}}^{\text{p}}$  is 0.25 times the mean value of  $W_{\text{critical}}^{\text{p}}$  obtained from the posterior distribution. From Figure 4.18,  $W_{\text{critical}}^{\text{p}}$  appears to decrease almost linearly with increasing temperature. However, more datapoints are necessary to confidently establish a temperature-dependent functional form for  $W_{\text{critical}}^{\text{p}}$ .

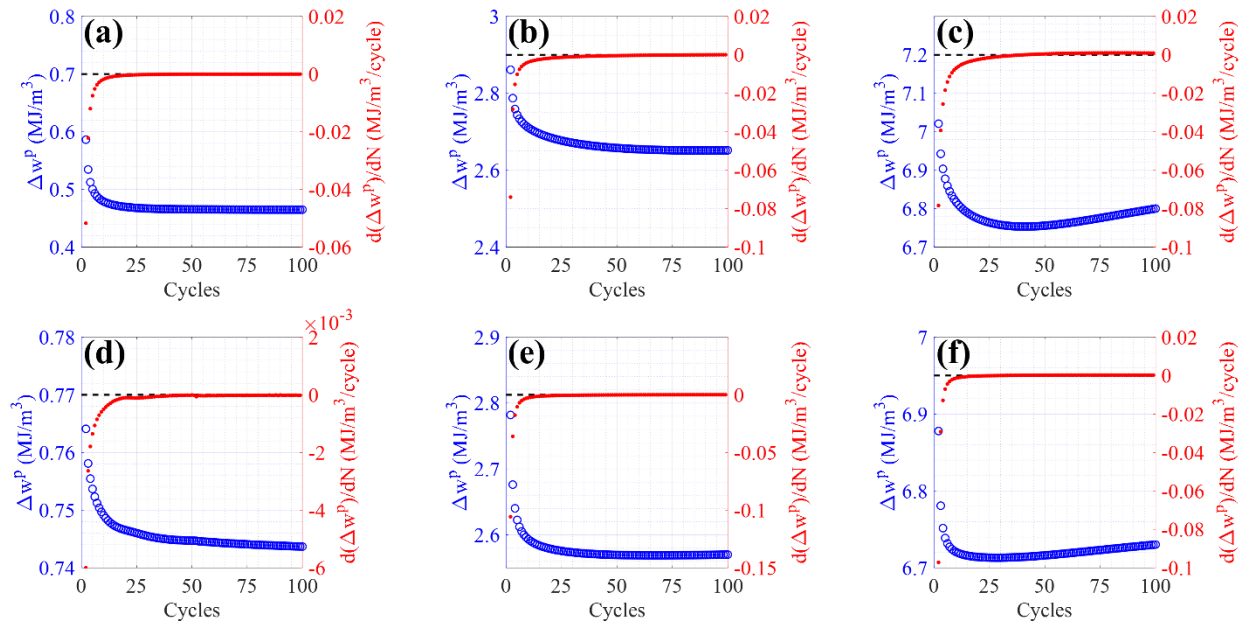


Figure 4.17. Evolution of plastic strain energy density per cycle with the number of cycles at the critical location within one of the SEMs under macroscopically applied strain,  $\Delta\varepsilon = 0.4\%$  (left column),  $0.6\%$  (middle column),  $0.75\%$  (right column), and temperature,  $T = 20^\circ\text{C}$  (top row),  $750^\circ\text{C}$  (bottom row).

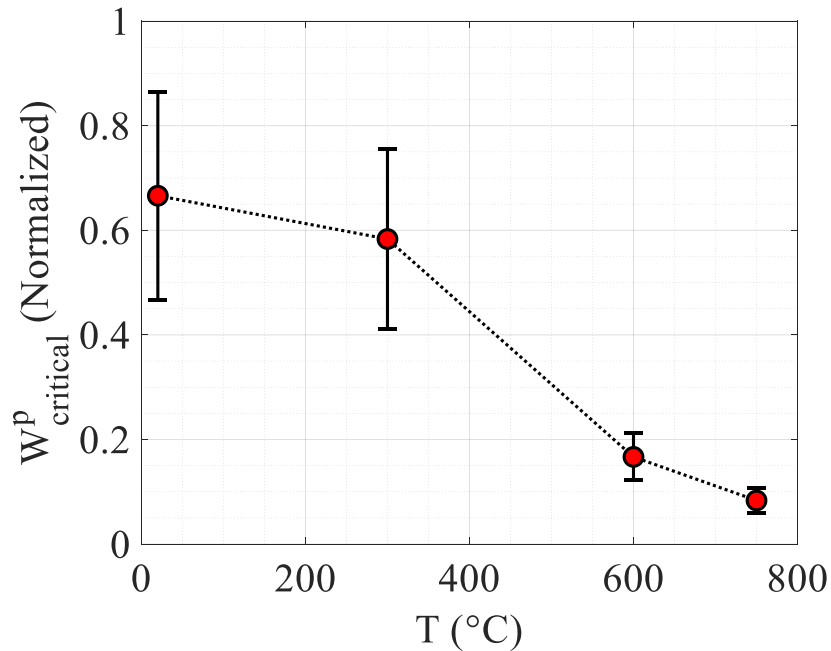


Figure 4.18. Variation of  $W^P_{\text{critical}}$  as a function of temperature.

### *Fatigue life prediction with associated failure modes*

The simulated  $w_{N_s}^p(\mathbf{x}^*)$  and  $\Delta w_{N_s}^p(\mathbf{x}^*)$  values from all SEMs and at all loading conditions, as mentioned before, are used within Eq. (3.18) along with the  $W_{\text{critical}}^p$  values, shown in Figure 4.18, to predict fatigue lives and associated failure modes. The probability of failure plots are obtained using `probplot` function in MATLAB considering log-normal distribution as a reference and shown in Figure 4.19. In Figure 4.19, the vertical axes are depicted in such a way that if data points are sampled from log-normal distributions, those will be aligned along a straight line.

From Figure 4.19, it is interesting to observe that although inclusions are present in 10 SEMs, only one inclusion-driven failure is predicted at 0.4% applied strain, consistently, at all temperatures. Further, the fatigue life associated with the inclusion-driven failure does not correspond to the minimum life predicted in simulation. In experiments, evidence of inclusion-driven failure is only observed for applied strain  $\leq 0.4\%$  and life associated with inclusion-driven failure does not correspond to the minimum life. Although  $\Delta\varepsilon < 0.4\%$  regime is not explored in this study, however, based on the results of the parametric study in Section 4.1.3 and accompanied discussion in Section 4.1.4, higher probability of inclusion-driven failure is expected in the  $\Delta\varepsilon < 0.4\%$  applied strain regime irrespective of the structural stiffness of the inclusion.

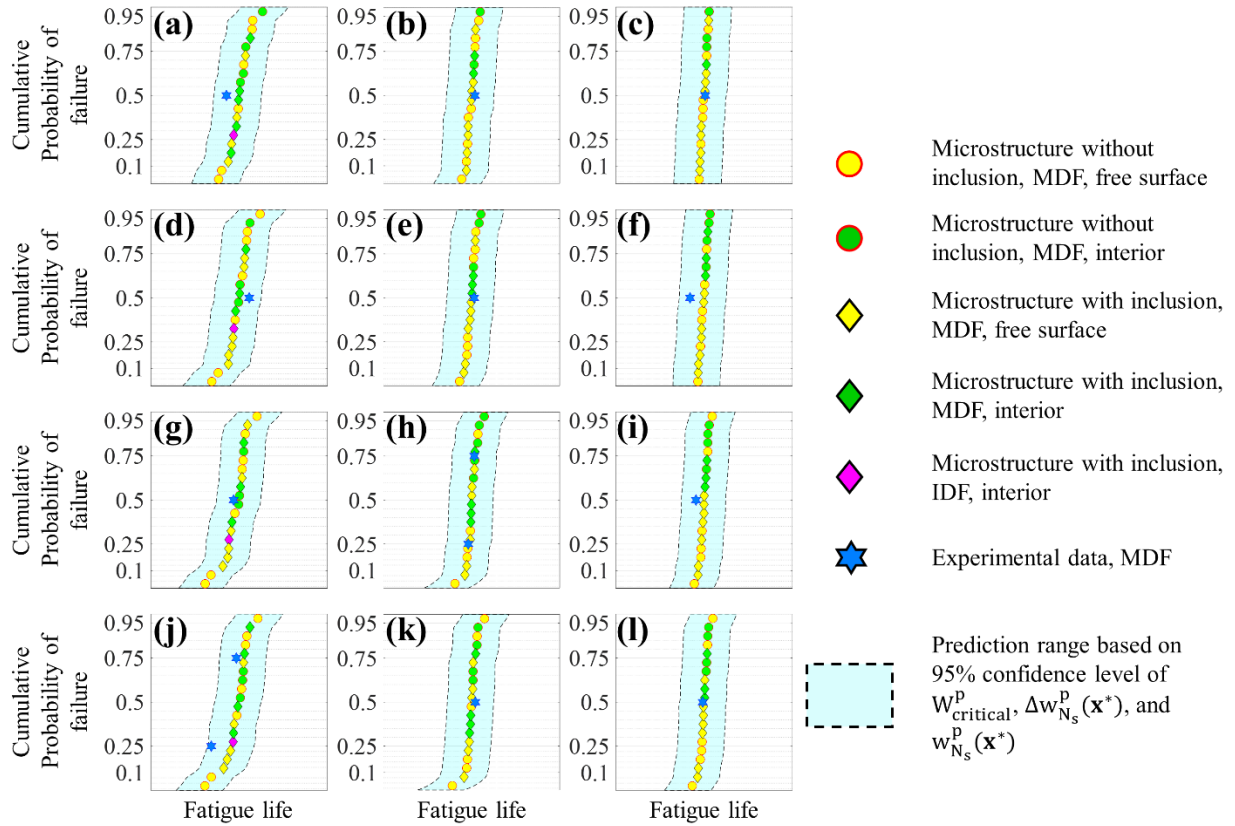


Figure 4.19. The probability of failure plots considering log-normal distribution as reference. Each row corresponds to a constant temperature with  $T = 20^{\circ}\text{C}$  for the first row (from top),  $T = 300^{\circ}\text{C}$  for the second row,  $T = 600^{\circ}\text{C}$  for the third row, and  $T = 750^{\circ}\text{C}$  for the fourth row. Each column corresponds to a constant applied strain with  $\Delta\varepsilon = 0.4\%$  for the first column (from left),  $\Delta\varepsilon = 0.6\%$  for the second column, and  $\Delta\varepsilon = 0.75\%$  for the third column. MDF stands for matrix-driven failure and IDF stands for inclusion-driven failure. ‘free surface’ represents failure originating from the free surface of the microstructure and ‘interior’ represents cases where failure originates within the bulk of the microstructure.

As mentioned in Section 1.1, a turbine disk which is subjected to DMHT shows fine grains near the bore region and coarse grain microstructure near the rim region. In an experimental research with turbine disk made of LSHR, a Ni-base superalloy, Gabb et al. [205] showed that the fine-grained microstructure leads to higher fatigue life compared to the coarse grain microstructure. In their research, Type 2 inclusion-driven failure is observed in the fine-grained region, whereas crystallographic surface and sub-surface facets are responsible for failure in the coarse grain region. The crystallographic facet resulted in minimum fatigue life in their samples. As mentioned before, the experimentally observed minimum life for RR1000 is associated with matrix-driven failure as

well. From Figure 4.19, one can verify that the predicted minimum life in all simulated loading conditions corresponded to matrix-driven failure. Further, the matrix-driven failure corresponding to the minimum life always originated from a microstructure without inclusion and thereby confirming that the minimum life is not influenced by inclusion. Gabb et al. [205] also reported that location of failure, associated with matrix-driven failure mode, shifted more towards interior of the samples with increasing temperature as opposed to originating from the free or near free surface. Further, failure originating at the free surface was associated with lower life compared to the life associated with failure originating from the interior. The present microstructure-sensitive energy-based fatigue life prediction framework is also seen capable of capturing such temperature-dependent behavior of failure location. For example, it can be seen in Figure 4.19 that (a) the minimum life is always associated with the matrix-driven failure originating from the free surface, (b) failure originating at the interior of the microstructures are, in general, observed to be associated with relatively higher fatigue life. Additionally, in Figure 4.20, one can verify that the percentage of predicted free surface failure decreases with increasing temperature. Such a predicted trend is in agreement with RR1000 data as well as reported trends by Gabb et al. [205].

From the results, as presented above, it is clear that the microstructure-sensitive energy-based approach, proposed in Section 3.2, is not only capable of capturing the median and scatter trend in fatigue life data but also efficient enough to capture multiple failure modes and realistic shift in the location of failure with varying applied strain and temperature.

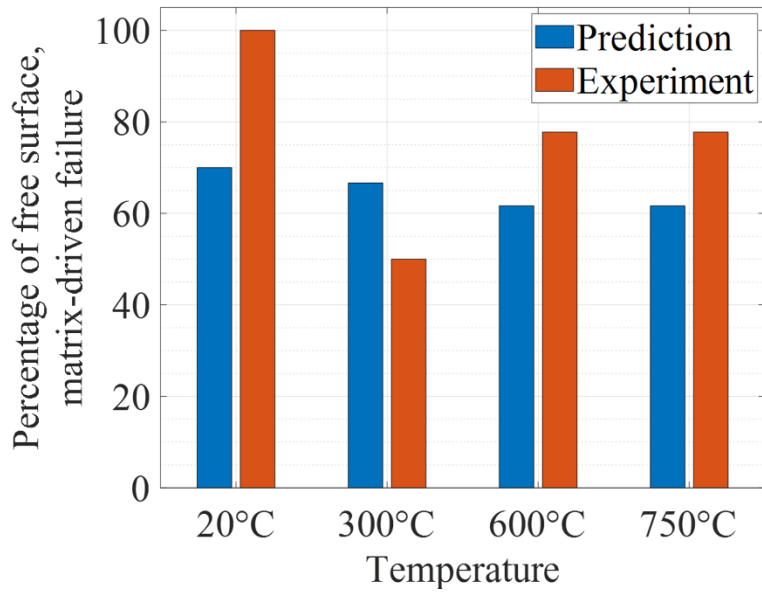


Figure 4.20. Comparison of percentage of free surface failure from simulation and experiments.

### 4.2.3 Summary

In Section 3.2, it has been shown that there exists a microstructure-sensitive critical stored plastic strain energy density of a material that can be used as a unified metric to predict fatigue life across several loading regimes. Here, the critical value of the energy has been calibrated for RR1000, a Ni-base superalloy, as a function of temperature. Subsequently, the calibrated energy has been used to predict inclusion- and matrix-driven competing failure modes in RR1000 as a function of applied strain and temperature. Specifically, 20 statistically equivalent microstructures, 10 of these containing inclusions and remaining 10 without inclusions, have been used to make the prediction. The key findings are summarized below.

- The microstructure-sensitive critical stored plastic strain energy density appears to decrease almost linearly with increasing temperature.
- Based on CPFE simulations, conducted at  $R_e = 0$ ,  $T = 20^\circ\text{C}$ ,  $300^\circ\text{C}$ ,  $600^\circ\text{C}$ ,  $750^\circ\text{C}$ , and  $\Delta\varepsilon = 0.4\%$ ,  $0.6\%$ ,  $0.75\%$ , inclusion-driven failure has been observed only at  $\Delta\varepsilon = 0.4\%$  across all temperatures. Experimentally, inclusion-driven failures are only observed for  $\Delta\varepsilon \leq 0.4\%$ . Although  $\Delta\varepsilon < 0.4\%$  regime is not explored explicitly in this study, it has been shown in Section 3.2.4 that there exists higher probability of inclusion-driven failure in the  $\Delta\varepsilon < 0.4\%$  regime.

- From simulations, inclusion-driven failure mode is not associated with minimum life, which is consistent with experimental observation.
- Experimentally, minimum life corresponded to the matrix-driven failure. In simulations, minimum life also corresponded to matrix-driven failure and originated from a microstructure that does not contain inclusion.
- In the literature, it is seen that the location of failure, associated with matrix-driven failure, shifts towards the interior of the specimen from free surface and the failure originating from the interior are typically associated with higher life. In simulations, the percentage of failure originating from the free surface is seen to be decreasing with increasing temperature as well. Further, life, associated with failure from interior, has been predicted to be consistently higher than the free surface failure life.

The above findings certainly make the framework, proposed in Section 3.2, promising and trustworthy for location-specific design and fatigue life prognosis of safety-critical components in aero-industry.

## **5. ASSURANCE OF PERFORMANCE IN THE LINEAR FRICTION WELDED TITANIUM ALLOYS**

In this Chapter, residual strain in the LFW of similar and dissimilar Ti alloys (in as-welded as well as heat-treated conditions) is first characterized using EDD experiments. Subsequently, observed trends in the residual strain profiles are rationalized via BSE imaging of the microstructure across the weld region. Since fatigue crack initiation does not usually take place in the weld region, fatigue analysis is carried out in the base material. With this, residual strain measurement using EDD and microstructural characterization using BSE imaging are described in Section 5.1. Next, HCF performance in Ti-6Al-4V, having a microstructure representative of the base Ti-6Al-4V material, is analyzed at high R ratio in Section 5.2.

### **5.1 Residual strain analysis in linear friction welds of similar and dissimilar Ti alloys using energy dispersive X-ray diffraction**

This section is organized as follows. Section 5.1.1 illustrates the weld materials, parameters, and electron microscopy (EM) characterization technique. Section 5.1.2 describes the EDD method and post-processing methodologies to obtain the residual strains. The residual strain results are reported in Section 5.1.3. Observed trends in the in-plane axial components of the residual strains are discussed and explained via BSE images in Section 5.1.4.

#### **5.1.1 Materials and methodology**

##### ***Materials***

In this study, several Ti alloys and combinations are selected for LFW, as shown in Table 5.1. For the first set of samples where two similar Ti alloys are joined by LFW, two pieces of Ti-6Al-4V alloy, denoted as Ti64 throughout Section 5.1 from here on, in alpha-beta processed state are used. The alpha phase has an HCP structure and the beta phase has a body centered cubic (BCC) structure. For the second set of samples where two dissimilar Ti alloys are joined by LFW, Ti-5Al-5V-5Mo-3Cr, denoted as Ti5553 throughout Section 5.1 from here on, is used in the oscillating side and Ti64 in mill-annealed state is used in the fixed side. The material with the greater flow stress at the evaluated temperature is selected for the oscillating component in the dissimilar weld

because a rigid oscillating component reduces unwanted deformation of the component during welding and generally leads to better weld quality. The difference between the two Ti64 variants is the morphology and volume fraction of the beta phase.

Table 5.1. Material for welded components. All heat treatments are followed by air cooling.

<b>Material Combination</b>	<b>Oscillating Side Material</b>	<b>Starting Microstructure of Oscillating Component</b>	<b>Fixed Side Material</b>	<b>Starting Microstructure of Fixed Component</b>
Ti64-Ti64	Ti64	Alpha-beta processed: Received in mill-annealed condition per AMS 4911 [206] followed by annealing at 704°C for 2 hr	Ti64	Alpha-beta processed: Received in mill-annealed condition per AMS 4911 [206] followed by annealing at 704°C for 2 hr
Ti64-Ti5553	Ti5553	Solution treated at 838°C for 2 hr and Aged at 593°C for 8 hr	Ti64	Mill-annealed per AMS 4911 [206]

Table 5.2. Linear friction weld parameters used to fabricate the weld samples. The programmed burn-off is defined as the displacement of the weld platen. The upset is the total loss in length of the joined component after welding.

<b>Material Combination</b>	<b>Frequency (Hz)</b>	<b>Amplitude (mm)</b>	<b>Weld Pressure (MPa)</b>	<b>Programmed Burn-off (mm)</b>	<b>Forge Pressure (MPa)</b>	<b>Forge Time (s)</b>	<b>Measured Upset (mm)</b>
Ti64-Ti64	35	2.5	100	2.48	100	5	3.51
Ti64-Ti5553	45	1.1	172.4	3.18	172.4	5	N/A

### ***Weld parameters and heat treatment***

Each set of material welding parameters underwent iterative development trials and parameter selection based upon previous welding trials at the Edison Welding Institute. Each weld's quality is assessed based upon flash curl, weld time, process forces, visual inspection, and a quick rudimentary pull test to assess ultimate tensile strength. The pull test is used as a qualitative measure and formal tensile testing is conducted on select welds. The welds characterized in this study represent the best or near best case welding conditions from the parameter development trials.

The weld is split into three distinct stages: scrub, weld, and forge. The scrub allows the oscillator to reach amplitude at the desired frequency under low load and can be used to build heat into the part. The scrub time and pressure (i.e. pressure applied at the beginning of oscillation) are 0.2 s and 22.8 MPa, respectively. The weld phase uses oscillation amplitude, frequency, and pressure of the moving component to deform the material and create a solid-state joint. Afterwards, oscillation is stopped and a forge pressure equal to or greater than the weld pressure is applied during the forge phase and held for a short duration (i.e. forge time). The LFW parameters for each weld are summarized in Table 5.2.

Two weld samples using Ti64-Ti64 combination and two samples using Ti64-Ti5553 combination are fabricated using the LFW parameters listed in Table 5.2. One sample for each combination is set aside and these are designated as the as-welded (AW) condition. The remaining samples underwent a post-weld heat treatment and are referred to as HT samples throughout Section 5.1. The Ti64-Ti64 sample is heat treated at 704°C for 2 hr followed by air cooling. Similarly, the Ti64-Ti5553 sample is heat treated below the beta solvus temperature of Ti5553.

### ***Electron microscopy characterization***

All sample pedigrees are characterized on a FEI Quanta 3D FEG Dual-beam scanning electron microscope with a four quadrant BSE detector. The BSE detector is used in Z-contrast mode; all four quadrants had a positive bias. Specimens are mechanically ground and polished using 0.3  $\mu\text{m}$  alumina suspension. The final polish is achieved by using vibratory polishing with a suspension of 0.05  $\mu\text{m}$  colloidal silica. Specimens are marked perpendicular to the weld interface of the joined materials. Indents are placed every 500  $\mu\text{m}$  across the 9 mm weld region, 4.5 mm on each side of the weld, and used for spatial positioning during BSE characterization (see Figure

5.1). Images are taken along the fiducially marked path, continuously 2 mm from the weld in both directions and every 500  $\mu\text{m}$  after that, until 4.5 mm is imaged on each side of the weld. This imaging scheme is used such that the microstructural transitions close to the weld would be captured, as well as the microstructure further away from the weld.

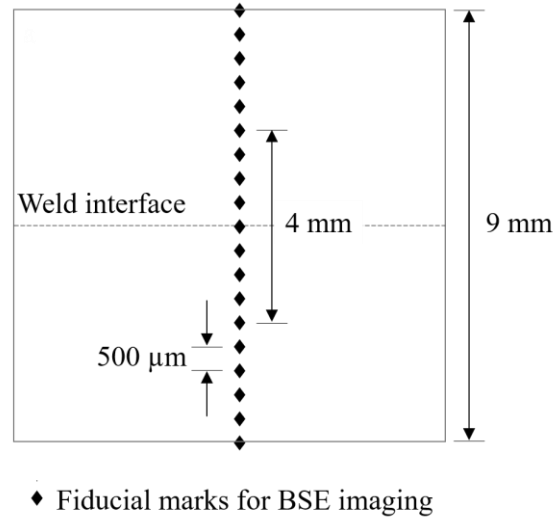


Figure 5.1. Schematic of the weld region showing fiducial marks for BSE imaging. Images are taken along the fiducially marked path, continuously 2 mm from the weld in both directions and every 500  $\mu\text{m}$  after that.

### 5.1.2 Residual strain measurement

#### *Energy dispersive X-ray diffraction experiment*

Figure 5.2 shows the setup for the EDD experiment at the 6-BM-A endstation of the Advanced Photon Source (APS), Argonne National Laboratory. Figure 5.3 shows a schematic view of the setup and Figure 5.4 illustrates the geometry in 2D view. In this schematic, the  $X$ - $Y$ - $Z$  coordinate system is fixed in the lab; slits 1 – 3 control the size of the incoming polychromatic X-ray beam and the filter removes the low energy photons which are not useful for strain measurements for this sample; slits 4 – 5 and 6 – 7 are associated with the vertical and horizontal detectors, respectively, and controlled the sizes of the gauge volumes interrogated by the detectors. Two germanium detectors are placed approximately 1 m away from the gauge volume – one on the  $Y$ - $Z$  plane and the other on the  $X$ - $Z$  plane. The detector placed on the  $Y$ - $Z$  plane is referred to as the vertical detector and  $\mathbf{q}_v$  is the corresponding scattering vector associated with the strain measurement direction. The detector placed on the  $X$ - $Z$  plane is referred to as the horizontal

detector and  $\mathbf{q}_h$  is the corresponding scattering vector. The vertical and horizontal detectors and associated slits are positioned such that  $2\theta_v$  and  $2\theta_h$  are  $5.00^\circ$  and  $4.90^\circ$ , respectively. Furthermore, the slits are adjusted such that the gauge volume viewed by the vertical detector and the gauge volume viewed by the horizontal detector coincide. The centroid of the gauge volume is denoted as  $O$  in Figure 5.3 and Figure 5.4(a). Calibration of the setup using a thin  $\text{CeO}_2$  powder sample indicates that the gauge volume is approximately 5 mm long in the  $Z$  direction. The incoming beam size is  $0.2 \text{ mm} \times 0.2 \text{ mm}$  defined by the upstream slits. At these slit settings and detector locations, the azimuthal coverage is approximately  $1^\circ$  for both detectors.

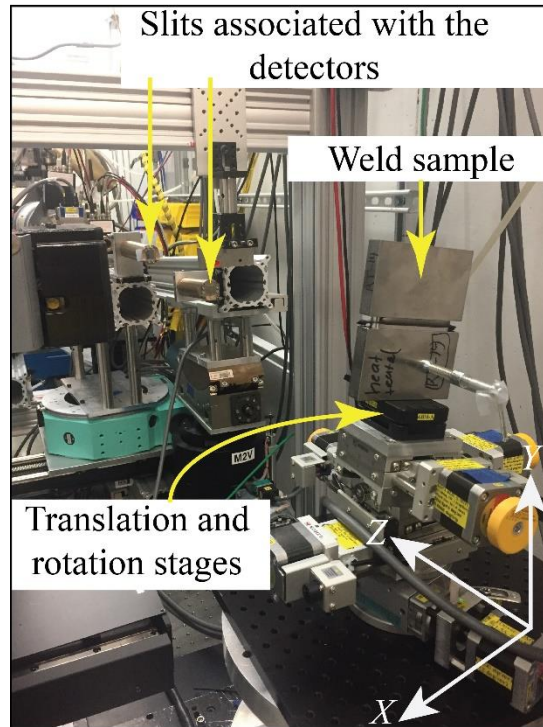


Figure 5.2. The overall experimental setup for the EDD measurement.

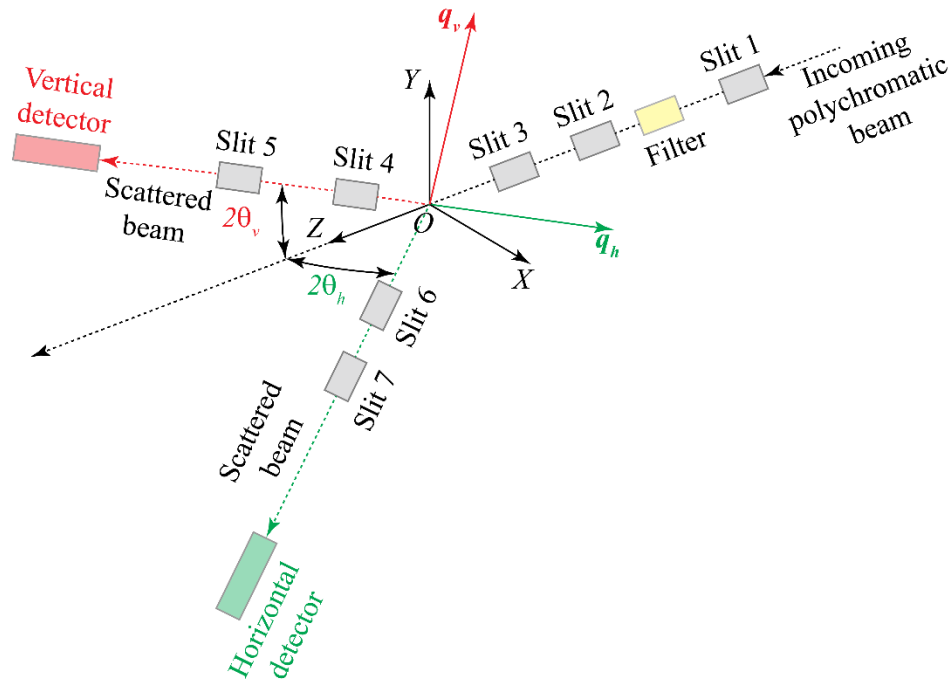


Figure 5.3. A schematic of the experimental setup, in which the X-Y-Z coordinate system is fixed in the lab.

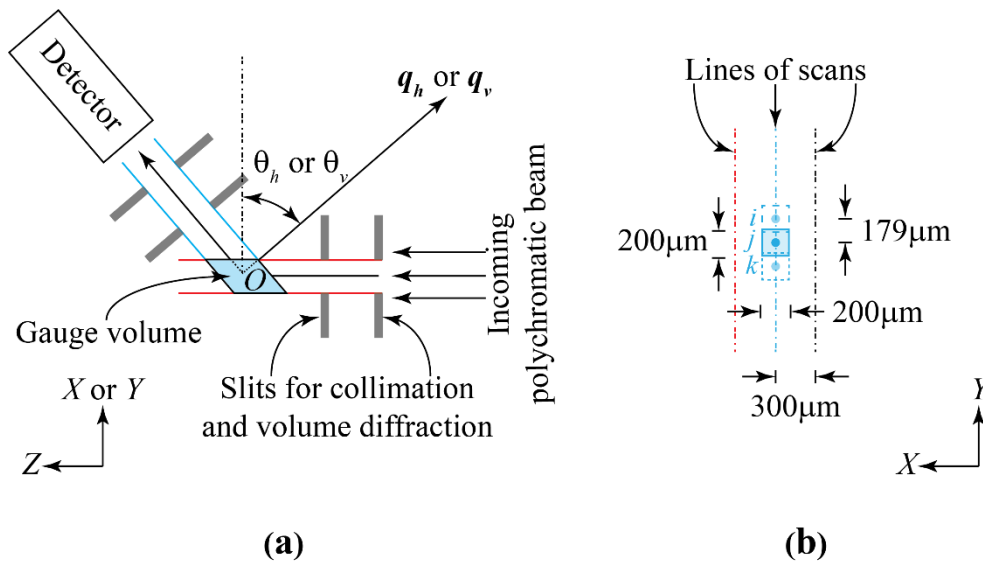


Figure 5.4. (a) 2D schematic of the gauge volume interrogated by a detector in the experimental setup. (b) The projection of the gauge volume on the X-Y plane. For the residual strain characterization of each specimen, multiple line scans 300  $\mu\text{m}$  apart are taken. Experimentally obtained lattice strain at a ‘point’ is defined by the average value of the same over the illuminated gauge volume, the centroid of which coincides with the ‘point’. In the figure  $i, j, k$  represent three such consecutive ‘points’ and the overlap of the illuminated gauge volume is shown.

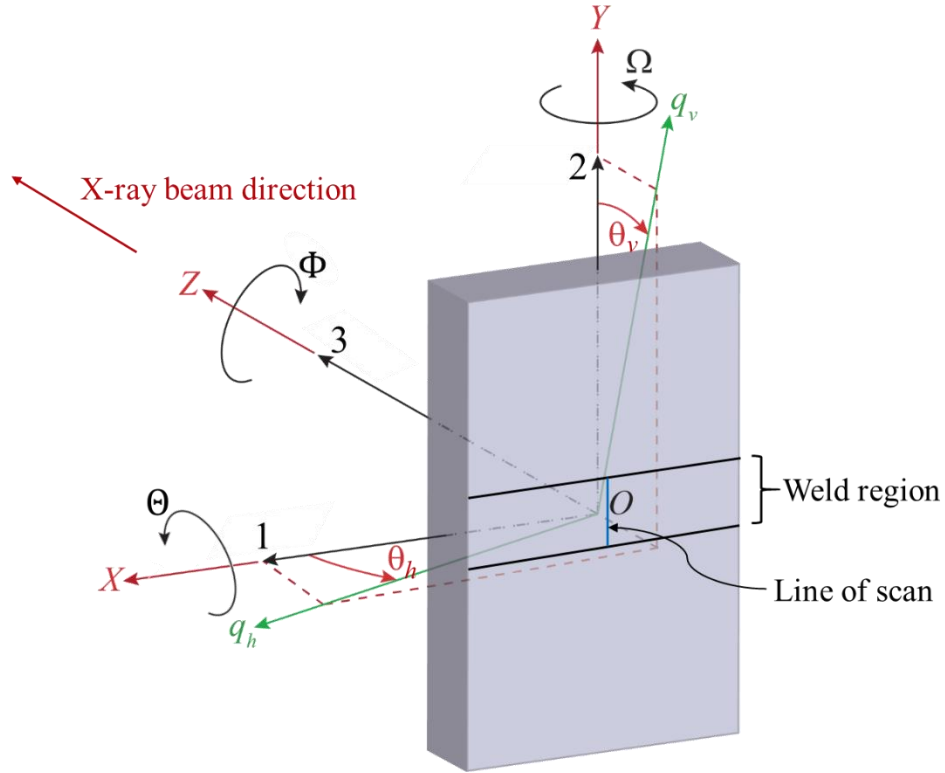


Figure 5.5. A schematic of the linear friction weld part is shown. The 1-2-3 coordinate system is fixed to the sample and rotates with the sample.

The goal of the EDD experiments is to obtain a strain tensor map in the weld region of a sample. Figure 5.5 illustrates how this goal is achieved. The sample is positioned such that the sample mid-plane along 3, coincide with  $O$ . All the crystal planes in the sample that reside in the gauge volume and satisfy the diffraction condition for  $\mathbf{q}_v$  and  $\mathbf{q}_h$  contribute to the spectra obtained by the vertical and horizontal detectors, respectively. Given the average grain size, around  $10^5$  grains are anticipated to be in the gauge volume. For a particular sample position  $P(x_1, x_2, x_3)$ , the sample is rotated by discrete values in  $\Omega$  (rotation about  $Y$  axis), while keeping  $\Theta$  (rotation about  $X$  axis) and  $\Phi$  (rotation about  $Z$  axis) at  $0^\circ$  and by discrete values in  $\Phi$ , while keeping  $\Omega$  and  $\Theta$  at  $0^\circ$ . The values of  $\Omega$  are  $-45^\circ, 0^\circ, 15^\circ, 30^\circ,$  and  $45^\circ$  and the values of  $\Phi$  are  $-8^\circ, 0^\circ,$  and  $8^\circ$ . With these angular motions, seven measurements of lattice strains are obtained from each detector. Later, these measurements are used to compute the components of the strain tensor. Rotation also implies that the crystals participating in diffraction is changing from one angle setting to the other even for the same sample position. In fact, because of the sample rotation, the spatial resolution attainable based on the size of slits for the incoming X-ray beam is compromised, most severely in the 1

direction. After the suite of rotations at the point P, the sample is translated along  $Y$  axis to interrogate a series of points across the weld. For the Ti64-Ti64 LFW samples (AW and HT), three line-scans along  $Y$  direction are performed with each line separated along  $X$  axis by 0.3 mm (see Figure 5.4(b)). For the Ti64-Ti5553 LFW samples (AW and HT), two line-scans are performed with lines separated by 0.3 mm. All line scans are nominally in the mid-section of the sample in 1 and 3.

### ***Data post-processing***

Post-processing of the diffraction spectra involves two steps, namely, obtaining the lattice strains via peak fitting, and computing the components of the residual strain tensor using the obtained lattice strains. First, the peak fitting and lattice strain measurement procedure will be outlined.

Figure 5.6 shows a representative diffraction pattern in the Ti64-Ti5553 HT LFW sample near the weld interface at  $\Omega = 0^\circ, \Phi = 0^\circ$ . Each peak corresponds to a family of planes as described in the Table 5.3.

Table 5.3. Description of first six alpha and first three beta peaks.

Phase	First peak	Second peak	Third peak	Fourth peak	Fifth peak	Sixth peak
Alpha	{100}	{002}	{101}	{102}	{110}	{103}
	{{10 $\bar{1}$ 0}}	{{0002}}	{{10 $\bar{1}$ 1}}	{{10 $\bar{1}$ 2}}	{{11 $\bar{2}$ 0}}	{{10 $\bar{1}$ 3}}
Beta	{110}	{200}	{211}	-	-	-

The first, fourth, and fifth peaks for the alpha phase are well separated from other alpha and beta peaks. Further, the fourth alpha peak is consistently present in all scanned locations and  $(\Omega, \Phi)$  combinations for each LFW sample. Hence, the fourth alpha peak is fit using the pseudo-Voigt function in MATLAB. The fit is used to compute the lattice strain using

$$\varepsilon_{q_h} = \frac{E_h^{hkl} - \frac{hc_0}{2d_0^{hkl} \sin \theta_h}}{\frac{hc_0}{2d_0^{hkl} \sin \theta_h}} \quad (5.1)$$

and

$$\varepsilon_{q_v} = \frac{E_v^{hkl} - \frac{hc_0}{2d_0^{hkl} \sin \theta_v}}{\frac{hc_0}{2d_0^{hkl} \sin \theta_v}} \quad (5.2)$$

where  $\varepsilon_{q_h}$  and  $\varepsilon_{q_v}$  are lattice strains from horizontal and vertical detectors, respectively;  $E_h^{hkl}$  and  $E_v^{hkl}$  are fitted energy values for the peaks corresponding to  $\{hkl\}$  planes from horizontal and vertical detectors, respectively;  $h$  is Planck's constant;  $c_0$  is speed of light in vacuum;  $d_0^{hkl}$  is the reference inter-planar spacing corresponding to  $\{hkl\}$  planes.

Similarly, it can be seen that the second beta peak is well isolated from other alpha and beta peaks. Hence, the second beta peak is chosen for peak fitting, and lattice strains are calculated using Eqs. (5.1) and (5.2). It is worthwhile to note that the alpha  $\{110\}$  and beta  $\{200\}$  are used as strain gauges embedded in the material.

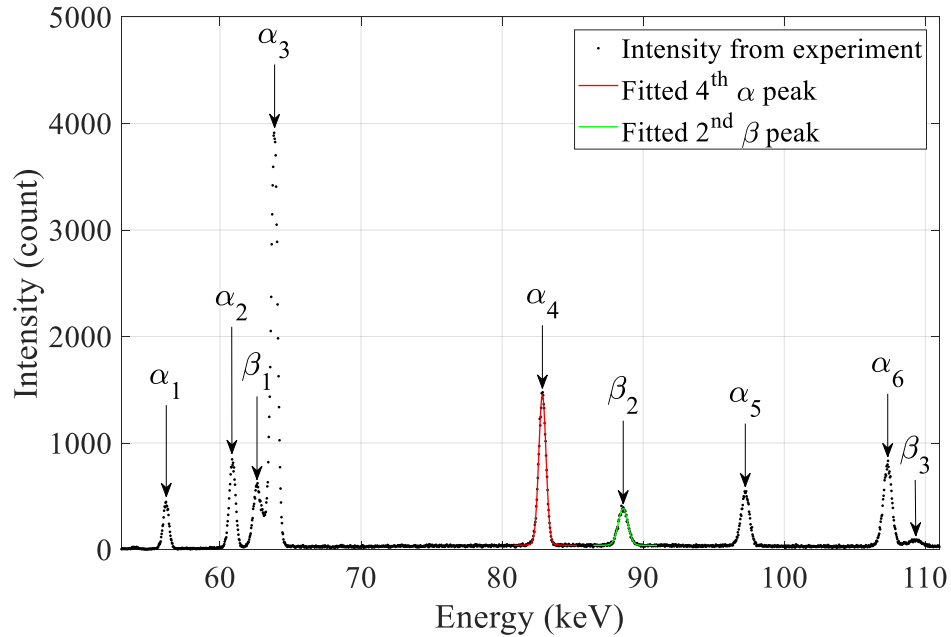


Figure 5.6. The diffraction pattern from Ti64-Ti5553 HT sample near the weld interface obtained at  $\Omega = 0^\circ$ ,  $\Phi = 0^\circ$  configuration. In the plot  $\alpha_i$  represents  $i^{\text{th}}$  peak corresponding to the alpha phase and  $\beta_i$  represents  $i^{\text{th}}$  peak corresponding to the beta phase. The first six alpha peaks correspond to the  $\{100\}$ ,  $\{002\}$ ,  $\{101\}$ ,  $\{102\}$ ,  $\{110\}$  and  $\{103\}$  planes, respectively. The first three beta peaks correspond to the  $\{110\}$ ,  $\{200\}$  and  $\{211\}$  planes, respectively.

For each measurement point, the residual strain tensor in the alpha and beta phases are computed using the lattice strain values obtained above. For each  $\Omega$  or  $\Phi$ , the lattice strains

measured from the horizontal and vertical detectors can be related to the residual strain tensor as follows:

$$\varepsilon_{q_h} = \mathbf{q}_h \mathbf{R} \boldsymbol{\varepsilon} \mathbf{R}^T \mathbf{q}_h^T \quad (5.3)$$

and

$$\varepsilon_{q_v} = \mathbf{q}_v \mathbf{R} \boldsymbol{\varepsilon} \mathbf{R}^T \mathbf{q}_v^T \quad (5.4)$$

where  $\boldsymbol{\varepsilon}$  is the residual strain tensor in the 1-2-3 coordinate system;  $\mathbf{R}$  is defined by

$$\mathbf{R}_\Omega = \begin{bmatrix} \cos \Omega & 0 & -\sin \Omega \\ 0 & 1 & 0 \\ \sin \Omega & 0 & \cos \Omega \end{bmatrix} \quad (5.5)$$

or

$$\mathbf{R}_\Phi = \begin{bmatrix} \cos \Phi & -\sin \Phi & 0 \\ \sin \Phi & \cos \Phi & 0 \\ 0 & 0 & 1 \end{bmatrix} \quad (5.6)$$

depending on the sample rotation executed to measure the strain component.

At each  $(\Omega, \Phi)$  combination, two equations exist, one from the horizontal detector and another from the vertical detector. Hence, an over-determined linear system can be formulated based on 14 equations and 6 unknowns for each measurement point, which can be written as:

$$\mathbf{A} \mathbf{x} = \mathbf{b} \quad (5.7)$$

where

$$\mathbf{x} = [\varepsilon_{11}, \varepsilon_{22}, \varepsilon_{33}, \varepsilon_{12}, \varepsilon_{13}, \varepsilon_{23}]^T \quad (5.8)$$

and

$$\mathbf{b} = \begin{bmatrix} \varepsilon_{q_h}^{\Omega=-45^\circ}, \varepsilon_{q_v}^{\Omega=-45^\circ}, \varepsilon_{q_h}^{\Omega=0^\circ}, \varepsilon_{q_v}^{\Omega=0^\circ}, \varepsilon_{q_h}^{\Omega=15^\circ}, \varepsilon_{q_v}^{\Omega=15^\circ}, \varepsilon_{q_h}^{\Omega=30^\circ}, \\ \varepsilon_{q_v}^{\Omega=30^\circ}, \varepsilon_{q_h}^{\Omega=45^\circ}, \varepsilon_{q_v}^{\Omega=45^\circ}, \varepsilon_{q_h}^{\Phi=-8^\circ}, \varepsilon_{q_v}^{\Phi=-8^\circ}, \varepsilon_{q_h}^{\Phi=8^\circ}, \varepsilon_{q_v}^{\Phi=8^\circ} \end{bmatrix}^T \quad (5.9)$$

and the  $14 \times 6$  coefficient matrix,  $\mathbf{A}$ , depends on the seven configurations defined by the associated angles,  $\Omega, \Phi, \theta_h, \theta_v$ . It should be noted that the coefficient matrix  $\mathbf{A}$  is the same at all measurement point, whereas the  $\mathbf{b}$  changes from point to point. Such a system is solved in MATLAB using a least square method wherein the  $\ell^2$  norm of the residual,  $\mathbf{e} = \mathbf{A} \mathbf{x} - \mathbf{b}$ , is minimized to determine the residual strain tensor. The above procedure is repeated at all points for each line scan for all LFW samples to find the components of the residual strain tensor. In the following section, the results from the MATLAB analysis are reported.

### 5.1.3 Residual strain results

The strain free lattice parameters for both the alpha and beta phases are determined using the Ti64-Ti64 HT sample. The lattice parameters are adjusted so that the lattice strains obtained after peak fitting (considering the fourth peak of the alpha phase and the second peak of the beta phase) from both detectors at all points on a line scan are minimized in an absolute sense. The results are  $a = 2.931\text{\AA}$ ,  $c = 4.660\text{\AA}$  for the alpha phase and  $a = 3.213\text{\AA}$  for the beta phase. These numbers are consistent with the reported range of values in the literature [207]–[210]. Subsequently, these lattice parameters are used to compute lattice strains in all LFW samples.

The numerical accuracy depends on the error associated with the lattice strains and the least squares solution. For a powder material, typical strain uncertainty of the experimental setup at the 6-BM-A EDD setup is approximately  $1 \times 10^{-4}$ . The least squares solution of the over determined linear system,  $\mathbf{Ax} = \mathbf{b}$ , is same as the solution of the square system  $\mathbf{A}^T\mathbf{Ax} = \mathbf{A}^T\mathbf{b}$ . Therefore, the condition number<sup>†††</sup> of  $\mathbf{A}^T\mathbf{A}$  is computed as a measure of the quality of the inverse operator  $(\mathbf{A}^T\mathbf{A})^{-1}$ . If all configurations and the associated angles (i.e.,  $\Omega, \Phi, \theta_v, \theta_h$ ) are considered, the condition number of  $\mathbf{A}^T\mathbf{A}$  is 6962.6. If small angles  $\theta_v, \theta_h$  are neglected (i.e., set  $\theta_v = 0^\circ, \theta_h = 0^\circ$ ), the condition number becomes 22.8. Further, if two configurations associated with the small angle  $\Phi$  are neglected (i.e., neglect  $\Phi = 8^\circ, -8^\circ$  and set  $\Phi = 0^\circ$ ), the condition number becomes 14.4<sup>§§§</sup>. Therefore, it is evident that the small angles for  $\theta_v, \theta_h$  result in a bad quality or unreliable inverse operation, whereas the configurations defined by small angle  $\Phi$  do not affect the inversion operation significantly. If  $\theta_v, \theta_h$  are set to  $0^\circ$ , the information related to  $\varepsilon_{23}$  component of the residual strain tensor is lost but the rest of the components can be captured with higher confidence. The variations of the residual strain tensor components (except  $\varepsilon_{23}$ ) in the alpha and beta phases, across the weld region of all LFW samples, are shown in Figure 5.7 through Figure 5.10.

---

<sup>†††</sup> If the condition number of the coefficient matrix of a linear system is very large ( $\gg 1$ ), it is practically singular. Hence, the solution of the linear system is prone to large numerical error.

<sup>§§§</sup> It is to be noted, when  $\theta_v, \theta_h$  or  $\Phi$  are neglected, a few columns of  $\mathbf{A}$  matrix only contain zeros. Those columns are neglected while calculating condition number.

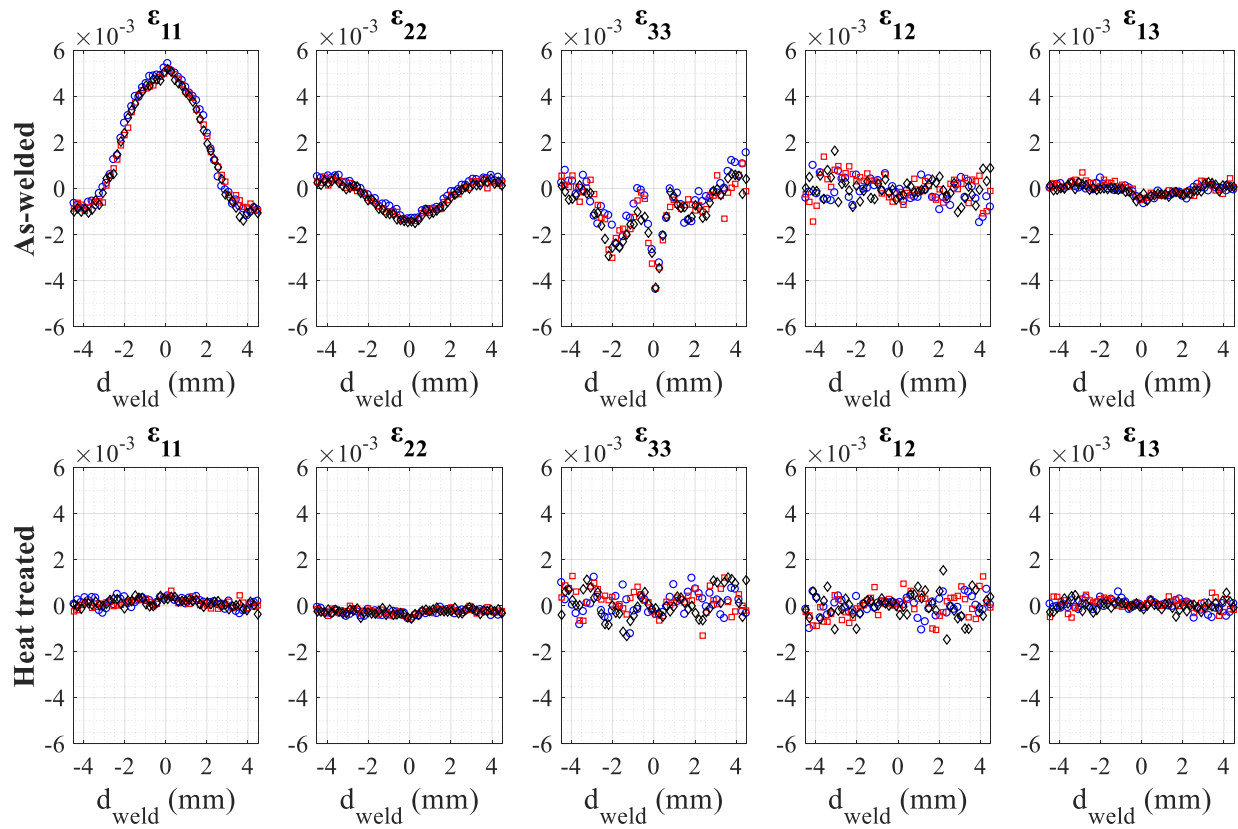


Figure 5.7. Residual strain components in the as-welded and heat-treated joints of Ti64-Ti64 LFW sample are shown. These are obtained from fitting the 4<sup>th</sup> peak of the alpha phase. Different markers in the plots correspond to different lines of scans.

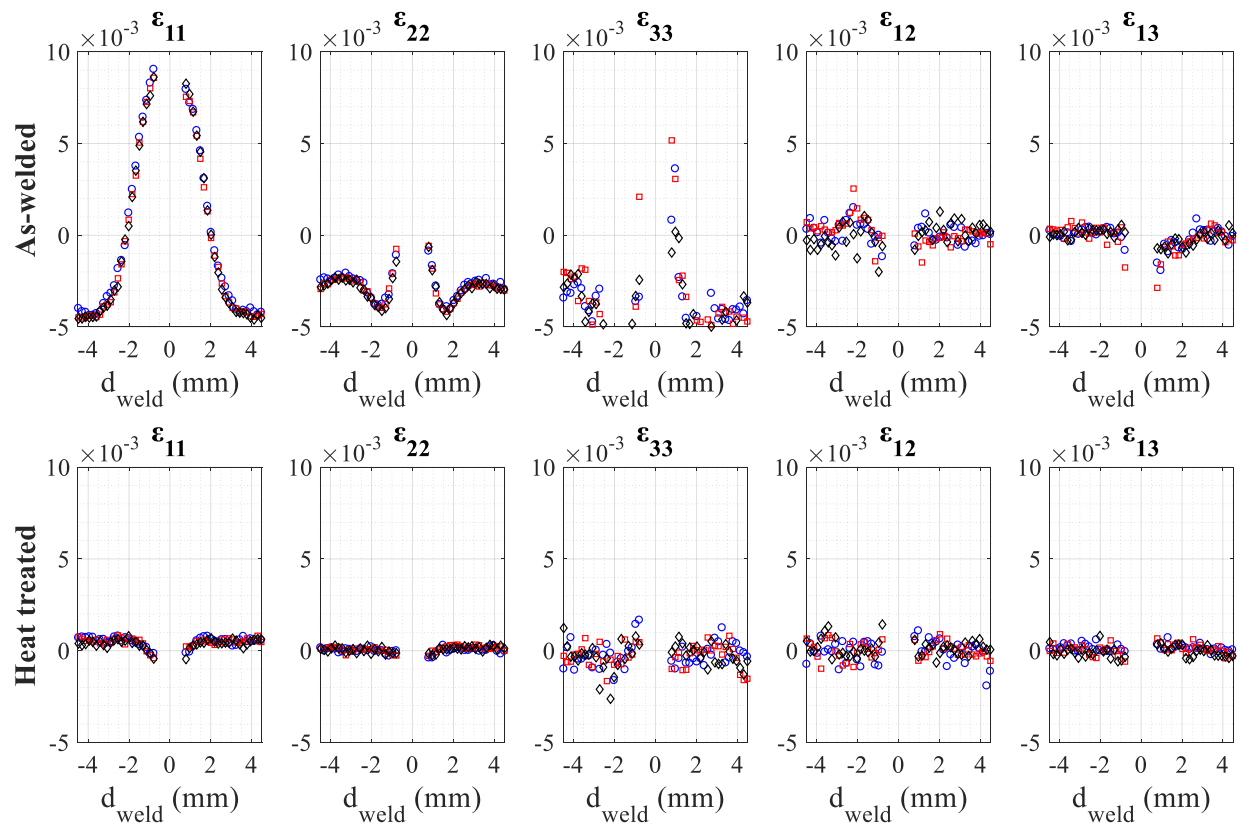


Figure 5.8. Residual strain components in the as-welded and heat-treated joints of Ti64-Ti64 LFW sample are shown. These are obtained from fitting the 2<sup>nd</sup> peak of the beta phase. Different markers in the plots correspond to different lines of scans.

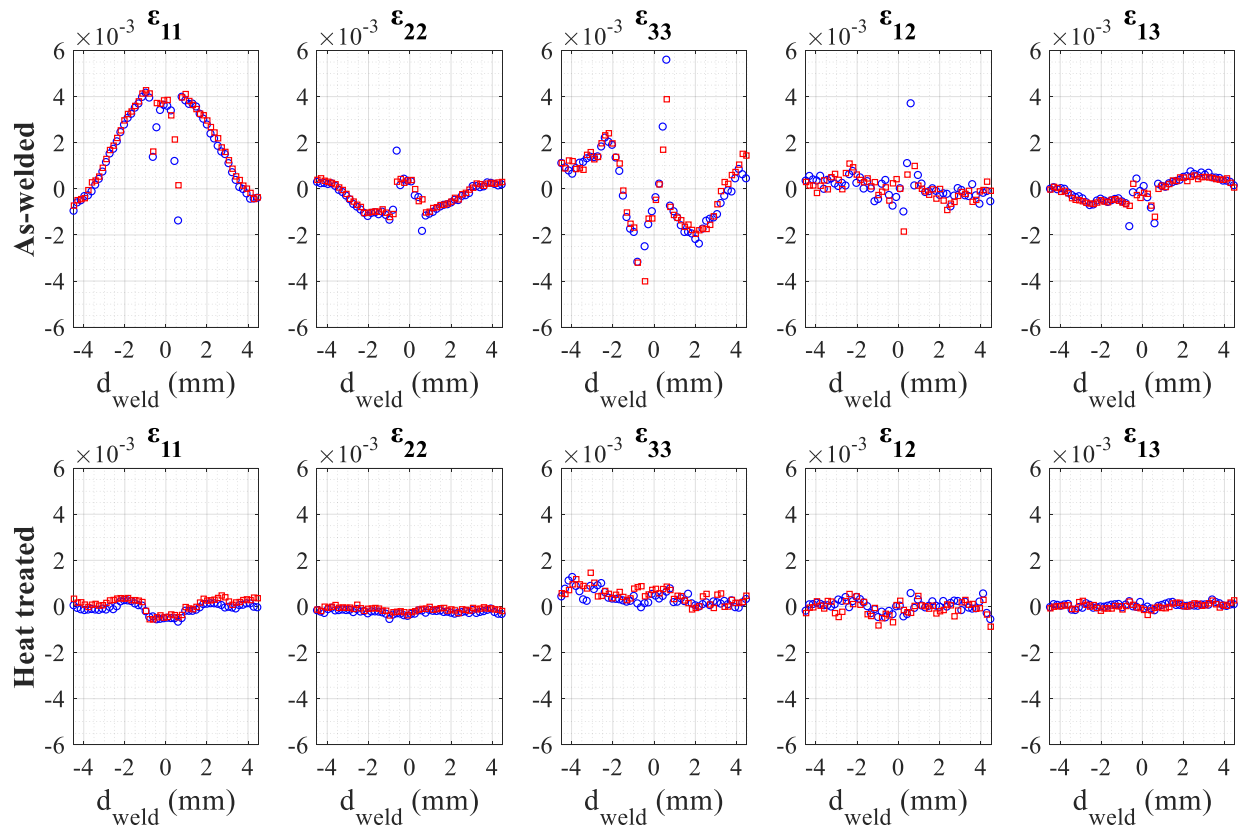


Figure 5.9. Residual strain components in the as-welded and heat-treated joints of Ti64-Ti5553 LFW sample are shown. These are obtained from fitting the 4<sup>th</sup> peak of the alpha phase. In the figure, Ti64 is to the left and Ti5553 is to the right. Different markers in the plots correspond to different lines of scans.

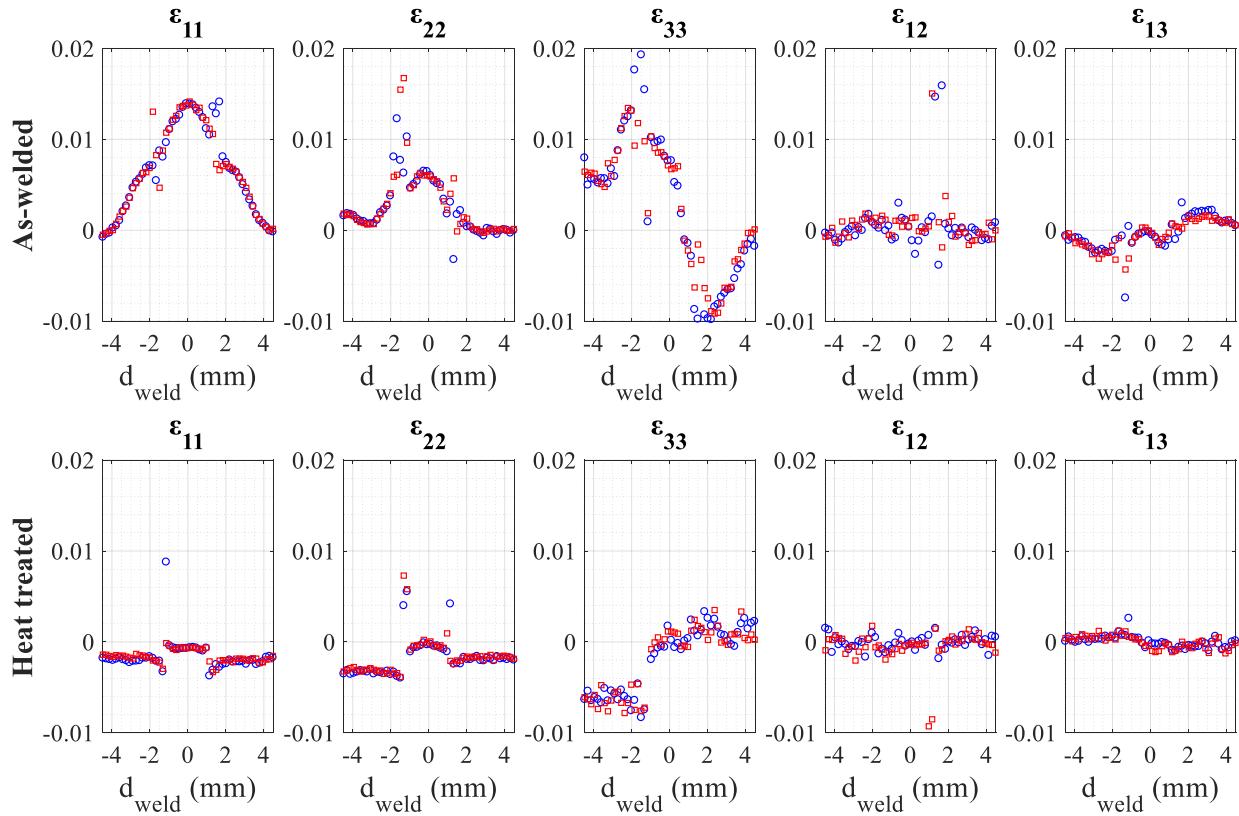


Figure 5.10. Residual strain components in the as-welded and heat-treated joints of Ti64-Ti5553 LFW sample are shown. These are obtained from fitting the 2<sup>nd</sup> peak of the beta phase. In the figure, Ti64 is to the left and Ti5553 is to the right. Different markers in the plots correspond to different lines of scans.

It can be seen from Figure 5.7-Figure 5.10 that shear strain components ( $\epsilon_{12}$ ,  $\epsilon_{13}$ ) are either near zero for HT condition or very small compared to normal components ( $\epsilon_{11}$ ,  $\epsilon_{22}$ ,  $\epsilon_{33}$ ) in the AW condition. Moreover, the rubbing action during the welding process took place on the 1-2 plane. Therefore, it can be reasonably assumed that the  $\epsilon_{23}$  will be very small for all the cases. In the next section, the trends observed in the in-plane axial components ( $\epsilon_{11}$ ,  $\epsilon_{22}$ ) are described and explained using micrographs obtained through BSE images.

#### 5.1.4 Discussion

BSE imaging is used to evaluate the microstructure across the weld region and correlate the varying microstructure to the residual strain measurements, specifically  $\epsilon_{11}$  and  $\epsilon_{22}$ . If not

stated explicitly, ‘strain’ in the following discussions corresponds only to the  $\varepsilon_{11}$  and  $\varepsilon_{22}$  components. For all BSE microstructure images, the beta phase appears as the light regions, whereas the alpha phase appears relatively darker.

### ***Ti64-Ti64 LFW in the as-welded condition***

The residual strain profiles in the alpha phase for Ti64-Ti64 AW sample show a symmetric and smooth behavior throughout the weld region (see Figure 5.7). In Figure 5.8, a similar trend is observed within the beta phase except a discontinuity within approximately  $\pm 0.8$  mm distance from the weld center (i.e.,  $d_{\text{weld}} = 0$ ). This discontinuity is attributed to the fact that the second peak corresponding to the beta phase is missing during the peak fitting process. The absence of the second beta peak, which is well isolated from other alpha and beta peaks, could be the result of a lack of beta phase resulting from the welding process.

Figure 5.11(a) is a schematic showing the spatial position in which the micrographs are acquired on the Ti64-Ti64 AW sample. The region immediately adjacent to the weld displays a variable microstructure with increasing grain size and equiaxed structure as the distance from the weld region is increased along the 2 direction, as seen in Figure 5.11(b) and (c). The variable grain morphology present in Figure 5.11(c) is consistent with the steep gradient of the measured residual strain, in both alpha and beta phases, close to the weld interface. As summarized in Table 5.4, the fine basket-weave structures are observed in close proximity to the weld due to the rapid cooling after the LFW process. Further from the weld interface, 1.5 mm or more, only globular alpha grains are observed. Figure 5.11(d) and (e) show the microstructures at 1 and 4.5 mm above the weld interface, respectively. Similarly, Figure 5.11(f) and (g) show the microstructures at 1 and 4.5 mm below the weld region. It should be noted that the microstructure remains unchanged when comparing the micrographs from 1 and 4.5 mm away from the weld region (both above and below) explaining the symmetric behavior in the plots.

The residual strain measured in the beta phase is greater than that in the alpha phase as seen in Figure 5.7 and Figure 5.8, where the beta phase has peak strain measurements of 0.009 compared to the alpha phase maximum strain of 0.005 in  $\varepsilon_{11}$ . The higher value of residual strain in the beta phase could be attributed to the choice of the second beta peak during the peak fitting process. It can be shown that the stiffness of the beta phase along the (100) direction, associated with the second beta peak, is much lower than the stiffness of the alpha phase along the (102) direction,

associated with the fourth alpha peak. For representative values of the elastic constants in the alpha and beta phases, the reader is referred to [127], [211], [212]; the procedure to calculate direction dependent stiffness in cubic and hexagonal systems can be found in [213], [214]. Finally,  $\varepsilon_{11}$  is found to be greater than  $\varepsilon_{22}$ . This could be due to the fact that the specimen is oscillated along 1 direction during the welding process.

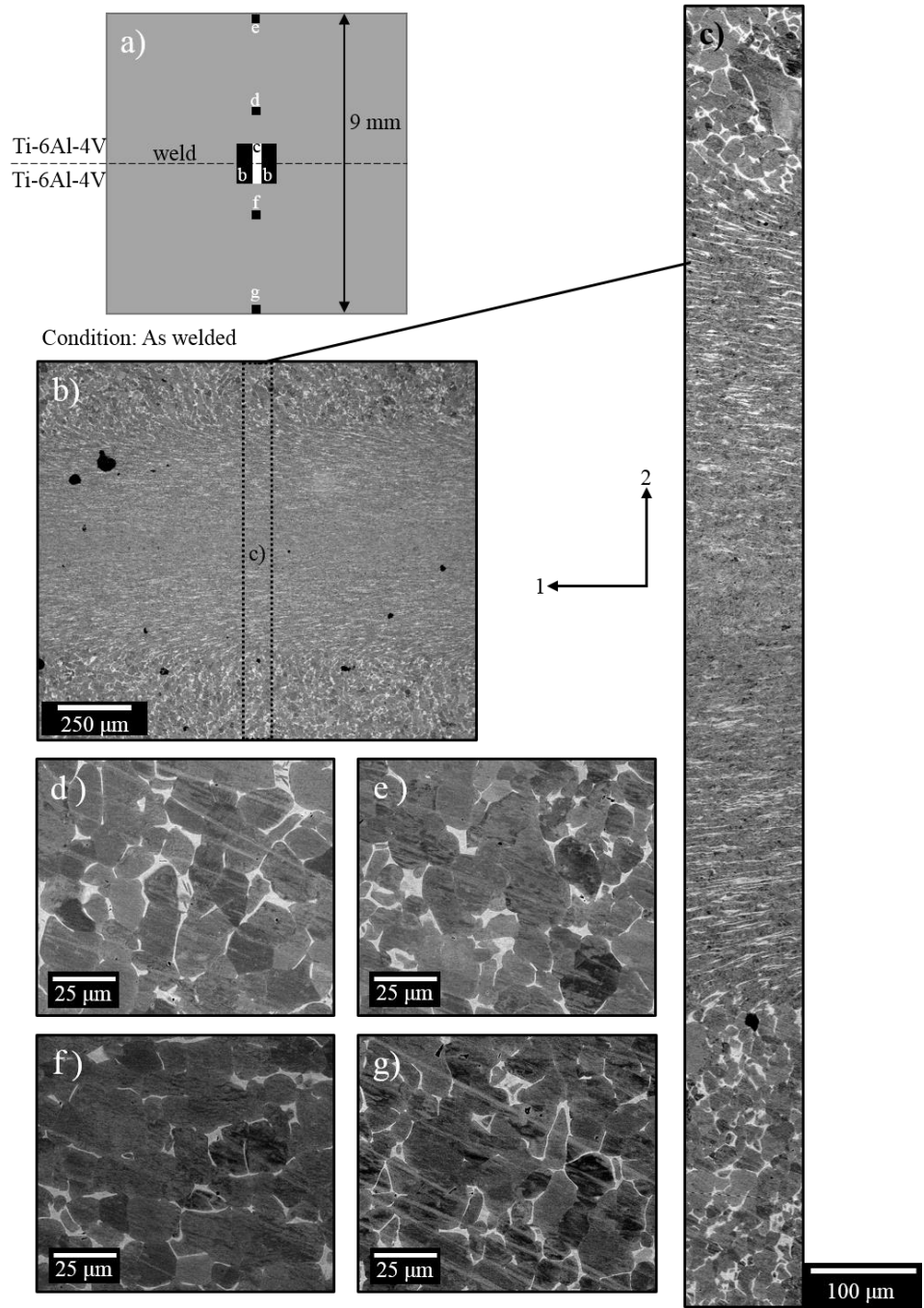


Figure 5.11. The Ti64-Ti64 sample in the as-welded condition, (a) a schematic representing the location of the following images, in relation to the weld area, (b) an overview of the weld area, (c) an enlarged region, 1.23 mm in height taken across the weld region, approximately 0.6 mm in each direction, (d) a field of view (FOV) 1.0 mm above the weld region, (e) a FOV 4.5 mm above the weld region, (f) a FOV 1 mm below the weld region, and (g) a FOV 4.5 mm below the weld region.

### ***Ti64-Ti64 LFW in the heat-treated condition***

Residual strain profiles in the alpha phase of Ti64-Ti64 HT sample, as seen in Figure 5.7, show a flat and smooth behavior throughout the weld area. A similar trend is observed in the beta phase (see Figure 5.8). Similar to the Ti64-Ti64 AW sample, a discontinuity is seen in the beta phase within approximately  $\pm 0.8$  mm distance from the weld interface. Figure 5.12(a) is a schematic showing the spatial position of the micrographs for the Ti64-Ti64 HT sample. The region immediately adjacent to the interface displays a variable microstructure with increasing grain size as distance is increased from the weld interface along the 2 direction, as seen in Figure 5.12(b) and (c) and as summarized in Table 5.5. In this case, the grains are fully recrystallized, even near the weld interface. This is supportive of the near-zero residual strain measured in both the alpha and beta phases.

Figure 5.12(d) and (e) show the microstructures at 1 and 4.5 mm above the weld interface, respectively. Similarly, Figure 5.12(f) and (g) show the microstructure at 1 and 4.5 mm below the weld interface, respectively. The microstructure remains unchanged when comparing the micrographs from 1 and 4.5 mm away from the weld interface (both above and below). Unlike the as-welded condition the heat-treated condition shows a very distinct weld interface, highlighted in Figure 5.12(h), where small grains have formed parallel to axis 1. Three forms of alpha phase are present in this condition, namely, globular, lamellar and basket-weave. Their size with respect to location from the weld interface are summarized in Table 5.5.

Table 5.4. Grain size measurements of different alpha grain structures in the Ti64-Ti64 AW sample. The thickness or width of the basket-weave and lamellar structures are reported and the average grain size of the globular alpha are reported using the line intercept method to measure grain size.

		<b>Ti64-Ti64 AW</b>				
		Distance from Weld	0 mm	1.5 mm	3.0 mm	4.5 mm
<b>Alpha grain size [<math>\mu\text{m}</math>]</b>	Basket-weave thickness		$0.376 \pm 0.09$	N/A	N/A	N/A
	Lamellar thickness		N/A	N/A	N/A	N/A
	Globular		N/A	$13.26 \pm 5.1$	$14.08 \pm 6.4$	$10.94 \pm 5.5$

Table 5.5. Grain size measurements of different alpha grain structures in the Ti64-Ti64 HT sample. The thickness or width of the basket-weave and lamellar structures are reported and the average grain size of the globular alpha are reported using the line intercept method to measure grain size.

		<b>Ti64-Ti64 HT</b>				
		Distance from Weld	0 mm	1.5 mm	3.0 mm	4.5 mm
<b>Alpha grain size [<math>\mu\text{m}</math>]</b>	Basket-weave thickness		N/A	$0.067 \pm 0.01$	$0.125 \pm 0.03$	$0.126 \pm 0.03$
	Lamellar thickness		$0.305 \pm 0.11$	N/A	N/A	N/A
	Globular		$1.65 \pm 0.80$	$9.62 \pm 5.5$	$8.90 \pm 4.5$	$11.06 \pm 5.2$

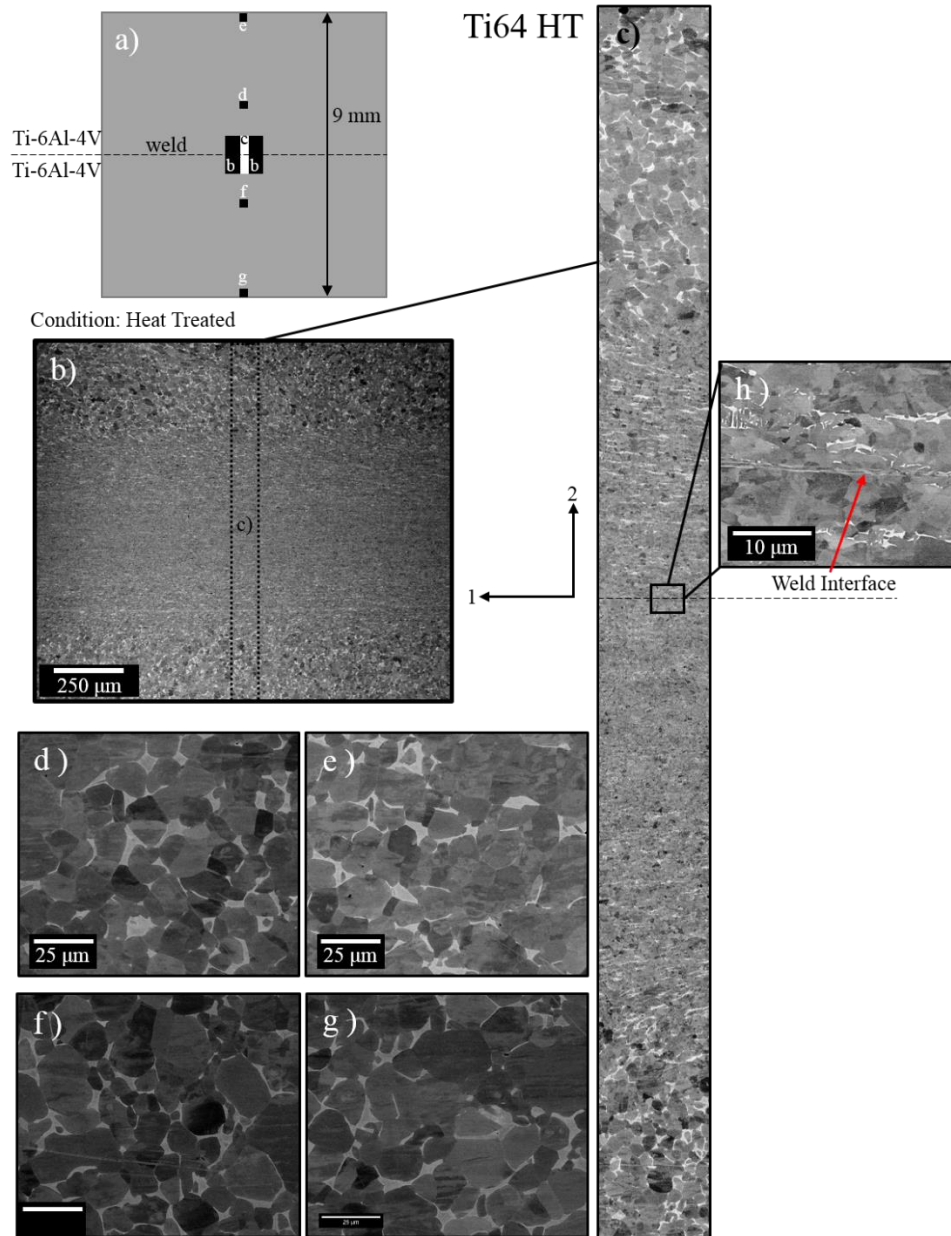


Figure 5.12. The Ti64-Ti64 sample in the heat-treated condition, (a) a schematic representing the location of the following images, in relation to the weld area, (b) an overview of the weld area, (c) an enlarged region, 1.23 mm in height taken across the weld region approximately 0.6 mm in each direction, (d) a FOV 1.0 mm above the weld region, (e) a FOV 4.5 mm above the weld region, (f) a FOV 1 mm below the weld region, (g) a FOV 4.5 mm below the weld region, and (h) the weld interface created at the joining point of the two materials.

### ***Ti64-Ti5553 LFW in the as-welded condition***

Residual strain profiles in the alpha phase of the Ti64-Ti5553 AW sample can be seen in Figure 5.9. The strain profiles have a symmetric behavior throughout the weld area. A similar trend is observed in the beta phase (see Figure 5.10). Strain profiles in both phases show jump discontinuities about 1 mm from both sides of the weld interface. Micrographs corresponding to this sample can be seen in Figure 5.13. Figure 5.13(a) displays a schematic representing the locations of the micrograph images on the sample. The jump discontinuities observed in strain measurements approximately 1 mm from the weld can be partly attributed to a change in microstructure at that point. Figure 5.13(d) shows an interface, on the Ti5553 side, that has formed where the microstructure abruptly changes. The top of this micrograph has even grey scale intensity but over this interface, as pointed out in Figure 5.13(d), a mix of dark and light areas in the BSE image are present. At these locations, there is a composition change, possibly responsible for the discontinuity in the data. At 4.5 mm away from the weld, the Ti5553 microstructure is more regular and indicative of the base material compared to the microstructure close to weld interface as seen in Figure 5.13(e). At the weld interface and on the Ti5553 side, no agglomerates of alpha phase are present in the BSE images. Similarly, the Ti64 side of the weld shows a discontinuity about 1 mm from the weld interface, this can be partly attributed to a transition from the presence of a fine basket-weave structure to a larger lamellar configuration of the alpha phase, in addition to the large globular grains as shown in Figure 5.13(f). These smaller basket-weave colonies that are present close to the weld transform completely to the larger lamellar configuration with increased distance from the weld, as shown in Figure 5.13(g), located 4.5 mm from the weld interface. The weld interface, Figure 5.13(h), shows a fine basket-weave structure on the Ti64 side meeting the larger beta grain structure in the Ti5553. The residual strain in the beta phase is approximately four times than that in the alpha phase in the proximity of the weld interface, which is attributed to the choice of the second beta peak during peak fitting. This sample displays a tri-modal size distribution of alpha grains at distances greater than 1.5 mm from the weld interface in the Ti64 material, with only the fine basket-weave structure present at the weld interface, due to the rapid cooling after the weld process. A tri-modal size distribution of alpha grains is observed in the Ti64 side of the LFW sample, in which the alpha grains sizes are summarized in Table 5.6.

Table 5.6. Grain size measurements of different alpha grain structures from the Ti64 side of the LFW Ti64-Ti5553 AW sample. The thickness or width of the basket-weave and lamellar structures are reported and the average grain size of the globular alpha are reported using the line intercept method to measure grain size.

<b>Ti64 grain size from LFW Ti64-Ti5553 AW</b>					
	Distance from Weld	0 mm	1.5 mm	3.0 mm	4.5 mm
<b>Alpha grain size [<math>\mu\text{m}</math>]</b>	Basket-weave thickness	$0.193 \pm 0.08$	$0.223 \pm 0.11$	$0.229 \pm 0.05$	$0.288 \pm 0.09$
	Lamellar thickness	N/A	$1.02 \pm 0.40$	$0.833 \pm 0.35$	$1.03 \pm 0.45$
	Globular	N/A	$7.53 \pm 3.2$	$8.27 \pm 4.2$	$7.06 \pm 3.0$

Table 5.7. Grain size measurements of different alpha grain structures from the Ti64 in the LFW Ti64-Ti5553 HT sample. The thickness or width of the basket-weave and lamellar structures are reported and the average grain size of the globular alpha are reported using the line intercept method to measure grain size.

<b>Ti64 grain size from LFW Ti64-Ti5553 HT</b>					
	Distance from Weld	0 mm	1.5 mm	3.0 mm	4.5 mm
<b>Alpha grain size [<math>\mu\text{m}</math>]</b>	Basket-weave thickness	$0.327 \pm 0.10$	$0.353 \pm 0.14$	$0.396 \pm 0.10$	$0.207 \pm 0.09$
	Lamellar thickness	N/A	$1.29 \pm 0.41$	$1.24 \pm 0.49$	$1.29 \pm 0.57$
	Globular	N/A	$10.99 \pm 4.3$	$8.63 \pm 3.8$	$12.40 \pm 6.5$

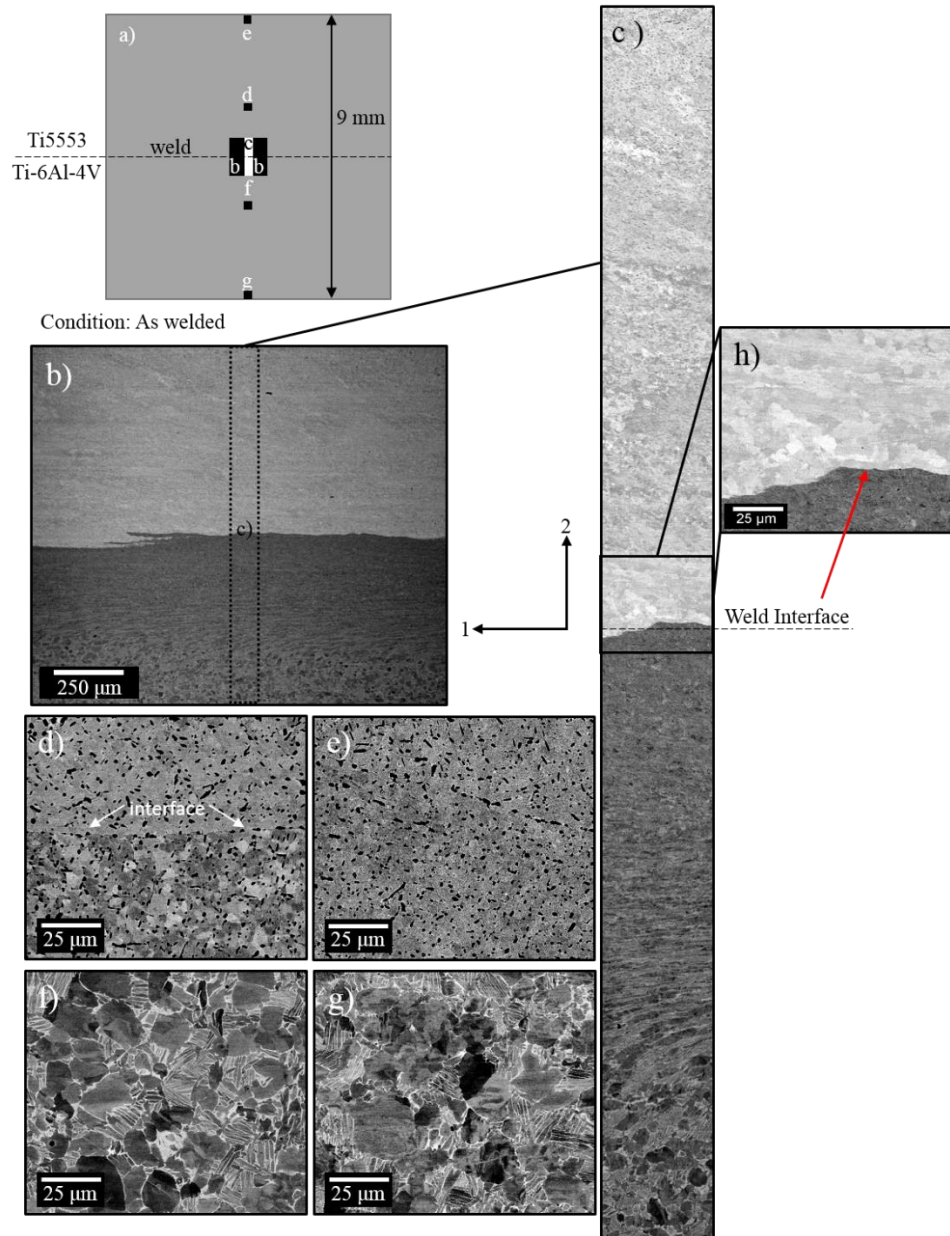


Figure 5.13. The Ti64-Ti5553 sample in the as-welded condition, (a) a schematic representing the location of the following images, in relation to the weld area, (b) an overview of the weld area, (c) an enlarged region, 1.23 mm in height taken across the weld region, approximately 0.6 mm in each direction, (d) a FOV 1.0 mm above the weld region, (e) a FOV 4.5 mm above the weld region, (f) a FOV 1 mm below the weld region, (g) A FOV 4.5 mm below the weld region, and (h) the weld interface created at the joining point of the two materials.

### ***Ti64-Ti5553 LFW in the heat-treated condition***

Residual strain profiles in the alpha phase of the Ti64-Ti5553 HT sample can be seen in Figure 5.9. The strain profiles show a flat and smooth behavior throughout the measured weld area. A similar trend is observed in the beta phase (see Figure 5.10) except for a jump discontinuity in close proximity to the weld interface. Figure 5.14(a) is a schematic showing the location of the micrographs for the Ti64-Ti5553 sample in the heat-treated condition. The weld region displays a variable microstructure with changing grain morphologies and size as distance is increased from the weld interface, along the 2 direction, as seen in Figure 5.14(b), with a magnified excerpt of this region seen in Figure 5.14(c). The grains are fully recrystallized, even in close proximity to the weld interface. This is consistent with the near-zero residual strain measured for  $\epsilon_{11}$  and  $\epsilon_{22}$ . The Ti5553 microstructure can be seen in Figure 5.14(d), 1 mm and Figure 5.14(e), 4.5 mm from the weld interface. One notable difference between these two areas is that the alpha phase at a distance of 4.5 mm from the weld interface, Figure 5.14(e), are more interconnected, forming elongated structures instead of the equiaxed morphologies as seen more prominently 1 mm from the weld in Figure 5.14(d). On the Ti64 side of the weld, a similar trend in microstructure is observed at 1 mm, Figure 5.14(f) and 4.5 mm, Figure 5.14(g). In this case, the fraction of the alpha lamellar structures is decreasing with increased distance from the weld interface. Lastly, the weld interface, Figure 5.14(h), shows the fine basket-weave structure of the Ti64 intermingled with the alpha-beta structure of the Ti5553. A tri-modal size distribution of alpha grains is observed in the Ti64 side of the weld, sizes are summarized in Table 5.7.

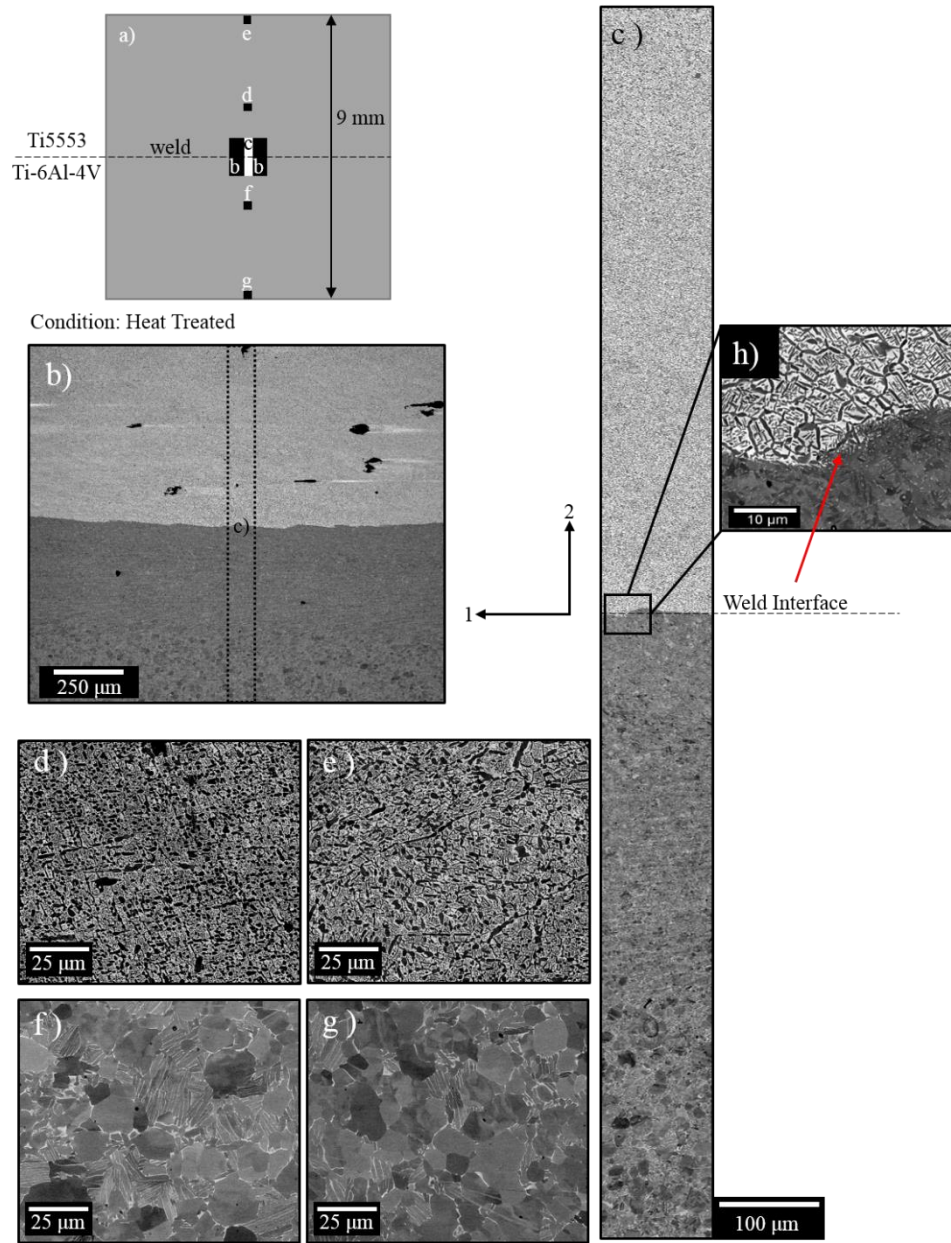


Figure 5.14. The Ti64-Ti5553 sample in the heat-treated condition, (a) a schematic representing the location of the following images, in relation to the weld area, (b) an overview of the weld area, (c) an enlarged region, 1.23 mm in height taken across the weld region, approximately 0.6 mm in each direction, (d) a FOV 1.0 mm above the weld region, (e) a FOV 4.5 mm above the weld region, (f) a FOV 1 mm below the weld region, (g) a FOV 4.5 mm below the weld region, and (h) the weld interface created at the joining point of the two materials.

### 5.1.5 Summary

In the present study, the residual strain distributions across the LFW joints of similar and dissimilar Ti alloys have been studied using energy dispersive X-ray diffraction (EDD) method considering both the alpha and beta phases and obtaining the five components (three axial and two shear) of the residual strain tensor. The key findings are summarized below.

- In-plane axial components of the residual strain tensor ( $\epsilon_{11}, \epsilon_{22}$ ) show a symmetric behavior across the weld center in LFW joints of both similar and dissimilar Ti alloys. The post-weld heat treatment significantly reduced the residual strain in both samples.
- Strain distributions have been separately studied in the alpha and beta phases. The residual strain in the beta phase has been found to be significantly higher than that in the alpha phase, which can be attributed to differences in the stress state between the two phases, elastic stress anisotropy, morphologies of the two phases.
- Two jump discontinuities have been observed approximately at  $\pm 1$  mm from the weld center in the case of the LFW joint of dissimilar Ti alloys. This jump behavior has been partly explained via abrupt changes in the microstructural features at the respective locations. Such jumps in the HT sample also indicate different strain free lattice parameter in the weld region as opposed to the parent materials, which is not accounted for in the present study. On the contrary, no such observation is made for the LFW joint of similar Ti alloys.
- A tri-modal distribution of the alpha phase grains is found in all specimens except the Ti64-Ti64 AW sample. Both AW conditions contained regions close to the weld that lacked a well-defined microstructure, upon heat treatment full recrystallization is observed in both the Ti64-Ti64 and Ti64-Ti5553 LFW samples. The Ti64-Ti64 sample in the HT condition contained finer grain sizes and lamellar alpha grains not present in the AW condition. While, the Ti64-Ti5553 sample in the AW condition contained finer grains than that measured in the HT condition. All three configurations of alpha phase are present in both the AW and HT conditions of the dissimilar LFW samples.

## 5.2 Crack initiation and heterogeneous deformation of Ti-6Al-4V during high cycle fatigue at high R ratios

HCF analysis is performed on two Ti-6Al-4V specimens with equiaxed alpha microstructure at a high R ratio ( $R = 0.6$ ) and  $\sigma_{\max} = 900 \text{ MPa}^{****}$ . In one of the specimens two different MTRs are identified. HR-DIC is performed within a scanning electron microscope to study grain level heterogeneous strain evolution in the MTRs. In the other specimen, DIC within an optical microscope is performed to monitor crack initiation and study the strain evolution within a larger area of interest during HCF loading. Subsequently, CPFEE simulations are carried out to systematically investigate micromechanical aspects of crack initiation at high R ratios. Finally, strain heterogeneity associated with each of the three regions (two MTRs in one specimen and microstructure around the crack initiation site in the other specimen) is systematically studied at the continuum and slip system levels as a function of stress ratio using the same CP model. With this, the current section is structured as follows: materials and experimental methods are presented in Section 5.2.1; CPFEE modeling is detailed in Section 5.2.2; DIC results are reported in Section 5.2.3; CPFEE simulation results are presented and discussed in relation to the experimental observations in Section 5.2.4.

### 5.2.1 Material and experimental methods

Strain localization and crack initiation in HCF are experimentally studied using DIC during interrupted loading in two different Ti-6Al-4V specimens having equiaxed alpha grains. The material is obtained in the mill-annealed condition as per AMS-4911 for Ti-6Al-4V plate and followed by an annealing/aging heat treatment at  $704.4^{\circ}\text{C}$  for 2 h and air cooled to obtain an equiaxed alpha structure with beta present at the alpha triple points. The Ti-6Al-4V is machined into dog-bone specimens of 48 mm in overall length and 10 mm gauge length. The gauge section is 3 mm wide and 1.25 mm thick. The sides and edges of the specimens are polished using a Dremel rotary tool.

The specimens are polished using 1200 and 2500 grit sandpaper on both the front and back faces for approximately 10 minutes. The back faces of the specimens are subsequently polished using a  $0.05 \mu\text{m}$  colloidal silica solution for 30 minutes. The front faces of the specimens are

---

\*\*\*\* 0.2% offset yield strength was found to be 920 MPa.

polished for 30 minutes using a solution made of one-part hydrogen peroxide, 30%, and four parts 0.05  $\mu\text{m}$  colloidal silica solution. Use of this solution results in improved EBSD results for Ti-6Al-4V. For the present work, EBSD characterization is performed with a step size of 0.6  $\mu\text{m}$ .

In one of the specimens, two different MTRs, 70  $\mu\text{m} \times 70 \mu\text{m}$  each and separated by 2 mm, are identified as shown in Figure 5.15. In the left spot in Figure 5.15, the basal planes of most of the grains are almost perpendicular to the loading direction ( $x$ -axis), whereas in the right spot the basal planes are nearly parallel to the loading direction. The former microstructure is referred to as the perpendicular MTR and the latter as the parallel MTR throughout the Section 5.2. Fiducial markings are placed at four corners of each MTR using a LECO microhardness tester LM247AT. HR-DIC within a scanning electron microscope is performed to study grain level strain localization in these two areas of interest (AOIs).

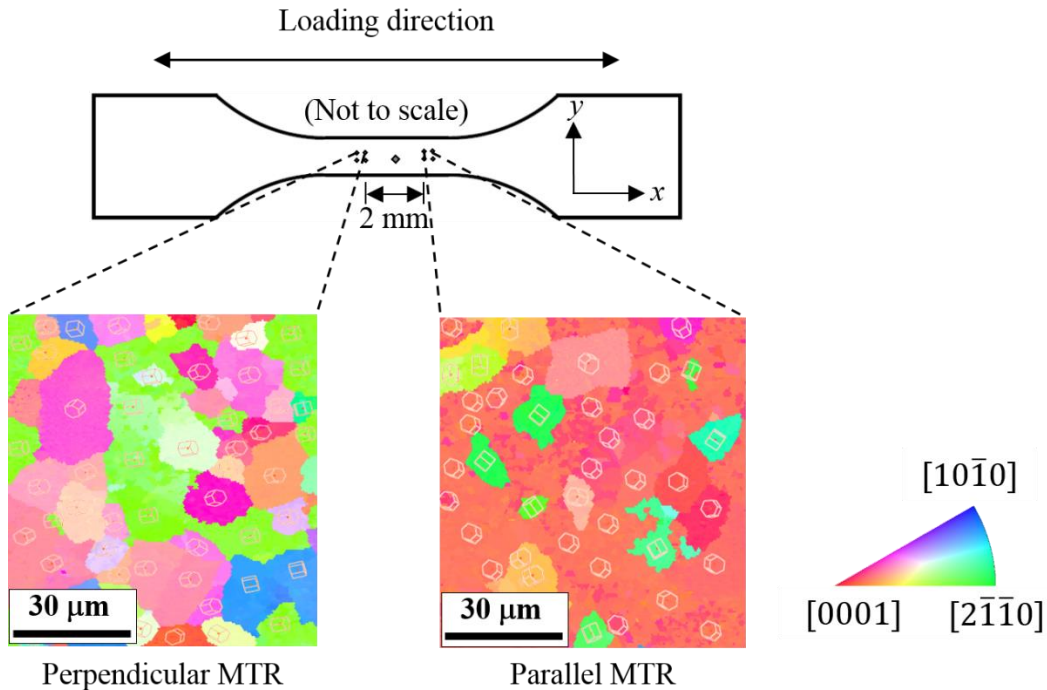


Figure 5.15. Schematic of the dog-bone specimen with two areas of interest (AOI). Both AOIs are characterized using electron backscattered diffraction before HCF loading and displayed different micro-textured regions (MTRs). In the perpendicular MTR, the basal planes of most of the grains are almost perpendicular to the loading direction ( $x$ -axis), whereas in the parallel MTR, the basal planes are nearly parallel to the loading direction. The inverse pole figures of the MTRs are obtained considering  $z$ -axis as reference.

In the other specimen, the gauge section is reduced to 1.5 mm by 1 mm, in order to facilitate crack initiation within the gauge section as shown in Figure 5.16(a). DIC via optical microscopy across the entire gauge section (1.5 mm  $\times$  1 mm) is performed to study crack initiation and heterogeneous strain evolution. Fiducial markings are placed in the 1.5 mm  $\times$  1 mm AOI in a 0.5 mm  $\times$  1 mm sequence, dividing the overall AOI into thirds as shown in Figure 5.16(b), using a LECO microhardness tester LM247AT.

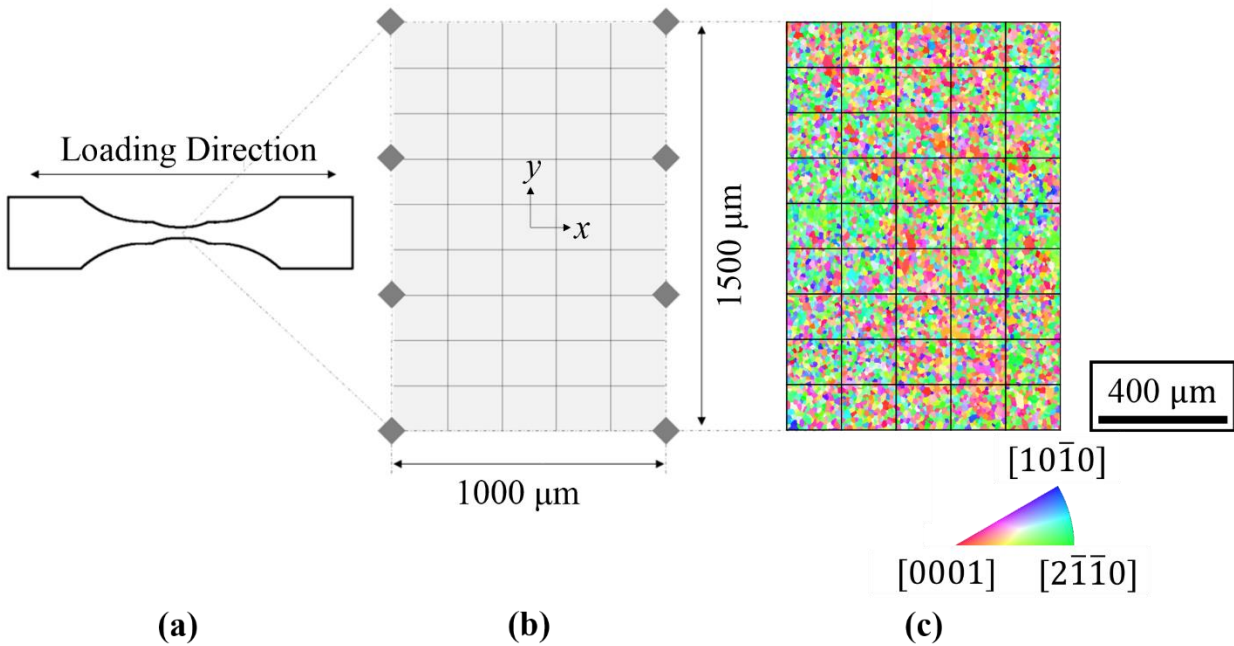


Figure 5.16. (a) Slightly modified dog-bone specimen and the area of interest for the optical microscopy digital image correlation. (b) The fiducial markings divide the entire AOI into thirds. (c) The inverse pole figure of the AOI.

The front face of each specimen is speckled with a Ti nano-powder following the methodology discussed by Tracy et al. [215]. First, 30 mg of Ti nano-powder (60 nm), 220 mg of bicine, and 10 mL of distilled water are mixed together. The mixture is then placed into a roll mill for 24 h to produce a homogeneous solution. The addition of G5 SiC bearing balls assists in breaking up the Ti agglomerates within the solution. Without the addition of G5 SiC bearing balls, the applied speckle pattern would have too many large Ti powder agglomerates resulting in inaccurate DIC strain maps. The solution is allowed to rest for 2 h so that heavier masses could

sink to the bottom. The solution is then applied to the surface of the AOIs using a syringe. After the solution dried on the surface of the AOIs, the bicine is burned off using a hot plate set to 300°C for 5 minutes. The application process is repeated twice to ensure the Ti speckling is sufficiently dense for the desired DIC resolution. The specimens are then sonicated in 99% isopropyl alcohol for one minute to remove any particles that are not rigidly attached to the surface of the specimen.

For the HR-DIC, reference images for the MTRs are taken at 4000x magnification within a scanning electron microscope. For the optical microscopy DIC, 45 reference images are taken in a  $9 \times 5$  grid representing the AOI (as per Figure 5.16(b)) at 50x magnification. Reference images are subsequently used to conduct DIC.

Both specimens are subjected to cyclic loading at  $\sigma_{\min} = 540$  MPa,  $\sigma_{\max} = 900$  MPa and  $R = \frac{\sigma_{\min}}{\sigma_{\max}} = 0.6$ . During interrupted HCF testing, the specimens are removed from the load frame and images are taken at aforementioned magnifications to obtain strain field maps using VIC 2D software. In particular, for the  $1.5 \text{ mm} \times 1 \text{ mm}$  AOI, the strain field maps are first obtained for all 45 zones. Subsequently, the strain field maps are stitched together using the Stream Motion commercial software which utilizes a Gaussian method of interpolation between overlapping images for stitching. Further, local spatial distortions resulting from capturing images within an electromagnetic field present within a scanning electron microscope leads to inaccuracies in the DIC analysis. To correct for this, a detailed distortion correction protocol based on a certified reference grid is applied and simultaneously ensured that ex-situ images are captured at the same magnification (details are presented in [216]). Finally, grain boundaries are overlaid on top of the DIC strain maps for each microstructure using fiducial marking as reference.

## 5.2.2 Crystal plasticity finite element simulation framework

### *Kinematics and kinetics*

The deformation gradient ( $\mathbf{F}$ ) at a material point during an elasto-plastic deformation of a solid body can be decomposed into elastic ( $\mathbf{F}^e$ ) and plastic ( $\mathbf{F}^p$ ) parts as follows:

$$\mathbf{F} = \mathbf{F}^e \cdot \mathbf{F}^p \quad (5.10)$$

A CP model starts with the assumption that the plastic part of the velocity gradient ( $\mathbf{L}^p$ ) at a material point can be written as a sum of contributions from all active slip systems as [156]

$$\mathbf{L}^{\mathbf{P}} = \sum_{k=1}^{N_{SS}} \dot{\gamma}^k \mathbf{s}^k \otimes \mathbf{n}^k \quad (5.11)$$

where  $\dot{\gamma}^k$  is the shear strain rate,  $\mathbf{s}^k$  is the slip direction, and  $\mathbf{n}^k$  is the slip plane normal associated with the slip system  $k$ ;  $N_{SS}$  is the number of active slip systems;  $\mathbf{L}^{\mathbf{P}}$  is related to  $\mathbf{F}^{\mathbf{P}}$  via

$$\mathbf{L}^{\mathbf{P}} = \dot{\mathbf{F}}^{\mathbf{P}} \cdot (\mathbf{F}^{\mathbf{P}})^{-1} \quad (5.12)$$

The shear strain rate  $\dot{\gamma}^k$  on the slip system  $k$  is related to the resolved shear stress  $\tau^k$  on the same slip system via a flow-rule. For the present work, the flow-rule is adopted from [123]

$$\dot{\gamma}^k = \dot{\gamma}_0 \left\langle \frac{|\tau^k - \chi^k| - \kappa^k}{D^k} \right\rangle^n \text{sgn}(\tau^k - \chi^k) \quad (5.13)$$

where  $\chi^k$ ,  $\kappa^k$ , and  $D^k$  are the backstress, threshold stress, and drag stress associated with the slip system  $k$ , respectively;  $\dot{\gamma}_0$  is the reference shearing rate;  $n$  is the inverse strain-rate sensitivity exponent;  $\langle x \rangle = x$  if  $x \geq 0$ ,  $\langle x \rangle = 0$  otherwise. The backstress evolves according to the Armstrong-Frederick relation given by

$$\dot{\chi}^k = A\dot{\gamma}^k - A_d\chi^k|\dot{\gamma}^k| \quad (5.14)$$

where  $A$  and  $A_d$  are constants associated with direct hardening and dynamic recovery, respectively. The threshold stress is given by [124]

$$\kappa^k = \frac{\kappa_y}{\sqrt{d^k}} + \kappa_s^k \quad (5.15)$$

where the first term incorporates hardening due to size effect via a Hall-Petch type relation and the second term evolves as [124]

$$\dot{\kappa}_s^k = -\lambda\kappa_s^k|\dot{\gamma}^k| \quad (5.16)$$

where  $\lambda$  is a constant. In Eq. (5.15),  $\kappa_y$  is the Hall-Petch slope and  $d^k$  is the characteristic microstructural dimension representing the free slip length. In the present work,  $d^k$  is set to the equivalent grain diameter. It is to be noted that Eq. (5.16) would capture a softening behavior for  $\lambda > 0$  and a hardening behavior for  $\lambda < 0$ . The drag stress  $D^k$  does not evolve with time and is consistent with past work [124]

$$D^k = \tau_{\text{CRSS}}^k - \kappa^k(0) = \tau_{\text{CRSS}}^k - \frac{\kappa_y}{\sqrt{d^k}} - \kappa_s^k(0) \quad (5.17)$$

where  $\tau_{\text{CRSS}}^k$  is the critical resolved shear stress for the slip system  $k$ ;  $\kappa^k(0)$  and  $\kappa_s^k(0)$  are the initial values of  $\kappa^k$  and  $\kappa_s^k$ , respectively.

Equations (5.10)-(5.17) are implemented in ABAQUS UMAT using a semi-implicit integration scheme proposed by McGinty [191]. Detailed derivations of the discretized versions of the differential equations and expression for the Jacobian are provided by McGinty [191] and Przybyla [217].

***Discretized polycrystalline microstructures and crystal plasticity model parameters***

For CPFEM simulations, three discretized polycrystalline microstructures are created corresponding to the random-textured area of interest (as per Figure 5.16) and perpendicular and parallel MTRs (as per Figure 5.15). A portion of the region of interest (middle third) of the specimen in Figure 5.16(c), representing a random texture (as shown in Figure 5.17(b)), is chosen to create the discretized model as shown in Figure 5.17(a). The discretized models for the MTRs are shown in Figure 5.18.

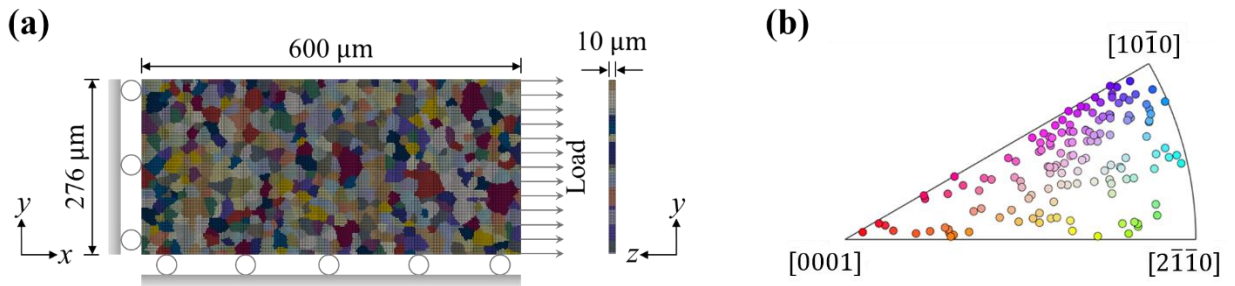


Figure 5.17. (a) Discretized microstructure corresponding to a portion of the middle third microstructure, shown in Figure 5.16(c). (b) The orientation of the grains within the microstructure with respect to the loading direction  $x$ .

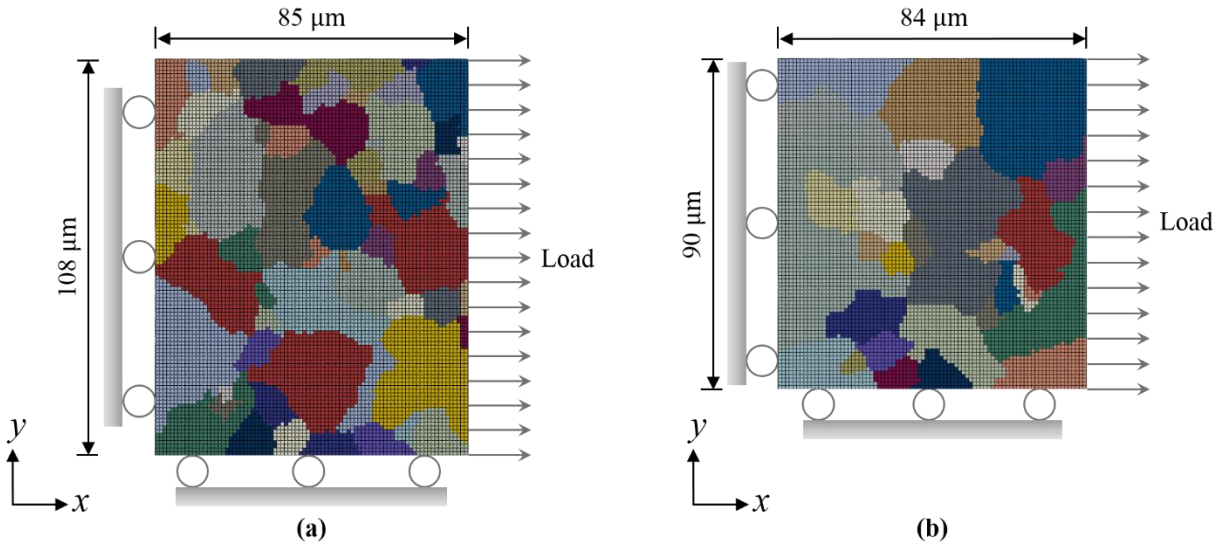


Figure 5.18. Discretized microstructures corresponding to the (a) perpendicular and (b) parallel MTRs as shown in Figure 5.15.

For each microstructure, the orientation of each grain is obtained from the EBSD characterization as described in Section 5.2.1. Since sub-surface grain morphology and orientation are not available for the present study, each grain is assumed to be extruded along the  $z$ -direction resulting in a 3D columnar microstructure. Subsequently, the microstructure is discretized using structured ‘C3D8’ elements, also known as eight-node brick or hexahedron elements. DREAM.3D software is used to obtain the final discretized microstructures starting from a 2D EBSD scan [144]. The thickness (dimension along the  $z$ -direction) of the microstructures is restricted to  $10\ \mu\text{m}$  and the number of elements along the same direction is set to five<sup>†††</sup>. The purpose behind the choice of five elements along the  $z$ -direction is to reduce the computation cost for the model shown in Figure 5.17(a), and the number is kept the same for the models in Figure 5.18 for consistency.

The discretized model, as shown in Figure 5.17(a), is composed of 512 randomly oriented grains, as evident from Figure 5.17(b), and chosen for the calibration of the CP model parameters. The Ti-6Al-4V material in this study is primarily composed of large equiaxed alpha grains, hence only the HCP alpha phase is modeled in the present work. Further, basal  $\{0001\}$ , prismatic  $\{10\bar{1}0\}$ , first order pyramidal  $\{10\bar{1}1\}$  slip planes with  $\langle a \rangle = \langle 1\bar{2}10 \rangle$  type slip directions and first order

<sup>†††</sup> The discretized models as shown in Figure 5.17(a), Figure 5.18(a) and (b) are composed of 207000, 45900 and 37800 hexahedron elements, respectively.

pyramidal  $\{10\bar{1}1\}$  slip planes with  $\langle c + a \rangle = \langle 11\bar{2}3 \rangle$  type slip directions could accommodate plastic deformation. Elastic constants for Ti-6Al-4V are taken from [211]. This set of constants is found to capture the elastic response of the material and is consistent with the modulus of the uniaxial tension experiments in this study. The remaining CP model parameters are adjusted using the GA-based framework described in Section 3.1.1. During fitting, bounds on the critical resolved shear stress of the prismatic slip system and the relative slip resistance of the basal and pyramidal slip systems are imposed based on [123], [124], [218], [219]. The bounds on the remaining parameters are chosen based on earlier works in Refs. [123], [124], [220]. During the finite element simulation, the normal displacements at the left ( $x = 0$ ), bottom ( $y = 0$ ) and back ( $z = 0$ ) surfaces of the model are restricted, and the load is applied on the right surface. Experimental and simulated macroscopic stress-strain curves are shown in Figure 5.19(a); elastic constants along with calibrated CP model parameters are reported in Table 5.8. Using the fitted parameters, the cyclic and monotonic responses (homogenized macroscopic) of the model are shown in Figure 5.19(b). The cyclic simulation is performed at the same stress level as the experiment.

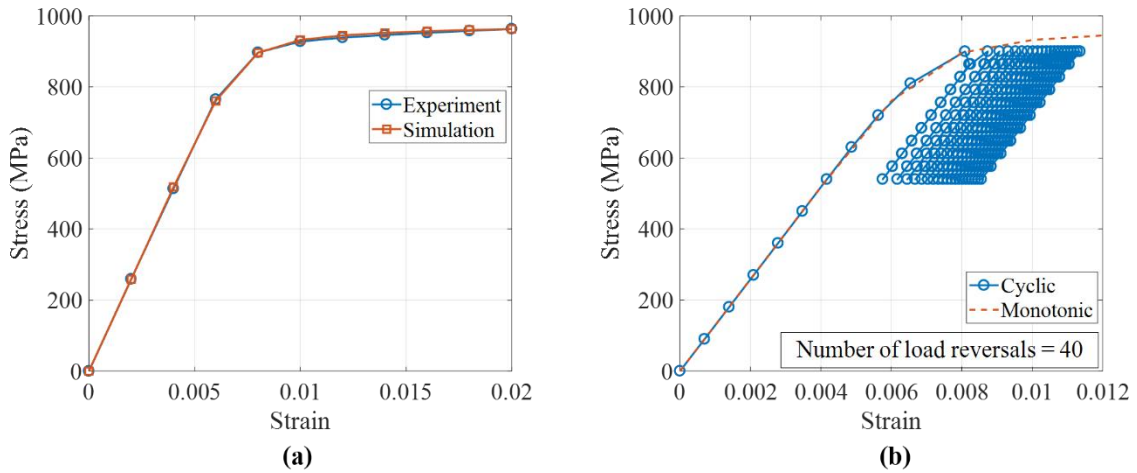


Figure 5.19. (a) Macroscopic stress-strain response during a uniaxial tension test, (b) cyclic and monotonic response of the calibrated model. The cyclic loading is performed at the same level as that of the experiment.

Table 5.8. Elastic constants and crystal plasticity model parameter details.

<b>Elastic constants (GPa) [211]</b>					
$C_{11}$	141	$C_{22}$	141	$C_{33}$	163
$C_{12}$	76.9	$C_{13}$	57.9	$C_{23}$	57.9
$C_{44}$	48.7	$C_{55}$	48.7	$C_{66}$	102.6
<b>Fitted crystal plasticity model parameters</b>					
$\tau_{\text{CRSS}}^{\langle 1\bar{2}10\rangle\{10\bar{1}0\}}$	365 MPa	$\frac{\tau_{\text{CRSS}}^{\langle 1\bar{2}10\rangle(0001)}}{\tau_{\text{CRSS}}^{\langle 1\bar{2}10\rangle\{10\bar{1}0\}}}$	1.1232	$\frac{\tau_{\text{CRSS}}^{\langle 1\bar{2}10\rangle\{10\bar{1}1\}}}{\tau_{\text{CRSS}}^{\langle 1\bar{2}10\rangle\{10\bar{1}0\}}}$	1.2238
$\frac{\tau_{\text{CRSS}}^{\langle 11\bar{2}3\rangle\{10\bar{1}1\}}}{\tau_{\text{CRSS}}^{\langle 1\bar{2}10\rangle\{10\bar{1}0\}}}$	1.1640	$\chi_0^k$	0	$\kappa_s^k(0)$	137 MPa
n	25	A	29404 MPa	$A_d$	3097
$\lambda$	-4	$\kappa_y$	14 MPa · mm <sup>0.5</sup>	$\dot{\gamma}_0$	0.001 s <sup>-1</sup>

### 5.2.3 DIC results

#### *Crack initiation*

After 1, 10, 100, 1000 and 10000 cycles, images for each of the 45 sub-regions (as per Figure 5.16(b)) are obtained from the optical microscope and DIC is conducted as described in Section 5.2.1. Resulting strain plots for all 45 sub-regions are stitched together to obtain the complete strain field map for the entire AOI. Figure 5.20 shows a contour plot for strain along the loading direction after 10000 cycles across the entire 1.5 mm × 1 mm AOI. It is to be noted from Figure 5.20 that the axial strain along loading direction appears to be localized in 45° bands relative to the tensile loading direction ( $x$ -axis). No cracks are observed within the AOI at 10000 cycles.

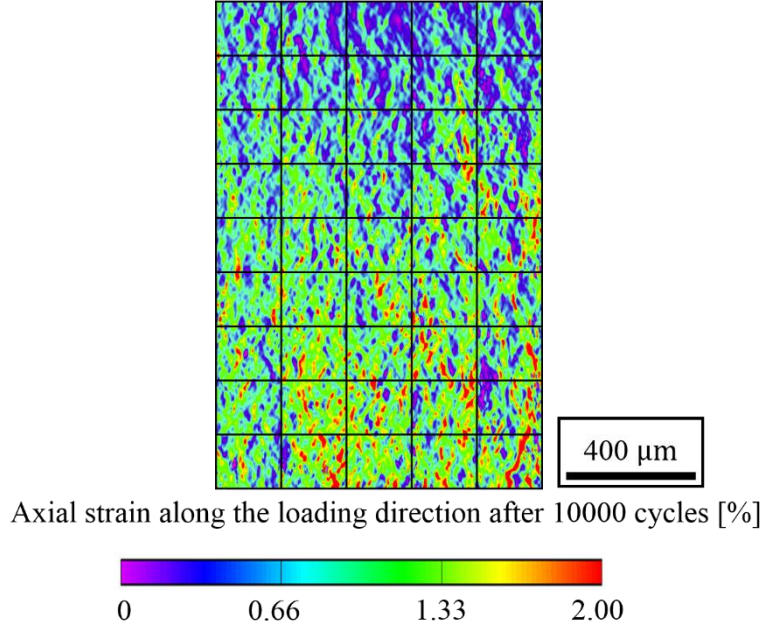


Figure 5.20. Strain along loading direction after 10000 cycles from optical microscopy DIC.

At 45000 cycles, the first crack is observed within the AOI. A scanning electron microscope image around the crack is shown in Figure 5.21(a). Several slip bands are observed surrounding the crack (see slip bands in Figure 5.21(a) indicated by yellow arrows). The maximum in-plane shear strain ( $\epsilon_{\max}$ ) is computed from the DIC strain results [221] at 10000 cycles using

$$\epsilon_{\max} = \sqrt{\left(\frac{\epsilon_{xx} - \epsilon_{yy}}{2}\right)^2 + \epsilon_{xy}^2} \quad (5.18)$$

and overlaid on top of the scanning electron microscope image around the crack at 45000 cycles in Figure 5.21(b). The contour plot of maximum in-plane shear strain indicates highly localized deformation around the crack initiation site confirming slip band activity as observed in Figure 5.21(a). Moreover, like the axial strain along the loading direction, the maximum in-plane shear strain is also observed to be localized in  $45^\circ$  bands relative to the tensile loading direction ( $x$ -axis) as seen in Figure 5.21(b). The evolution of the maximum in-plane shear strain in the region surrounding the crack is shown in Figure 5.22. Significant evolution of the strain localization is not observed at the early phases of HCF loading as evident from strain plots after 10 (Figure 5.22(a)) and 100 (Figure 5.22(b)) cycles. However, with increasing number of cycles, more localized hot spots are observed (see strain plots after 1000 (Figure 5.22(c)) and 10000 (Figure 5.22(d)) cycles).

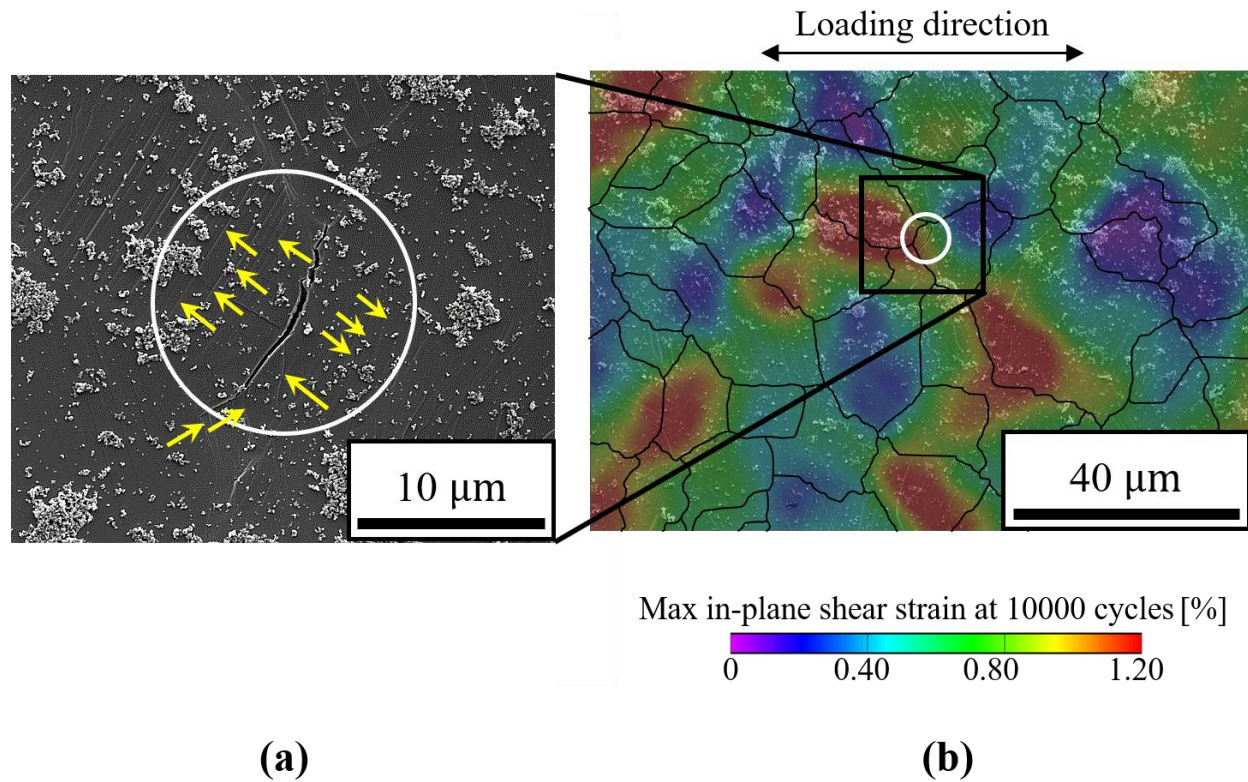


Figure 5.21. (a) Scanning electron microscope image around the crack after 45000 cycles. Several slip bands are observed around the crack. Slip bands are indicated by yellow arrows. (b) Maximum in-plane shear strain after 10000 cycles. The strain map is obtained from optical microscopy DIC.

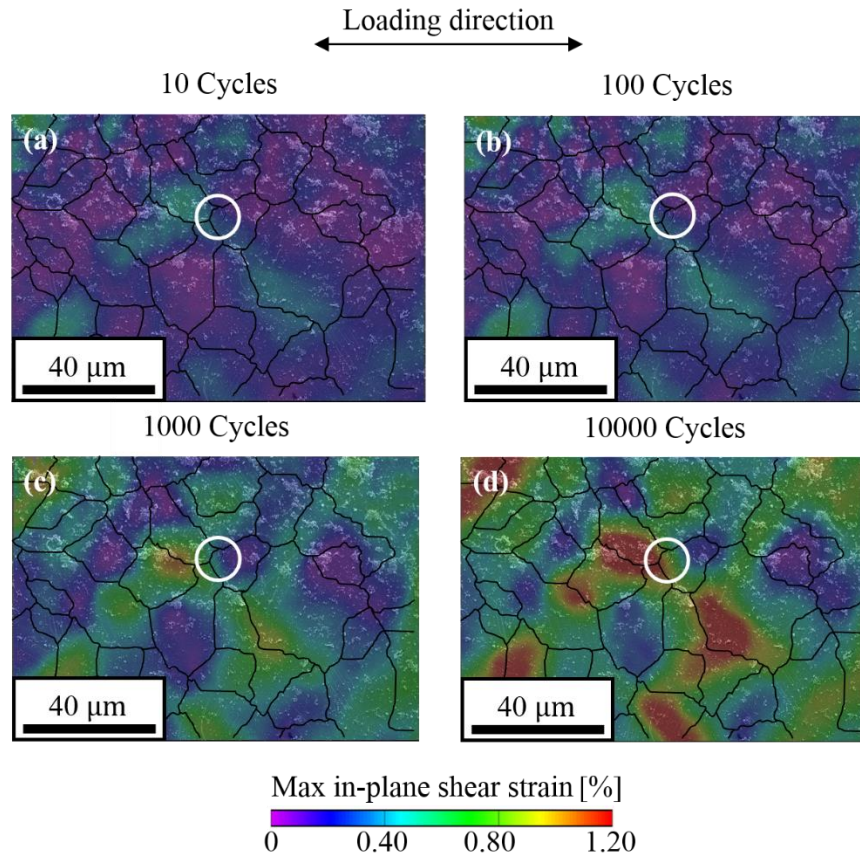


Figure 5.22. In-plane shear strain evolution around the crack initiation site during high R ratio HCF loading. The location of crack initiation is within the white circle. DIC strain maps are obtained via optical microscopy and overlaid on top of the scanning electron microscope image at 45000 cycles.

The experiment showed that crack initiation for high R ratio fatigue cycling tends towards regions of high localized principal shear strain, concentrated in 45° bands, relative to the tensile loading direction (see Figure 5.21(b) and Figure 5.22). However, multiple hot spots are observed in Figure 5.21(b) indicating equally likely locations for crack initiation based on the relatively low resolution of the optical DIC performed here. In Section 5.2.4, further micromechanical aspects of crack initiation at high R ratios are investigated using CPFEM simulations.

### ***Strain accumulation in macrozones***

As mentioned in Section 5.2.1, HR-DIC is performed within the MTRs to study systematic differences in grain level strain localization and evolution of the same under high R ratio ( $R=0.6$ )

HCF loading. The reader is reminded that the two MTRs, under present consideration, lie on the same sample and therefore experience identical externally applied loading. The axial strain along the loading direction within the MTRs after the first cycle is shown in Figure 5.23. In Figure 5.23, strain localization on the order of 1.5% is observed on distinctive slip lines in both MTRs. It is to be noted that the slip lines in the perpendicular MTR are oriented differently than that in the parallel MTR with respect to the loading direction. Such a difference in relative orientation of the slip lines is primarily because of the different textures that are observed within the AOIs. The evolution of the slip lines during HCF loading is tracked via interrupted HR-DIC after 1, 10, 100 and 1000 cycles and the resulting contour plots for the strain along the loading direction are shown in Figure 5.24. It is evident from Figure 5.24 that with the increase in number of cycles the slip lines appear thicker and spread into multiple grains resulting in strain localization of the order of 4.5%. After 1000 cycles, high strained spots at the parallel MTR are found to be mostly scattered across the entire AOI, whereas a relatively larger region of high strain is observed within the perpendicular MTR. Unlike the specimen with a large AOI, early failure is observed for the specimen having MTRs. For the specimen with a large AOI, the first crack is observed at 45000 cycles, whereas the specimen with MTRs fractured at 2921 cycles near the perpendicular MTR (see Figure 5.25(a)). After 1000 cycles, a portion of the high strained region within the perpendicular MTR (as per Figure 5.25(b)) is monitored with higher magnification and multiple oriented slip bands, along with accentuated out of plane deformation, are observed as shown in Figure 5.25(c). Such observation might indicate activation of multiple slip systems (pyramidal along with basal and prismatic slip systems). The relative activity of the different families of slip systems within the perpendicular and parallel MTRs are systematically investigated using CPFE simulations towards the end of Section 5.2.4.





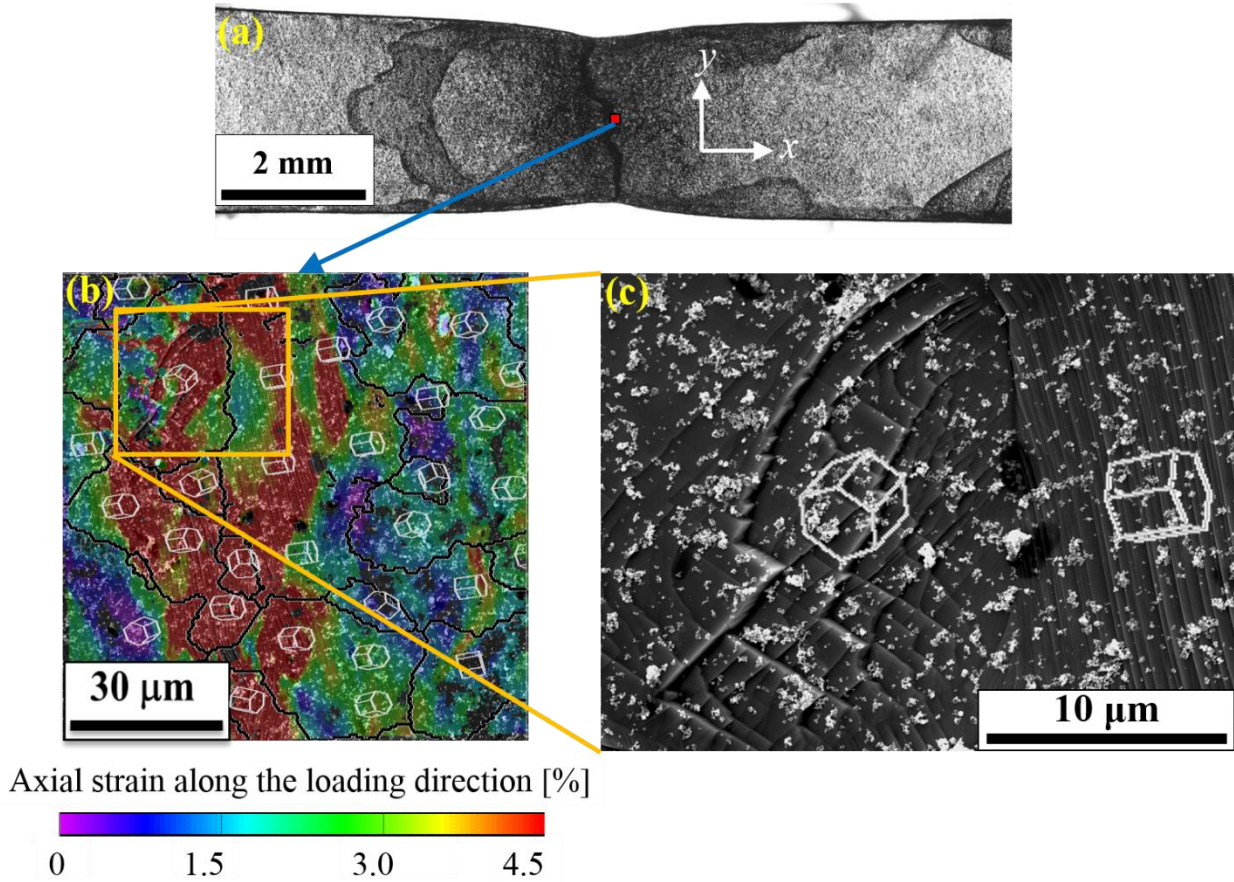


Figure 5.25. (a) Fracture of the specimen near the perpendicular MTR at 2921 cycles. (b) DIC strain map after 1000 cycles for the perpendicular MTR. (c) Multiple slip bands within a grain and accentuated out of plane slip are observed in the scanning electron microscope image.

## 5.2.4 Crystal plasticity results and discussion

### *Crack initiation*

The discretized polycrystalline microstructure, which is shown in Figure 5.17(a), is used to investigate the crack initiation because the experimentally observed crack (as seen in Figure 5.21(a)) corresponds to a region near the center of the microstructure. Further, such a large microstructure would eliminate any local effect of the boundary conditions on any mechanical field variable around the crack initiation site.

The physics of fatigue crack initiation is strongly dependent on the material, crystal structure (FCC, BCC, HCP), microstructure (grain size distribution, phase distribution, morphology, and orientation), and loading regime (e.g., stress ratio) [23]. PSB-driven failure is

widely accepted and common mode of failure in FCC alloys. However, for alpha Ti-6Al-4V (HCP), no single failure mechanism exists across all loading regimes. In a recent experimental work, Joseph et al. investigated crack initiation mechanism in near alpha Ti-6242Si during low cycle fatigue loading [222]. They observed dislocation pile-ups within primary alpha grains sharing boundaries with the two-phase regions and postulated that crack nucleation occurred near the basal planes within the same grains by sub-surface double-ended pile-up mechanism. On the other hand, many Ti alloys (e.g., Ti-6Al-4V, Ti-6Al-2Sn-4Zr-2Mo) creep at room temperature, which results in dwell sensitivity of these alloys at the service condition. For cold dwell fatigue of Ti alloys, a *rouge grain* combination might result in significant load shedding and plastic strain accumulation leading to fracture of the specimen [67], [68], [122], [128], [129], [223]–[225]. Strictly speaking, HCF and dwell fatigue are not the same from a design perspective. However, HCF performed at a high R ratio involves very low-stress amplitude and high mean stress, which potentially leads to progressive creep at room temperature resulting in similar consequences as in dwell fatigue [14]. Hence, we start with the notion of the *rouge grain* combination and investigate micromechanical aspects of crack initiation during high R ratio HCF loading of Ti-6Al-4V. A *rouge grain* combination is identified by a hard grain surrounded by two soft grains [128]. In HCP alloys, a grain with its basal plane near normal to the loading direction would represent a hard grain and a grain with its basal plane parallel to the loading direction would represent a soft grain.

As shown in Figure 5.22, the DIC strain map exhibited multiple hot spots or equally probable locations for crack initiation. However, a crack is observed in only one of these locations. Here, starting from the geometric idea (relative orientation of the c-axis with respect to the loading direction) of the *soft-hard-soft* grain combinations, the critical location of crack initiation is identified in four steps as demonstrated below. First, several *soft-hard-soft* grain combinations are identified in the microstructure based on their orientation with respect to the loading direction. Such grain combinations are connected by black dotted lines in Figure 5.26. In Figure 5.26, the red color represents geometrically hard grains, whereas the blue color represents soft grains.

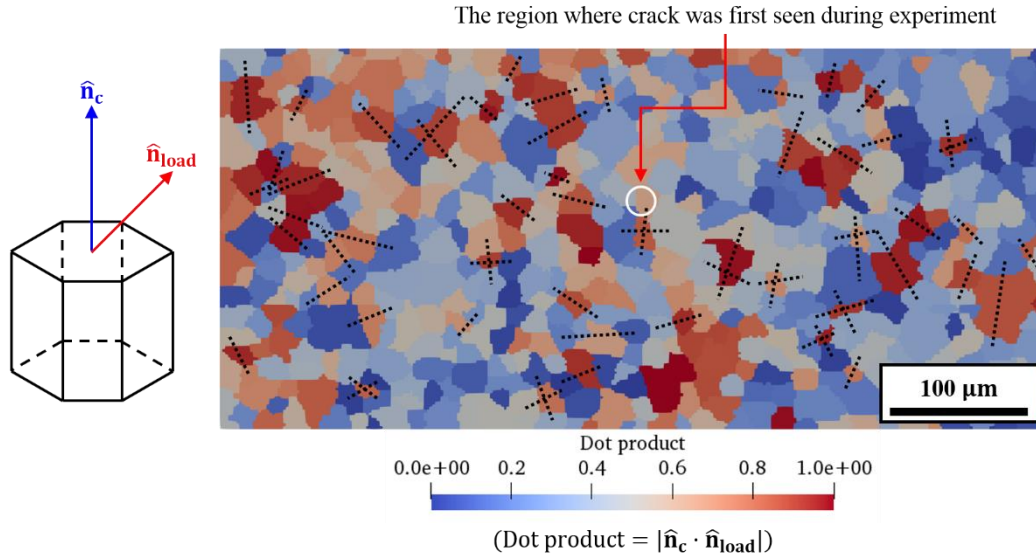


Figure 5.26. Identification of *soft-hard-soft* grain combinations based on the orientation of individual grains with respect to the loading direction before the application of fatigue loading.

It is to be noted that such identification of *soft-hard-soft* grain combinations does not take into consideration the local state of stress. In other words, within the geometric definition of hard or soft grains, it is assumed that all grains experience a similar overall stress state as the applied macroscopic stress state. However, in reality, each grain experiences a unique stress state based on the anisotropic mechanical response of the neighbouring grains<sup>\*\*\*</sup>. Therefore, in the second step *real* hard grains are identified based on the normal stress on the basal plane as calculated from the CP simulation. It turns out many hard grains, as identified in Figure 5.27, actually experience lower stress levels compared to the geometric definition. Corresponding *soft-hard-soft* grain combinations are connected by white dotted lines and are ruled out for further consideration.

\*\*\* All micromechanical field variables in Figure 5.27 through Figure 5.29 correspond to the maximum macroscopic stress ( $\sigma_{max} = 900$  MPa) after 40 load reversals.

The region where crack was first seen during experiment

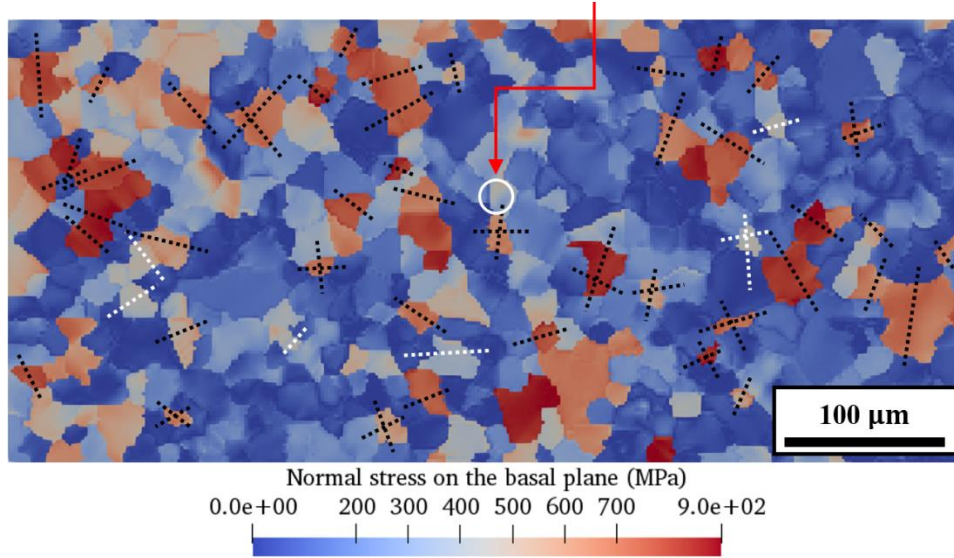


Figure 5.27. Normal stress on the basal plane from CPFE simulation.

If one hard grain sits in between two soft grains, one would expect dislocations piling up on one of the prismatic slip systems within the soft grain at the grain boundary separating the hard and soft grains [128]. In the present work, the dislocation density is not modeled explicitly. However, the effect of dislocation pile-up can be captured implicitly by observing strain accumulation on different slip systems. Here, strain accumulation on the basal and prismatic slip systems are considered. In Figure 5.28, strain accumulation on the prismatic slip systems is shown.

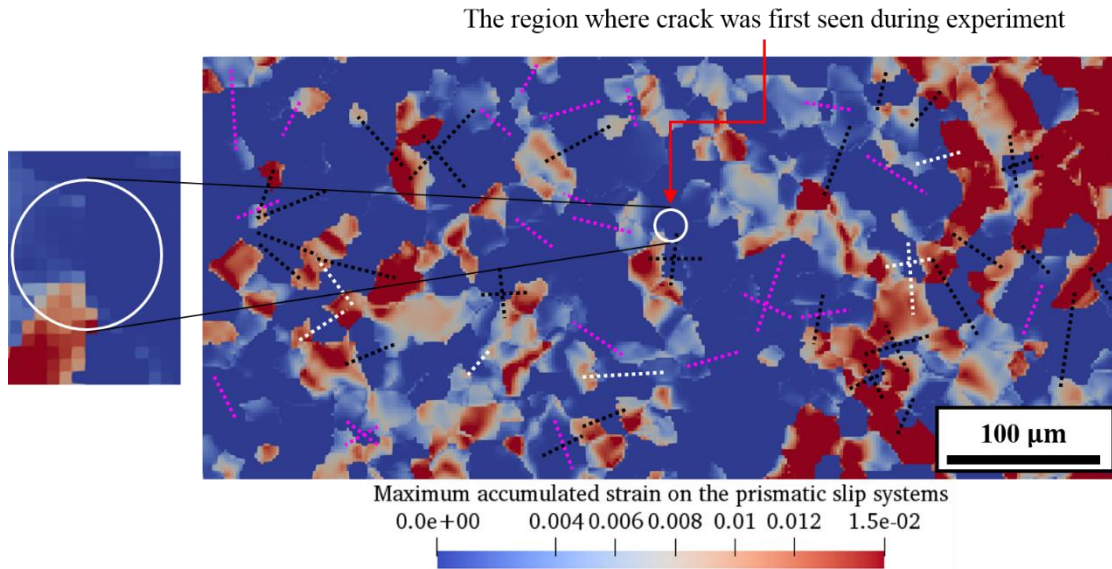


Figure 5.28. Strain accumulation on the prismatic slip systems. At each material point, the maximum value from the three prismatic slip systems is plotted.

From Figure 5.28, one can identify three categories of *soft-hard-soft* grain combinations: (a) the combinations where soft grains do not show any prismatic slip activity, (b) the combinations where soft grains show insignificant prismatic slip activity, and (c) the combinations where soft grains show a significant amount of prismatic slip activity. The first two categories are ruled out for the potential site of crack initiation and connected via magenta dotted lines. Finally, strain accumulation on the basal slip systems is considered in Figure 5.29.

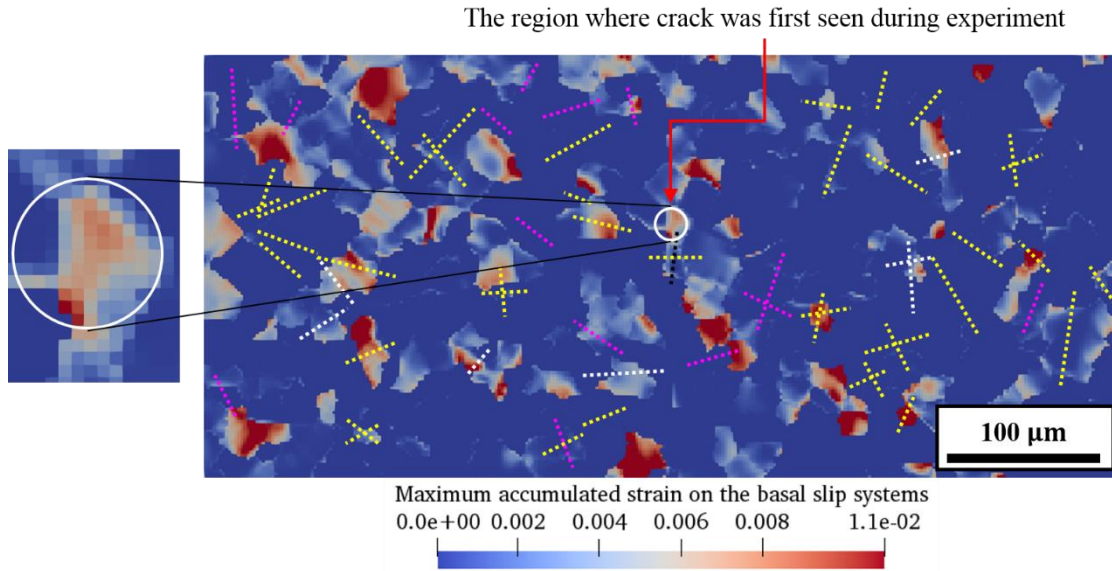


Figure 5.29. Strain accumulation on the basal slip systems. At each material point, the maximum value from the three basal slip systems is plotted.

From Figure 5.29, the combinations are ruled out if: (a) soft grains do not show any basal slip activity, or (b) the hard grain shows basal slip activity. Consequently, one can observe that there is only one grain combination which passed all four steps. Moreover, this observation is in accordance with the experiment, as crack initiation is observed in one of the soft grains of the same combination of grains identified from the CP modeling. Further, significantly high basal slip activity is observed in the location of crack initiation and significantly high prismatic slip activity is observed in an adjacent soft grain as shown in the inset (magnified regions) of Figure 5.28 and Figure 5.29.

Thus, starting from the geometric notion of soft-hard grain combinations, the normal stress on the basal planes of the hard grains along with the basal and prismatic slip activities in the adjacent soft grains are used to identify the critical *soft-hard-soft* grain combination for crack initiation. With this observation, it is reasonable to surmise that the dwell effect is also established at high R ratios of HCF in Ti-6Al-4V.

### ***Heterogeneous deformation as a function of stress ratio***

Strain accumulation or heterogeneity is studied at two different length-scales, that of the continuum and slip system level. In the present context, the sources of the heterogeneity are the

anisotropic mechanical response of the polycrystalline aggregate and asymmetric slip systems with different critical resolved shear stresses for the HCP crystal structure. At the continuum level, heterogeneity is quantified as the standard deviation in the effective value of plastic strain increment ( $\Delta E_{\text{eff}}^{\text{plastic}}$ ) which is defined as

$$\Delta E_{\text{eff}}^{\text{plastic}} = \sqrt{\frac{2}{3} \Delta E_{ij}^{\text{plastic}} \Delta E_{ij}^{\text{plastic}}} \quad (5.19)$$

where

$$\Delta E_{ij}^{\text{plastic}} = E_{ij}^{\text{plastic}} \Big|_{\sigma_{\text{max}}} - E_{ij}^{\text{plastic}} \Big|_{\sigma_{\text{min}}} \quad (5.20)$$

At the slip system level, heterogeneity associated with  $k^{\text{th}}$  slip system is quantified as the standard deviation in the strain increment ( $\Delta \gamma^k$ ) which is defined as

$$\Delta \gamma^k = \gamma^k \Big|_{\sigma_{\text{max}}} - \gamma^k \Big|_{\sigma_{\text{min}}} \quad (5.21)$$

where

$$\gamma^k(t) = \int_0^t \dot{\gamma}^k dt \quad (5.22)$$

In the present context, infinitesimally small standard deviation would imply either no strain increment or nearly uniform strain throughout the microstructure. Therefore, in order to properly study strain localization, two more quantities are defined, namely, the degree of plastic deformation, which is quantified as a mean value of the effective value of plastic strain increment ( $\Delta E_{\text{eff}}^{\text{plastic}}$ ) and degree of slip, which is quantified as a mean value of the strain increment at the slip system level ( $\Delta \gamma^k$ ). The mean along with standard deviation would give a clearer picture of strain localization as a function of stress ratio and microstructure.

#### *Heterogeneity in microstructure having random texture*

Three types of HCF simulations are performed<sup>§§§§</sup> with the microstructure having random texture (as shown in Figure 5.17(a)) at different stress ratios: (a) simulations at constant stress amplitude, (b) simulations at constant mean stress, and (c) simulations at constant maximum stress. The results from all simulations are reported in Figure 5.30 through Figure 5.32.

---

<sup>§§§§</sup> All simulations for heterogeneity study were stopped after 10 load reversals. All results in Figure 5.30 through Figure 5.39 correspond to the final loading step in the simulations.

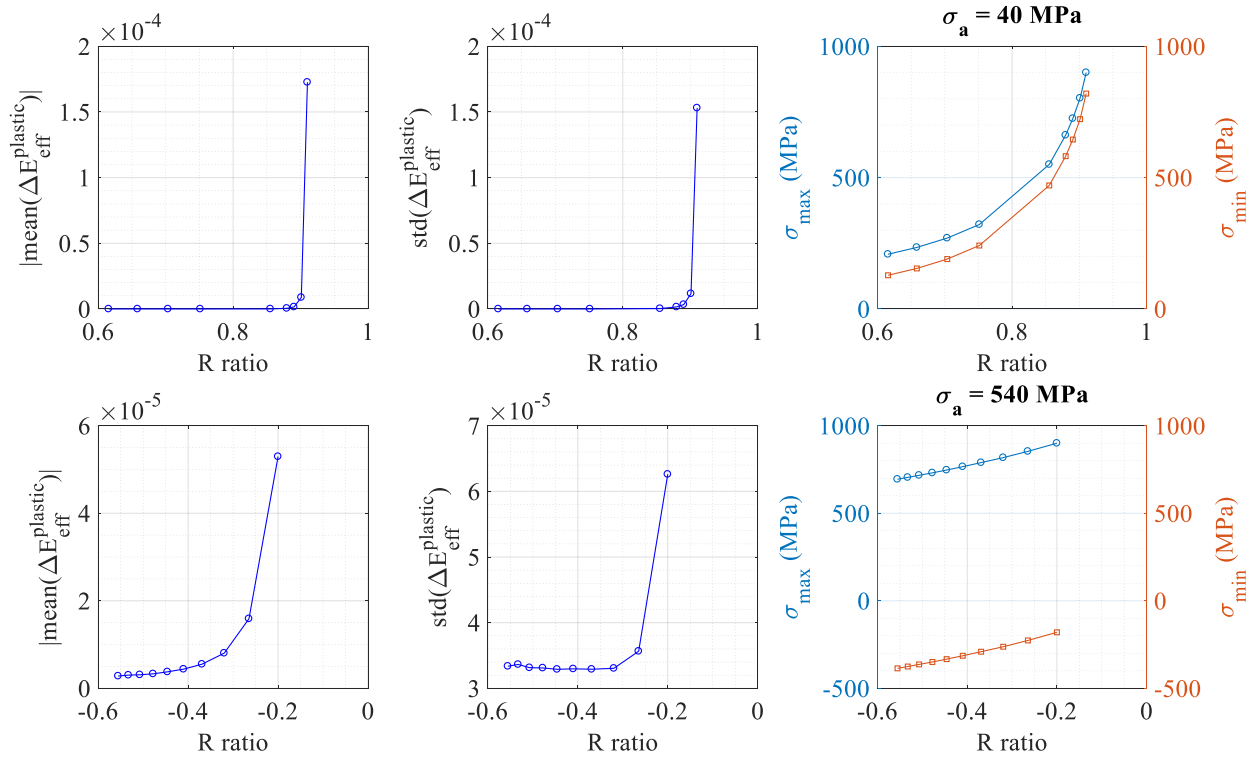


Figure 5.30. Strain heterogeneity and degree of plastic deformation as a function of stress ratio, while keeping the stress amplitude fixed: top row,  $\sigma_a = 40$  MPa, and bottom row,  $\sigma_a = 540$  MPa.

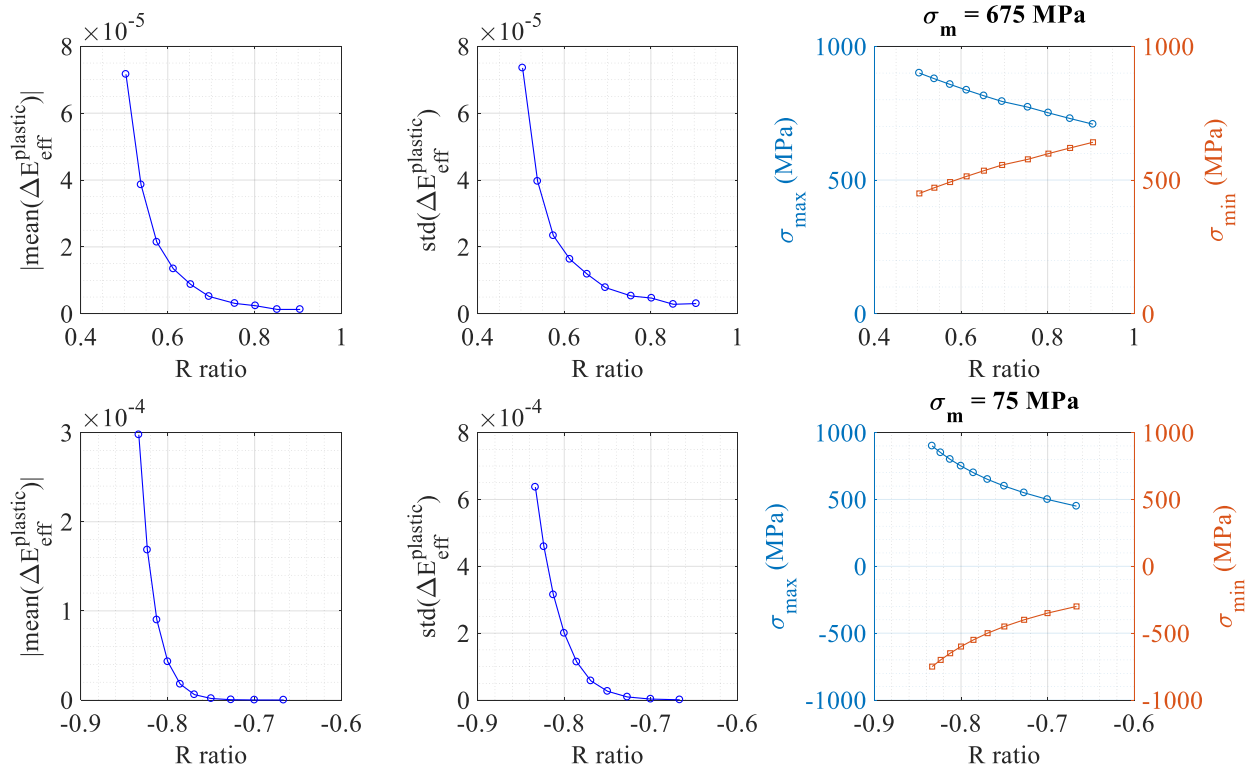


Figure 5.31. Strain heterogeneity and degree of plastic deformation as a function of stress ratio, while keeping the mean stress fixed: top row,  $\sigma_m = 675$  MPa, and bottom row,  $\sigma_m = 75$  MPa.

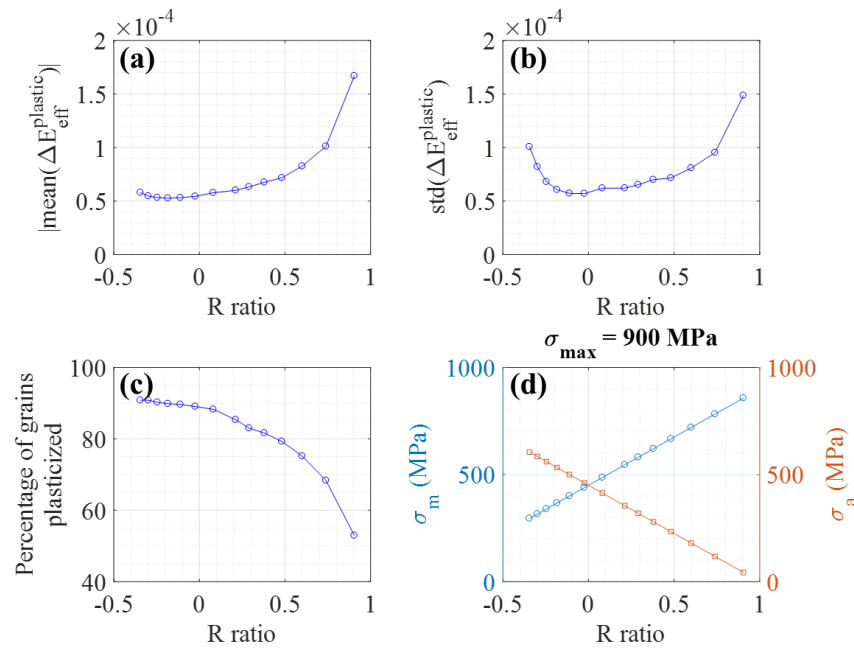


Figure 5.32. Strain heterogeneity, degree of plastic deformation and percentage of grains plasticized as a function of the stress ratio, while keeping the maximum stress fixed at  $\sigma_{\max} = 900$  MPa.

From Figure 5.30, it is observed that the degree of plastic deformation and strain heterogeneity increase with R ratio at a constant stress amplitude. Both quantities are one order of magnitude higher at a lower stress amplitude (i.e., 40 MPa but higher mean stress) compared to a higher stress amplitude (i.e., 540 MPa but lower mean stress). Therefore, it can be said that the degree of plastic deformation and strain heterogeneity are directly correlated to mean stress when the stress amplitude is kept constant. Similarly, from Figure 5.31, it is observed that both the degree of plastic deformation and strain heterogeneity decrease with the R ratio at a constant mean stress. Further, both quantities are one order of magnitude higher at a lower mean stress value (i.e., 75 MPa but higher stress amplitude) compared to a higher mean stress (i.e., 675 MPa but lower stress amplitude). Therefore, it can be said that the degree of plastic deformation and strain heterogeneity are directly correlated to stress amplitude when the mean stress is kept constant. From Figure 5.30 and Figure 5.31, it is interesting to note that both the degree of plastic deformation and strain heterogeneity always attain their maximum value when the maximum stress reaches its upper limit, which is set to 900 MPa for all simulations. Therefore, strain heterogeneity is subsequently studied as a function of R ratio keeping the maximum stress fixed to 900 MPa.

From Figure 5.32, we can observe that both the degree of plastic deformation and strain heterogeneity decrease with R ratio for  $R < 0$ . However, for  $R > 0$ , both quantities increase monotonically. We also observe that the percentage of grains, which deform plastically, monotonically decreases with an increasing R ratio, therefore implying that the incremental plastic deformation is highly localized at higher R ratios. Further, it is noted from Figure 5.32 that the mean stress increases and stress amplitude decreases with an increasing R ratio. Therefore, the degree of plastic deformation and associated heterogeneity are positively correlated with mean stress for  $R > 0$  and negatively correlated with the same for  $R < 0$ ; the percentage of grains plasticized is negatively correlated with mean stress for both  $R < 0$  and  $R > 0$ . Now, the degree of slip associated with each family of slip systems for the same discretized microstructure with random texture is shown in Figure 5.33, and strain heterogeneity at slip system level is shown in Figure 5.34.

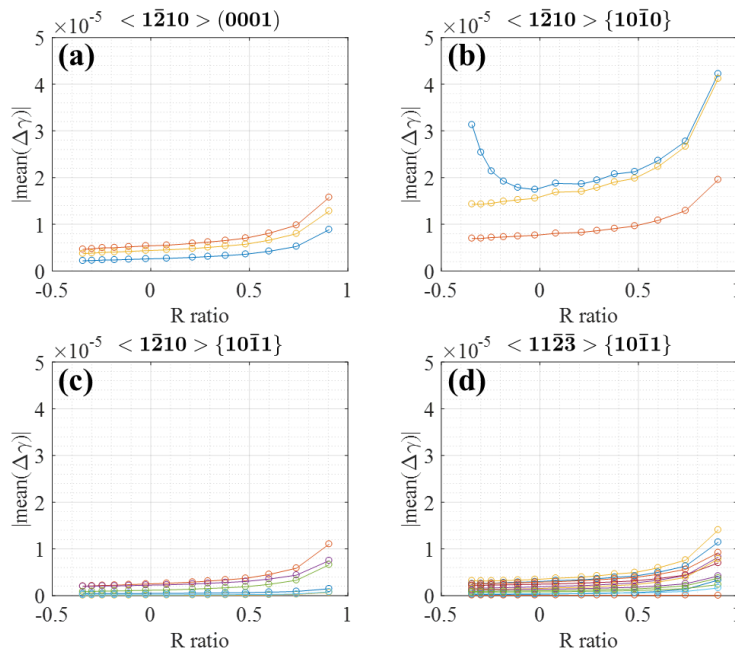


Figure 5.33. Degree of incremental slip on each slip system as a function of the R ratio for the random-textured region. Each subplot represents a family of slip systems ((a) basal, (b) prismatic, (c) first order pyramidal with  $\langle a \rangle$  type slip direction, and (d) first order pyramidal with  $\langle c + a \rangle$  type slip direction) and each curve within one subplot represents the behavior of each slip systems in that family.

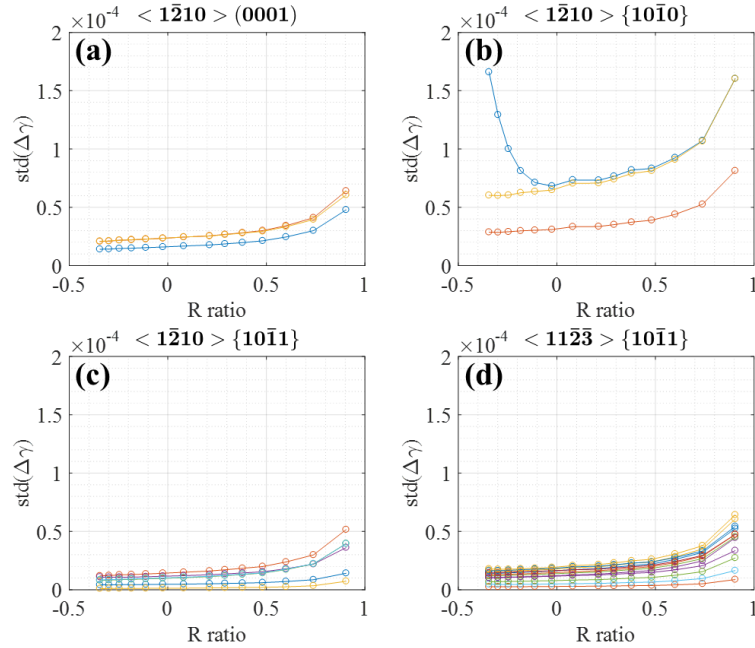


Figure 5.34. Heterogeneity associated with incremental slip on each slip system as a function of the R ratio for the random-textured region. Each subplot represents a family of slip systems ((a) basal, (b) prismatic, (c) first order pyramidal with (a) type slip direction, and (d) first order pyramidal with (c + a) type slip direction) and each curve within one subplot represents the behavior of each slip systems in that family.

From Figure 5.33 and Figure 5.34, it is evident that for the random-textured microstructure the prismatic slip systems dominate over the other slip systems at all R ratios. This observation could be attributed to the fact that the critical resolved shear stress (CRSS) for prismatic slip systems is the lowest in the present modeling. However, contributions from the basal and pyramidal slip systems are observed to be significantly higher at higher R ratios. Therefore, for tensile-tensile HCF loading with random-textured microstructure at high R ratios, multiple slip systems are likely to be activated within fewer grains leading to high strain localization. However, as evident from Figure 5.33(b) and Figure 5.34(b), for tensile-compressive fatigue loading, only prismatic slip system would contribute significantly with more grains being plasticized (see Figure 5.32(c)) leading to relatively homogeneous deformation.

### Heterogeneity in the micro-textured regions

All the results, as discussed above, are only applicable for a microstructure having random texture. Now, systematic differences in the degree of plastic deformation and strain heterogeneity within MTRs are explored by performing similar HCF simulations with the discretized microstructures as shown in Figure 5.18. In Figure 5.35, the degree of plastic deformation and strain heterogeneity of the random-textured microstructure are compared to that of the perpendicular and parallel MTRs. The reader is reminded that the perpendicular MTR corresponds to the microstructure shown in Figure 5.18(a) with basal planes nearly perpendicular to the loading direction, whereas the parallel MTR corresponds to the microstructure shown in Figure 5.18(b) with the basal planes near parallel to the loading direction.

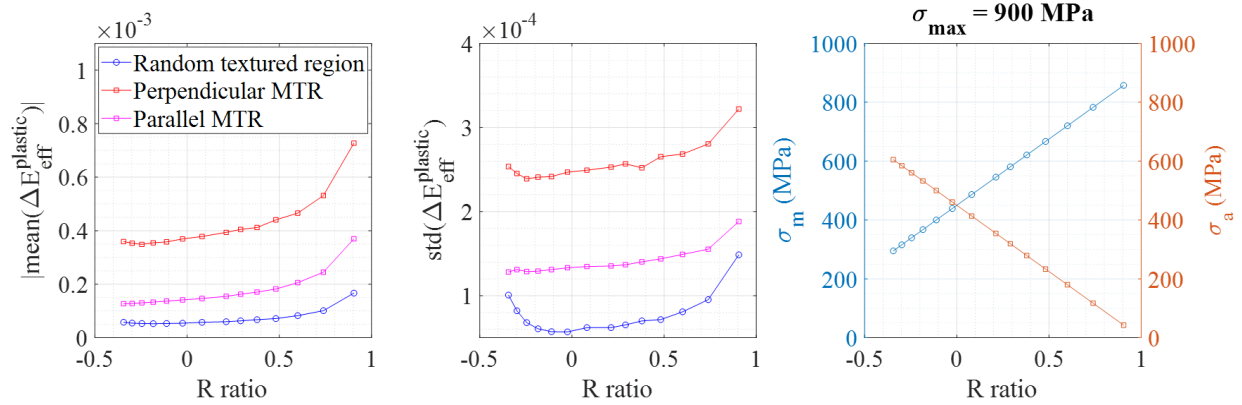


Figure 5.35. Effect of texture on the heterogeneous deformation as a function of R ratio, while keeping the maximum stress fixed at  $\sigma_{\max} = 900$  MPa.

From Figure 5.35, it is evident that the perpendicular MTR has maximum impact on the degree of plastic deformation and strain heterogeneity. As a consequence, the perpendicular MTR (basal planes near perpendicular to the loading direction) would experience significantly higher progressive damage in terms of plastic strain accumulation compared to a completely random texture under identical loading situations. This conjecture is consistent with the fact that the specimen with MTRs (a) fractured near the perpendicular MTR and (b) showed significantly low HCF life (fracture at 2921 cycles) compared to the specimen with random texture (first crack observed at 45000 cycles). It has been mentioned before that the presence of a perpendicular MTR

is associated with the anomalous mean stress sensitivity of Ti-6Al-4V leading to significantly lower HCF life [14]–[18]; the present experiment and Figure 5.35 also confirm the same.

In Figure 5.25(c), activation of multiple slip systems is indicated at a high strained region within the perpendicular MTR, in terms of differently oriented slip bands within a grain via scanning electron microscope imaging. Now, slip system activities within the MTRs are explored using CPFE simulations by considering the degree of slip and strain heterogeneity for different slip systems. To this end, the degrees of slip and strain heterogeneity at the slip system level are plotted in Figure 5.36 and Figure 5.37 for the perpendicular MTR, and in Figure 5.38 and Figure 5.39 for the parallel MTR. From Figure 5.36–Figure 5.39, it can be observed that the basal and prismatic slip systems show similar behavior within both MTRs. Strictly speaking, under identical loading situations, the contributions from the prismatic slip systems in the perpendicular MTR are slightly higher than that in the parallel MTR. Moreover, within the perpendicular MTR, significantly higher slip activities are observed in the first order pyramidal slip systems with the  $\langle c + a \rangle$  type slip directions contributing more than the  $\langle a \rangle$  type slip directions. The degree of slip for the first order pyramidal slip systems with the  $\langle c + a \rangle$  type slip directions can be compared between two MTRs by looking at Figure 5.36(d) and Figure 5.38(d), and strain heterogeneity at the same slip systems can be compared between two MTRs by observing Figure 5.37(d) and Figure 5.39(d).

In an earlier CPFE work, Kasemer et al. systematically showed that the activation of a family of slip systems within a MTR is highly sensitive to the initial relative CRSS [126]. In the present work, the relative CRSS for the first order pyramidal and basal slip systems with respect to the prismatic slip systems are fit as described in Section 5.2.2 and consistent with the range given in the Table 1 of Ref. [226]. When the CP parameters, defined for a single crystal, are fitted to the macroscopic response of the material, there exists a non-uniqueness issue in the fitted numerical values of the parameters due to a multitude of microscopic slip events that can lead to the same macroscopic deformation state. Such uncertainty in the CP parameters would have significant implications in the quantitative predictions, such as fatigue life, from CPFE simulations [25]. The objective of the present work is not to predict fatigue life, rather to offer mechanistic insights into the anomalous mean stress behavior shown by Ti-6Al-4V using CPFE simulations at the mesoscopic length-scale. The uncertainty in the CP parameter would have implications in the local heterogeneous deformation within a microstructure [25], but not on the overall statistical

behavior of each of the three microstructures as a function of the R ratio as shown in Figure 5.30- Figure 5.39.

From the results and discussion, as presented above, it is evident that the participation of fewer grains in the plastic deformation and activation of multiple families of slip systems, irrespective of the texture of the microstructure, make the high R ratio regime unique, as well as critical regarding fatigue damage accumulation in alpha Ti-6Al-4V. However, from CPFE simulations, preferential slip activity of the pyramidal slip systems with  $\langle c + a \rangle$  type slip direction is observed within the perpendicular MTR, which is known to be associated with the anomalous mean stress behavior of Ti-6Al-4V in the literature [14]–[18]. Hence, preferential slip activity of the pyramidal slip systems, particularly with  $\langle c + a \rangle$  type slip directions, within the perpendicular MTR can be considered as one of the primary mechanisms (in addition to the prismatic and basal slip activities), which results in consistently higher degree of plastic deformation and strain heterogeneity in the perpendicular MTR (as seen in Figure 5.35) making it responsible for anomalous mean stress sensitivity, especially at high R ratios.

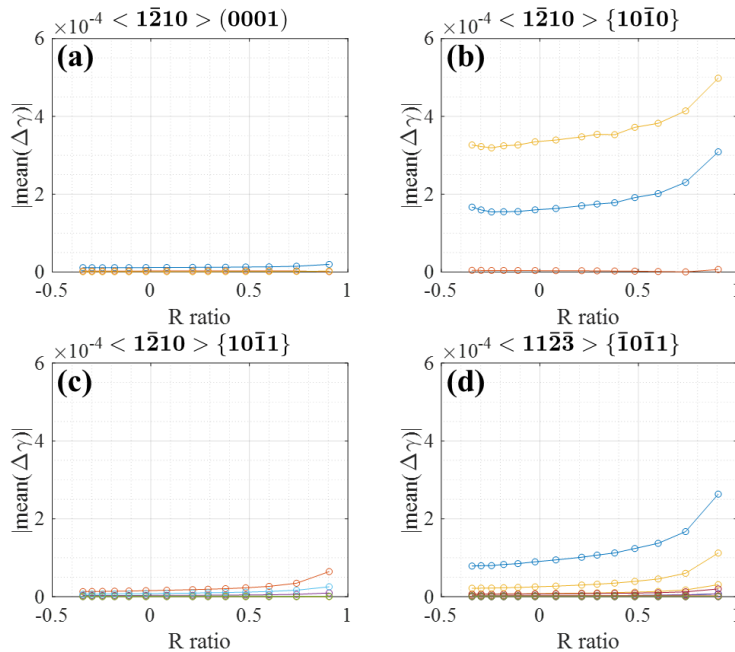


Figure 5.36. Degree of incremental slip on each slip system as a function of R ratio for the perpendicular MTR. Each subplot represents a family of slip systems ((a) basal, (b) prismatic, (c) first order pyramidal with  $\langle a \rangle$  type slip direction, and (d) first order pyramidal with  $\langle c + a \rangle$  type slip direction) and each curve within one subplot represents the behavior of each slip systems in that family.

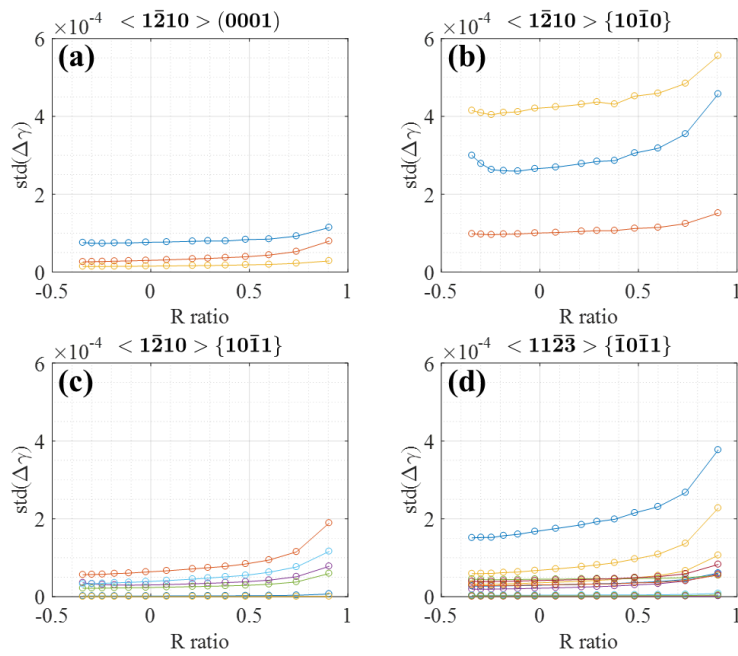


Figure 5.37. Heterogeneity associated with incremental slip on each slip system as a function of R ratio for perpendicular MTR. Each subplot represents a family of slip systems ((a) basal, (b) prismatic, (c) first order pyramidal with  $\langle a \rangle$  type slip direction, and (d) first order pyramidal with  $\langle c + a \rangle$  type slip direction) and each curve within one subplot represents the behavior of each slip systems in that family.

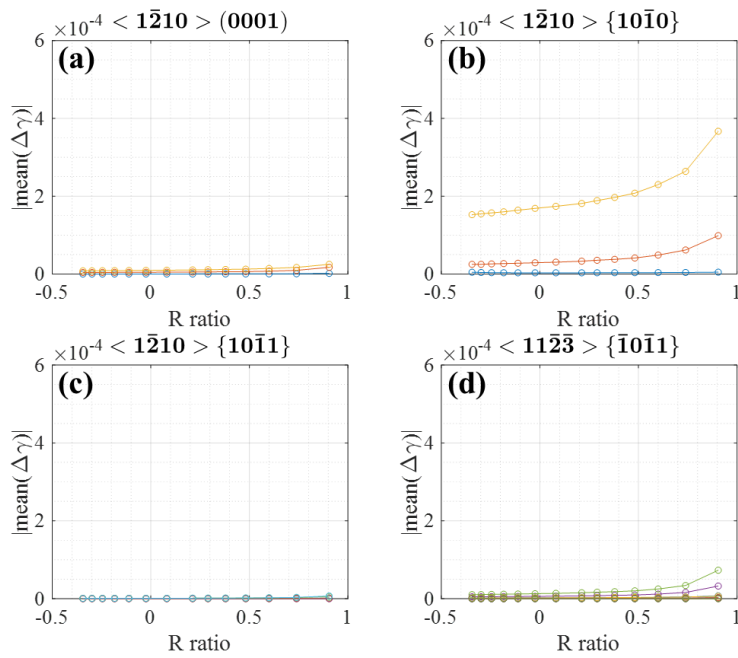


Figure 5.38. Degree of incremental slip on each slip system as a function of R ratio for the parallel MTR. Each subplot represents a family of slip systems ((a) basal, (b) prismatic, (c) first order pyramidal with  $\langle a \rangle$  type slip direction, and (d) first order pyramidal with  $\langle c + a \rangle$  type slip direction) and each curve within one subplot represents the behavior of each slip systems in that family.

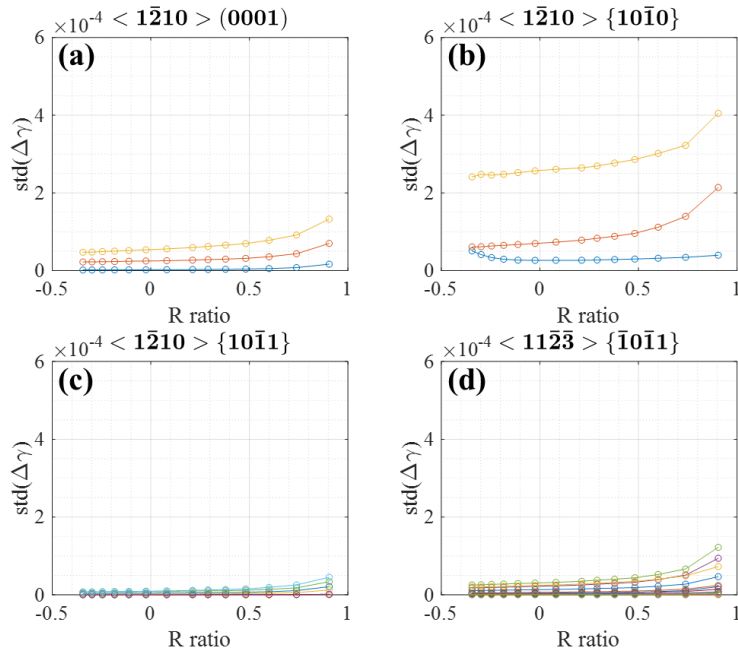


Figure 5.39. Heterogeneity associated with incremental slip on each slip system as a function of R ratio for parallel MTR. Each subplot represents a family of slip systems ((a) basal, (b) prismatic, (c) first order pyramidal with  $\langle a \rangle$  type slip direction, and (d) first order pyramidal with  $\langle c + a \rangle$  type slip direction) and each curve within one subplot represents the behavior of each slip systems in that family.

### 5.2.5 Summary

High cycle fatigue analyses at high R ratios are performed on two Ti-6Al-4V specimens having equiaxed alpha microstructure. HR-DIC within a scanning electron microscope is performed on the MTRs for one specimen to study grain level strain localization. DIC within an optical microscope is carried out in the other specimen to study the evolution of heterogeneous deformation and crack initiation. Subsequently, CPFE simulations are carried out to investigate the mechanistic aspects of crack initiation and study heterogeneous deformation at the continuum and slip system levels as a function of stress ratio and microstructure. The present work offers several new insights into the relative contributions of the different families of slip systems towards the microscopic cyclic plasticity as a function of stress ratio and shed light onto a practical issue of the anomalous mean stress behavior of Ti-6Al-4V at high R ratios. The key findings are summarized below.

- From optical microscopy DIC, it is observed that crack initiation at high R ratio HCF loading tends towards regions of highly localized principal shear strain, concentrated in 45° bands, relative to the tensile loading direction. However, multiple hot spots are observed in the DIC strain map indicating the equally likely location for crack initiation. From the CPFE simulation, it is found that the crack initiation could be attributed to the presence of a critical *soft-hard-soft* grain combination, characterized by a high normal stress on the basal plane of the hard grain and significantly higher basal and prismatic slip activities in the adjacent soft grains. Such a grain combination is typically believed to be the reason for failure during dwell fatigue of Ti alloys. Therefore, such an observation suggests possible dwell effect during HCF loading at the high R ratio, which could be tied to high mean stress applied loading and high creep tendency of Ti-6Al-4V at room temperature.
- CPFE simulations indicate that the degree of plastic deformation and associated heterogeneity are: (a) directly correlated to maximum stress, (b) higher when operating far away from  $R = 0$ . However, tensile-compressive HCF (i.e.,  $R < 0$ ) has been found to be different from tensile-tensile HCF (i.e.,  $R > 0$ ) as far as slip activity is concerned. At an R ratio approaching 1, all slip systems are found to contribute to strain localization with a smaller number of grains being plasticized, whereas for tensile-compressive HCF, only prismatic slip systems contribute to strain localization with a greater number of grains being plasticized. Therefore, HCF in Ti-6Al-4V at high R ratios results in severely localized plasticity and demands special care for design against failure.
- From the CPFE simulations, significantly higher slip activity is observed in the first order pyramidal slip systems, particularly along  $\langle c + a \rangle$  directions, within a MTR characterized by basal planes oriented nearly perpendicular to the loading direction. Such slip activity can be considered as one of the major mechanisms (in addition to the prismatic and basal slip), which results in a consistently higher degree of plastic deformation and strain heterogeneity in the same MTR, thus making it responsible for anomalous mean stress sensitivity in Ti-6Al-4V, especially at high R ratios.

The remarks, presented above, indicate the distinctive features of microscopic plasticity associated with high cycle fatigue behavior at high stress ratios. Such features make not only the

high stress ratio regime distinct but also more vulnerable in terms of fatigue damage accumulation for Ti-6Al-4V, thus rationalizing the high mean stress anomalous behavior experienced for this material.

## 6. CONCLUDING REMARKS AND FUTURE WORK

### 6.1 Concluding remarks

The objective of the present thesis has been to ensure fatigue performance via location-specific lifing in aerospace components made of Ti alloys and Ni-base superalloys. Although there are several differences in the macroscopic characteristics of fatigue behavior in these two materials, there exists an underlying unity in terms of the origin of fatigue damage, namely, the irreversible motion of dislocations on slip systems. Historically, CP constitutive relations were developed to model the plastic deformation of metals accounting for the dislocation glide on slip systems. In this thesis, CPFEM simulations have been used to resolve some of the outstanding issues in the fatigue performance of Ti alloys and Ni-base superalloys. To this end, this thesis has broadly been divided into three parts:

- Part 1: building confidence in the CPFEM simulations
- Part 2: analysis and prediction of inclusion- and matrix-driven competing failure modes in a Ni-base superalloy
- Part 3: assurance of performance in the LFW Ti alloys

In Part 1 (see Chapter 3), it is observed that (a) uncertainty in the mechanical response from CPFEM simulations depends on the quantity of interest, such as SPSSED, PSA, stress along loading direction, (b) the contribution of a specific CP parameter towards the overall uncertainty of a quantity is path-dependent, i.e., varies based on the load step under consideration, (c) a single critical SPSSED value is good enough to predict median as well as scatter trends in fatigue life at multiple applied strain ranges and ratios, and (d) a Bayesian inference framework provides a path forward to incorporate uncertainties from the CPFEM simulations in the calibration of the critical SPSSED and subsequent fatigue life prediction.

The results from Part 2 (see Chapter 4), suggest that (a) emergence of inclusion- or matrix-driven failure is an outcome of the complex interactions between a multitude of parameters, (b) a simple parametric study can provide a path forward to obtain statistically equivalent microstructures with realistic inclusion attributes for fatigue life prediction, (c) critical SPSSED decreases almost linearly with increasing temperature and is appropriate to predict the realistic emergence of the competing failure modes as a function of applied strain range and temperature.

From Part 3 (see Chapter 5), predominantly equiaxed alpha microstructure is observed at and beyond ~1 mm on either side from the weld center in Ti-6Al-4V welded to Ti-6Al-4V samples or on the Ti-6Al-4V side of Ti-6Al-4V welded to Ti-5Al-5V-5Mo-3Cr samples on both as-welded and heat-treated conditions. In the literature, as reviewed in Section 2.3, fatigue crack initiations in the Ti-6Al-4V welded to Ti-6Al-4V samples are typically reported at a similar distance from the weld. HCF analyses on the equiaxed microstructure at a high R ratio reveals that a critical *soft-hard-soft* grain combination is associated with crack initiation, indicating possible dwell effect at high R ratios, which could be attributed to the high applied mean stress and high creep sensitivity of Ti-6Al-4V at room temperature. Further, CPFÉ simulations indicate more heterogeneous deformation, specifically the activation of multiple families of slip systems with fewer grains being plasticized, at higher R ratios. Such behavior is exacerbated within MTRs, especially the MTR composed of grains with their c-axes near parallel to the loading direction. These features of microplasticity make the high R ratio regime more vulnerable to fatigue damage accumulation and demand special attention during the design of LFW components made of Ti-6Al-4V.

## 6.2 Future work

Some of the possible future works from the present thesis are suggested below.

The microstructure-sensitive critical SPSED is certainly promising towards the prediction of fatigue life at diverse loading conditions. Some of the areas wherein this metric can be tested are (a) in the presence of an environmental effect, such as corrosion, hydrogen embrittlement, (b) in the presence of notches, (c) other material systems, such as HCP material (e.g., the alpha phase of Ti alloys) and BCC material (e.g., beta phase of Ti alloys), (d) in the presence of multiple phases, such as alpha-beta processed Ti alloys.

In this thesis, UQ of a CP model has been carried out considering an FCC material. However, a similar study in the HCP material, such as the alpha phase of Ti alloys, will be interesting. Unlike Ni-base superalloy, an FCC material, alpha Ti alloys, an HCP material, have multiple families slip systems. Each family of slip systems is associated with different critical resolved shear stresses and strain-rate sensitivity exponents. It would be interesting to investigate how uncertainty in the relative slip system strength influence the macroscopic as well as microscopic mechanical response, potentially as a function of the micro-texture of the material.

## REFERENCES

- [1] R. C. Reed, *The Superalloys: Fundamentals and Applications*. 2006.
- [2] G. Lütjering and J. C. Williams, *Titanium : Engineering Materials and Processes*. Springer, 2007.
- [3] D. Socie and G. Marquis, *Multiaxial Fatigue*. SAE International, 1999.
- [4] S. Suresh, *Fatigue of Materials*. Cambridge: Cambridge University Press, 1998.
- [5] G. F. Mathey, "Method of making superalloy turbine disks having graded coarse and fine grains," US5312497A, 1994.
- [6] J. Gayda and D. Furrer, "Dual-Microstructure Heat Treatment," *Adv. Mater. Process.*, no. July, pp. 36–39, 2003.
- [7] J. Cho, K. Conlon, and R. Reed, "Residual stresses in an electron beam weld of Ti-834: Characterization and numerical modeling," *Metall. Mater. Trans. A*, vol. 34, no. 12, pp. 2935–2946, 2003.
- [8] I. Bhamji, M. Preuss, P. L. Threadgill, and A. C. Addison, "Solid state joining of metals by linear friction welding: a literature review," *Mater. Sci. Technol.*, vol. 27, no. 1, pp. 2–12, 2011.
- [9] R. Turner, R. M. Ward, R. March, and R. C. Reed, "The magnitude and origin of residual stress in Ti-6Al-4V linear friction welds: An investigation by validated numerical modeling," *Metall. Mater. Trans. B Process Metall. Mater. Process. Sci.*, vol. 43, no. 1, pp. 186–197, 2012.
- [10] P. J. Withers, "Residual stress and its role in failure," *Reports Prog. Phys.*, vol. 70, no. 12, pp. 2211–2264, 2007.
- [11] O. H. Basquin, "The exponential law of endurance tests," *Proc. Am. Soc. Test. Mater.*, vol. 10, pp. 625–630, 1910.
- [12] L. F. Coffin Jr, "A study of the effects of cyclic thermal stresses on a ductile metal," *Trans. Am. Soc. Mech. Eng. New York*, vol. 76, pp. 931–950, 1954.
- [13] S. S. Manson, "Behavior of materials under conditions of thermal stress," Cleveland, Ohio, 1953.

- [14] B. Oberwinkler, “On the anomalous mean stress sensitivity of Ti-6Al-4V and its consideration in high cycle fatigue lifetime analysis,” *Int. J. Fatigue*, vol. 92, pp. 368–381, 2016.
- [15] S. Adachi, L. Wagner, and G. Lütjering, “Influence of microstructure and mean stress on fatigue strength of Ti-6Al-4V,” in *Titanium '84 - Science and Technology*, 1985, pp. 2139–2149.
- [16] K. Le Biavant, S. Pommier, and C. Prioul, “Local texture and fatigue crack initiation in a Ti-6Al-4V titanium alloy,” *Fatigue Fract. Eng. Mater. Struct.*, vol. 25, no. 6, pp. 527–545, 2002.
- [17] S. G. Ivanova, R. R. Biederman, and R. D. Sisson Jr., “Investigation of Fatigue Crack Initiation in Ti-6Al-4V During Tensile-Tensile Fatigue,” *J. Mater. Eng. Perform.*, vol. 11, no. 2, pp. 226–231, 2002.
- [18] I. Bantounas, D. Dye, and T. C. Lindley, “The role of microtexture on the faceted fracture morphology in Ti-6Al-4V subjected to high-cycle fatigue,” *Acta Mater.*, vol. 58, no. 11, pp. 3908–3918, 2010.
- [19] W. E. Frazier, “Metal additive manufacturing: A review,” *Journal of Materials Engineering and Performance*, vol. 23, no. 6. Springer New York LLC, pp. 1917–1928, 08-Apr-2014.
- [20] S. K. Bhaumik, T. A. Bhaskaran, R. Rangaraju, M. A. Venkataswamy, M. A. Parameswara, and R. V. Krishnan, “Failure of turbine rotor blisk of an aircraft engine,” *Eng. Fail. Anal.*, vol. 9, no. 3, pp. 287–301, 2002.
- [21] J. C. Stinville, F. Bridier, D. Ponsen, P. Wanjara, and P. Bocher, “High and low cycle fatigue behavior of linear friction welded Ti-6Al-4V,” *Int. J. Fatigue*, vol. 70, pp. 278–288, Jan. 2015.
- [22] P. G. Forrest, *Fatigue of metals*. Elsevier, 2013.
- [23] M. D. Sangid, “The physics of fatigue crack initiation,” *Int. J. Fatigue*, vol. 57, pp. 58–72, 2013.
- [24] P. A. Shade *et al.*, “Exploring new links between crystal plasticity models and high-energy X-ray diffraction microscopy,” *Curr. Opin. Solid State Mater. Sci.*, Jul. 2019.
- [25] R. Bandyopadhyay, V. Prithvirajan, and M. D. Sangid, “Uncertainty Quantification in the Mechanical Response of Crystal Plasticity Simulations,” *JOM*, vol. 71, no. 8, pp. 2612–2624, 2019.

- [26] R. Bandyopadhyay, V. Prithivirajan, A. D. Peralta, and M. D. Sangid, "Microstructure sensitive critical plastic strain energy density criterion for fatigue life prediction across various loading regimes," *Proc. R. Soc. A*, p. 20190766, 2020.
- [27] R. Bandyopadhyay and M. D. Sangid, "Crystal plasticity assessment of inclusion- and matrix-driven competing failure modes in a nickel-base superalloy," *Acta Mater.*, vol. 177, pp. 20–34, 2019.
- [28] R. Bandyopadhyay, J. Rotella, D. Naragani, J.-S. S. Park, M. Eff, and M. D. Sangid, "Residual Strain Analysis in Linear Friction Welds of Similar and Dissimilar Titanium Alloys Using Energy Dispersive X-ray Diffraction," *Metall. Mater. Trans. A Phys. Metall. Mater. Sci.*, vol. 50, pp. 704–718, Feb. 2019.
- [29] R. Bandyopadhyay, A. W. Mello, K. Kapoor, M. P. Reinhold, T. F. Broderick, and M. D. Sangid, "On the crack initiation and heterogeneous deformation of Ti-6Al-4V during high cycle fatigue at high R ratios," *J. Mech. Phys. Solids*, vol. 129, pp. 61–82, Aug. 2019.
- [30] J. D. Morrow, "Cyclic plastic strain energy and fatigue of metals," in *Internal friction, damping, and cyclic plasticity*, ASTM STP 378, Philadelphia: American Society for Testing and Materials, 1965, pp. 45–87.
- [31] Y. S. Garud, "A new approach to the evaluation of fatigue under multiaxial loadings," *J. Eng. Mater. Technol.*, vol. 103, no. 118, pp. 118–125, 1981.
- [32] F. Ellyin and D. Kujawski, "Plastic strain energy in fatigue failure," *J. Press. Vessel Technol.*, vol. 106, no. 4, pp. 342–347, 1984.
- [33] J. Park and D. Nelson, "Evaluation of an energy-based approach and a critical plane approach for predicting constant amplitude multiaxial fatigue life," *Int. J. Fatigue*, vol. 22, no. 1, pp. 23–39, 2000.
- [34] A. Varvani-Farahani, "New energy-critical plane parameter for fatigue life assessment of various metallic materials subjected to in-phase and out-of-phase multiaxial fatigue loading conditions," *Int. J. Fatigue*, vol. 22, no. 4, pp. 295–305, 2000.
- [35] T. Łagoda, "Energy models for fatigue life estimation under uniaxial random loading. Part II: Verification of the model," *Int. J. Fatigue*, vol. 23, no. 6, pp. 481–489, 2001.
- [36] T. Łagoda, "Energy models for fatigue life estimation under uniaxial random loading. Part I: The model elaboration," *Int. J. Fatigue*, vol. 23, no. 6, pp. 467–480, 2001.

- [37] K. C. Liu and J. A. Wang, "An energy method for predicting fatigue life, crack orientation, and crack growth under multiaxial loading conditions," *Int. J. Fatigue*, vol. 23, no. 2001, pp. 129–134, 2001.
- [38] G. Gasiak and R. Pawliczek, "Application of an energy model for fatigue life prediction of construction steels under bending, torsion and synchronous bending and torsion," *Int. J. Fatigue*, vol. 25, no. 12, pp. 1339–1346, 2003.
- [39] X. Chen, S. Xu, and D. Huang, "Critical plane-strain energy density criterion for multiaxial low-cycle fatigue life under non-proportional loading," *Fatigue Fract. Eng. Mater. Struct.*, vol. 22, no. 8, pp. 679–686, 1999.
- [40] A. Syed, "Accumulated creep strain and energy density based thermal fatigue life prediction models for SnAgCu solder joints," in *Proceedings of the 54th Electronic Components and Technology Conference (IEEE Cat. No.04CH37546)*, 2004, pp. 737–746.
- [41] H. Jahed and A. Varvani-Farahani, "Upper and lower fatigue life limits model using energy-based fatigue properties," *Int. J. Fatigue*, vol. 28, no. 5–6, pp. 467–473, 2006.
- [42] M. M. Shokrieh and F. Taheri-Behrooz, "A unified fatigue life model based on energy method," *Compos. Struct.*, vol. 75, no. 1–4, pp. 444–450, 2006.
- [43] F. Ellyin and K. Golos, "Multiaxial fatigue damage criterion," *J. Eng. Mater. Technol.*, vol. 110, no. 1, pp. 63–68, 1988.
- [44] H. Jahed, A. Varvani-Farahani, M. Noban, and I. Khalaji, "An energy-based fatigue life assessment model for various metallic materials under proportional and non-proportional loading conditions," *Int. J. Fatigue*, vol. 29, no. 4, pp. 647–655, 2007.
- [45] K.-O. Lee, S.-G. Hong, and S.-B. Lee, "A new energy-based fatigue damage parameter in life prediction of high-temperature structural materials," *Mater. Sci. Eng. A*, vol. 496, no. 1–2, pp. 471–477, 2008.
- [46] O. E. Scott-Emuakpor, H. Shen, T. George, and C. Cross, "An energy-based uniaxial fatigue life prediction method for commonly used gas turbine engine materials," *J. Eng. Gas Turbines Power*, vol. 130, no. 6, p. 062504, 2008.
- [47] M. Naderi, M. Amiri, and M. M. Khonsari, "On the thermodynamic entropy of fatigue fracture," *Proc. R. Soc. A Math. Phys. Eng. Sci.*, vol. 466, no. 2114, pp. 423–438, 2010.

- [48] S.-P. Zhu, H.-Z. Huang, L.-P. He, Y. Liu, and Z. Wang, “A generalized energy-based fatigue-creep damage parameter for life prediction of turbine disk alloys,” *Eng. Fract. Mech.*, vol. 90, pp. 89–100, 2012.
- [49] K. Golos and F. Ellyin, “A total strain energy density theory for cumulative fatigue damage,” *J. Press. Vessel Technol.*, vol. 110, no. 1, pp. 36–41, 1988.
- [50] F. Ellyin and Z. Xia, “A general fatigue theory and its application to out-of-phase cyclic loading,” *J. Eng. Mater. Technol.*, vol. 115, no. 4, pp. 411–416, 1993.
- [51] F. Ellyin and D. Kujawski, “A multiaxial fatigue criterion including mean-stress effect,” in *Advances in Multiaxial Fatigue, ASTM STP 1191*, vol. 1191, D. L. McDowell and R. Ellis, Eds. 1993, pp. 55–66.
- [52] K. C. Liu, “A method based on virtual strain-energy parameters for multiaxial fatigue life prediction,” in *Advances in Multiaxial Fatigue, ASTM STP 1191*, D. L. McDowell and R. Ellis, Eds. Philadelphia: American Society for Testing and Materials, 1993, pp. 67–84.
- [53] C.-C. Chu, F. A. Conle, and J. J. F. Bonnen, “Multiaxial stress-strain modeling and fatigue life prediction of SAE axle shafts,” in *Advances in Multiaxial Fatigue*, D. L. McDowell and R. Ellis, Eds. Philadelphia: American Society for Testing and Materials, 1993, pp. 37–54.
- [54] G. Glinka, G. Shen, and A. Plumtree, “A multiaxial fatigue strain energy density parameter related to the critical fracture plane,” *Fatigue Fract. Eng. Mater. Struct.*, vol. 18, no. 1, pp. 37–46, 1995.
- [55] G. Glinka, G. Wang, and A. Plumtree, “Mean stress effects in multiaxial fatigue,” *Fatigue Fract. Eng. Mater. Struct.*, vol. 18, no. 7, pp. 755–764, 1995.
- [56] N. Thompson, N. Wadsworth, and N. Louat, “The origin of fatigue fracture in copper,” *Philos. Mag.*, vol. 1, no. 2, pp. 113–126, 1956.
- [57] A. Fatemi and D. F. Socie, “A critical plane approach to multiaxial fatigue damage including out-of-phase loading,” *Fatigue Fract. Eng. Mater. Struct.*, vol. 11, no. 3, pp. 149–165, 1988.
- [58] D. L. McDowell, “Microstructure-sensitive computational fatigue analysis,” in *Handbook of Materials Modeling*, S. Yip, Ed. Springer, 2005, pp. 1193–1214.
- [59] M. M. Shenoy, A. P. Gordon, D. L. McDowell, and R. W. Neu, “Thermomechanical fatigue behavior of a directionally solidified Ni-base superalloy,” *J. Eng. Mater. Technol.*, vol. 127, no. 3, pp. 325–336, 2005.

- [60] M. Shenoy, J. Zhang, and D. L. McDowell, "Estimating fatigue sensitivity to polycrystalline Ni-base superalloy microstructures using a computational approach," *Fatigue Fract. Eng. Mater. Struct.*, vol. 30, no. 10, pp. 889–904, 2007.
- [61] Y. Xue, D. L. McDowell, M. F. Horstemeyer, M. H. Dale, and J. B. Jordon, "Microstructure-based multistage fatigue modeling of aluminum alloy 7075-T651," *Eng. Fract. Mech.*, vol. 74, no. 17, pp. 2810–2823, 2007.
- [62] C. P. Przybyla, R. Prasannavenkatesan, N. Salajegheh, and D. L. McDowell, "Microstructure-sensitive modeling of high cycle fatigue," *Int. J. Fatigue*, vol. 32, no. 3, pp. 512–525, 2010.
- [63] C. P. Przybyla and D. L. McDowell, "Microstructure-sensitive extreme value probabilities for high cycle fatigue of Ni-base superalloy IN100," *Int. J. Plast.*, vol. 26, no. 3, pp. 372–394, 2010.
- [64] C. P. Przybyla and D. L. McDowell, "Microstructure-sensitive extreme-value probabilities of high-cycle fatigue for surface vs. subsurface crack formation in duplex Ti-6Al-4V," *Acta Mater.*, vol. 60, no. 1, pp. 293–305, 2012.
- [65] C. P. Przybyla, W. D. Musinski, G. M. Castelluccio, and D. L. McDowell, "Microstructure-sensitive HCF and VHCF simulations," *Int. J. Fatigue*, vol. 57, pp. 9–27, 2013.
- [66] S. Sinha and S. Ghosh, "Modeling cyclic ratcheting based fatigue life of HSLA steels using crystal plasticity FEM simulations and experiments," *Int. J. Fatigue*, vol. 28, no. 12, pp. 1690–1704, 2006.
- [67] K. Kirane and S. Ghosh, "A cold dwell fatigue crack nucleation criterion for polycrystalline Ti-6242 using grain-level crystal plasticity FE Model," *Int. J. Fatigue*, vol. 30, no. 12, pp. 2127–2139, 2008.
- [68] M. Anahid, M. K. Samal, and S. Ghosh, "Dwell fatigue crack nucleation model based on crystal plasticity finite element simulations of polycrystalline titanium alloys," *J. Mech. Phys. Solids*, vol. 59, no. 10, pp. 2157–2176, 2011.
- [69] M. D. Sangid, H. J. Maier, and H. Sehitoglu, "A physically based fatigue model for prediction of crack initiation from persistent slip bands in polycrystals," *Acta Mater.*, vol. 59, no. 1, pp. 328–341, 2011.

- [70] M. D. Sangid, H. J. Maier, and H. Sehitoglu, “An energy-based microstructure model to account for fatigue scatter in polycrystals,” *J. Mech. Phys. Solids*, vol. 59, no. 3, pp. 595–609, 2011.
- [71] S. R. Yeratapally, M. G. Glavicic, M. Hardy, and M. D. Sangid, “Microstructure based fatigue life prediction framework for polycrystalline nickel-base superalloys with emphasis on the role played by twin boundaries in crack initiation,” *Acta Mater.*, vol. 107, pp. 152–167, 2016.
- [72] A. M. Korsunsky, D. Dini, F. P. E. Dunne, and M. J. Walsh, “Comparative assessment of dissipated energy and other fatigue criteria,” *Int. J. Fatigue*, vol. 29, no. 9–11, pp. 1990–1995, 2007.
- [73] V. V. C. Wan, D. W. Maclachlan, and F. P. E. Dunne, “A stored energy criterion for fatigue crack nucleation in polycrystals,” *Int. J. Fatigue*, vol. 68, pp. 90–102, 2014.
- [74] J. Jiang *et al.*, “Microstructurally sensitive crack nucleation around inclusions in powder metallurgy nickel-based superalloys,” *Acta Mater.*, vol. 117, pp. 333–344, 2016.
- [75] B. Chen, J. Jiang, and F. P. E. Dunne, “Is stored energy density the primary meso-scale mechanistic driver for fatigue crack nucleation?,” *Int. J. Plast.*, vol. 101, pp. 213–229, 2018.
- [76] D. Wilson, Z. Zheng, and F. P. E. Dunne, “A microstructure-sensitive driving force for crack growth,” *J. Mech. Phys. Solids*, vol. 121, pp. 147–174, 2018.
- [77] D. Wilson and F. P. E. Dunne, “A mechanistic modelling methodology for microstructure-sensitive fatigue crack growth,” *J. Mech. Phys. Solids*, vol. 124, pp. 827–848, 2019.
- [78] D. Wilson, W. Wan, and F. P. E. Dunne, “Microstructurally-sensitive fatigue crack growth in HCP, BCC and FCC polycrystals,” *J. Mech. Phys. Solids*, vol. 126, pp. 204–225, 2019.
- [79] A. Cruzado, S. Lucarini, J. LLorca, and J. Segurado, “Microstructure-based fatigue life model of metallic alloys with bilinear Coffin-Manson behavior,” *Int. J. Fatigue*, vol. 107, pp. 40–48, 2018.
- [80] A. Pineau, “The Randomness of Fatigue and Fracture Behaviour in Metallic Materials and Mechanical Structures,” in *Mechanics of Random and Multiscale Microstructures*, D. Jeulin and M. Ostojca-Starzewski, Eds. Vienna: Springer Vienna, 2001, pp. 163–219.
- [81] M. Detrois, J. Rotella, M. Hardy, S. Tin, and M. D. Sangid, “Tailoring the Properties of a Ni-Based Superalloy via Modification of the Forging Process: an ICME Approach to Fatigue Performance,” *Integr. Mater. Manuf. Innov.*, vol. 6, no. 4, pp. 265–278, Dec. 2017.

- [82] K. Tanaka and T. Mura, "A theory of fatigue crack initiation at inclusions," *Metall. Trans. A*, vol. 13, no. 1, pp. 117–123, 1982.
- [83] M. Caton, S. Jha, A. Rosenberger, and J. Larsen, "Divergence of Mechanisms and the Effect on the Fatigue Life Variability of Rene' 88 DT," *Superalloys*, pp. 305–312, 2004.
- [84] D. Texier *et al.*, "Crack initiation sensitivity of wrought direct aged alloy 718 in the very high cycle fatigue regime: the role of non-metallic inclusions," *Mater. Sci. Eng. A*, vol. 678, pp. 122–136, 2016.
- [85] D. Texier *et al.*, "Microstructural Features Controlling the Variability in Low-Cycle Fatigue Properties of Alloy Inconel 718DA at Intermediate Temperature," *Metall. Mater. Trans. A Phys. Metall. Mater. Sci.*, vol. 47, no. 3, pp. 1096–1109, 2016.
- [86] C. Qiu and X. Wu, "High cycle fatigue and fracture behaviour of a hot isostatically pressed nickel-based superalloy," *Philos. Mag.*, vol. 94, no. 3, pp. 242–264, 2014.
- [87] F. Alexandre, S. Deyber, and A. Pineau, "Modelling the optimum grain size on the low cycle fatigue life of a Ni based superalloy in the presence of two possible crack initiation sites," *Scr. Mater.*, vol. 50, no. 1, pp. 25–30, 2004.
- [88] J. M. Hyzak and I. M. Bernstein, "The effect of defects on the fatigue crack initiation process in two p/m superalloys: part i. fatigue origins," *Metall. Trans. A*, vol. 13, no. 1, pp. 33–43, 1982.
- [89] E. S. Huron and P. G. Roth, "The Influence of Inclusions on Low Cycle Fatigue Life in a P/M Nickel-Base Disk Superalloy," *Superalloys*, pp. 359–368, 1996.
- [90] P. R. Bhowal and A. M. Wusatowska-Sarnek, "Carbides and Their Influence on Notched Low Cycle Fatigue Behavior of Fine-Grained IN718 Gas Turbine," in *Superalloys 718, 625, 706 and Derivatives*, E. A. Loria, Ed. The Minerals, Metals & Materials Society, 2005, pp. 341–349.
- [91] J. D. Eshelby, "The determination of the elastic field of an ellipsoidal inclusion, and related problems," *Proc. R. Soc. A Math. Phys. Eng. Sci.*, vol. 241, no. 1226, pp. 376–396, Aug. 1957.
- [92] J. D. Eshelby, "The elastic field outside an ellipsoidal inclusion," *Proc. R. Soc. London. Ser. A. Math. Phys. Sci.*, vol. 252, no. 1271, pp. 561–569, Oct. 1959.
- [93] M. F. Ashby and L. M. Brown, "On diffraction contrast from inclusions," *Philos. Mag.*, vol. 8, no. 94, pp. 1649–1676, 1963.

- [94] M. M. Shenoy, R. S. Kumar, and D. L. McDowell, "Modeling effects of nonmetallic inclusions on LCF in DS nickel-base superalloys," *Int. J. Fatigue*, vol. 27, no. 2, pp. 113–127, Feb. 2005.
- [95] T. Zhang, D. M. Collins, F. P. E. Dunne, and B. A. Shollock, "Crystal plasticity and high-resolution electron backscatter diffraction analysis of full-field polycrystal Ni superalloy strains and rotations under thermal loading," *Acta Mater.*, vol. 80, pp. 25–38, 2014.
- [96] T. Zhang, J. Jiang, B. A. Shollock, T. Ben Britton, and F. P. E. Dunne, "Slip localization and fatigue crack nucleation near a non-metallic inclusion in polycrystalline nickel-based superalloy," *Mater. Sci. Eng. A*, vol. 641, pp. 328–339, 2015.
- [97] J. Jiang, J. Yang, T. Zhang, F. P. E. Dunne, and T. Ben Britton, "On the mechanistic basis of fatigue crack nucleation in Ni superalloy containing inclusions using high resolution electron backscatter diffraction," *Acta Mater.*, vol. 97, pp. 367–379, 2015.
- [98] T. Zhang, J. Jiang, B. Britton, B. Shollock, and F. Dunne, "Crack nucleation using combined crystal plasticity modelling, high-resolution digital image correlation and high-resolution electron backscatter diffraction in a superalloy containing non-metallic inclusions under fatigue," *Proc. R. Soc. A Math. Phys. Eng. Sci.*, vol. 472, no. 2189, 2016.
- [99] D. Naragani *et al.*, "Investigation of fatigue crack initiation from a non-metallic inclusion via high energy x-ray diffraction microscopy," *Acta Mater.*, vol. 137, pp. 71–84, 2017.
- [100] J.-C. Stinville *et al.*, "Competing Modes for Crack Initiation from Non-metallic Inclusions and Intrinsic Microstructural Features During Fatigue in a Polycrystalline Nickel-Based Superalloy," *Metall. Mater. Trans. A*, vol. 49, no. 9, pp. 3865–3873, Sep. 2018.
- [101] R. Prasannavenkatesan, J. Zhang, D. L. McDowell, G. B. Olson, and H. Jou, "3D modeling of subsurface fatigue crack nucleation potency of primary inclusions in heat treated and shot peened martensitic gear steels," *Int. J. Fatigue*, vol. 31, no. 7, pp. 1176–1189, 2009.
- [102] J. Zhang, R. Prasannavenkatesan, M. M. Shenoy, and D. L. McDowell, "Modeling fatigue crack nucleation at primary inclusions in carburized and shot-peened martensitic steel," *Eng. Fract. Mech.*, vol. 76, no. 3, pp. 315–334, Feb. 2009.
- [103] J. D. Hochhalter *et al.*, "A geometric approach to modeling microstructurally small fatigue crack formation: II. Physically based modeling of microstructure-dependent slip localization and actuation of the crack nucleation mechanism in AA 7075-T651," *Model. Simul. Mater. Sci. Eng.*, vol. 18, no. 4, p. 045004, Jun. 2010.

- [104] J. D. Hochhalter *et al.*, “A geometric approach to modeling microstructurally small fatigue crack formation: III. Development of a semi-empirical model for nucleation,” *Model. Simul. Mater. Sci. Eng.*, vol. 19, no. 3, p. 035008, Apr. 2011.
- [105] A. Pineau and S. D. Antolovich, “Probabilistic approaches to fatigue with special emphasis on initiation from inclusions,” *Int. J. Fatigue*, vol. 93, pp. 422–434, 2016.
- [106] P. J. Withers and H. K. D. H. Bhadeshia, “Residual stress. Part 1 – Measurement techniques,” *Mater. Sci. Technol.*, vol. 17, no. 4, pp. 355–365, 2001.
- [107] V. Hauk, *Structural and Residual Stress Analysis by Nondestructive Methods*. Elsevier, 1997.
- [108] I. A. Denks, M. Klaus, and C. Genzel, “Determination of Real Space Residual Stress Distributions  $\sigma_{ij}(z)$  of Surface Treated Materials with Diffraction Methods Part II: Energy Dispersive Approach,” *Mater. Sci. Forum*, vol. 524–525, pp. 37–44, 2006.
- [109] C. Genzel *et al.*, “Exploiting the features of energy-dispersive synchrotron diffraction for advanced residual stress and texture analysis,” *J. Strain Anal. Eng. Des.*, vol. 46, no. 7, pp. 615–625, 2011.
- [110] W. Reimers *et al.*, “Evaluation of Residual Stresses in the Bulk of Materials by High Energy Synchrotron Diffraction,” *J. Non-Destructive Eval.*, vol. 17, no. 17, pp. 129–140, 1998.
- [111] A. Steuwer, J. R. Santisteban, M. Turski, P. J. Withers, and T. Buslaps, “High-resolution strain mapping in bulk samples using full-profile analysis of energy-dispersive synchrotron X-ray diffraction data,” *J. Appl. Crystallogr.*, vol. 37, no. 6, pp. 883–889, 2004.
- [112] M. Croft *et al.*, “Strain field and scattered intensity profiling with energy dispersive x-ray scattering,” *J. Appl. Phys.*, vol. 92, no. 1, pp. 578–586, 2002.
- [113] M. R. Daymond and N. W. Bonner, “Measurement of strain in a titanium linear friction weld by neutron diffraction,” *Phys. B Condens. Matter*, vol. 325, pp. 130–137, 2003.
- [114] M. Preuss, J. Quinta Da Fonseca, A. Steuwer, L. Wang, P. J. Withers, and S. Bray, “Residual stresses in linear friction welded IMI550,” *J. Neutron Res.*, vol. 12, no. 1–3, pp. 165–173, 2004.
- [115] J. Romero, M. M. Attallah, M. Preuss, M. Karadge, and S. E. Bray, “Effect of the forging pressure on the microstructure and residual stress development in Ti-6Al-4V linear friction welds,” *Acta Mater.*, vol. 57, no. 18, pp. 5582–5592, 2009.

- [116] P. Frankel, M. Preuss, A. Steuwer, P. J. Withers, and S. Bray, “Comparison of residual stresses in Ti-6Al-4V and Ti-6Al-2Sn-4Zr-2Mo linear friction welds,” *Mater. Sci. Technol.*, vol. 25, no. 5, pp. 640–650, 2009.
- [117] P. Xie, H. Zhao, and Y. Liu, “Measuring residual stresses in linear friction welded joints composed by dissimilar titanium,” *Sci. Technol. Weld. Join.*, vol. 21, no. 5, pp. 351–357, 2016.
- [118] G. Q. Wu, C. L. Shi, W. Sha, A. X. Sha, and H. R. Jiang, “Effect of microstructure on the fatigue properties of Ti-6Al-4V titanium alloys,” *Mater. Des.*, vol. 46, pp. 668–674, 2013.
- [119] R. J. Morrissey, D. L. McDowell, and T. Nicholas, “Frequency and stress ratio effects in high cycle fatigue of Ti-6Al-4V,” *Int. J. Fatigue*, vol. 21, no. 7, pp. 679–685, 1999.
- [120] R. J. Morrissey, D. L. McDowell, and T. Nicholas, “Microplasticity in HCF of Ti-6Al-4V,” *Int. J. Fatigue*, vol. 23, pp. 55–64, 2001.
- [121] X. Liu, C. Sun, and Y. Hong, “Effects of stress ratio on high-cycle and very-high-cycle fatigue behavior of a Ti-6Al-4V alloy,” *Mater. Sci. Eng. A*, vol. 622, pp. 228–235, 2015.
- [122] K. Kirane, S. Ghosh, M. Groeber, and A. Bhattacharjee, “Grain Level Dwell Fatigue Crack Nucleation Model for Ti Alloys Using Crystal Plasticity Finite Element Analysis,” *J. Eng. Mater. Technol.*, vol. 131, no. 2, p. 021003, 2009.
- [123] M. Zhang, J. Zhang, and D. L. McDowell, “Microstructure-based crystal plasticity modeling of cyclic deformation of Ti-6Al-4V,” *Int. J. Plast.*, vol. 23, no. 8, pp. 1328–1348, 2007.
- [124] F. Bridier, D. L. McDowell, P. Villechaise, and J. Mendez, “Crystal plasticity modeling of slip activity in Ti-6Al-4V under high cycle fatigue loading,” *Int. J. Plast.*, vol. 25, no. 6, pp. 1066–1082, 2009.
- [125] C. P. Przybyla and D. L. McDowell, “Simulated microstructure-sensitive extreme value probabilities for high cycle fatigue of duplex Ti-6Al-4V,” *Int. J. Plast.*, vol. 27, no. 12, pp. 1871–1895, 2011.
- [126] M. Kasemer, M. P. Echlin, J. C. Stinville, T. M. Pollock, and P. Dawson, “On slip initiation in equiaxed  $\alpha/\beta$  Ti-6Al-4V,” *Acta Mater.*, vol. 136, pp. 288–302, 2017.
- [127] M. Kasemer, R. Quey, and P. Dawson, “The influence of mechanical constraints introduced by  $\beta$  annealed microstructures on the yield strength and ductility of Ti-6Al-4V,” *J. Mech. Phys. Solids*, vol. 103, pp. 179–198, 2017.

- [128] F. P. E. Dunne, A. Walker, and D. Rugg, “A systematic study of hcp crystal orientation and morphology effects in polycrystal deformation and fatigue,” *Proc. R. Soc. A Math. Phys. Eng. Sci.*, vol. 463, no. 2082, pp. 1467–1489, 2007.
- [129] F. P. E. Dunne and D. Rugg, “On the mechanisms of fatigue facet nucleation in titanium alloys,” *Fatigue Fract. Eng. Mater. Struct.*, vol. 31, no. 11, pp. 949–958, 2008.
- [130] T. A. Book and M. D. Sangid, “Strain localization in Ti-6Al-4V Widmanstätten microstructures produced by additive manufacturing,” *Mater. Charact.*, vol. 122, pp. 104–112, 2016.
- [131] M. P. Echlin, J. C. Stinville, V. M. Miller, W. C. Lenthe, and T. M. Pollock, “Incipient slip and long range plastic strain localization in microtextured Ti-6Al-4V titanium,” *Acta Mater.*, vol. 114, pp. 164–175, 2016.
- [132] D. Lunt, J. Q. da Fonseca, D. Rugg, and M. Preuss, “Microscopic strain localisation in Ti-6Al-4V during uniaxial tensile loading,” *Mater. Sci. Eng. A*, vol. 680, no. October 2016, pp. 444–453, 2017.
- [133] D. Lunt, X. Xu, T. Busolo, J. Quinta da Fonseca, and M. Preuss, “Quantification of strain localisation in a bimodal two-phase titanium alloy,” *Scr. Mater.*, vol. 145, pp. 45–49, 2018.
- [134] E. H. Lee, “Elastic-Plastic Deformation at Finite Strains,” *J. Appl. Mech.*, vol. 36, no. 1, pp. 1–6, 1969.
- [135] I. Karaman, H. Sehitoglu, A. J. Beaudoin, Y. I. Chumlyakov, H. J. Maier, and C. N. Tome, “Modeling the deformation behavior of hadfield steel single and polycrystals due to twinning and slip,” vol. 48, pp. 2031–2047, 2000.
- [136] S. Balasubramanian and L. Anand, “Plasticity of initially textured hexagonal polycrystals at high homologous temperatures: Application to titanium,” *Acta Mater.*, vol. 50, no. 1, pp. 133–148, 2002.
- [137] A. Guery, F. Hild, F. Latourte, and S. Roux, “Identification of crystal plasticity parameters using DIC measurements and weighted FEMU,” *Mech. Mater.*, vol. 100, pp. 55–71, 2016.
- [138] P. Dawson, D. Boyce, S. MacEwen, and R. Rogge, “Residual strains in HY100 polycrystals: comparisons of experiments and simulations,” *Metall. Mater. Trans. A Phys. Metall. Mater. Sci.*, vol. 31, no. 6, pp. 1543–1555, 2000.
- [139] D. C. Pagan *et al.*, “Modeling slip system strength evolution in Ti-7Al informed by in-situ grain stress measurements,” *Acta Mater.*, vol. 128, pp. 406–417, 2017.

- [140] S. R. Yeratapally, M. G. Glavicic, C. Argyrakis, and M. D. Sangid, “Bayesian uncertainty quantification and propagation for validation of a microstructure sensitive model for prediction of fatigue crack initiation,” *Reliab. Eng. Syst. Saf.*, vol. 164, pp. 110–123, Aug. 2017.
- [141] R. C. Smith, *Uncertainty Quantification: Theory, Implementation, and Applications*. SIAM, 2013.
- [142] A. Haldar and S. Mahadevan, *Probability, reliability, and statistical methods in engineering design*. Wiley, 2000.
- [143] M. D. Sangid *et al.*, “Role of heat treatment and build orientation in the microstructure sensitive deformation characteristics of IN718 produced via additive manufacturing,” *Addit. Manuf.*, vol. 22, pp. 479–496, 2018.
- [144] M. A. Groeber and M. A. Jackson, “DREAM.3D: a digital representation environment for the analysis of microstructure in 3D,” *Integr. Mater. Manuf. Innov.*, vol. 3, no. 5, pp. 1–17, 2014.
- [145] <http://dream3d.bluequartz.net/binaries/Help/DREAM3D/>,  
“<http://dream3d.bluequartz.net/binaries/Help/DREAM3D/>,” 2013. .
- [146] M. Groeber, “Development of an Automated Characterization- Representation Framework for the Modeling of Polycrystalline Materials in 3D,” Ohio State University, 2007.
- [147] M. D. Sangid, H. Sehitoglu, H. J. Maier, and T. Niendorf, “Grain boundary characterization and energetics of superalloys,” *Mater. Sci. Eng. A*, vol. 527, no. 26, pp. 7115–7125, 2010.
- [148] L. H. Chan, “Synthetic three-dimensional voxel-based microstructures that contain annealing twins,” Carnegie Mellon University, 2010.
- [149] G. Taylor, “Plastic strain in metals,” *J. Inst. Met.*, vol. 62, no. 307, 1938.
- [150] J. Bishop and R. Hill, “A theory of the plastic distortion of a polycrystalline aggregate under combined stresses,” *Philos. Mag.*, vol. 42, no. 1298, 1951.
- [151] H. J. Bunge, “Some applications of the Taylor theory of polycrystal plasticity,” *Krist. und Tech.*, vol. 5, no. 1, pp. 145–175, 1970.
- [152] C. Geuzaine and J.-F. Remacle, “Gmsh: a three-dimensional finite element mesh generator with built-in pre- and post-processing facilities,” *Int. J. Numer. Methods Eng.* 79(11), vol. 0, pp. 1309–1331, 2009.

- [153] R. J. Asaro, “Crystal Plasticity,” *J. Appl. Mech.*, vol. 50, no. 4b, p. 921, Dec. 1983.
- [154] L. Anand and M. Kothari, “A computational procedure for rate-independent crystal plasticity,” *J. Mech. Phys. Solids*, vol. 44, no. 4, pp. 525–558, 1996.
- [155] F. Roters, P. Eisenlohr, L. Hantcherli, D. D. Tjahjanto, T. R. Bieler, and D. Raabe, “Overview of constitutive laws, kinematics, homogenization and multiscale methods in crystal plasticity finite-element modeling: Theory, experiments, applications,” *Acta Mater.*, vol. 58, no. 4, pp. 1152–1211, 2010.
- [156] J. R. Rice, “Inelastic constitutive relations for solids: An internal variables theory and its application to metal plasticity,” *J. Mech. Phys. Solids*, vol. 19, no. 6, pp. 433–455, 1971.
- [157] J. W. Hutchinson, “Creep and plasticity of hexagonal polycrystals as related to single crystal slip,” *Metall. Trans. A*, vol. 8A, no. September, pp. 1465–1469, 1977.
- [158] C. O. Frederick and P. J. Armstrong, “A mathematical representation of the multiaxial Bauschinger effect A mathematical representation of the multiaxial Bauschinger effect,” vol. 3409, no. December, 1966.
- [159] M. F. Horstemeyer, D. L. McDowell, and R. D. McGinty, “Design of experiments for constitutive model selection: application to polycrystal elastoviscoplasticity,” *Model. Simul. Mater. Sci. Eng.*, vol. 7, pp. 253–273, 1999.
- [160] U. F. Kocks, “The relation between polycrystal deformation and single-crystal deformation,” *Metall. Mater. Trans.*, vol. 1, no. 5, pp. 1121–1143, 1970.
- [161] V. Prithvirajan and M. D. Sangid, “The role of defects and critical pore size analysis in the fatigue response of additively manufactured IN718 via crystal plasticity,” *Mater. Des.*, vol. 150, pp. 139–153, 2018.
- [162] A. Manonukul and F. P. E. Dunne, “High- and low-cycle fatigue crack initiation using polycrystal plasticity,” *Proc. R. Soc. A Math. Phys. Eng. Sci.*, vol. 460, no. 2047, pp. 1881–1903, 2004.
- [163] A. D. Peralta, M. Enright, M. Megahed, J. Gong, M. Roybal, and J. Craig, “Towards rapid qualification of powder-bed laser additively manufactured parts,” *Integr. Mater. Manuf. Innov.*, vol. 5, no. 1, p. 8, 2016.
- [164] J. Gong *et al.*, “Integrated Thermal Process Optimization of Alloy 718Plus<sup>®</sup> for Additive Manufacturing,” *Superalloys 2016*, pp. 1031–1040, 2016.

- [165] Allegheny Technologies Incorporated, “ATI 718Plus® Alloy Technical Data Sheet, UNS N07818,” 2013. [Online]. Available: [https://www.atimetals.com/Products/Documents/datasheets/nickel-cobalt/nickel-based/ati\\_718plus\\_tds\\_en\\_v3.pdf](https://www.atimetals.com/Products/Documents/datasheets/nickel-cobalt/nickel-based/ati_718plus_tds_en_v3.pdf).
- [166] ASTM Standard E606/E606M-12, “Standard test method for strain-controlled fatigue testing,” in *Annual Book of ASTM Standards*, vol. 03.01, 2012.
- [167] P. Haldipur, F. J. Margetan, and R. B. Thompson, “Estimation of single-crystal elastic constants from ultrasonic measurements on polycrystalline specimens,” in *AIP Conference Proceedings*, 2004, vol. 700, no. 1, pp. 1061–1068.
- [168] J. Cheng, A. Shahba, and S. Ghosh, “Stabilized tetrahedral elements for crystal plasticity finite element analysis overcoming volumetric locking,” *Comput. Mech.*, vol. 57, no. 5, pp. 733–753, 2016.
- [169] G. M. Castelluccio and D. L. McDowell, “Microstructure and mesh sensitivities of mesoscale surrogate driving force measures for transgranular fatigue cracks in polycrystals,” *Mater. Sci. Eng. A*, vol. 639, pp. 626–639, 2015.
- [170] A. Rovinelli, M. D. Sangid, H. Proudhon, Y. Guilhem, R. A. Lebensohn, and W. Ludwig, “Predicting the 3D fatigue crack growth rate of small cracks using multimodal data via Bayesian networks: In-situ experiments and crystal plasticity simulations,” *J. Mech. Phys. Solids*, vol. 115, pp. 208–229, Jun. 2018.
- [171] A. Rovinelli, M. D. Sangid, H. Proudhon, and W. Ludwig, “Using machine learning and a data-driven approach to identify the small fatigue crack driving force in polycrystalline materials,” *npj Comput. Mater.*, vol. 4, no. 1, Dec. 2018.
- [172] A. Nicolas, N. E. C. Co, J. T. Burns, and M. D. Sangid, “Predicting fatigue crack initiation from coupled microstructure and corrosion morphology effects,” *Eng. Fract. Mech.*, vol. 220, p. 106661, Oct. 2019.
- [173] R. C. Smith, *Uncertainty quantification: theory, implementation, and applications*. SIAM, 2013.
- [174] N. Metropolis, A. W. Rosenbluth, M. N. Rosenbluth, A. H. Teller, and E. Teller, “Equation of state calculations by fast computing machines,” *J. Chem. Phys.*, vol. 21, no. 6, pp. 1087–1092, 1953.

- [175] W. K. Hastings, “Monte Carlo sampling methods using Markov chains and their applications,” *Biometrika*, vol. 57, no. 1, pp. 97–109, 1970.
- [176] R. Cross, A. Makeev, and E. Armanios, “Simultaneous uncertainty quantification of fracture mechanics based life prediction model parameters,” *Int. J. Fatigue*, vol. 29, no. 8, pp. 1510–1515, 2007.
- [177] D. Macdougall, “Determination of the plastic work converted to heat using radiometry,” *Exp. Mech.*, vol. 40, no. 3, pp. 298–306, 2000.
- [178] P. Knysh and Y. P. Korkolis, “Determination of the fraction of plastic work converted into heat in metals,” *Mech. Mater.*, vol. 86, pp. 71–80, 2015.
- [179] D. R. Chang, D. D. Krueger, and R. A. Sprague, “Superalloy Powder Processing, Properties, and Turbine Disk Applications,” in *Proceedings of the Fifth International Symposium on Superalloys*, 1984, pp. 245–273.
- [180] I. M. D. Parr *et al.*, “Inhomogeneous Grain Coarsening Behavior in Supersolvus Heat Treated Nickel-Based Superalloy RR1000,” in *Superalloys 2016*, Hoboken, NJ, USA: John Wiley & Sons, Inc., 2016, pp. 447–456.
- [181] A. W. Mello, A. Nicolas, and M. D. Sangid, “Fatigue strain mapping via digital image correlation for Ni-based superalloys: The role of thermal activation on cube slip,” *Mater. Sci. Eng. A*, vol. 695, pp. 332–341, May 2017.
- [182] H. Wadell, “Volume, Shape and Roundness of Quartz Particles,” *J. Geol.*, vol. 43, no. 3, pp. 250–280, 1935.
- [183] C. Geuzaine and J. F. Remacle, “Gmsh: A 3-D finite element mesh generator with built-in pre- and post-processing facilities,” *Int. J. Numer. Methods Eng.*, vol. 79, pp. 1309–1331, 2012.
- [184] J. W. Hutchinson, “Bounds and self-consistent estimates for creep of polycrystalline materials,” *Proc. R. Soc. A Math. Phys. Eng. Sci.*, vol. 348, no. 1652, pp. 101–127, 1976.
- [185] U. Essmann and H. Mughrabi, “Annihilation of dislocations during tensile and cyclic deformation and limits of dislocation densities,” *Philos. Mag. A Phys. Condens. Matter, Struct. Defects Mech. Prop.*, vol. 40, no. 6, pp. 731–756, 1979.
- [186] H. Mecking and U. F. Kocks, “Kinetics of flow and strain-hardening,” *Acta Metall.*, vol. 29, no. 11, pp. 1865–1875, 1981.

- [187] U. F. Kocks and H. Mecking, “Physics and phenomenology of strain hardening: the FCC case,” *Prog. Mater. Sci.*, vol. 48, pp. 171–273, 2003.
- [188] U. F. Kocks, A. S. Argon, and M. F. Ashby, “Thermodynamics and kinetics of slip,” *Prog. Mater. Sci.*, vol. 19, 1975.
- [189] I. J. Beyerlein and C. N. Tomé, “A dislocation-based constitutive law for pure Zr including temperature effects,” *Int. J. Plast.*, vol. 24, no. 5, pp. 867–895, 2008.
- [190] C. O. Frederick and P. J. Armstrong, “A mathematical representation of the multiaxial Bauschinger effect,” *Mater. High Temp.*, vol. 24, no. 1, pp. 1–26, 2007.
- [191] R. D. McGinty, “Multiscale Representation of Polycrystalline Inelasticity,” Georgia Institute of Technology, 2001.
- [192] Y. Wang *et al.*, “A first-principles approach to finite temperature elastic constants,” *J. Phys. Condens. Matter*, vol. 22, no. 22, p. 225404, 2010.
- [193] S. D. Antolovich and R. W. Armstrong, “Plastic strain localization in metals: Origins and consequences,” *Prog. Mater. Sci.*, vol. 59, no. 1, pp. 1–160, 2014.
- [194] R. Deng, F. Liu, L. Tan, S. Zhang, Y. Liu, and L. Huang, “Effects of scandium on microstructure and mechanical properties of RR1000,” *J. Alloys Compd.*, vol. 785, pp. 634–641, May 2019.
- [195] M. Gell and G. Leverant, “Mechanisms of High-Temperature Fatigue,” in *Fatigue at Elevated Temperatures*, West Conshohocken, PA: ASTM International, 1973, pp. 37–67.
- [196] D. A. Jablonski, “The effect of ceramic inclusions on the low cycle fatigue life of low carbon astroloy subjected to hot isostatic pressing,” *Mater. Sci. Eng.*, vol. 48, no. 2, pp. 189–198, May 1981.
- [197] R. N. Patil and E. C. Subbarao, “Axial thermal expansion of  $ZrO_2$  and  $HfO_2$  in the range room temperature to  $1400^\circ C$ ,” *J. Appl. Crystallogr.*, vol. 2, no. 6, pp. 281–288, Dec. 2002.
- [198] R. V Miner, T. P. Gabb, J. Gayda, and K. J. Hemker, “Orientation and Temperature Dependence of Some Mechanical Properties of the Single-Crystal Nickel-Base Superalloy Ren6 N4: Part III. Tension-Compression Anisotropy,” *Metall. Trans. A*, vol. 17, no. 3, pp. 507–512, 1986.
- [199] G. Hoinard, R. Estevez, and P. Franciosi, “Hardening anisotropy of  $\gamma/\gamma'$  superalloy single crystals—I. Experimental estimates at  $650^\circ C$  from a homogeneous analysis,” *Acta Metall. Mater.*, vol. 43, no. 4, pp. 1593–1607, Apr. 1995.

- [200] M. Kolbe, K. Neuking, and G. Eggeler, “Dislocation reactions and microstructural instability during 1025 °C shear creep testing of superalloy single crystals,” *Mater. Sci. Eng. A*, vol. 234–236, pp. 877–879, Aug. 1997.
- [201] A. Nitz and E. Nembach, “Anisotropy of the critical resolved shear stress of a  $\gamma'$ (47 vol.%) - hardened nickel-base superalloy and its constituent  $\gamma$ - and  $\gamma'$ -single-phases,” *Mater. Sci. Eng. A*, vol. 234–236, pp. 684–686, Aug. 1997.
- [202] D. Bettge and W. Österle, “‘Cube slip’ in near-[111] oriented specimens of a single-crystal nickel-base superalloy,” *Scr. Mater.*, vol. 40, no. 4, pp. 389–395, Jan. 1999.
- [203] J. Rolph *et al.*, “Residual Stress Evolution during Manufacture of Aerospace Forgings,” in *Superalloys 2012*, Hoboken, NJ, USA: John Wiley & Sons, Inc., 2012, pp. 881–891.
- [204] B. M. B. Grant, H. J. Stone, P. J. Withers, and M. Preuss, “High-temperature strain field measurement using digital image correlation,” *J. Strain Anal. Eng. Des.*, vol. 44, no. 4, pp. 263–271, May 2009.
- [205] T. P. Gabb, P. T. Kantzos, J. Telesman, J. Gayda, C. K. Sudbrack, and B. Palsa, “Fatigue resistance of the grain size transition zone in a dual microstructure superalloy disk,” *Int. J. Fatigue*, vol. 33, no. 3, pp. 414–426, Mar. 2011.
- [206] SAE-AMS 4911H, “Titanium Alloy, Sheet, Strip, and Plate, 6Al-4V, Annealed,” SAE International, Warrendale, PA, USA, 1995, p. 1.
- [207] S. L. R. da Silva, L. O. Kerber, L. Amaral, and C. A. dos Santos, “X-ray diffraction measurements of plasma-nitrided Ti-6Al-4V,” *Surf. Coatings Technol.*, vol. 116–119, pp. 342–346, 1999.
- [208] M. B. Ivanov, S. S. Manokhin, Y. R. Kolobov, and D. A. Nechayenko, “Phase composition and microstructure of Ti-6Al-4V alloy after hydrogen-plastic working,” *Mater. Phys. Mech.*, vol. 10, no. 1–2, pp. 62–71, 2010.
- [209] A. K. Swarnakar, O. Van Der Biest, and B. Baufeld, “Thermal expansion and lattice parameters of shaped metal deposited Ti-6Al-4V,” *J. Alloys Compd.*, vol. 509, no. 6, pp. 2723–2728, 2011.
- [210] L. Thijs, F. Verhaeghe, T. Craeghs, J. Van Humbeeck, and J. P. Kruth, “A study of the microstructural evolution during selective laser melting of Ti-6Al-4V,” *Acta Mater.*, vol. 58, no. 9, pp. 3303–3312, 2010.

- [211] J. V. Bernier, J.-S. Park, A. L. Pilchak, M. G. Glavicic, and M. P. Miller, “Measuring Stress Distributions in Ti-6Al-4V Using Synchrotron X-Ray Diffraction,” *Metall. Mater. Trans. A*, vol. 39, no. 13, pp. 3120–3133, 2008.
- [212] T. Ozturk and A. D. Rollett, “Effect of microstructure on the elasto-viscoplastic deformation of dual phase titanium structures,” *Comput. Mech.*, pp. 1–16, 2017.
- [213] K. M. Knowles and P. R. Howie, “The Directional Dependence of Elastic Stiffness and Compliance Shear Coefficients and Shear Moduli in Cubic Materials,” *J. Elast.*, vol. 120, no. 1, pp. 87–108, 2015.
- [214] D. Tromans, “Elastic Anisotropy of HCP Metal Crystals and Polycrystals,” *Int. J. Res. Rev. Appl. Sci.*, vol. 6, no. March, pp. 462–483, 2011.
- [215] J. Tracy, A. Waas, and S. Daly, “A new experimental approach for in situ damage assessment in fibrous ceramic matrix composites at high temperature,” *J. Am. Ceram. Soc.*, vol. 98, no. 6, pp. 1898–1906, 2015.
- [216] A. W. Mello, T. A. Book, A. Nicolas, S. E. Otto, C. J. Gilpin, and M. D. Sangid, “Distortion Correction Protocol for Digital Image Correlation after Scanning Electron Microscopy: Emphasis on Long Duration and Ex-Situ Experiments,” *Exp. Mech.*, vol. 57, no. 9, pp. 1395–1409, 2017.
- [217] C. P. Przybyla, “Microstructure-Sensitive Extreme Value Probabilities of Fatigue in Advanced Engineering Alloys,” Georgia Institute of Technology, 2010.
- [218] J. A. Medina Perilla and J. Gil Sevillano, “Two-dimensional sections of the yield locus of a Ti-6Al-4V alloy with a strong transverse-type crystallographic  $\alpha$ -texture,” *Mater. Sci. Eng. A*, vol. 201, no. 1–2, pp. 103–110, Oct. 1995.
- [219] J. J. Fundenberger, M. J. Philippe, F. Wagner, and C. Esling, “Modelling and prediction of mechanical properties for materials with hexagonal symmetry (zinc, titanium and zirconium alloys),” *Acta Mater.*, vol. 45, no. 10, pp. 4041–4055, Oct. 1997.
- [220] K. Kapoor, Y. S. J. Yoo, T. A. Book, J. P. Kacher, and M. D. Sangid, “Incorporating grain-level residual stresses and validating a crystal plasticity model of a two-phase Ti-6Al-4 V alloy produced via additive manufacturing,” *J. Mech. Phys. Solids*, vol. 121, pp. 447–462, Dec. 2018.
- [221] F. Di Gioacchino and J. Quinta da Fonseca, “Plastic Strain Mapping with Sub-micron Resolution Using Digital Image Correlation,” *Exp. Mech.*, vol. 53, no. 5, pp. 743–754, 2013.

- [222] S. Joseph, T. C. Lindley, and D. Dye, "Dislocation interactions and crack nucleation in a fatigued near-alpha titanium alloy," *Int. J. Plast.*, no. June, pp. 0–1, 2018.
- [223] M. R. Bache, "A review of dwell sensitive fatigue in titanium alloys: The role of microstructure, texture and operating conditions," *Int. J. Fatigue*, vol. 25, no. 9–11, pp. 1079–1087, 2003.
- [224] M. R. Bache and W. J. Evans, "Dwell Sensitive Fatigue Response of Titanium Alloys for Power Plant Applications," *J. Eng. Gas Turbines Power*, vol. 125, no. 1, p. 241, 2003.
- [225] V. Sinha, M. J. Mills, and J. C. Williams, "Crystallography of fracture facets in a near-alpha titanium alloy," *Metall. Mater. Trans. A*, vol. 37, no. 6, pp. 2015–2026, 2006.
- [226] J. R. Mayeur and D. L. McDowell, "A three-dimensional crystal plasticity model for duplex Ti-6Al-4V," *Int. J. Plast.*, vol. 23, no. 9, pp. 1457–1485, 2007.